FULL-SCALE SIMULATION OF MULTIPLE SCATTERING OF ELASTIC WAVES IN FIBER REINFORCED COMPOSITES

by

Liang-Wu Cai

B.S., Applied Mechanics
The University of Science and Technology of China (1985)

M.E., Solid Mechanics
The Chinese Academy of Sciences (1988)

Submitted to the Department of Mechanical Engineering
in partial fulfillment of the requirements for the degree of

DOCTOR OF SCIENCE IN MECHANICAL ENGINEERING

at the

Massachusetts Institute of Technology

June 1998

Signature of Author: _____
Department of Mechanical Engineering
May 11, 1998

Certified by: _____
James H. Williams, Jr.
SEPTE Professor of Engineering
Thesis Supervisor

Accepted by: _____
Anthony T. Patera, Acting Chairman
Departmental Committee on Graduate Studies

FULL-SCALE SIMULATION OF MULTIPLE SCATTERING OF ELASTIC WAVES IN FIBER REINFORCED COMPOSITES

by

Liang-Wu Cai

Submitted to the Department of Mechanical Engineering on May 11, 1998
in partial fulfillment of the requirements for the degree of
Doctor of Science in Mechanical Engineering

ABSTRACT

Multiple scattering phenomena are of enormous interest in many disciplines, especially nondestructive evaluation of materials. Starting from a single fiber scattering model, a computational system is built for conducting full-scale deterministic simulations of multiple scattering of elastic waves in fiber reinforced composites.

The computational system is based on two theoretical developments. The first is the formulation of two-dimensional multiple scattering problems involving arbitrary numbers of scatterers. The resulting solutions are analytically exact, for scatterers that may be similar or dissimilar. The second theoretical development, which we name *scatterer polymerization*, enables assemblages of arbitrary numbers of scatterers to be modeled as single scatterers in sequential analyses, while maintaining analytically exact solutions.

Both the multiple scattering solutions and the scatterer polymerization methodology can be used as independent tools to analyze multiple scattering problems. Each has been implemented and verified. By combining these tools, analytically exact solutions have been obtained for multiple scattering phenomena in models of composites containing thousands of fibers. The feasibility and the procedures for such full-scale simulations are demonstrated.

Finally, as a comprehensive example, a ceramic-fiber reinforced metal-matrix composite plate is modeled, and the effects on the scattered waves due to changing microstructural parameters of the composite are examined.

Thesis Committee:

Professor Triantaphyllos R. Akylas (Mechanical Engineering)
Professor Henrik Schmidt (Ocean Engineering)
Professor James H. Williams, Jr. (Committee Chairman, Mechanical Engineering)

Acknowledgments

I am extremely grateful to my thesis advisor Professor James H. Williams, Jr. for his guidance, support and understanding, both academically and personally, for the past six years. His magnanimous smile and faith in me during my "low time" made my tumultuous years in Hell so much easier to endure—in fact something to linger—as compared to other aspects of my life, if there is such a thing at all.

I am also very grateful to Professors Triantaphyllos R. Akylas and Henrik Schmidt for their insightful advice while serving as my thesis committee members.

I would like to gratefully acknowledge the financial support provided by Dr. Yapa D. S. Rajapakse of the Office of Naval Research that made this research possible.

I would like to express my gratitude to former and current members of the Composite Materials and Nondestructice Evaluation Lab, Dr. Hyunjune Yim, Mr. Steve Cimaszewski, Dr. Vojo Kecman, Professor Raymond J. Nagem, for the quality time we have shared, and to our secretaries Ms. Laurie McLaughlin and Ms. Debra Blanchard, for all their support that made everything smooth.

Many of my friends outside the Lab help, in one way or another, to make my MIT years a memorable experience. My thanks go to Guoling Shen and Qinghua Zheng for the countless all-nighters we pulled together; Dan Li for guiding us while chasing the Sun on Cape Cod; Feng Ruan for hosting poker nights at Ashdown; Wenjie Hu for managing the gang; Yining Zhang for enticing me with the scent of Wall Street; Huaiyu Fan for organizing the volleyball club; Yifang Gong and Jie Yu for serving cozy meals above the Royal East; Yiping Geng for always being there when needed; and Liping Li for the comradeship during the Doctoral Qualifiers.

Finally, I would like to thank a small hacking group of East Campus for showing me some unorthodox perspectives of MIT to complete my MIT experience.

To My Parents

Table of Contents

1

Thesis Introduction

Contents:

1-1 Introduction

Significant developments in engineering applications of fiber reinforced composite materials have occurred during the past two decades. One of the advantages of fiber reinforced composites over conventional materials is that, as micro-structurually engineered materials, fiber reinforced composites allow engineers to design a specific material for a specific purpose by altering microscopic parameters. Designing of materials requires knowledge relating the properties and parameters at the microscopic (fiber) scale and the macroscopic scale. Such knowledge are in general acquired through experimental testings and measurements or analytical modelings and simulations.

In many nondestructive evaluation (NDE) techniques, the procedure involves sending energy into the material and measuring the corresponding response. Such NDE techniques rely on understanding wave phenomena in composite materials since interpretation of test data is frequently an inverse wave propagation problem. Thus, a better understanding of the NDE of composites involves the analytical modeling and simulation of wave phenomena in composites.

Traditionally, analytical predictions of macroscopic properties of composites using micromechanics models have been based on statistical or probabilistic assumptions. Such assumptions omit many microscopic parameters and localized variations. Such assumptions frequently lead to "averaged" results in a statistical or probabilistic sense, which are frequrently not sufficiently accurate for some applications. To circumvent such assumptions, full-scale analyses or simulations of a particular composite may be more desirable.

Recent developments in computer technologies provide computational powers that are magnitudes greater than those of a decade ago. Such computation power enables materials engineers to simulate some wave analyses of fiber reinforced composites in full scale. This thesis is an attempt to develop a computational system — via a sombination theoretical and computational tools — that would allow engineers to deterministically perform simulations of the scattering of elastic waves within fiber reinforced composites in full scale. The qualifying term "full-scale" means that the computational model should contain a sufficiently large number of fibers such that the full model is macroscopic in size.

1-2 Approaches

1-2.1 Theoretical Aspects

Wave scattering phenomena in fiber reinforced composites involve both single and multiple scattering of elastic waves. In general, *scattering* of a wave refers to the phenomenon in which tlie wave changes its propagation direction or splits into several waves upon encountering a physical boundary, which may be an anomoy, along its propagation path. The abnomoly is referred to as a *scatterer. Single scattering* and *multiple scattering* are the conventional terminologies to distinguish the phenomena involving different numbers of scatterers.

Single scattering problems have been studied extensively during the past few decades. Some of the classical theories have been summarized in the treatise by Pao and Mow[1], and a more recent review has been written by Hackman[2]. The emphasize of this thesis is on multiple-scattering phenomena, and it is assumed that single-scattering problems for the scatterers under consideration have been solved.

Several approaches for analyzing multiple-scattering problems exist. One approach is the eigenfunction expansion technique for variable-separable problems. Within this approach, one of the solution procedures is to express the total wave in the field in each scatterer's local coordinate system, then to match the boundary conditions for every scatterer. Following this line, Bose and Mal obtained solutions for an arbitrary number of identical circular elastic cylinders, for anti-plane shear (SH) waves[3] and longitudinal (P) and in-plane shear (SV) waves[4]. Sancar and Pao[5] obtained a solution for two cylindrical cavities of different radii subjected to P/SV waves.

Another procedure in the eigenfunction expansion approach is "ordered scattering", used by Twersky[6] for acoustic waves. This is an iterative procedure in which the boundary-value problem is decomposed into different orders. Using ordered scattering, Cheng[7] solved a problem involving an arbitrary number of identical circular rigid cylinders subjected to elastic P/SV waves.

A second approach is the "T-matrix approach." The T-matrix, introduced by Waterman[8], represents a linear transformation between the wave expansion coefficients of the scattered and incident waves. Waterman used the integral equation method to obtain the T-matrix of a scatterer that could not be analyzed by the separation-of-variables method. Directly applying Waterman's approach for multiple-scatterer problems to acoustic waves was accomplished by Peterson and Ström[9] and was extended to elastic waves by Boström[10].

Realizing that the T-matrix for a scatterer remains the same in a multiple-scatterer setting, Varadan *et al.* proposed a significantly simpler T-matrix formulation for the case of an arbitrary number of identical elastic cylinders having arbitrary

cross sections, for both SH waves[11] and P/SV waves[12].

In this thesis, the theoretical developments are centered around the T-matrix concept.

In essence, a T-matrix represents the complete solution, in the form of a matrix, to the single-scattering problem. Such a representation allows the mathematical formulation of a multiple-scattering problem, such that a generally complicated boundary-value problem of wave scattering is simplified into a combination of elementary matrix manipulations, where the final solution form remains the same for all kinds of classical waves.

The theoretical developments in this thesis consist of three stages. In the first, the concept of the T-matrix itself is clarified, and its properties are explored. In the second, an analytically exact solution for a general two-dimensional multiple scattering problem is derived, implemented and verified. Lastly, based on the solution found in the second stage, the concept of the T-matrix is extended to represent an assemblage of physical scatterers. This extended representation of the T-matrix overcomes a major numerical obstacle to full-scale simulation of multiple-scattering in composites.

1-2.2 Computational Aspects

Numerical results on multiple-scattering problems in the literature are scarce, but fall basically into two categories. In the first category, bulk properties of a material that contains a large number of identical scatterers, such as fiber reinforced composites, are evaluated in a probabilistic sense[3,4,11,17]. In the second category, spectra or scattering cross-sections for a deterministic assemblage of scatterers are evaluated. For cylindrical scatterers, Olaofe[13] calculated the electromagnetic scattering cross section of two identical dielectric cylinders. Young and Bertrand[14] computed and measured backscattering of plane acoustic waves by two identical rigid cylinders. Radlinski and Meyers[15] computed the radiation of a larger cylinder surrounded by several smaller cylinders. Scharstein[16] computed the acoustic scattering by two cylinders of different radii, which is similar to the configuration studied by Sancar and Pao[5].

The approach taken in this thesis falls into the second category. Unfortunately, during the literature survey for this study, a closer look at the numerical results in this category revealed that they either involve additional approximations in the formulation or are presented for a particular parameter in a particular problem. Hence no numerical results have been found to be directly comparable to those in this thesis. For this reason, the computational aspect of this thesis emphasizes the verification of numerical results based on physical principles or theorems. The computer implementation of the theoretical developments in this thesis is aimed at the best cross-platform portability.

The computer codes for this thesis are primarily written in the C^{++} programming language. The well-organized object-oriented programming style embedded in the C^{++} language is well suited for representing each scatterer as a single object in the computer program. This language also allows custom-defined data types such as complex numbers and matrices such that the computer programs correspond more directly to the represented mathematical equations. These benefits might appear trivial as many other computer programming languages are similarly capable of performing the same tasks of scientific computation, nevertheless they assist in avoiding some potential coding errors, and in turn ensure their correctness. The computer programs develpoed for this thesis have been tested on a Sun SPARC 5 workstation using Gnu and Cygnus C^{++} compilers, a Silicon Graphics Indigo^2 workstation using SGI's C^{++} compiler, and a PC using Microsoft's Visual C^{++} compiler.

1-2.3 Choice of Numerical Examples

In choosing the examples, it was noted that the fiber-matrix interface in composites possesses very distinctive physical properties from either of the two constituents, due to either chemical interactions between the constituents or coating treatments in the material processing to improve bonding. In some micromechanical models, this distinctive layer at the interface is treated as a third phase of the material constituents and is called the *interphase*. The interphase plays a pivotal roll in some of the macroscopic properties of the composites, but characterizing its properties is a challenging task. In fact, the ultimate goal of our current project, of which this thesis is a part, is to explore the possibilities of using ultrasonic waves to characterize the interphase.

With this goal in mind, numerical examples throughout the thesis are variations of such a micromechanical model, called the *fiber-interphase-matrix model*. This thesis concentrates on one particular common material system of known (fixed) properties of the fiber and the matrix. The characteristics of the interphase, geometric or physical, are hypothesized. It is expected that by solving forward problems involving hypothetically varying characteristics of the interphase, better understanding of the inverse problem can be achieved.

Neverhteless, the emphasis of this thesis is building the computational systems for performing deterministic full-scale simulations.

1-3 Thesis Organization

This thesis contains nine chapters.

Chapter 1 outlines the objectives of the research and the basic approaches to the problem.

Chapter 2 serves as a reference in which the fundamentals of elastic wave scattering are reviewed. The review also defines a set of mathematical notation to be used throughout the thesis. The single-scattering problem for our particular model, *fiber-interphase-matrix model*, is solved in this chapter. For brevity, no numerical results are explored.

Chapter 3 reviews a central concept of the thesis: the T-matrix. Some ambiguities in the literature are rectified, and some properties of the T-matrix, as imposed by physical laws or by the geometry of the scatterer itself, are explored. These properties effort the porpose of checking the accuracy of numerical computations in later chapters.

Chapter 4 presents an analytically exact solution for a general two-dimensional multiple-scattering problem. The solution is specifically formulated for the scattering of elastic waves, for both the SH and P/SV wave cases. The physical process envisioned therein and followed by the solution procedure is equally applicable to multiple-scattering problems of any other classical wave fields.

Chapter 5 discusses the implementation of the multiple-scattering solution in Chapter 4. The implimentation is limited to the case of SH waves. Various solution forms are all implemented and verified, and their computational characteristics are examined. Numerical examples are also presented.

Chapter 6 presents yet another theoretical development called the *scatterer polymerization* methodology. This methodology further extends the power of the multiple-scattering solution. It allows a multiple-scattering problem involving a large number of scatterers to be decomposed into several multiple-scattering problems involving smaller numbers of scatterers. In essence, it folds the problem size and makes it possible for a typical desk-top computer to analyze a large number of scatterers. The implementation and verification of the methodology are also discussed, as well as its computational characteristics.

Chapter 7 explores the procedure to perform a full-scale deterministic simulation via the multiple-scattering solution and the scatterer polymerization methodology developed in earlier chapters. It also establishes the relationships between the simulated field quantities and experimentally measurable parameters.

Chapter 8 is a comprehensive example of the full-scale deterministic simulation. It explores, through simulations, the relations between several parameters of the micromechanics model of a composite plate and several characteristics of the response spectra.

Chapter 9 summarizes the achievements in this thesis and discusses the directions of future work.

References

[1] Y.-H. Pao, C.-C. Mow, *Diffraction of Elastic Waves and Dynamic Stress Concentrations,* Crane Russak & Co., New York, 1971.

[2] R. H. Hackman, Acoustic scattering of elastic waves, *Physical Acoustics, Vol. 22: Underwater Scattering and Radiation,* A. D. Pierce & R. N. Thurston eds., pp. 1–194, Academic Press, Boston, 1993.

[3] S.K. Bose, A.K. Mal, Longitudinal Shear Waves in a Fiber-Reinforced Composite, *Int. J. Solids & Struct.*, **9**, 1075–1085, 1973.

[4] S.K. Bose, A.K. Mal, Elastic Waves in a Fiber-Reinforced Composite, *J. Mech. Phys. Solids,* **22**, 217–229, 1974.

[5] S. Sancar, Y.-H. Pao, Spectrual analysis of elastic pulses backscattered from two cylindrical cavities in a solid, part I, and part II *J. Acoust. Soc. Am.* **69**, 1591–1609, 1981.

[6] V. Twersky, Multiple scattering of radiation by an arbitrary configuration of parallel cylinders *J. Acoust. Soc. Am.*, **24**, 42–46, 1952.

[7] S. L. Cheng, Multiple Scattering of elastic waves by parallel cylinders, *Trans. ASME, J. Appl. Mech.*, **36**, 523–527, 1969.

[8] P. C. Waterman, New formulation of acoustic scattering, *J. Acoust. Soc. Am.*, **45**, 1417–1429, 1969.

[9] B. Peterson, S. Ström, Matrix formulation of acoustic scattering from an arbitrary number of scatterers, *J. Acoust. Soc. Am.*, **56**, 771–780, 1974.

[10] A. Boström, Multiple-scattering of elastic waves by bounded obstacles, *J. Acoust. Soc. Am.*, **67**, 399–413, 1980.

[11] V. K. Varadan, V. V. Varadan, Y.-H. Pao, Multiple scattering of elastic waves by cylinders of arbitrary cross section. I. SH waves, *J. Acoust. Soc. Am.*, **63**, 1310–1319, 1978.

[12] V. K. Varadan, Y. Ma, V. V. Varadan, Multiple scattering of compressional and shear waves by fiber reinforced composite materials, *J. Acoust. Soc. Am.*, **80**, 333–339, 1986.

[13] G. O. Olaofe, Scattering by two cylinders, *Radio Science,* **5**, 1351–1360, 1970.

[14] J. W. Young, J. C. Bertran, Multiple-scattering by two cylinders, *J. Acoust. Soc. Am.* **58**, 1190–1195, 1975.

[15] R. P. Radlinski, T. J. Meyers, Radiation patterns and radiation impedances of a pulsating cylinder surrounded by a circular cage of parallel cylindrical rods, *J. Acoust. Soc. Am.* **56**, 842–848, 1974.

[16] R. W. Scharstein, Acoustic scattering from two parallel soft cylinders, *Proc. of the IEEE Southeast Conference,* Pisataway, New Jersey, vol. **2**, 534–537, 1992.

[17] M. F. McCarthy, M. M. Carrol, Multiple scattering of SH waves by randomly distributed dissimilar scatterers, In *Wave Phenomena: Modern Theory and Applications,* C. Rogers, T. B. Moodie eds., pp. 433–451, Elisver-Science Publishers, North-Holland, 1984.

2

Basics of Elastic Wave Scattering

Abstract: *The purposes of this chapter are to build a basic set of vocabulary for the subject of elastic wave scattering and to serve as a reference of useful formulas and equations. Basic concepts and equations are introduced. Some single scatterer problems, their solutions and numerical results are presented.*

Contents:

Nomenclature

General Conventions

- Matrices are denoted by bold-faced symbols; symbols for column matrices are enclosed by flower brackets ({}); symbols for rectangular matrices are enclosed by square brackets ([]).
- When referring to a matrix entry, the entry's indicial number is to appear as subscript(s) *outside* the brackets. This distinguishes the indicial subscript(s) from the subscript(s), if any, associated with the entire matrix.

Symbols

$\{A\}, \{B\}, \cdots$	Wave expansion coefficient (column) matrices.
$\mathfrak{C}_n(x)$	Formal notation for cylindrical function at order n, which can be any one of the followings: $J_n(x)$, $Y_n(x)$, $H_n^{(1)}(x)$, or $H_n^{(2)}(x)$.
c_p, c_s	Wave speeds of the longitudinal and shear waves, respectively.
$\mathfrak{E}(r)$	Differential wave expansion basis function, as defined in Appendix 2-C.
$H_n^{(1)}(x), H_n^{(2)}(x)$	Hankel function of the first and second kinds, respectively, and order n.
$\{\boldsymbol{H}(r,\theta)\}$	Singular (Hankel) wave expansion basis matrix.
$\hat{\imath}$	Unit of imaginary number, $\hat{\imath} = \sqrt{-1}$.
Im	Imaginary part of a complex number.
$J_n(x)$	Bessel function of the first kind and order n.
$\{\boldsymbol{J}(r,\theta)\}$	Regular wave expansion basis matrix, same as $\{\Re\boldsymbol{H}(r,\theta)\}$.
κ, k	Wave numbers, for longitudinal and shear waves, respectively.
$\Re$	Regular counterpart of a singular function or functional basis.
Re	Real part of a complex number.
$[\boldsymbol{T}]$	T-matrix for a scatterer.
$\boldsymbol{u}$	Displacement of a field point. Its components are u, v and w.
$Y_n(x)$	Bessel function of the second kind and order n.
δ_{ij}	Kronecker delta: equals unity when $i = j$ and equals 0 otherwise.
$\boldsymbol{\epsilon}$	Strain tensor. Components of engineering shear strain are denoted as γ.
λ, μ	Lamé constants of an elastic material.
Φ	Scalar displacement potential.
Ψ	The z-component of vector displacement potential.
ϕ	Spatial factor (complex magnitude) of displacement w for SH wave cases.
φ	Spatial factor (complex magnitude) of Φ, $\Phi(\boldsymbol{r},t) = \varphi(\boldsymbol{r})\mathrm{e}^{-\hat{\imath}\omega t}$.
ψ	Spatial factor (complex magnitude) of Ψ, $\Psi(\boldsymbol{r},t) = \psi(\boldsymbol{r})\mathrm{e}^{-\hat{\imath}\omega t}$.
$\boldsymbol{\sigma}$	Stress tensor. Components of shear stress are denoted as τ.
ω	Circular (angular) frequency of a time-harmonic wave.

Superscripts

inc, total, s, r, i	Quantities that belong to the incident, total, scattered, refracted waves, and the waves in the interphase, respectively.
P, S	Characteristic of or pertinent to P and S waves, respectively.
$*$	Conjugate transpose of a matrix: $[M]^* = \overline{[M]}^T = \overline{[M]^T}$

Subscripts

m, f, i	Physical quantities that belong to the matrix, the fiber and the interphase.

2-1 Introduction

The scattering of an elastic wave is a process during which the wave interacts with one or more discontinuities or boundaries and generates waves that contain components that may propagate in all directions. The study of scattering phenomena is a narrow branch of wave mechanics; any discussion of scattering phenomena will inevitably involve a tremendous amount of terminologies of wave mechanics. Therefore, the *first objective* of this chapter is to build a small set of vocabulary for the subject. The selection of the topics is restricted to those that are specifically related to scattering and are essential to the developments in later chapters.

As stated in Chapter 1, the emphasis of this entire thesis is on building a methodology to simulate multiple scattering of elastic waves in fiber reinforced composites. In such a multiple-scattering analysis, one of the assumptions that might not be emphasized sufficiently is that single-scatterer problems have been solved. Therefore, the *second objective* of this chapter is to review some single-scatterer problems for the models that will be used later. Such a review also serves as a reference for related formulas, equations, and mathematical notation.

The structure of this chapter is as follows: Section 2-2 first introduces the basic concepts, equations, notation and observations concerning the wave motion in elastic solids; it then focuses on the steady-state governing equations and their complete solutions in various forms. A collection of single-scatterer solutions is presented in Section 2-3, along with some numerical results. Finally, in Section 2-4, the principles of energy conservation and reciprocity for scattering problems are discussed.

2-2 Basics of Elastic Wave Motion

In this section, basic concepts and equations of the classical theory of elastodynamics are briefly reviewed. Comprehensive theoretical presentations can be found in many textbooks on elastic waves, such as [1] and [2].

2-2.1 Basic Equations for Elastic Solids

For a linearly elastic medium, the governing equations consist of the following[1], in Einstein's tensor notation,

$$\text{Equations of motion:} \qquad \rho \ddot{u}_i = \sigma_{ij,j} + \rho f_i \tag{2-1}$$

$$\text{Constitutive equations:} \qquad \sigma_{ij} = \lambda \varepsilon_{kk} \delta_{ij} + 2\mu \varepsilon_{ij} \tag{2-2}$$

$$\text{Geometry equations:} \qquad \varepsilon_{ij} = \tfrac{1}{2}\left(u_{i,j} + u_{j,i}\right) \tag{2-3}$$

where ρ, λ and μ are the density and two Lamé constants of the medium, respectively, σ and ε are the stress and strain tensors at a field point, respectively, $\boldsymbol{u}$ is the displacement vector of a field point, $\boldsymbol{f}$ is the externally applied body force per unit mass of the medium, and δ_{ij} is the *Kronecker delta* which is defined as

$$\delta_{ij} = \begin{cases} 1 & \text{when } i = j \\ 0 & \text{when } i \neq j \end{cases} \tag{2-4}$$

In this thesis, only cases in which the body force vanishes are considered.

2-2.2 Wave Equations for Displacement Potentials

In terms of the displacement $\boldsymbol{u}$, the equation of motion, known as *Navier's equation*, can be written as[1] (for the case in which the body force vanishes)

$$(\lambda + \mu)\nabla\nabla \cdot \boldsymbol{u} + \nabla^2 \boldsymbol{u} = \rho \ddot{\boldsymbol{u}} \tag{2-5}$$

By recalling *Helmholtz's theorem* for vector decomposition[3] in the field theory, the displacement $\boldsymbol{u}$ can be written as

$$\boldsymbol{u} = \nabla\Phi + \nabla \times \boldsymbol{H} \qquad \nabla \cdot \boldsymbol{H} = 0 \tag{2-6}$$

By substituting eqn. (2–6) into eqn. (2–5), Navier's equation can be equivalently written into the following set of two wave equations[1]

$$\frac{\partial^2 \Phi}{\partial t^2} = c_p^2 \nabla^2 \Phi \tag{2-7}$$

$$\frac{\partial^2 \boldsymbol{H}}{\partial t^2} = c_s^2 \nabla^2 \boldsymbol{H} \tag{2-8}$$

where

$$c_p^2 = \frac{\lambda + 2\mu}{\rho} \qquad \text{and} \qquad c_s^2 = \frac{\mu}{\rho} \tag{2-9}$$

Equations (2–7) and (2–8) imply that two types of waves can coexist in an elastic medium. They propagate independently at different speeds. In general, upon encountering a material discontinuity or a boundary, one type of wave will generate both types of waves, a phenomenon that is particular to elastic waves and is known as *mode conversion.*

Due to eqn. (2–6), Φ and $\boldsymbol{H}$ are called the *scalar displacement potential* and the *vector displacement potential*, respectively.

The wave associated with the scalar potential Φ propagates at the speed c_p. This wave is called by such names as *dilatational wave*, *irrotational wave*, *pressure wave*, *etc.*, and is referred to as the *P wave* throughout the thesis. It is also sometimes called the *primary wave* as the P wave is the faster of the two waves.

The wave associated with the vector potential $\boldsymbol{H}$ propagates at the speed c_s. This wave is called by such names as *equivoluminal wave*, *distortional wave*, *shear wave*, *etc.*, and is referred to as the *S wave* throughout the thesis. It is also sometimes called the *secondary wave* as the S wave is the slower of the two waves.

It can be further shown[1] that the P wave propagates along the same direction as the displacement, and that the S wave propagates in a direction that is perpendicular to the displacement. For this reason, the P wave is also called the *longitudinal wave*, and the S wave is also called the *transverse wave*. The displacement direction of the wave is called the *polarization direction* of the wave.

2-2.3 Problems in Two Dimensional Space

Problems modeled in a two-dimensional space are usually problems in which the displacements are independent of one of the coordinates. Without loss of generality, the z coordinate in a Cartesian coordinate system is conventionally chosen as the independent coordinate, such that the displacement can be expressed as $\boldsymbol{u} = \boldsymbol{u}(x, y, t)$ and that the wave propagates in the xy-plane. In most cases, it is also assumed that the medium is of infinite extent in the z direction.

It can be shown[1] that a 2-D problem can be readily decomposed, due to the linearity of the system, into two problems noted below.

Anti-Plane Problem—SH Waves

One of the problems is when the displacements conform to the following form:

$$u = v = 0 \qquad w = w(x, y, t) \tag{2–10}$$

That is, the only displacement component is the out-of-plane displacement; and the wave propagates in a direction perpendicular to the displacement, a characteristic of the S wave. Conventionally (in seismology), this type of wave is called the *SH wave* where H stands for *horizontally polarized* when the xz-plane lies horizontally and the y-axis points vertically. For 2-D SH wave problems, no mode conversions occur during encountering with the interfaces or boundaries.

It can be shown[1] that in such cases, the contributing displacement potentials are the H_x and H_y components of the vector potential $\boldsymbol{H}$. However, if the displacements in eqn. (2–10) are substituted into eqn. (2–5), Navier's equation reduces to the following single wave equation

$$\frac{\partial^2 w}{\partial t^2} = c_s^2 \nabla^2 w \tag{2–11}$$

Therefore, there is no need to solve the anti-plane problem via displacement potentials, which would require solving two wave equations for H_x and H_y.

Plane-Strain Problem—P/SV Waves

Another problem is when the displacements conform to the following form:

$$u = u(x, y, t) \qquad v = v(x, y, t) \qquad w = 0 \tag{2–12}$$

This is the case in which the displacement components are in the same plane, the xy-plane, as the wave's propagation. In general, both P and S waves may coexist. Conventionally (in seismology), the S wave in this case is called the *SV wave* where V stands for *vertically polarized.*

It can be shown[1] that in such cases, only the scalar displacement potential Φ and the H_z component of the vector displacement potential contribute to the wave fields. By denoting the H_z component of the vector potential as Ψ, the problem is usually formulated by solving the following set of two wave equations

$$\frac{\partial^2 \Phi}{\partial t^2} = c_p^2 \nabla^2 \Phi \tag{2-13}$$

$$\frac{\partial^2 \Psi}{\partial t^2} = c_s^2 \nabla^2 \Psi \tag{2-14}$$

2-2.4 Steady State and Helmholtz Equations

Often, the steady-state response of a system due to a time harmonic input is desired. More often, the steady-state response is first sought since it brings out important physics of the system yet avoids the complexity introduced by the time dependency. The scattering problems studied in this thesis are confined to steady-state responses. Once the steady-state solution has been obtained, it is possible to obtain the time-dependent transient solution by a Fourier transformation.

Analyses of the steady-state responses are often called the *frequency domain analyses* since a major parameter characterizing the input is the frequency of the time-harmonic input. In such analyses, complex notations of field quantities are usually adopted.

Complex Notation

In general, a time-harmonic physical quantity can be expressed as

$$A(t) = A_0 \cos(\omega t + \alpha) = Re\{B e^{-i\omega t}\} \tag{2-15}$$

where $A_0 > 0$ is the *(real) amplitude*, ω is the *circular frequency* or the *angular frequency*, α is the *phase*, B is a complex number called the *complex amplitude*, and $\hat{\imath}$ is the unit of imaginary numbers, $\hat{\imath} = \sqrt{-1}$. Obviously,

$$A_0 \cos\alpha = Re\{B\} \qquad A_0 \sin\alpha = -Im\{B\} \tag{2-16}$$

and

$$A_0 = |B| \tag{2-17}$$

where Re and Im denote the real and imaginary parts of a complex number, respectively, and $|\cdot|$ denotes the modulus of a complex number.

In the *complex notation*, the symbol "Re" is omitted in eqn. (2–15) to write

$$A(t) = B e^{-i\omega t} \tag{2-18}$$

with the understanding that only the real part is sought. In other words, when the expression for any real field quantity is desired, it is necessary to convert the complex notation back to the real form as in eqn. (2–15).

Helmholtz Equations

When the steady-state response to a time-harmonic wave is sought, in general, the response, say, the displacement $\boldsymbol{u}$, is assumed to be of the form

$$\boldsymbol{u} = \boldsymbol{u}(\boldsymbol{r}, t) = \boldsymbol{U}(\boldsymbol{r})\mathrm{e}^{-i\omega t} \tag{2–19}$$

And in writing eqn. (2–19), it is implied that all field quantities will be addressed in complex notations. $\boldsymbol{U}(\boldsymbol{r})$ is sometimes called the *spatial factor* of $\boldsymbol{u}(\boldsymbol{r}, t)$.

In fact, in the steady state, all field quantities such as the displacement potentials possess the same temporal factor $\mathrm{e}^{-i\omega t}$. That is, the potentials involved in eqns. (2–11), (2–13) and (2–14) can be written as

$$w(\boldsymbol{r}, t) = \phi(\boldsymbol{r})\mathrm{e}^{-i\omega t} \tag{2–20}$$

$$\Phi(\boldsymbol{r}, t) = \varphi(\boldsymbol{r})\mathrm{e}^{-i\omega t} \tag{2–21}$$

$$\Psi(\boldsymbol{r}, t) = \psi(\boldsymbol{r})\mathrm{e}^{-i\omega t} \tag{2–22}$$

and their governing equations, eqns. (2–11), (2–13) and (2–14), become the *Helmholtz equations*

$$\nabla^2\phi + k^2\phi = 0 \tag{2–23}$$

$$\nabla^2\varphi + \kappa^2\varphi = 0 \tag{2–24}$$

$$\nabla^2\psi + k^2\psi = 0 \tag{2–25}$$

where

$$\kappa = \frac{\omega}{c_p} = \omega\sqrt{\frac{\rho}{\lambda + 2\mu}} \qquad \text{and} \qquad k = \frac{\omega}{c_s} = \omega\sqrt{\frac{\rho}{\mu}} \tag{2–26}$$

are the *wave numbers* of the longitudinal and shear waves, respectively.

2-2.5 General Solution of Helmholtz Equation

Without loss of generality, the general solution to eqn. (2–23) is derived in a polar (cylindrical) coordinate system. In polar coordinates, $\phi = \phi(r, \theta)$, and eqn. (2–23) can be written as

$$\frac{\partial^2\phi}{\partial r^2} + \frac{1}{r}\frac{\partial\phi}{\partial r} + \frac{1}{r^2}\frac{\partial^2\phi}{\partial\theta} + k^2\phi = 0 \tag{2–27}$$

Equation (2–27) can be solved via the classical *separation of variables* technique in which the solution is assumed to be of the form

$$\phi(r, \theta) = R(r)\Theta(\theta) \tag{2–28}$$

Substituting eqn. (2–28) into eqn. (2–27) and then multiplying both sides of the resulting equation by $\frac{r^2}{R(r)\Theta(\theta)}$ give

$$r^2\frac{R''}{R} + r\frac{R'}{R} + \frac{\Theta''}{\Theta} + k^2r^2 = 0 \tag{2–29}$$

which can be separated, by noting that Θ depends only on θ whereas R depends only on r, into the following two ordinary differential equations

$$\frac{\Theta''}{\Theta} + \gamma = 0 \tag{2–30}$$

$$r^2\frac{R''}{R} + r\frac{R'}{R} + k^2r^2 = \gamma \tag{2–31}$$

where γ is the separation constant. It is well known that eqn. (2–30) has eigenvalues $\gamma_n = n^2$, where n is an arbitrary integer, and the eigenfunctions are

$$\Theta_n(\theta) = A_{1n}\sin n\theta + A_{2n}\cos n\theta = C_{1n}e^{in\theta} + C_{2n}e^{-in\theta} \tag{2–32}$$

where A_{1n}, A_{2n}, C_{1n} and C_{2n} are arbitrary constants. Substituting the eigenvalues into eqn. (2–31) gives the following *Bessel equation* of order n

$$r^2R''(r) + rR'(r) + (k^2r^2 - n^2)R(r) = 0 \tag{2–33}$$

whose general solution can be written as

$$R_n(r) = A_{3n}J_n(kr) + A_{4n}Y_n(kr) = C_{3n}H_n^{(1)}(kr) + C_{4n}H_n^{(2)}(kr) \tag{2–34}$$

where A_{3n}, A_{4n}, C_{3n} and C_{4n} are arbitrary constants, $J_n(z)$ and $Y_n(z)$ are *Bessel functions* of the first and the second kinds of order n, respectively, and $H_n^{(1)}(kr)$ and $H_n^{(2)}(kr)$ are *Hankel functions* of the first and the second kinds of order n, respectively. Hankel functions are related to Bessel functions by the following relation

$$H_n^{(1),(2)}(z) = J_n(z) \pm iY_n(z) \tag{2–35}$$

Sometimes, Bessel functions and Hankel functions are collectively called the *cylindrical functions*. Hankel functions of both kinds are also known as Bessel functions of the third kind, thus they can also be collectively called *Bessel functions*, or *cylindrical Bessel functions* to be more specific.

Therefore, the complete general solution for eqn. (2–27) is any one of the following, which are generally called *eigenfunction expansions*,

$$\begin{aligned}\phi(r,\theta) = &\sum_{n=1}^{\infty}[a_nJ_n(kr) + b_nY_n(kr)]\sin n\theta \\ &+ \sum_{n=0}^{\infty}[c_nJ_n(kr) + d_nY_n(kr)]\cos n\theta\end{aligned} \tag{2–36}$$

$$\begin{aligned}\phi(r,\theta) = &\sum_{n=1}^{\infty}[a_n'H_n^{(1)}(kr) + b_n'H_n^{(2)}(kr)]\sin n\theta \\ &+ \sum_{n=0}^{\infty}[c_n'J_n(kr) + d_n'H_n^{(2)}(kr)]\cos n\theta\end{aligned} \tag{2–37}$$

$$\phi(r,\theta) = \sum_{n=-\infty}^{\infty} [A_n J_n(kr) + B_n Y_n(kr)]\, e^{in\theta} \tag{2-38}$$

$$\phi(r,\theta) = \sum_{n=-\infty}^{\infty} [A'_n H_n^{(1)}(kr) + B'_n H_n^{(2)}(kr)]\, e^{in\theta} \tag{2-39}$$

where a_n, b_n, c_n, d_n, a'_n, b'_n, c'_n, d'_n, A_n, B_n, A'_n and B'_n are unknown *complex* constants and are called *wave expansion coefficients.* Functions $J_n(kr)\begin{matrix}\sin\\ \cos\end{matrix} n\theta$, $Y_n(kr)\begin{matrix}\sin\\ \cos\end{matrix} n\theta$, $H_n^{(1)}(kr)\begin{matrix}\sin\\ \cos\end{matrix} n\theta$, $H_n^{(2)}(kr)\begin{matrix}\sin\\ \cos\end{matrix} n\theta$, $J_n(kr)e^{in\theta}$, $Y_n(kr)e^{in\theta}$, $H_n^{(1)}(kr)e^{in\theta}$ and $H_n^{(2)}(kr)e^{in\theta}$ are called *wave expansion basis functions*, or simply *wave expansion bases.* Sometimes, they are called the *wave functions.*

It is noted that all the above expressions are equivalent, and one can be easily converted to another. Each of these solutions has its own characteristics, and the choice of any particular one can be made in accordance with the nature of the problem under consideration. Equations (2–38) and (2–39) are concise since there are only two series of unknowns involved in each solution. Equations (2–36) and (2–37) have four series of unknowns but have the symmetric (about the x-axis) and skew-symmetric terms clearly separated. For this reason, eqns. (2–36) and (2–37) are called *even-odd expansions*, and eqns. (2–38) and (2–39) are called *uniform expansions.*

It is noted that in many cases some of the terms in the above equations are not present. Some of the terms may be eliminated on the basis of physical ground, such as the boundary conditions at the infinity, which is known as the *radiation condition.* For example, it is known that Hankel functions have the following asymptotic behavior for large argument z:

$$H_n^{(1),(2)}(z) \to \sqrt{\frac{2}{\pi z}} e^{\pm i(z - \frac{1+2n}{4}\pi)} \tag{2-40}$$

Physically, Hankel functions of the first and the second kinds, which correspond to the plus and the minus signs in the above asymptotic expressions, respectively, represent *outgoing* and *incoming* waves[4], respectively. In most scattering problems, the scattered wave is an outgoing wave as if it were originating from the scatterer and thus expressible in $H_n^{(1)}(kr)$. Also, it is known that $J_n(kr)$ is *regular* (non-singular) in the entire plane, which is suitable for expressing sourceless waves, such as the incident wave for a scattering problem. In contrast, a Bessel function of the second kind is singular at the origin, as well as Hankel functions. Thus, if the problem domain contains the origin, the solution should consist only of $J_n(kr)$ terms.

2-3 Some Basic Principles in Elastodynamics

In this section, two basic principles in elastodynamics and their implications in scattering problems are explored.

The first is the *principle of energy conservation.* One of the forms of this principle that is frequently used in scattering problems, known as the *energy balance requirement*, states that for any closed surface that encloses neither a source nor a sink, the energy (power) transmitted into the surface equals the energy (power) emitted from the surface.

The second is the *reciprocity principle.* One of the forms of this principle that is frequently used in scattering problems is known as the *Betti-Rayleigh reciprocal theorem* that relates two dynamic states of an elastic system. This theorem is the elastodynamics equivalent of the Betti reciprocal theorem in elastostatics. It is also called the *Graffi elastodynamic reciprocal theorem*[5]. In essence, in two different loading situations for the same elastic system, the reciprocity principle requires that the work done by the first set of loading on the displacements caused by the second set of loading equals the work done by the second set of loading on the displacements caused by the first set of loading.

Since these principles hold for any situation, for a particular choice of wave expansion form, they impose some restrictions on the elements of the corresponding T-matrices. These properties are useful for ensuring the correctness of a numerical computation.

2-3.1 Energy Balance Requirement

By definition, the *energy flux* is the energy flow rate (power) through a cross section; that is

$$\dot{E} = \boldsymbol{f} \cdot \boldsymbol{v} = \boldsymbol{f} \cdot \dot{\boldsymbol{u}} \tag{2-41}$$

where $\boldsymbol{f}$ is the force exerted on the surface, and $\boldsymbol{u}$ and $\boldsymbol{v}$ are the displacement and velocity, respectively, of the point where the force acts.

In an elastic solid, the surface traction can be obtained from the stress tensor by the surface traction–stress relation. As the stress varies from one point to another, the total energy flux across a finite area $\mathcal{A}$ is an integral as

$$\dot{E} = -\int_{\mathcal{A}} (\boldsymbol{\sigma} : \boldsymbol{n}) \cdot \dot{\boldsymbol{u}} d\mathcal{A} = -\int_{\mathcal{A}} \sigma_{ij} n_j \dot{u}_i d\mathcal{A} \tag{2-42}$$

where $\boldsymbol{\sigma}$ is the stress tensor, $\boldsymbol{n}$ is the unit normal vector of the surface, and the operator ":" denotes the inner product between a tensor and a vector. The minus sign is added so that the power emitting from the closed surface is positive. Noting that the stress tensor is symmetric, that is, $\sigma_{ij} = \sigma_{ji}$, eqn. (2–42) can be written as

$$\dot{E} = -\int_{\mathcal{A}} (\sigma_{ji} \dot{u}_i) n_j d\mathcal{A} = -\int_{\mathcal{A}} (\boldsymbol{\sigma} : \dot{\boldsymbol{u}}) \cdot \boldsymbol{n} d\mathcal{A} \tag{2-43}$$

where $-(\boldsymbol{\sigma} : \dot{\boldsymbol{u}}) \cdot \boldsymbol{n} = -(\boldsymbol{\sigma} : \boldsymbol{n}) \cdot \dot{\boldsymbol{u}}$ is sometimes called the *energy flux density.*

In problems concerning time-harmonic inputs, such as the scattering problems discussed in §2-3, the *time-averaged energy flux* is often used and defined as

$$\langle \dot{E} \rangle = \frac{1}{T} \int_0^T \dot{E} dt \tag{2-44}$$

where $\langle \square \rangle$ denotes the average of the quantity $\square$ over a complete period of $\square$, T.

Suppose a generic stress component and a generic displacement component, both in complex notation, have been found and their complex amplitudes are Σ and U, respectively. Then, the *real* expressions for the stress, displacement and velocity are

$$\sigma = Re\{\Sigma e^{-\hat{\imath}\omega t}\} = \frac{1}{2}\left(\Sigma e^{-\hat{\imath}\omega t} + \overline{\Sigma} e^{\hat{\imath}\omega t}\right) \tag{2-45}$$

$$u = Re\{U e^{-\hat{\imath}\omega t}\} = \frac{1}{2}\left(U e^{-\hat{\imath}\omega t} + \overline{U} e^{\hat{\imath}\omega t}\right) \tag{2-46}$$

$$\dot{u} = \frac{1}{2}\frac{\partial}{\partial t}\left(U e^{-\hat{\imath}\omega t} + \overline{U} e^{\hat{\imath}\omega t}\right) = \frac{1}{2}\hat{\imath}\omega\left(-U e^{-\hat{\imath}\omega t} + \overline{U} e^{\hat{\imath}\omega t}\right) \tag{2-47}$$

where the overbar denotes a *complex conjugate* and the following relations have been used

$$z + \overline{z} = 2Re\, z \qquad \text{and} \qquad z - \overline{z} = 2\hat{\imath}\, Im\, z \tag{2-48}$$

Thus,

$$-\sigma\dot{u} = -\frac{\hat{\imath}\omega}{4}\left(\Sigma\overline{U} - \overline{\Sigma}U - \Sigma U e^{-2\hat{\imath}\omega t} + \overline{\Sigma U} e^{2\hat{\imath}\omega t}\right) \tag{2-49}$$

and, in turn,

$$-\langle\sigma\dot{u}\rangle = -\frac{\pi\hat{\imath}}{2}\cdot\frac{\omega}{2\pi}\left(\Sigma\overline{U} - \overline{\Sigma}U\right) = \frac{\omega}{2} Im\left\{\Sigma\overline{U}\right\} \tag{2-50}$$

since

$$\int_0^{\frac{2\pi}{\omega}} e^{2\hat{\imath}\omega t} dt = \int_0^{\frac{2\pi}{\omega}} e^{-2\hat{\imath}\omega t} dt = 0 \tag{2-51}$$

where $\frac{2\pi}{\omega}$ is the period of the temporal factor $e^{-\hat{\imath}\omega t}$.

Therefore, the general expression for the time-averaged energy flux can be written in terms of the spatial factors of the complex stress tensor $\boldsymbol{\Sigma}$ and the complex displacement vector $\boldsymbol{U}$ as

$$\langle \dot{E} \rangle = \frac{\omega}{2}\int_{\mathcal{A}} \left(Im\left\{\boldsymbol{\Sigma} : \overline{\boldsymbol{U}}\right\}\cdot\boldsymbol{n}\right) d\mathcal{A} = \frac{\omega}{2}\int_{\mathcal{A}} Im\left\{\left(\boldsymbol{\Sigma} : \overline{\boldsymbol{U}}\right)\cdot\boldsymbol{n}\right\} d\mathcal{A} \tag{2-52}$$

In particular, consider the energy balance requirement for a 2-D problem in which a polar (cylindrical) coordinate system is used. In such problems, an integral over a closed surface becomes an integral over a closed path in the problem plane. The simplest path is a circle that is centered at the origin of the coordinate system. If the radius of the circle is R, then,

$$\boldsymbol{n} = \boldsymbol{e}_r \qquad d\mathcal{A} = R d\theta \tag{2-53}$$

where $\boldsymbol{e}_r$ is the unit vector in the radial direction, and

$$\boldsymbol{\Sigma} : \overline{\boldsymbol{U}} = \begin{bmatrix} \Sigma_{rr} & \Sigma_{r\theta} & \Sigma_{rz} \\ \Sigma_{r\theta} & \Sigma_{\theta\theta} & \Sigma_{\theta z} \\ \Sigma_{rz} & \Sigma_{\theta z} & \Sigma_{zz} \end{bmatrix} \begin{Bmatrix} \overline{U}_r \\ \overline{U}_\theta \\ \overline{U}_z \end{Bmatrix} = \begin{Bmatrix} \Sigma_{rr}\overline{U}_r + \Sigma_{r\theta}\overline{U}_\theta + \Sigma_{rz}\overline{U}_z \\ \Sigma_{r\theta}\overline{U}_r + \Sigma_{\theta\theta}\overline{U}_\theta + \Sigma_{\theta z}\overline{U}_z \\ \Sigma_{rz}\overline{U}_r + \Sigma_{\theta z}\overline{U}_\theta + \Sigma_{zz}\overline{U}_z \end{Bmatrix} \tag{2-54}$$

Thus, along the circular integration path,

$$(\boldsymbol{\Sigma} : \overline{\boldsymbol{U}}) \cdot \boldsymbol{n} = \Sigma_{rr}\overline{U}_r + \Sigma_{r\theta}\overline{U}_\theta + \Sigma_{rz}\overline{U}_z \tag{2-55}$$

and the energy flux through such a closed path is

$$\langle \dot{E} \rangle = \frac{\omega R}{2} \int_0^{2\pi} \left(Im\left\{\Sigma_{rr}\overline{U}_r\right\} + Im\left\{\Sigma_{r\theta}\overline{U}_\theta\right\} + Im\left\{\Sigma_{rz}\overline{U}_z\right\}\right)\Big|_{r=R} d\theta \tag{2-56}$$

For the case of SH waves, $U_r = U_\theta = 0$, $\Sigma_{rr} = \Sigma_{r\theta} = 0$, the energy balance requirement can be written as

$$\langle \dot{E} \rangle_{\text{SH}} = \frac{\omega R}{2} \int_0^{2\pi} \left(Im\left\{\Sigma_{rz}\overline{U}_z\right\}\right)\Big|_{r=R} d\theta = 0 \tag{2-57}$$

For the case of P/SV waves, $U_z = 0$, $\Sigma_{rz} = 0$, the energy balance requirement can be written as

$$\langle \dot{E} \rangle_{\text{P/SV}} = \frac{\omega R}{2} \int_0^{2\pi} \left(Im\left\{\Sigma_{rr}\overline{U}_r\right\} + Im\left\{\Sigma_{r\theta}\overline{U}_\theta\right\}\right)\Big|_{r=R} d\theta = 0 \tag{2-58}$$

2-3.2 Betti-Rayleigh Reciprocity Theorem

For steady-state problems in which all field quantities in both loading situations possess the same temporal factor $e^{-i\omega t}$, the Betti-Rayleigh reciprocal theorem can be expressed as[6], which is a reduced form of *Betti's third identity*,

$$\int_{\mathcal{A}} (\boldsymbol{f}_1 \cdot \boldsymbol{u}_2 - \boldsymbol{f}_2 \cdot \boldsymbol{u}_1) d\mathcal{A} = 0 \tag{2-59}$$

where $\boldsymbol{f}$ and $\boldsymbol{u}$ are the force and displacement, respectively, for a field point, where the subscripts 1 and 2 represent the first and the second loadings, respectively, and $\mathcal{A}$ is a closed surface that encompasses the same material discontinuities, if any, in both loadings.

By using the surface traction–stress relation and the symmetry of the stress tensor, eqn. (2-59) can be written as

$$\int_{\mathcal{A}} (\boldsymbol{\sigma}_1 : \boldsymbol{u}_2 - \boldsymbol{\sigma}_2 : \boldsymbol{u}_1) \cdot \boldsymbol{n} d\mathcal{A} = 0 \tag{2-60}$$

In complex notation, it can be shown that

$$\boldsymbol{\sigma} : \boldsymbol{u} = Re\{\boldsymbol{\Sigma} \boldsymbol{U} e^{-2i\omega t}\} + Re\{\boldsymbol{\Sigma}\overline{\boldsymbol{U}}\} \tag{2-61}$$

Since eqn. (2-60) holds for any time t in the steady state, it follows that reciprocity requires

$$\int_{\mathcal{A}} (\boldsymbol{\Sigma}_1 \boldsymbol{U}_2 - \boldsymbol{\Sigma}_2 \boldsymbol{U}_1) \cdot \boldsymbol{n} d\mathcal{A} = 0 \tag{2-62}$$

and

$$\int_{\mathcal{A}} Re\left\{\boldsymbol{\Sigma}_1 : \overline{\boldsymbol{U}}_2 - \overline{\boldsymbol{\Sigma}}_2 : \boldsymbol{U}_1\right\} \cdot \boldsymbol{n} d\mathcal{A} = 0 \tag{2-63}$$

Similarly, the above expressions can be particularized to 2-D problems in which a polar coordinate system is used and a circular integration path is taken.

For the case of SH waves, $U_r = U_\theta = 0$ and $\Sigma_{rr} = \Sigma_{r\theta} = 0$, reciprocity gives

$$\int_0^{2\pi} \left[(\Sigma_{rz})_1 (U_z)_2 - (\Sigma_{rz})_2 (U_z)_1\right]\Big|_{r=R} d\theta = 0 \tag{2-64}$$

and

$$\int_0^{2\pi} Re\left\{(\Sigma_{rz})_1 (\overline{U}_z)_2 - (\overline{\Sigma}_{rz})_2 (U_z)_1\right\}\Big|_{r=R} d\theta = 0 \tag{2-65}$$

For the case of P/SV waves, $U_z = 0$ and $\Sigma_{rz} = 0$, reciprocity gives

$$\int_0^{2\pi} \left\{\left[(\Sigma_{rr})_1 (U_r)_2 + (\Sigma_{r\theta})_1 (U_\theta)_2\right] - \left[(\Sigma_{rr})_2 (U_r)_1 + (\Sigma_{r\theta})_2 (U_\theta)_1\right]\right\}\Big|_{r=R} d\theta = 0 \tag{2-66}$$

and

$$\int_0^{2\pi} Re\left\{\left[(\Sigma_{rr})_1 (\overline{U}_r)_2 + (\Sigma_{r\theta})_1 (\overline{U}_\theta)_2\right] - \left[(\overline{\Sigma}_{rr})_2 (U_r)_1 + (\overline{\Sigma}_{r\theta})_2 (U_\theta)_1\right]\right\}\Big|_{r=R} d\theta = 0 \tag{2-67}$$

2-4 Solutions to Some Single-Scatterer Problems

In this section, solutions to some single-scatterer problems that are pertinent to modeling of fiber reinforced composites are presented.

In all the problems to be discussed, it is assumed that a circular cylindrical scatterer of radius a is located at the origin of the coordinate system and is surrounded by a linearly elastic medium of infinite extent. All material properties are assumed to be known. A time-harmonic incident wave impinges onto the scatterer, as sketched in Fig. 2–1. The resulting waves in the steady state are sought.

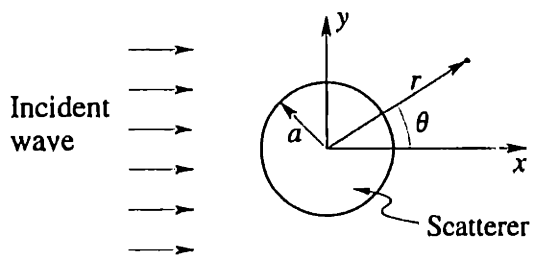

Fig. 2–1 Geometry of single scattering problem.

The configuration shown in Fig. 2–1 is often used to model, though in a highly simplified way, fiber reinforced composites. In such a model, the scatterer represents

a fiber and the infinite elastic medium represents the matrix. To extend the model, the scatterer can be modified to be a layered scatterer such that the outer layer represents an interphase[8], which exists as a third phase between the fiber and the matrix, or it represents a fiber having a layered structure, such as a SiC (Silicon Carbide) fiber[9].

Throughout this section, when necessary, subscripts m, f and i are used to designate physical quantities that belong to the matrix, the fiber and the interphase, respectively. However, the subscripts are omitted for the cases of a void and a rigid scatterer since no wave exists in such scatterers. The words "fiber" and "scatterer" are often used interchangeably in the following discussions. For brevity, complex notation is used, and the temporal factor $e^{-i\omega t}$ is suppressed for all field quantities.

2-4.1 SH Waves

For SH waves, the displacements are $u = v = 0$ and $w = \phi(r, \theta)$. Stresses in terms of displacements are

$$\tau_{rz} = \tau_{zr} = 2\mu \frac{\partial \phi}{\partial r} \qquad \tau_{\theta z} = \tau_{z\theta} = \frac{2\mu}{r} \frac{\partial \phi}{\partial \theta} \tag{2-68}$$

and all other stress components vanish.

For all the cases to be discussed, it is assumed that the incident wave is regular throughout the entire plane and thus expressible as[4]

$$\phi^{\text{inc}} = \sum_{n=-\infty}^{\infty} A_n J_n(kr) e^{in\theta} \tag{2-69}$$

Although eqn. (2-69) is the expression for the incident wave to be used in order to maintain the generality of the solution, one special case that is worth mentioning is the planar wave of amplitude ϕ_0, propagating along the $+x$ direction. The expression for such a wave is[4]

$$\phi = \phi_0 e^{ikx} = \phi_0 e^{ikr\cos\theta} = \sum_{n=-\infty}^{\infty} i^n J_n(kr) e^{in\theta} \tag{2-70}$$

The scattered wave is an outgoing wave and thus is expressible as Hankel functions of the first kind; that is,

$$\phi^{\text{s}} = \sum_{n=-\infty}^{\infty} B_n H_n^{(1)}(kr) e^{in\theta} \tag{2-71}$$

The total wave in the matrix is the sum of the incident wave and the scattered wave; that is,

$$\phi^{\text{total}} = \phi^{\text{inc}} + \phi^{\text{s}} \tag{2-72}$$

Rigid Scatterer

The boundary condition for a rigid scatterer is that the displacement at the interface $r = a$ is zero. That is,

$$\left(\phi^s + \phi^{\text{inc}}\right)\Big|_{r=a} = 0 \tag{2-73}$$

Substituting eqns. (2-69) and (2-71) into the boundary condition in eqn. (2-73) gives

$$\sum_{n=-\infty}^{\infty} \left[A_n J_n(ka) + B_n H_n^{(1)}(ka)\right] e^{in\theta} = 0 \tag{2-74}$$

Due to the orthogonality of the harmonic basis function $e^{in\theta}$, the boundary condition is satisfied if and only if each term under the summation vanishes; that is, for every n,

$$A_n J_n(ka) + B_n H_n^{(1)}(ka) = 0 \tag{2-75}$$

which gives

$$B_n = -\frac{J_n(ka)}{H_n^{(1)}(ka)} A_n \tag{2-76}$$

Thus, substituting eqn. (2-76) into eqn. (2-71) gives

$$\phi^s = -\sum_{n=-\infty}^{\infty} \frac{J_n(ka)}{H_n^{(1)}(ka)} A_n H_n^{(1)}(kr) e^{in\theta} \tag{2-77}$$

In all the cases that follow, the procedure of substituting the found wave expansion coefficients into eqn. (2-71) will be skipped for brevity.

Void Scatterer

The boundary condition for a void scatterer is that the stress component τ_{rz} vanishes at the interface $r = a$. That is,

$$2\mu \left(\frac{\partial \phi^s}{\partial r} + \frac{\partial \phi^{\text{inc}}}{\partial r}\right)\Bigg|_{r=a} = 0 \tag{2-78}$$

Substituting eqns. (2-69) and (2-71) into the boundary condition in eqn. (2-78) gives

$$B_n = -\frac{J_n'(ka)}{H_n^{(1)\prime}(ka)} A_n \tag{2-79}$$

Elastic Scatterer

In this case, there exists a wave in the scatterer, called the *refracted wave*. Since the elastic scatterer is located at the origin of the coordinate system, the refracted wave contains only the regular components; that is,

$$\phi^r = \sum_{n=-\infty}^{\infty} C_n J_n(k_f r) e^{in\theta} \tag{2-80}$$

It is noted that in the steady state, the refracted wave has the same frequency as the incident wave. Since the wave speed in the fiber is different from that in the

matrix, due to the differences in material properties, the wave number in the fiber, k_f, is also different from that in the matrix, k_m.

The boundary conditions for this case are that the stress component τ_{rz} and the displacement w are continuous across the interface $r = a$. That is,

$$\left(\phi^{\text{inc}} + \phi^{\text{s}}\right)\Big|_{r=a} = \phi^{r}|_{r=a} \tag{2-81}$$

$$2\mu_m \left(\frac{\partial \phi^{\text{inc}}}{\partial r} + \frac{\partial \phi^{\text{s}}}{\partial r}\right)\Bigg|_{r=a} = 2\mu_f \frac{\partial \phi^{r}}{\partial r}\Bigg|_{r=a} \tag{2-82}$$

Substituting eqns. (2–69), (2–71) and (2–80) into the boundary conditions in eqns. (2–81) and (2–82) gives

$$-B_n H_n^{(1)}(k_m a) + C_n J_n(k_f a) = A_n J_n(k_m a) \tag{2-83}$$

$$-\mu_m k_m B_n H_n^{(1)\prime}(k_m a) + \mu_f k_f C_n J_n'(k_f a) = \mu_m k_m A_n J_n'(k_m a) \tag{2-84}$$

Solving this set of equations gives

$$B_n = -\frac{\mu_f k_f J_n'(k_f a) J_n(k_m a) - \mu_m k_m J_n(k_f a) J_n'(k_m a)}{\mu_f k_f J_n'(k_f a) H_n^{(1)}(k_m a) - \mu_m k_m J_n(k_f a) H_n^{(1)\prime}(k_m a)} A_n \tag{2-85}$$

$$\begin{aligned} C_n &= \frac{\mu_m k_m J_n'(k_m a) H_n^{(1)}(k_m a) - \mu_m k_m J_n(k_m a) H_n^{(1)\prime}(k_m a)}{\mu_f k_f J_n'(k_f a) H_n^{(1)}(k_m a) - \mu_m k_m J_n(k_f a) H_n^{(1)\prime}(k_m a)} A_n \\ &= -\frac{2i}{\pi a} \frac{\mu_m A_n}{\mu_f k_f J_n'(k_f a) H_n^{(1)}(k_m a) - \mu_m k_m J_n(k_f a) H_n^{(1)\prime}(k_m a)} \end{aligned} \tag{2-86}$$

where in writing the last equation, the following Wronskian relation[7] of Bessel functions has been used

$$\mathcal{W}(J_n(z), H_n^{(1)}(z)) \equiv J_n(z) H_n^{(1)\prime}(z) - J_n'(z) H_n^{(1)}(z) = \frac{2i}{\pi z} \tag{2-87}$$

Layered Elastic Scatterer

In this case, a two-layer elastic cylinder is considered as the scatterer. The outer layer is assumed to be linearly elastic and having an outer radius b ($b > a$).

The refracted wave within the inner layer of the scatterer (fiber) is still expressible as eqn. (2–80). Within the outer layer (interphase), the wave can be expressed, using the general form of the solution of the Helmholtz equation, as

$$\phi^{\text{i}} = \sum_{n=-\infty}^{\infty} \left[D_n H_n^{(1)}(k_i r) + E_n H_n^{(2)}(k_i r)\right] \mathrm{e}^{in\theta} \tag{2-88}$$

The boundary conditions for this case are that the stress component τ_{rz} and the displacement w are continuous across both interfaces at $r = a$ and $r = b$. That is,

$$\left(\phi^{\text{inc}} + \phi^{\text{s}}\right)\Big|_{r=b} = \phi^{\text{i}}\Big|_{r=b} \tag{2-89}$$

$$\phi^{\text{i}}\Big|_{r=a} = \phi^{\text{f}}\Big|_{r=a} \tag{2-90}$$

$$2\mu_m \left(\frac{\partial \phi^{\text{inc}}}{\partial r} + \frac{\partial \phi^{\text{s}}}{\partial r} \right) \Bigg|_{r=b} = 2\mu_i \frac{\partial \phi^{\text{i}}}{\partial r} \Bigg|_{r=b} \tag{2-91}$$

$$2\mu_i \frac{\partial \phi^{\text{i}}}{\partial r} \Bigg|_{r=a} = 2\mu_f \frac{\partial \phi^{\text{f}}}{\partial r} \Bigg|_{r=a} \tag{2-92}$$

Substituting the wave expressions in eqns. (2-69), (2-71), (2-80) and (2-88) into the boundary conditions in eqns. (2-89) through (2-92) gives the following linear equation system, in matrix form,

$$\begin{bmatrix} -H_n^{(1)}(k_m b) & H_n^{(1)}(k_i b) & H_n^{(2)}(k_i b) & 0 \\ -\mu_m k_m H_n^{(1)\prime}(k_m b) & \mu_i k_i H_n^{(1)\prime}(k_i b) & \mu_i k_i H_n^{(2)\prime}(k_i b) & 0 \\ 0 & H_n^{(1)}(k_i a) & H_n^{(2)}(k_i a) & -J_n(k_f a) \\ 0 & \mu_i k_i H_n^{(1)\prime}(k_i a) & \mu_i k_i H_n^{(2)\prime}(k_i a) & -\mu_f k_f J_n'(k_f a) \end{bmatrix} \begin{Bmatrix} B_n \\ D_n \\ E_n \\ C_n \end{Bmatrix}$$

$$= \begin{Bmatrix} J_n(k_m b) \\ \mu_m k_m J_n'(k_m b) \\ 0 \\ 0 \end{Bmatrix} A_n \tag{2-93}$$

Solving this set of equations gives (see Appendix 2-A for a detailed derivation)

$$B_n = -\frac{\mu_m k_m M_1 J_n'(k_m b) - \mu_i k_i M_2 J_n(k_m b)}{\mu_m k_m M_1 H_n^{(1)\prime}(k_m b) - \mu_i k_i M_2 H_n^{(1)}(k_m b)} A_n \tag{2-94}$$

$$C_n = -\frac{4\hat{\imath}}{\pi^2 a b} \frac{\mu_i \mu_m}{\mu_m k_m M_1 H_n^{(1)\prime}(k_m b) - \mu_i k_i M_2 H_n^{(1)}(k_m b)} A_n \tag{2-95}$$

$$D_n = -\frac{\mu_m}{\pi b} \frac{\mu_f k_f J_n'(k_f a) H_n^{(2)}(k_i a) - \mu_i k_i J_n(k_f a) H_n^{(2)\prime}(k_i a)}{\mu_m k_m M_1 H_n^{(1)\prime}(k_m b) - \mu_i k_i M_2 H_n^{(1)}(k_m b)} A_n \tag{2-96}$$

$$E_n = \frac{\mu_m}{\pi b} \frac{\mu_f k_f J_n'(k_f a) H_n^{(1)}(k_i a) - \mu_i k_i J_n(k_f a) H_n^{(1)\prime}(k_i a)}{\mu_m k_m M_1 H_n^{(1)\prime}(k_m b) - \mu_i k_i M_2 H_n^{(1)}(k_m b)} A_n \tag{2-97}$$

where

$$M_1 = \left[\mu_f k_f J_n'(k_f a) Y_n(k_i a) - \mu_i k_i J_n(k_f a) Y_n'(k_i a)\right] J_n(k_i b) - \left[\mu_f k_f J_n'(k_f a) J_n(k_i a) - \mu_i k_i J_n(k_f a) J_n'(k_i a)\right] Y_n(k_i b) \tag{2-98}$$

$$M_2 = \left[\mu_f k_f J_n'(k_f a) Y_n(k_i a) - \mu_i k_i J_n(k_f a) Y_n'(k_i a)\right] J_n'(k_i b) - \left[\mu_f k_f J_n'(k_f a) J_n(k_i a) - \mu_i k_i J_n(k_f a) J_n'(k_i a)\right] Y_n'(k_i b) \tag{2-99}$$

2-4.2 P/SV Waves

Expressions for Displacements, Stresses, and Strains

For P/SV waves, the wave equations are set up for displacement potentials, while the boundary conditions require expressions for stresses and displacements. Thus it is necessary to derive the expressions for the displacements, strains and stresses in terms of the displacement potentials φ and ψ.

Without loss of generality, the displacement potentials are assumed to be of the following forms

$$\varphi = \sum_{n=-\infty}^{\infty} \alpha_n \mathfrak{C}_n(\kappa r) e^{in\theta} \tag{2-100}$$

$$\psi = \sum_{n=-\infty}^{\infty} \beta_n \mathfrak{C}_n(k r) e^{in\theta} \tag{2-101}$$

where $\mathfrak{C}_n(z)$ is a formal notation for *cylindrical functions*, which can be either kind of Bessel functions, $J_n(z)$ or $Y_n(z)$, or either kind of Hankel functions, $H_n^{(1)}(z)$ or $H_n^{(2)}(z)$, and it is noted that the wave numbers κ and k are different. Then, the expressions for the displacements, strains and stresses can be found (see Appendix 2-B for a detailed derivation) as

$$u_r = \frac{1}{r} \sum_{n=-\infty}^{\infty} [\alpha_n \mathfrak{E}_{71n}(r) + \beta_n \mathfrak{E}_{72n}(r)] e^{in\theta} \tag{2-102}$$

$$u_\theta = \frac{1}{r} \sum_{n=-\infty}^{\infty} [\alpha_n \mathfrak{E}_{81n}(r) + \beta_n \mathfrak{E}_{82n}(r)] e^{in\theta} \tag{2-103}$$

$$\varepsilon_{rr} = \frac{1}{r^2} \sum_{n=-\infty}^{\infty} [\alpha_n \mathfrak{E}_{51n}(r) + \beta_n \mathfrak{E}_{52n}(r)] e^{in\theta} \tag{2-104}$$

$$\varepsilon_{\theta\theta} = \frac{1}{r^2} \sum_{n=-\infty}^{\infty} [\alpha_n \mathfrak{E}_{61n}(r) + \beta_n \mathfrak{E}_{62n}(r)] e^{in\theta} \tag{2-105}$$

$$\varepsilon_{r\theta} = \frac{1}{r^2} \sum_{n=-\infty}^{\infty} [\alpha_n \mathfrak{E}_{41n}(r) + \beta_n \mathfrak{E}_{42n}(r)] e^{in\theta} \tag{2-106}$$

$$\sigma_{rr} = \frac{2\mu}{r^2} \sum_{n=-\infty}^{\infty} [\alpha_n \mathfrak{E}_{11n}(r) + \beta_n \mathfrak{E}_{12n}(r)] e^{in\theta} \tag{2-107}$$

$$\sigma_{\theta\theta} = \frac{2\mu}{r^2} \sum_{n=-\infty}^{\infty} [\alpha_n \mathfrak{E}_{21n}(r) + \beta_n \mathfrak{E}_{22n}(r)] e^{in\theta} \tag{2-108}$$

$$\sigma_{zz} = \frac{2\mu}{r^2} \sum_{n=-\infty}^{\infty} \alpha_n \mathfrak{E}_{31n}(r) e^{in\theta} \tag{2-109}$$

$$\sigma_{r\theta} = \frac{2\mu}{r^2} \sum_{n=-\infty}^{\infty} [\alpha_n \mathfrak{E}_{41n}(r) + \beta_n \mathfrak{E}_{42n}(r)] e^{in\theta} \tag{2-110}$$

where the functions $\mathfrak{E}$ are called *differential wave expansion bases* which were originally introduced by Pao and Mow in [4], and the modified definitions, which are used here, are given in Appendix 2-C. These functions are invoked in a form such as $\mathfrak{E}_{11n}^{1f}(r)$ where the first two subscripts specify the functional form, and the third subscript specifies the order of the involved cylindrical function(s). The first superscript specifies the type of the cylindrical function to be used. It ranges from 1 to 4 and corresponds to $J_n(\cdot)$, $Y_n(\cdot)$, $H_n^{(1)}(\cdot)$ and $H_n^{(2)}(\cdot)$, respectively. The second superscript, when it appears, specifies the medium in which the function is to be

evaluated. In the event that no second superscript is specified, the function is to be evaluated in the infinite host medium is assumed.

Wave Fields in the Matrix

For all the cases to be discussed, it is assumed that the incident waves are regular throughout the entire plane and are expressible as[4]

$$\varphi^{\text{inc}} = \sum_{n=-\infty}^{\infty} A_n J_n(\kappa_m r) e^{in\theta} \tag{2-111}$$

$$\psi^{\text{inc}} = \sum_{n=-\infty}^{\infty} a_n J_n(k_m r) e^{in\theta} \tag{2-112}$$

The scattered waves in the matrix contain both P and SV waves, and are expressible as

$$\varphi^{\text{s}} = \sum_{n=-\infty}^{\infty} B_n H_n^{(1)}(\kappa_m r) e^{in\theta} \tag{2-113}$$

$$\psi^{\text{s}} = \sum_{n=-\infty}^{\infty} b_n H_n^{(1)}(k_m r) e^{in\theta} \tag{2-114}$$

The total wave in the matrix is the sum of the incident waves and the scattered waves. That is,

$$\varphi^{\text{total}} = \varphi^{\text{inc}} + \varphi^{\text{s}} \tag{2-115}$$

$$\psi^{\text{total}} = \psi^{\text{inc}} + \psi^{\text{s}} \tag{2-116}$$

Thus, the following expressions for the displacements and stresses in the matrix can be obtained as

$$u_{rm} = \frac{1}{r} \sum_{n=-\infty}^{\infty} \left[A_n \mathfrak{E}_{71n}^{1m}(r) + a_n \mathfrak{E}_{72n}^{1m}(r) + B_n \mathfrak{E}_{71n}^{3m}(r) + b_n \mathfrak{E}_{72n}^{3m}(r) \right] e^{in\theta} \tag{2-117}$$

$$u_{\theta m} = \frac{1}{r} \sum_{n=-\infty}^{\infty} \left[A_n \mathfrak{E}_{81n}^{1m}(r) + a_n \mathfrak{E}_{82n}^{1m}(r) + B_n \mathfrak{E}_{81n}^{3m}(r) + b_n \mathfrak{E}_{82n}^{3m}(r) \right] e^{in\theta} \tag{2-118}$$

$$\sigma_{rm} = \frac{2\mu_m}{r^2} \sum_{n=-\infty}^{\infty} \left[A_n \mathfrak{E}_{11n}^{1m}(r) + a_n \mathfrak{E}_{12n}^{1m}(r) + B_n \mathfrak{E}_{11n}^{3m}(r) + b_n \mathfrak{E}_{12n}^{3m}(r) \right] e^{in\theta} \tag{2-119}$$

$$\sigma_{r\theta m} = \frac{2\mu_m}{r^2} \sum_{n=-\infty}^{\infty} \left[A_n \mathfrak{E}_{41n}^{1m}(r) + a_n \mathfrak{E}_{42n}^{1m}(r) + B_n \mathfrak{E}_{41n}^{3m}(r) + b_n \mathfrak{E}_{42n}^{3m}(r) \right] e^{in\theta} \tag{2-120}$$

Rigid Scatterer

For this case, the boundary conditions are that the displacement components u_r and u_θ at the interface $r = a$ vanish. That is,

$$u_r|_{r=a} = 0 \qquad u_\theta|_{r=a} = 0 \tag{2-121}$$

Substituting eqns. (2–117) and (2–118) into eqn. (2–121) yields the following set of linear equations, in matrix form,

$$\begin{bmatrix} \mathfrak{E}^3_{71n}(a) & \mathfrak{E}^3_{72n}(a) \\ \mathfrak{E}^3_{81n}(a) & \mathfrak{E}^3_{82n}(a) \end{bmatrix} \begin{Bmatrix} B_n \\ b_n \end{Bmatrix} = - \begin{Bmatrix} \mathfrak{E}^1_{71n}(a)A_n + \mathfrak{E}^1_{72n}(a)a_n \\ \mathfrak{E}^1_{81n}(a)A_n + \mathfrak{E}^1_{82n}(a)a_n \end{Bmatrix} \tag{2–122}$$

Solution of eqn. (2–122) is straightforward and is omitted for brevity.

Void Scatterer

For this case, the boundary conditions are that the radial and shear stresses at the interface $r = a$ vanish. That is,

$$\sigma_r|_{r=a} = 0 \qquad \sigma_{r\theta}|_{r=a} = 0 \tag{2–123}$$

Substituting eqns. (2–119) and (2–120) into eqn. (2–123) yields

$$\begin{bmatrix} \mathfrak{E}^3_{11n}(a) & \mathfrak{E}^3_{12n}(a) \\ \mathfrak{E}^3_{41n}(a) & \mathfrak{E}^3_{42n}(a) \end{bmatrix} \begin{Bmatrix} B_n \\ b_n \end{Bmatrix} = - \begin{Bmatrix} \mathfrak{E}^1_{11n}(a)A_n + \mathfrak{E}^1_{12n}(a)a_n \\ \mathfrak{E}^1_{41n}(a)A_n + \mathfrak{E}^1_{42n}(a)a_n \end{Bmatrix} \tag{2–124}$$

Elastic Scatterer

In this case, the refracted waves have both P and SV components, and are expressible as[4]

$$\varphi^r = \sum_{n=-\infty}^{\infty} C_n J_n(\kappa_f r) e^{in\theta} \tag{2–125}$$

$$\psi^r = \sum_{n=-\infty}^{\infty} c_n J_n(k_f r) e^{in\theta} \tag{2–126}$$

The following expressions for the displacements and stresses in the scatterer (fiber) can be obtained as

$$u_{r\,f} = \frac{1}{r} \sum_{n=-\infty}^{\infty} \left[C_n \mathfrak{E}^{1f}_{71n}(r) + c_n \mathfrak{E}^{1f}_{72n}(r) \right] e^{in\theta} \tag{2–127}$$

$$u_{\theta\,f} = \frac{1}{r} \sum_{n=-\infty}^{\infty} \left[C_n \mathfrak{E}^{1f}_{81n}(r) + c_n \mathfrak{E}^{1f}_{82n}(r) \right] e^{in\theta} \tag{2–128}$$

$$\sigma_{r\,f} = \frac{2\mu_f}{r^2} \sum_{n=-\infty}^{\infty} \left[C_n \mathfrak{E}^{1f}_{11n}(r) + c_n \mathfrak{E}^{1f}_{12n}(r) \right] e^{in\theta} \tag{2–129}$$

$$\sigma_{r\theta\,f} = \frac{2\mu_f}{r^2} \sum_{n=-\infty}^{\infty} \left[C_n \mathfrak{E}^{1f}_{41n}(r) + c_n \mathfrak{E}^{1f}_{42n}(r) \right] e^{in\theta} \tag{2–130}$$

The boundary conditions for this case are that all the displacements and the radial and shear stresses are continuous across the interface $r = a$. That is,

$$u_{r\,m}|_{r=a} = u_{r\,f}|_{r=a} \tag{2–131}$$

$$u_{\theta\,m}|_{r=a} = u_{\theta\,f}|_{r=a} \tag{2–132}$$

$$\sigma_{r\,m}|_{r=a} = \sigma_{r\,f}|_{r=a} \tag{2–133}$$

$$\sigma_{r\theta m}|_{r=a} = \sigma_{r\theta f}|_{r=a} \tag{2-134}$$

Substituting eqns. (2–117) through (2–120) and eqns. (2–127) through (2–130) into eqns. (2–131) through (2–134) yields

$$\begin{bmatrix} -\mathfrak{E}^{3m}_{71n}(a) & -\mathfrak{E}^{3m}_{72n}(a) & \mathfrak{E}^{1f}_{71n}(a) & \mathfrak{E}^{1f}_{72n}(a) \\ -\mathfrak{E}^{3m}_{81n}(a) & -\mathfrak{E}^{3m}_{82n}(a) & \mathfrak{E}^{1f}_{81n}(a) & \mathfrak{E}^{1f}_{82n}(a) \\ -\mu_m\mathfrak{E}^{3m}_{11n}(a) & -\mu_m\mathfrak{E}^{3m}_{12n}(a) & \mu_f\mathfrak{E}^{1f}_{11n}(a) & \mu_f\mathfrak{E}^{1f}_{12n}(a) \\ -\mu_m\mathfrak{E}^{3m}_{41n}(a) & -\mu_m\mathfrak{E}^{3m}_{42n}(a) & \mu_f\mathfrak{E}^{1f}_{41n}(a) & \mu_f\mathfrak{E}^{1f}_{42n}(a) \end{bmatrix} \begin{Bmatrix} B_n \\ b_n \\ C_n \\ c_n \end{Bmatrix}$$

$$= \begin{Bmatrix} \mathfrak{E}^{1m}_{71n}(a)A_n + \mathfrak{E}^{1m}_{72n}(a)a_n \\ \mathfrak{E}^{1m}_{81n}(a)A_n + \mathfrak{E}^{1m}_{82n}(a)a_n \\ \mu_m[\mathfrak{E}^{1m}_{11n}(a)A_n + \mathfrak{E}^{1m}_{12n}(a)a_n] \\ \mu_m[\mathfrak{E}^{1m}_{21n}(a)A_n + \mathfrak{E}^{1m}_{22n}(a)a_n] \end{Bmatrix} \tag{2-135}$$

Layered Elastic Scatterer

This case has been addressed in great detail in [8]. However, difficulties have been encountered in the present research when attempting to numerically solve the linear equation system contained therein. Thus, this case is reformulated here to resolve the difficulties.

The refracted waves within the inner layer of the scatterer (fiber) are still expressible as in eqns. (2–125) and (2–126). Assume the waves in the outer layer (interphase) are of the following forms

$$\varphi^{\mathrm{i}} = \sum_{n=-\infty}^{\infty} [D_n J_n(\kappa_i r) + E_n Y_n(\kappa_i r)]\mathrm{e}^{\mathrm{i}n\theta} \tag{2-136}$$

$$\psi^{\mathrm{i}} = \sum_{n=-\infty}^{\infty} [d_n J_n(k_i r) + e_n Y_n(k_i r)]\mathrm{e}^{\mathrm{i}n\theta} \tag{2-137}$$

Thus the following expressions for the displacements and stresses in the interphase can be obtained as

$$u_{r\,i} = \frac{1}{r}\sum_{n=-\infty}^{\infty}\left[D_n\mathfrak{E}^{1i}_{71n}(r) + E_n\mathfrak{E}^{2i}_{71n}(r) + d_n\mathfrak{E}^{1i}_{72n}(r) + e_n\mathfrak{E}^{2i}_{72n}(r)\right]\mathrm{e}^{\mathrm{i}n\theta} \tag{2-138}$$

$$u_{\theta\,i} = \frac{1}{r}\sum_{n=-\infty}^{\infty}\left[D_n\mathfrak{E}^{1i}_{81n}(r) + E_n\mathfrak{E}^{2i}_{81n}(r) + d_n\mathfrak{E}^{1i}_{82n}(r) + e_n\mathfrak{E}^{2i}_{82n}(r)\right]\mathrm{e}^{\mathrm{i}n\theta} \tag{2-139}$$

$$\sigma_{r\,i} = \frac{2\mu_i}{r^2}\sum_{n=-\infty}^{\infty}\left[D_n\mathfrak{E}^{1i}_{11n}(r) + E_n\mathfrak{E}^{2i}_{11n}(r) + d_n\mathfrak{E}^{1i}_{12n}(r) + e_n\mathfrak{E}^{2i}_{12n}(r)\right]\mathrm{e}^{\mathrm{i}n\theta} \tag{2-140}$$

$$\sigma_{r\theta\,i} = \frac{2\mu_i}{r^2}\sum_{n=-\infty}^{\infty}\left[D_n\mathfrak{E}^{1i}_{41n}(r) + E_n\mathfrak{E}^{2i}_{41n}(r) + d_n\mathfrak{E}^{1i}_{42n}(r) + e_n\mathfrak{E}^{2i}_{42n}(r)\right]\mathrm{e}^{\mathrm{i}n\theta} \tag{2-141}$$

The boundary conditions for this case are that all the displacements and the radial and shear stresses are continuous across both interfaces at $r = a$ and $r = b$. That is,

$$u_{r\,m}|_{r=b} = u_{r\,i}|_{r=b} \qquad u_{r\,i}|_{r=a} = u_{r\,f}|_{r=a} \tag{2-142}$$

$$u_{\theta m}|_{r=b} = u_{\theta i}|_{r=b} \qquad u_{\theta i}|_{r=a} = u_{\theta f}|_{r=a} \tag{2-143}$$

$$\sigma_{r m}|_{r=b} = \sigma_{r i}|_{r=b} \qquad \sigma_{r i}|_{r=a} = \sigma_{r f}|_{r=a} \tag{2-144}$$

$$\sigma_{r\theta m}|_{r=b} = \sigma_{r\theta i}|_{r=b} \qquad \sigma_{r\theta i}|_{r=a} = \sigma_{r\theta f}|_{r=a} \tag{2-145}$$

Substituting eqns. (2–117) through (2–120), eqns. (2–127) through (2–130) and eqns. (2–138) through (2–141) into eqns. (2–142) through (2–145) yields

$$\begin{bmatrix}
\mathfrak{E}^{3m}_{71n}(b) & \mathfrak{E}^{3m}_{72n}(b) & -\mathfrak{E}^{1i}_{71n}(b) & -\mathfrak{E}^{2i}_{71n}(b) & -\mathfrak{E}^{1i}_{72n}(b) & -\mathfrak{E}^{2i}_{72n}(b) \\
\mathfrak{E}^{3m}_{81n}(b) & \mathfrak{E}^{3m}_{82n}(b) & -\mathfrak{E}^{1i}_{81n}(b) & -\mathfrak{E}^{2i}_{81n}(b) & -\mathfrak{E}^{1i}_{82n}(b) & -\mathfrak{E}^{2i}_{82n}(b) \\
\mathfrak{E}^{3m}_{11n}(b) & \mathfrak{E}^{3m}_{12n}(b) & -\frac{\mu_i}{\mu_m}\mathfrak{E}^{1i}_{11n}(b) & -\frac{\mu_i}{\mu_m}\mathfrak{E}^{2i}_{11n}(b) & -\frac{\mu_i}{\mu_m}\mathfrak{E}^{1i}_{12n}(b) & -\frac{\mu_i}{\mu_m}\mathfrak{E}^{2i}_{12n}(b) \\
\mathfrak{E}^{3m}_{41n}(b) & \mathfrak{E}^{3m}_{42n}(b) & -\frac{\mu_i}{\mu_m}\mathfrak{E}^{1i}_{41n}(b) & -\frac{\mu_i}{\mu_m}\mathfrak{E}^{2i}_{41n}(b) & -\frac{\mu_i}{\mu_m}\mathfrak{E}^{1i}_{42n}(b) & -\frac{\mu_i}{\mu_m}\mathfrak{E}^{2i}_{42n}(b) \\
0 & 0 & \mathfrak{E}^{1i}_{71n}(a) & \mathfrak{E}^{2i}_{71n}(a) & \mathfrak{E}^{1i}_{72n}(a) & \mathfrak{E}^{2i}_{72n}(a) \\
0 & 0 & \mathfrak{E}^{1i}_{81n}(a) & \mathfrak{E}^{2i}_{81n}(a) & \mathfrak{E}^{1i}_{82n}(a) & \mathfrak{E}^{2i}_{82n}(a) \\
0 & 0 & \frac{\mu_i}{\mu_m}\mathfrak{E}^{1i}_{11n}(a) & \frac{\mu_i}{\mu_m}\mathfrak{E}^{2i}_{11n}(a) & \frac{\mu_i}{\mu_m}\mathfrak{E}^{1i}_{12n}(a) & \frac{\mu_i}{\mu_m}\mathfrak{E}^{2i}_{12n}(a) \\
0 & 0 & \frac{\mu_i}{\mu_m}\mathfrak{E}^{1i}_{41n}(a) & \frac{\mu_i}{\mu_m}\mathfrak{E}^{2i}_{41n}(a) & \frac{\mu_i}{\mu_m}\mathfrak{E}^{1i}_{42n}(a) & \frac{\mu_i}{\mu_m}\mathfrak{E}^{2i}_{42n}(a)
\end{bmatrix}$$

$$\begin{bmatrix}
0 & 0 \\
0 & 0 \\
0 & 0 \\
0 & 0 \\
-\mathfrak{E}^{1f}_{71n}(a) & -\mathfrak{E}^{1f}_{72n}(a) \\
-\mathfrak{E}^{1f}_{81n}(a) & -\mathfrak{E}^{1f}_{82n}(a) \\
-\frac{\mu_f}{\mu_m}\mathfrak{E}^{1f}_{11n}(a) & -\frac{\mu_f}{\mu_m}\mathfrak{E}^{1f}_{12n}(a) \\
-\frac{\mu_f}{\mu_m}\mathfrak{E}^{1f}_{41n}(a) & -\frac{\mu_f}{\mu_m}\mathfrak{E}^{1f}_{42n}(a)
\end{bmatrix}
\begin{Bmatrix} B_n \\ b_n \\ D_n \\ E_n \\ d_n \\ e_n \\ C_n \\ c_n \end{Bmatrix}
= -
\begin{Bmatrix}
\mathfrak{E}^{1m}_{71n}(b)A_n + \mathfrak{E}^{1m}_{72n}(b)a_n \\
\mathfrak{E}^{1m}_{81n}(b)A_n + \mathfrak{E}^{1m}_{82n}(b)a_n \\
\mathfrak{E}^{1m}_{11n}(b)A_n + \mathfrak{E}^{1m}_{12n}(b)a_n \\
\mathfrak{E}^{1m}_{41n}(b)A_n + \mathfrak{E}^{1m}_{42n}(b)a_n \\
0 \\ 0 \\ 0 \\ 0
\end{Bmatrix} \tag{2-146}$$

In [8], expressions similar to eqn. (2–39) were used for φ^i and ψ^i, which resulted in a slightly different equation system. It is discovered in the present research that, at a moderately high order n, which probably was not reached in the computations in [8][10], the equation system becomes very ill-conditioned, rendering erroneous results.

It is noted that eqn. (2–146) may also become ill-conditioned at high order n, but the ill-conditioning is remediable. The ill-conditioning symptom is that the elements of the third and fifth columns have very small magnitudes while those of the fourth and sixth columns have very large magnitudes. This is due to the fact that, at high orders, $J_n(x)$ approaches 0, $Y_n(x)$ diverges, and yet $J_n(x)Y_n(x)$ remains $O(1)$. The ill-conditioning problem can be remedied by a normalization procedure. Define a series of normalized coefficients such as $\overline{B}_n = B_n|H_n(\kappa a)|$ and reorganize the system matrix. It can be found that the system matrix is correspondingly normalized if each column is divided by the corresponding normalizing factor. Denormalize the solution to obtain the solution for the original equation system. A good set of normalizing factors for eqn. (2–146) has been found as, from the first to eighth columns, $|H_n(\kappa_m a)|$, $|H_n(k_m a)|$, $|J_n(\kappa_i a)|$, $|Y_n(\kappa_i a)|$, $|J_n(k_i a)|$, $|Y_n(k_i a)|$, $|J_n(\kappa_f a)|$ and $|J_n(k_f a)|$, respectively.

2-4.3 Numerical Results and Discussions

The solutions and numerical results for P/SV wave scattering due to rigid, void and elastic scatterers have been discussed extensively in Pao and Mow's treatise[4]. Some experimental results for the elastic scatterer case are reported in [13]. P/SV wave scattering due to a layered scatterer has been discussed in [8] and in greater detail in [12], and some experimental results are reported in [14]. In this subsection, some numerical results for SH wave scattering problems solved in §2-4.1 are presented, with an emphasis on the case of the layered scatterer, whose solution has not yet appeared in the literature However, it must be noted that this is not intended to be a comprehensive numerical analysis or comparison of the solved cases. It is only intended to provide a glimpse into the main characteristics of single fiber models.

Computations are performed for a ceramic-fiber reinforced metal-matrix composite system whose constituents' material properties are listed in Table 2-1. The fiber radius can be taken as $a = 10\,\mu$m[11]. However, it is noted that, since a is a characteristic length of the problem, and in all the following examples, the nondimensionalized frequency $k_m a$ is used, the particular value of a is not important. For simplicity, a can be assumed to be of unit length. Unless otherwise specified, the outer radius of the interphase, when present, is assumed to be $b = 1.1a$. The incident wave is a planar wave of unit amplitude propagating along the $+x$ direction, whose expression is given in eqn. (2-70), with $\phi_0 = 1$.

The spectra shown in the following results correspond to the following measuring points: the far-field forward and backward measuring points are $(x, y) = (50a, 0)$ and $(-50a, 0)$, respectively; the near-field measuring points are $(\pm 5a, 0)$, see Fig. 2-1.

Prior to computations, a criterion must be established to truncate the infinite series that represent the various wave fields, such as the scattered wave in eqn. (2-71) and the incident wave in eqn. (2-69). Consider first the scattered

Table 2-1: Constituent Material Properties for a Metal-Matrix Ceramic-Fiber Composite System[11]

Property	Matrix (AA520 Aluminium)	Fiber (Alumina, Al_2O_3)	Interphase (Zirconia, ZrO_2)
Density (kg/m^3)	2600	3700	6300
Young's Modulus (GPa)	66	360	97
Poisson's Ratio	0.31	0.25	0.33
Lamé Constant λ (GPa)	41	144	71
Lamé Constant μ (GPa)	25	144	37
P Wave Speed (m/s)	5930	10800	4780
S Wave Speed (m/s)	3110	6240	2400

wave in eqn. (2–71). In general, such a series can be truncated at order N when $\left|B_N H_N^{(1)}(k_m r)\right| = \left|B_{-N} H_{-N}^{(1)}(k_m r)\right|$ is smaller than a prescribed error tolerance ε, where to "*truncate at order N*" means using the partial sum of the series from term $n = -N$ up to term $n = N$ to approximate the infinite sum. Note that the scattered wave is to be evaluated only outside the scatterer; that is $r > a$, and that, for a given n, $|H_n^{(1)}(k_m r)|$ (the modulus of the Hankel function) is a monotonically decreasing function of r[7]. Therefore, the criterion is simply to truncate the series at N when

$$\left|B_N H_N^{(1)}(k_m a)\right| < \varepsilon \tag{2–147}$$

More importantly, such a truncated expression is accurate enough everywhere the scattered wave is to be evaluated. In the results presented, ε is taken as 10^{-8}.

On the other hand, when the series is truncated at order N as determined by eqn. (2–147), the expression for the incident wave in eqn. (2–69) may not be accurate for a large r. For example, according to eqn. (2–70), the planar incident wave has $|A_n| = 1$ for any n, but $|J_n(kr)|$ does not decrease as r increases. Thus, a significant error could result from using the truncated series. The most convenient way to avoid such a problem is to use the analytical expression $\phi^{\text{inc}} = e^{ik_m x} = e^{ik_m r\cos\theta}$ for the incident wave. That is, the computational form of the total wave in the matrix is

$$\phi^{\text{total}} = \phi^{\text{inc}} + \phi^{\text{s}} = e^{ik_m r\cos\theta} + \sum_{n=-N}^{N} B_n H_n(k_m r) e^{in\theta} \tag{2–148}$$

where in computing B_n, $A_n = i^n$ is used.

Figures 2–2 and 2–3 show the normalized far-field forward displacement response spectra; that is, the normalized displacement amplitude $|\phi^{\text{total}}|/|\phi^{\text{inc}}|$ versus the nondimensionalized frequency $k_m a$, for all four solved cases of SH wave scattering in §2-4.1.

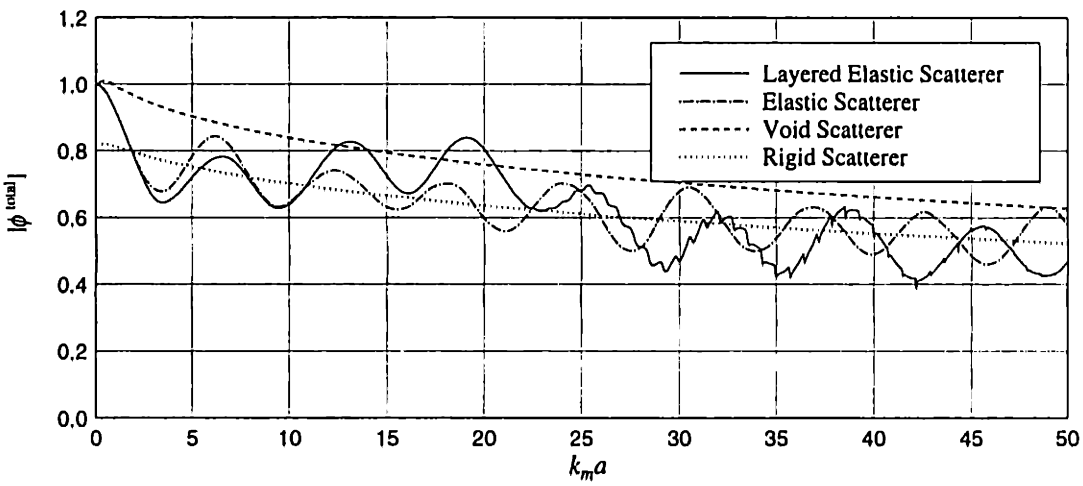

Fig. 2–2 Far-field forward response spectrum for a fiber-interphase-matrix model (layered elastic scatterer), and some other models.

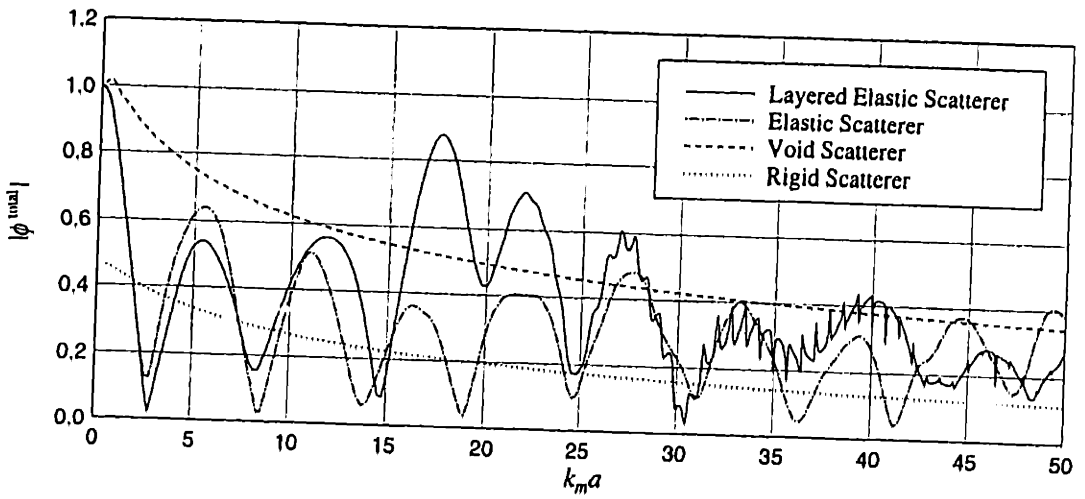

Fig. 2–3 Near-field forward response spectrum for a fiber-interphase-matrix model (layered elastic scatterer), and some other models.

Figures 2–4 and 2–5 show the normalized far-field backward response spectra for the displacement amplitude of the scattered waves; that is, $|\phi^s|/|\phi^{\text{inc}}|$ vs. $k_m a$.

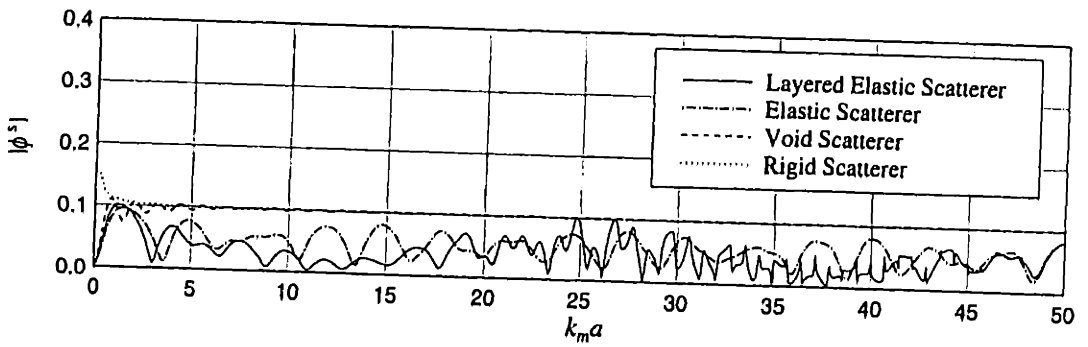

Fig. 2–4 Far-field backward response spectrum for a fiber-interphase-matrix model (layered elastic scatterer), and some other models.

In general, the total wave in the backward direction is highly oscillatory. This is due to the interference of the two waves traveling in opposite directions: the scattered wave travels in the backward direction whereas the incident wave travels in the forward direction.

Recall the asymptotic expressions for Hankel functions in eqn. (2–40). In the far-field (when $k_m r$ is large), the total wave in the matrix can be written as

$$\phi^{\text{total}} = e^{ik_m x} + \sum_{n=-\infty}^{\infty} B_n \sqrt{\frac{2}{\pi k_m r}} e^{i(k_m r - \frac{1+2n}{4}\pi)} e^{in\theta} \qquad (2\text{–}149)$$

In the forward direction, $\theta = 0$ and $x = r$,

$$\phi^{\text{total}}\Big|_{\text{forward}} = e^{ik_m r}\left(1 + \sqrt{\frac{2}{\pi k_m r}} \sum_{n=-\infty}^{\infty} B_n e^{-i\frac{1+2n}{4}}\right) \equiv e^{ik_m r}\left[1 + f_1(k_m)\right] \qquad (2\text{–}150)$$

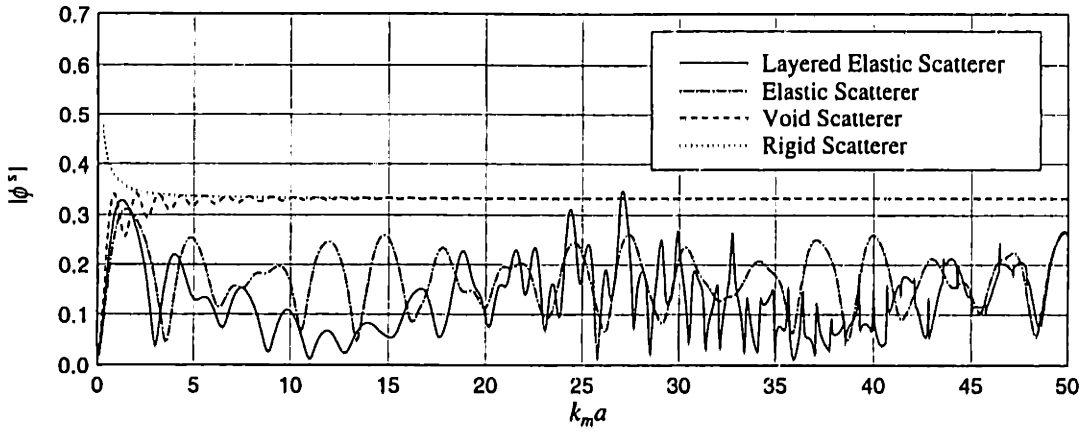

Fig. 2–5 Near-field backward response spectrum for a fiber-interphase-matrix model (layered elastic scatterer), and some other models.

$$\left|\phi^{\text{total}}\right|_{\text{forward}} = |1 + f_1(k_m)| \tag{2-151}$$

Whereas in the backward direction, $\theta = \pi$ and $x = -r$,

$$\begin{aligned}\phi^{\text{total}}\Big|_{\text{backward}} &= e^{\hat{i}k_m r}\left(e^{-2\hat{i}k_m r} + \sqrt{\frac{2}{\pi k_m r}}\sum_{n=-\infty}^{\infty} B_n e^{\hat{i}\frac{2n-1}{4}}\right) \\ &\equiv e^{\hat{i}k_m r}\left[e^{-2\hat{i}k_m r} + f_2(k_m)\right] \qquad (2\text{–}152)\end{aligned}$$

$$\left|\phi^{\text{total}}\right|_{\text{backward}} = \left|e^{-2\hat{i}k_m r} + f_2(k_m)\right| \tag{2-153}$$

Therefore, for a fixed r in the frequency domain, high oscillation of $\left|\phi^{\text{total}}\right|_{\text{backward}}$ is attributed to the term $e^{-2\hat{i}k_m r}$ if the function $f_2(k_m)$ is not highly oscillatory, or at least oscillates at a far different "period" from $\Delta k_m = \pi/r$, which is the "period" of the oscillation $e^{-2\hat{i}k_m r}$ in the frequency domain. In fact, this "period" can be used to determine the measuring distance r from the spectrum.

Figure 2–6 shows both the scattered wave and the total wave for an enlarged portion of the far-field backward displacement spectra for both the total wave and the scattered wave for the case of a layered scatterer (fiber-interphase-matrix model). In Fig. 2–6, the total wave spectrum contains approximately 77.7 "periods" in a range in which $k_m a$ changes from 5 to 10. This information could be used to estimate the distance between the scatterer and the measuring point as $r = \frac{77.7\pi a}{10-5} = 48.82a$, which is quite close to the exact value of $50a$.

Since it is generally the case, at least in the far-field, that the function $f_2(k_m)$ is not highly oscillatory compared with $e^{-2\hat{i}k_m r}$, it follows that $|1 \pm f_2(k_m)|$ are the envelopes of the backward spectrum of the total displacement, as shown in the dot-dashed curve in Fig. 2–6. For this reason, the scattered wave, such as $f_2(k_m)$ for the displacement, generally suffices for the purpose of observing the main characteristics of the backward scattering.

It is noted that the "period" of the total wave in the backward direction depends

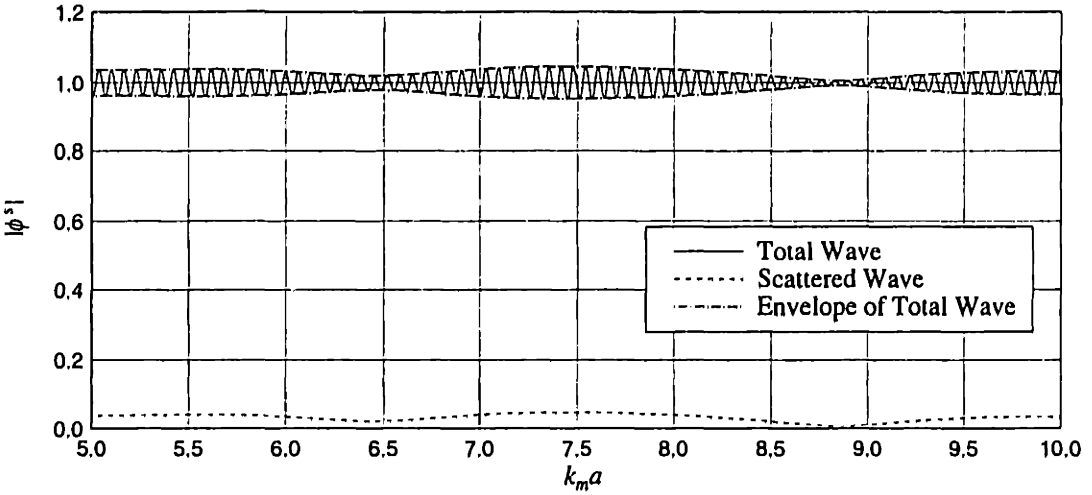

Fig. 2–6 Far-field backward scattering spectra of the total wave and the scattered wave, and the envelope of the total wave.

on the measuring distance r. Figure 2–7 shows the near-field backward displacement spectra of the total and the scattered waves, and the envelopes of the total wave. It is observed that the "period" increases as r decreases, and the curve for the total wave does not exhibit as clear a periodicity as in the case of far-field, since the "periods" of $f_2(k_m)$ and $e^{-2ik_m r}$ are closer than in the far-field case such that the interference between them becomes severe.

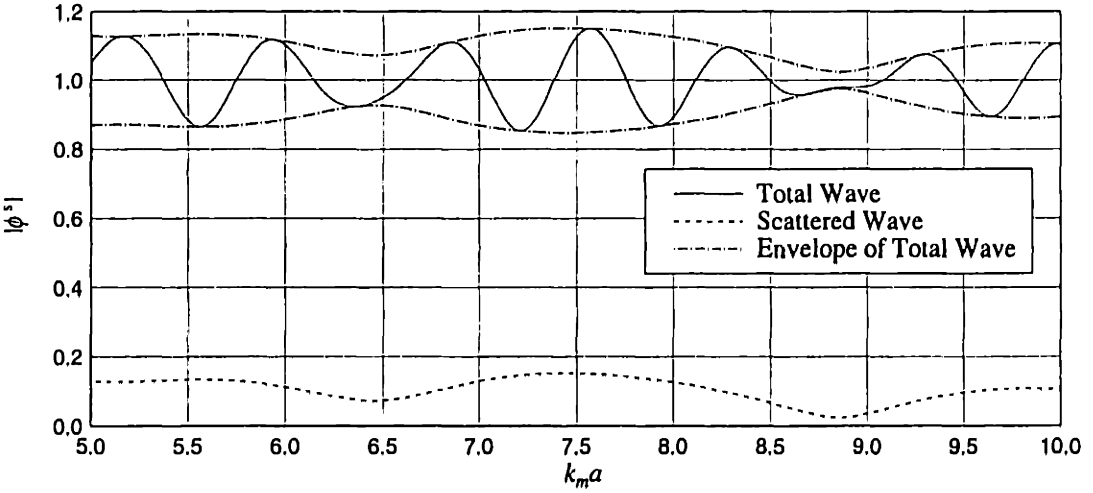

Fig. 2–7 Near-field backward scattering spectra of the total wave and the scattered wave, and the envelope of the total wave.

Comparing the spectra for the elastic scatterer with those for the rigid and void scatterers in Figs. 2–2 through 2–5, it is observed that a spectrum for the elastic scatterer has an oscillatory structure whose "period" in the frequency domain appears to be roughly a constant. On the other hand, the spectra for both the rigid and void scatterers are almost monotonic, except in the low frequency range. As

compared with the rigid and void scatterer cases, the difference in the case of an elastic scatterer is that it has a refracted wave that resides within the scatterer. Therefore the oscillatory structure can be attributed to the existence of the refracted wave that resides within the scatterer.

Comparing the curves for the layered scatterer and the elastic scatterer in Figs. 2–2 through 2–5, the most striking difference observed is that there appears to be a secondary oscillatory structure in the spectra for the case of the layered scatterer. At relatively low frequencies (from $ka = 20$ to 32), this secondary structure appears as a smooth oscillation that is superposed onto the main oscillatory structure, but at relatively high frequencies (from $ka = 42$ to 45), the secondary structure turns into sharp spikes. At even higher frequencies ($ka > 45$), the secondary structure tends to diminish. This secondary spectrum structure is believed to be due to resonance, which is beyond the scope of this thesis. References [15] and [16] provide detailed reviews of this subject matter.

Figure 2–8 shows the forward spectra for two degenerate cases of the layered elastic scatterer (the fiber-interphase-matrix model): one is that the interphase has the same properties as the matrix, which is designated as "Interphase = Matrix", and the other is that the interphase has the same properties as the fiber, which is designated as "Interphase = Fiber". Naturally the solution for the "Interphase = Matrix" case should reduce to that of the elastic scatterer. Indeed, the curve for this case in Fig. 2–8 matches exactly the curve for the case of the elastic scatterer in Fig. 2–2.

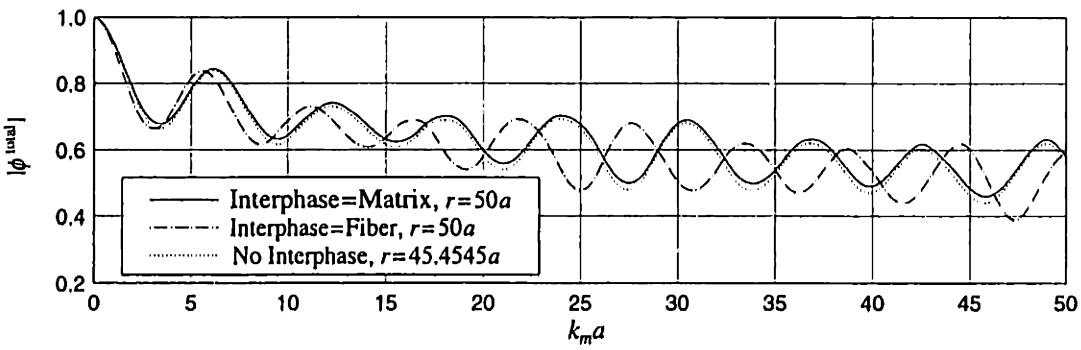

Fig. 2–8 Far-field forward spectra of the layered scatterer for two degenerated cases, with comparion to the case of the elastic scatterer at equivalent measuring location.

The "Interphase = Fiber" case is equivalent to the case of the elastic scatterer (without the interphase) where the fiber has the radius of $b = 1.1a$. The following equivalences between such a degenerated case and the case of the elastic scatterer can be observed: the frequency k_m in the degenerated case is equivalent to the frequency $k'_m = \frac{b}{a}k_m$ in the elastic case (such that $k_m b = k'_m a$); the measuring distance r in the degenerated case is equivalent to a measuring distance of $r' = \frac{a}{b}r$ in the elastic

case (such that $k_m r = k'_m r'$). These equivalences actually reflect a simple fact: there is only a single characteristic length of the elastic scatterer problem — the radius of the fiber. The dotted curve in Fig. 2–8 is the spectrum for the elastic scatterer at the measuring point $(x, y) = (45.4545a, 0)$. It can be verified that if the curve of the degenerated case of "Interphase = Fiber", the dot-dashed curve, is stretched by a factor of 1.1 along the abscissa, the two curves will match exactly.

Figure 2–9 shows the far-field forward spectra of the layered elastic scatterer for a series of different interphase thicknesses. The case $b = 1.00a$ represents yet another degenerated case in which the interphase simply vanishes, and again, it can be verified that this curve matches exactly with the curve for the case of the elastic scatterer in Fig. 2–2.

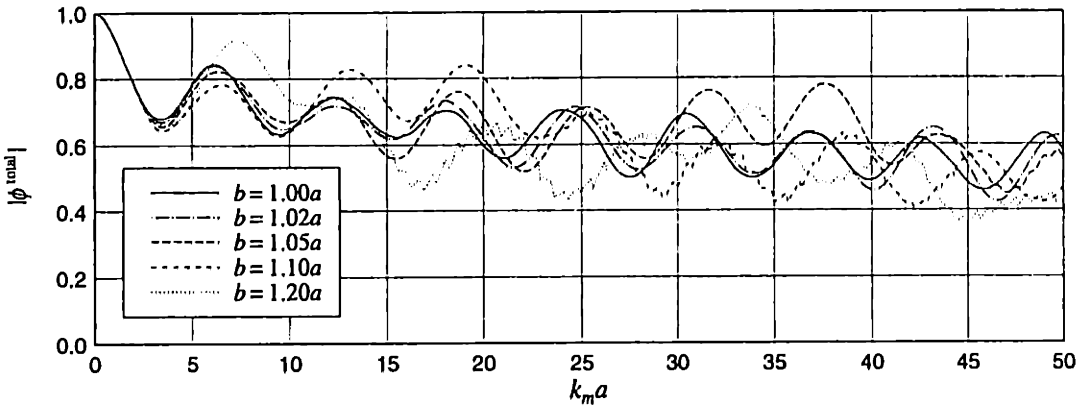

Fig. 2–9 Far-field forward spectra for a series of different interphase thicknesses.

It is observed from Fig. 2–9 that the interphase thickness has a profound effect on the secondary spectrum structure. When the interphase is very thin (less than $0.05a$), the secondary structure does not appear for the frequencies up to $k_m a = 50$. In a separate computation for $b = 1.02a$, no secondary structure is observed for frequencies up to $k_m a = 300$. As the interphase becomes thicker, the secondary structure begins to appear, judged by the appearance of the first secondary peak, at lower frequencies. For interphase thicknesses of $0.05a$, $0.10a$ and $0.20a$ ($b = 1.05a$, $1.10a$ and $1.20a$, respectively), the secondary structures in the spectra begin to appear near $k_m a = 43$, 24 and 12, respectively.

For stress and strain fields, the expressions for the stresses are

$$\sigma_{rz} = 2\mu k_m \left(\hat{\imath} \cos\theta e^{\hat{\imath} k_m r \cos\theta} + \sum_{n=-\infty}^{\infty} B_n H_n^{(1)\prime}(k_m r) e^{\hat{\imath} n\theta} \right) \tag{2-154}$$

$$\sigma_{\theta z} = 2\mu k_m \left(-\hat{\imath} \sin\theta e^{\hat{\imath} k_m r \cos\theta} + \sum_{n=-\infty}^{\infty} \frac{\hat{\imath} n}{k_m r} B_n H_n^{(1)}(k_m r) e^{\hat{\imath} n\theta} \right) \tag{2-155}$$

Since the incident wave has unit amplitude, the stress fields are correspondingly normalized by a factor of $2\mu k_m$ for both components; that is, $\overline{\sigma}_{rz} = \sigma_{rz}/(2\mu k)$ and $\overline{\sigma}_{\theta z} = \sigma_{\theta z}/(2\mu k)$. It is noted that such normalized stresses have identical expressions

as the corresponding normalized strains, normalized by k_m; that is, $\overline{\sigma}_{rz} = \overline{\varepsilon}_{rz}$ and $\overline{\sigma}_{\theta z} = \overline{\varepsilon}_{\theta z}$.

Due to the symmetry of the problem, $\sigma_{\theta z} = 0$ along the x-axis. Figure 2–10 shows the far-field spectra of the normalized shear stress $|\overline{\sigma}_{rz}|$ in both forward and backward directions. Again, the backward spectrum shows only the contribution due to the scattered waves. It is observed that the stress spectra $|\overline{\sigma}_{rz}|$ in Fig. 2–10 resemble the corresponding displacement spectra in Figs. 2–2 and 2–4.

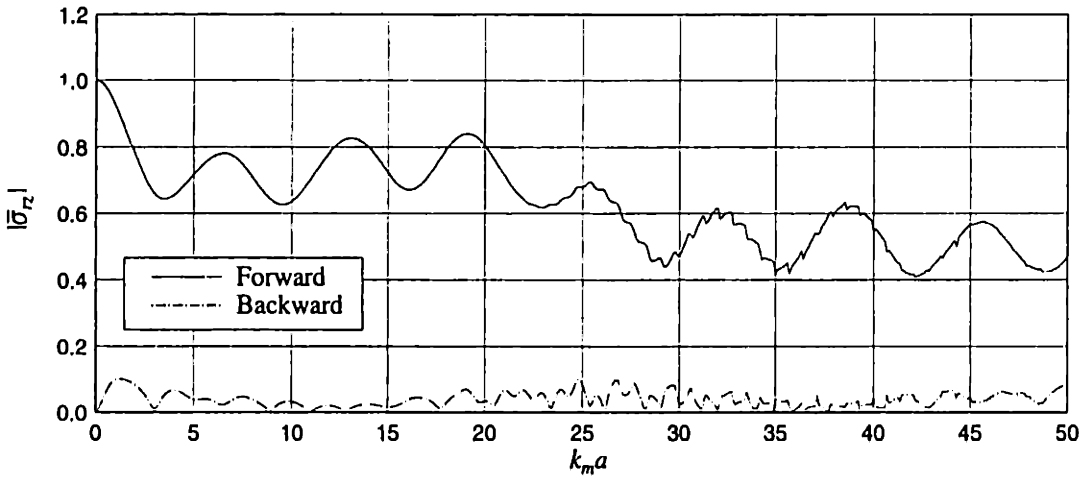

Fig. 2–10 Far-field spectra of the normalized shear stress $|\overline{\sigma}_{rz}|$ of the layered elastic scatterer.

Finally, spatial distributions of various fields are given in Figs. 2–11 through 2–16. Figures 2–11, 2–12 and 2–13 show the distributions of the displacement amplitude $|w|$, and the normalized stresses $|\overline{\sigma}_{rz}|$ and $|\overline{\sigma}_{\theta z}|$, respectively, for the fiber-interphase-matrix model at the frequency $k_m a = 1$. Figures 2–14, 2–15 and 2–16 are the corresponding *snap shots* of the displacement w, and the normalized stresses $\overline{\sigma}_{rz}$ and $\overline{\sigma}_{\theta z}$, respectively, in the vicinity of the fiber at a particular instant t such that ωt is an integer multiple of 2π. "Snap shot" means that the real values of the physical quantity are shown. For displacements, for example, from eqn. (2–15),

$$w = Re\{\phi^{\text{total}} e^{-i\omega t}\} \tag{2–156}$$

When ωt is an integer multiple of 2π, $w = Re\{\phi^{\text{total}}\}$. In Figs. 2–11 through 2–16, the fields inside the scatterer are not calculated and are set to zero. The curves projected onto the bottom planes are contours of the surfaces with an arbitrarily chosen contour value of 0.25.

To summarize, the following conclusions can be drawn from the numerical results presented:

- As expected, the fiber-interphase-matrix model degenerates into the simpler fiber-matrix model (elastic scatterer case) under several different situations. The fiber-matrix model has only one characteristic length so problems for different fiber

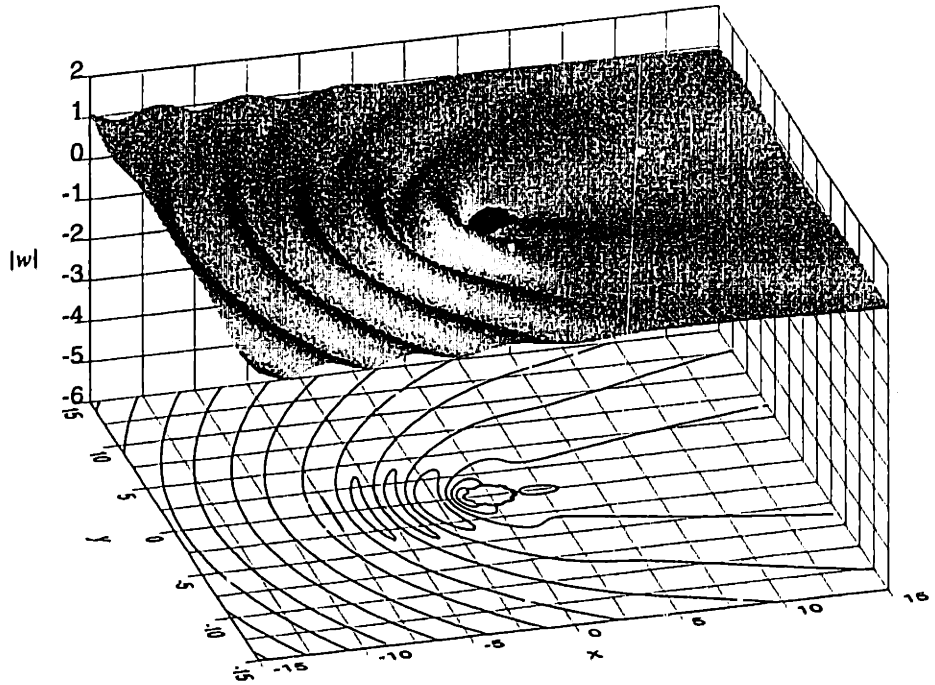

Fig. 2–11 Spatial distribution of the displacement amplitude $|w|$ in the vicinity of the fiber at the frequency $k_m a = 1$.

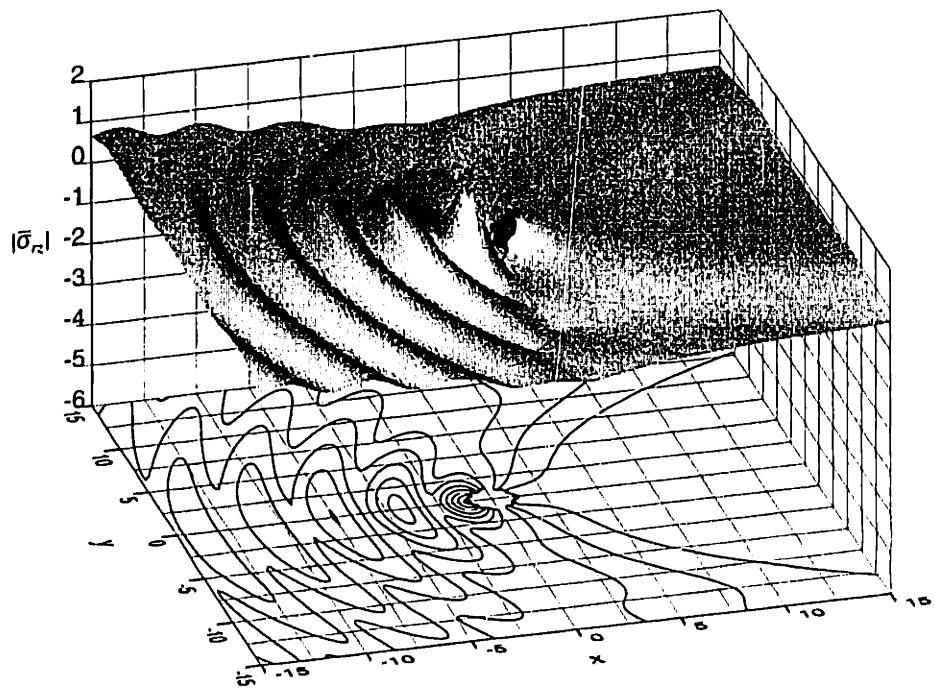

Fig. 2–12 Spatial distribution of the magnitude of the normalized shear stress $|\bar{\sigma}_{rz}|$ in the vicinity of the fiber at the frequency $k_m a = 1$.

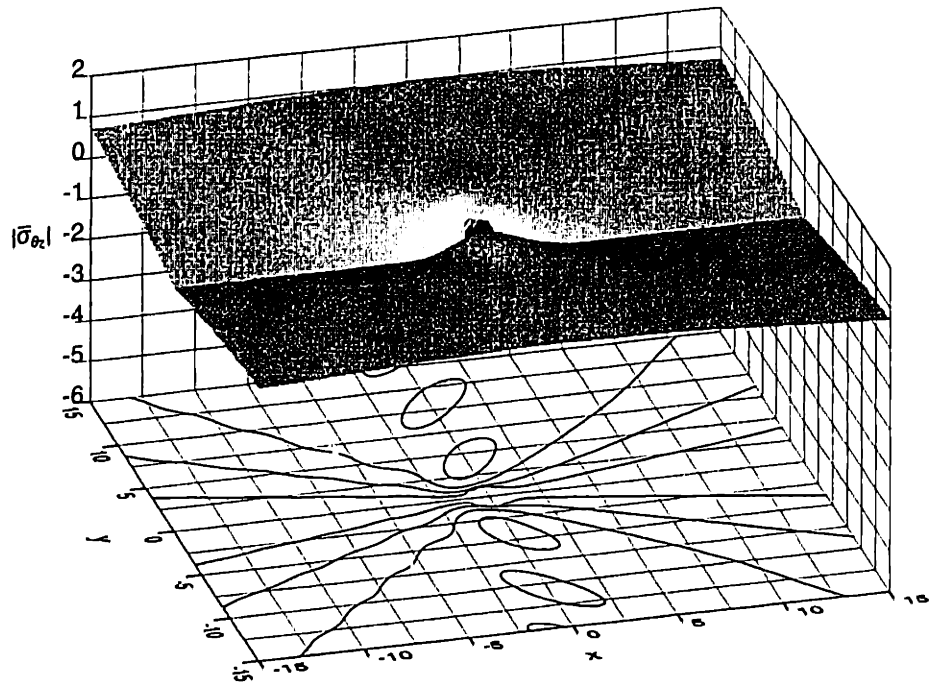

Fig. 2–13 Spatial distribution of the amplitude of the normalized shear stress $|\bar{\sigma}_{\theta z}|$ in the vicinity of the fiber at the frequency $k_m a = 1$.

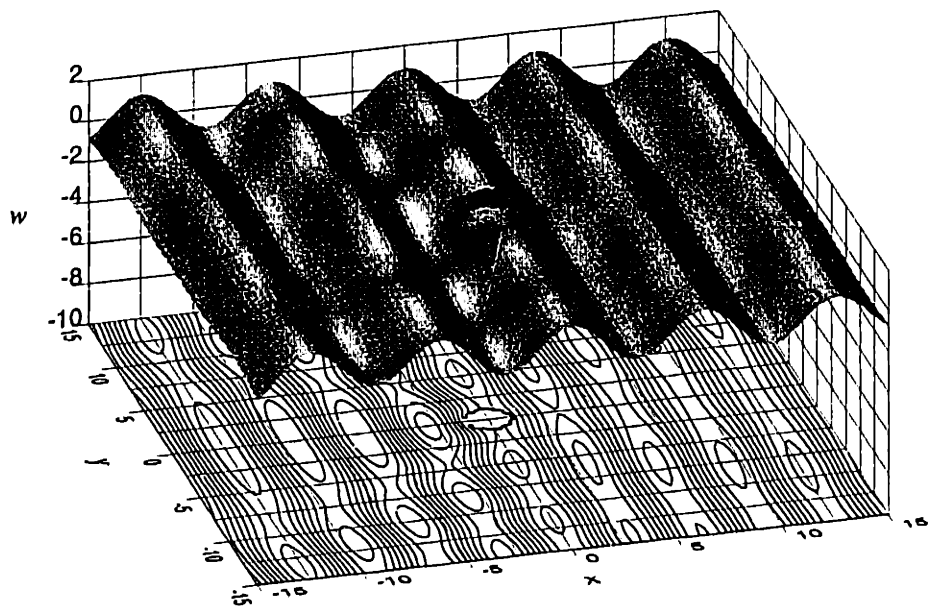

Fig. 2–14 Snap shot of the displacement w in the vicinity of the fiber at the frequency $k_m a = 1$.

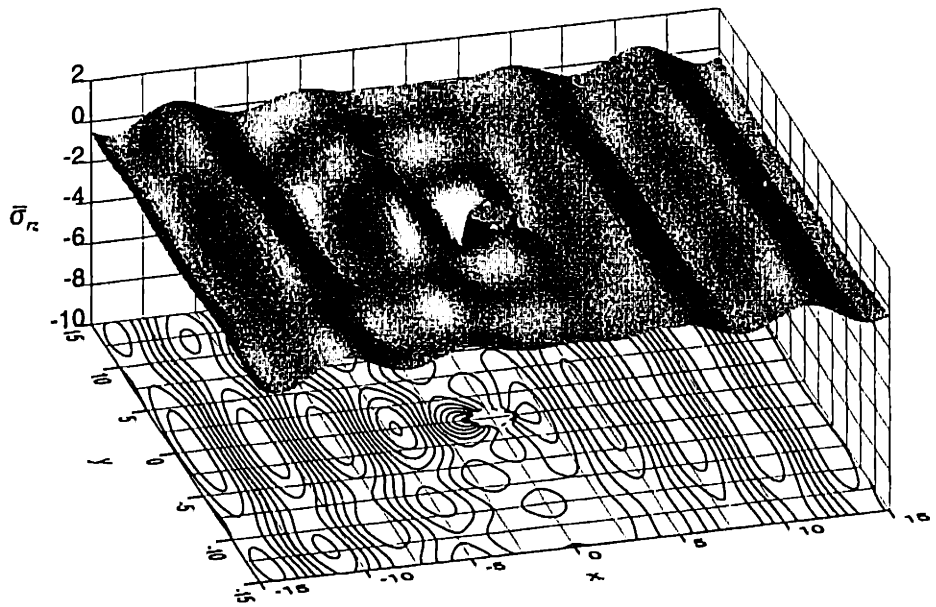

Fig. 2–15 Snap shot of the normalized shear stress $\bar{\sigma}_{rz}$ in the vicinity of the fiber at the frequency $k_m a = 1$.

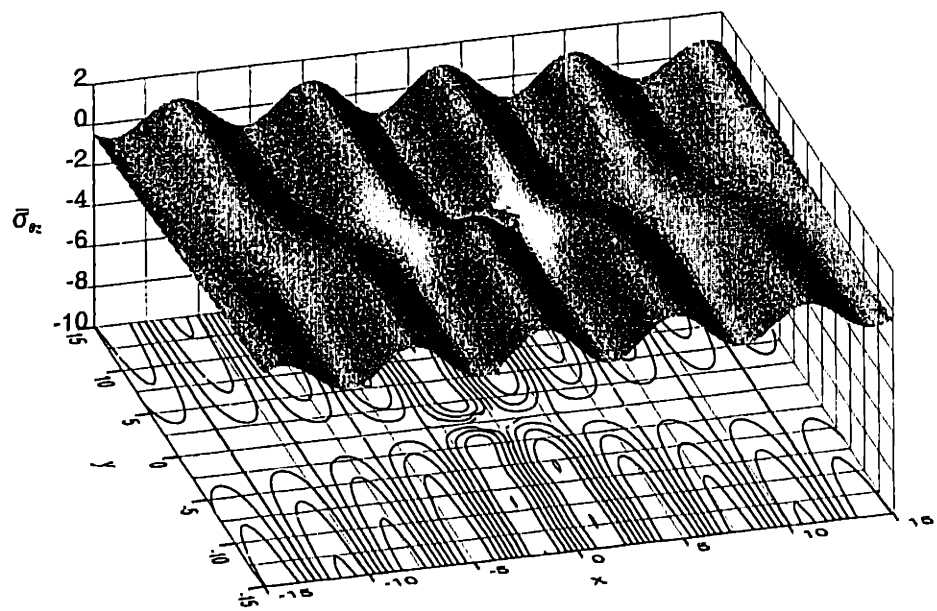

Fig. 2–16 Snap shot of the normalized shear stress $\bar{\sigma}_{\theta z}$ in the vicinity of the fiber at the frequency $k_m a = 1$.

radii can be reduced into the same problem by proper scalings.

- For any single scattering problem, the backward scattering spectrum of the *total* wave is highly oscillatory, and its characteristic "period" in the frequency domain Δk_m is related to the measuring distance r by the relation $\Delta k_m = \pi/r$. The envelopes of the backward spectrum are given by $|1 \pm f_2(k_m)|$ where $f_2(k_m)$ is the backward spectrum of the *scattered* wave.
- The existence of the refracted wave inside the scatterer introduces the main oscillatory structure of the spectrum.
- The presence of the interphase introduces a secondary oscillatory structure into the spectrum, but there might exist a threshold thickness of the interphase, below which no secondary structure would appear.
- The interphase thickness affects the spectrum in two ways: first, the thicker the interphase, the earlier (at lower frequencies) the secondary structure appears; second, it shifts the peaks of the main oscillatory structure of the spectrum.

The results for the single layered scatterer in SH wave case suggest that the case might be worth exploring further.

References

[1] K. F. Graff, *Wave Motion in Elastic Solids,* Dover, New York, 649 pp., 1975.

[2] J. D. Achenbach, *Wave Propagation in Elastic Solids,* North-Holland Publ. Co., Amsterdam, 425 pp., 1975.

[3] P. M. Morse, H. Feshbach, *Methods of Theoretical Physics, Vol. 1,* McGraw-Hill, N. Y., 1953.

[4] Y.-H. Pao, C.-C. Mow, *Diffraction of Elastic Waves and Dynamic Stress Concentrations,* Crane Russak & Co., New York, 1971.

[5] J. Miklowitz, *The Theory of Elastic Waves and Wave Guides,* North-Holland Publ. Co., Amsterdam, 1978.

[6] Y.-H. Pao, Betti's identity and transition matrix for elastic waves, *J. Acoust. Soc. Am.,* **64**, 302–310, 1978.

[7] M. Abramowiz, I. Stegun, *Handbook of Mathematical Functions,* Dover, New York, 1965.

[8] H. Yim, J. H. Williams, Jr, Formulation and its energy balance verification for ultrasonic non-destructive characterization of a single fiber composite interphase, *Ultrasonics,* **33**, 377–387, 1995.

[9] A. N. Sinclair, R. C. Addison, Jr., Acoustic diffraction spectrum of a SiC fiber in a solid elastic medium, *J. Acoust. Soc. Am.,* **94**, 1126–1135, 1993.

[10] H. Yim, *Private communications,* 1996.

[11] H. Yim, J. H. Williams, Jr, Database generation and parametric study for ultrasonic non-destructive characterization of a single fiber composite interphase, *Ultrasonics,* **33**, 389–401, 1995.

[12] H. Yim, *Acousto-Ultrasonic Nondestructive Characterization of Interphases in Fiber Composites,* Ph. D. Thesis, Massachusetts Institute of Technology, May 1993.

[13] P. Beattie, R. C. Chivas, L. W. Anson, Ultrasonic backscattering from solid cylindrical inclusions in solid elastic matrices: a comparison of theory and experiment, *J. Acoust. Soc. Am.,* **94**, 3421–3427, 1993.

[14] R. C. Addison, Jr., A. N. Sinclair, Calculated and measured ultrasonic response of an elastic cylinder embedded in an elastic medium, *Review of progress in quantitative nondestructive evaluation, Vol.* **11A**, 105–111, D. O. Thompson, D. E. Chimenti, eds., Plenum Press, New York, 1992.

[15] D. Brill, G. Gaunaurd, Resonance theory of elastic waves ultrasonically scattered from an elastic sphere, *J. Acoust. Soc. Am.,* **81**, 1–21, 1987.

[16] G. C. Gaunaurd, Elastic and acoustic resonance wave scattering, *Appl. Mech. Rev.,* **42**, 143–192, 1989.

Appendix

2-A Analytical Solution for Equation (2–93)

For a easy reference, eqn. (2–93) is repeated here, in the expanded form as

$$-B_n H_n^{(1)}(k_m b) + D_n H_n^{(1)}(k_i b) + E_n H_n^{(2)}(k_i b) = A_n J_n(k_m b) \tag{2-A.1}$$

$$-\mu_m k_m B_n H_n^{(1)\prime}(k_m b) + \mu_i k_i D_n H_n^{(1)\prime}(k_i b) + \mu_i k_i E_n H_n^{(2)\prime}(k_i b) = \mu_m k_m A_n J_n'(k_m b) \tag{2-A.2}$$

$$D_n H_n^{(1)}(k_i a) + E_n H_n^{(2)}(k_i a) - C_n J_n(k_f a) = 0 \tag{2-A.3}$$

$$\mu_i k_i D_n H_n^{(1)\prime}(k_i a) + \mu_i k_i E_n H_n^{(2)\prime}(k_i a) - \mu_f k_f C_n J_n'(k_f a) = 0 \tag{2-A.4}$$

Solving eqns. (2-A.3) and (2-A.4) for C_n and D_n in terms of E_n gives

$$C_n = -\frac{\mu_i k_i E_n}{\Delta}\left[H_n^{(1)\prime}(k_i a)H_n^{(2)}(k_i a) - H_n^{(1)}(k_i a)H_n^{(2)\prime}(k_i a)\right] = -\frac{4\hat{\imath}\mu_i E_n}{\pi a \Delta} \tag{2-A.5}$$

$$D_n = -\frac{E_n}{\Delta}\left[\mu_f k_f J_n'(k_f a)H_n^{(2)}(k_i a) - \mu_i k_i J_n(k_f a)H_n^{(2)\prime}(k_i a)\right] \tag{2-A.6}$$

where

$$\Delta = \mu_f k_f J_n'(k_f a)H_n^{(1)}(k_i a) - \mu_i k_i J_n(k_f a)H_n^{(1)\prime}(k_i a) \tag{2-A.7}$$

and the following Wronskian relation for Hankel functions has been used

$$\mathcal{W}(H_n^{(1)}(z), H_n^{(2)}(z)) \equiv H_n^{(1)}(z)H_n^{(2)\prime}(z) - H_n^{(1)\prime}(z)H_n^{(2)}(z) = -\frac{4\hat{\imath}}{\pi z} \tag{2-A.8}$$

Denote

$$\Delta_1 = \mu_f k_f J_n'(k_f a)J_n(k_i a) - \mu_i k_i J_n(k_f a)J_n'(k_i a) \tag{2-A.9}$$

$$\Delta_2 = \mu_f k_f J_n'(k_f a)Y_n(k_i a) - \mu_i k_i J_n(k_f a)Y_n'(k_i a) \tag{2-A.10}$$

then,

$$\Delta = \Delta_1 + \hat{\imath}\Delta_2 \tag{2-A.11}$$

$$C_n = -\frac{4\hat{\imath}\mu_i}{\pi a(\Delta_1 + \hat{\imath}\Delta_2)}E_n \qquad D_n = -\frac{\Delta_1 - \hat{\imath}\Delta_2}{\Delta_1 + \hat{\imath}\Delta_2}E_n \tag{2-A.12}$$

Substitute eqn. (2-A.12) into eqns. (2-A.1) and (2-A.2), and note that

$$(\Delta_1 + \hat{\imath}\Delta_2)H_n^{(2)}(k_i b) - (\Delta_1 - \hat{\imath}\Delta_2)H_n^{(1)}(k_i b) = 2\hat{\imath}M_1 \tag{2-A.13}$$

$$(\Delta_1 + \hat{\imath}\Delta_2)H_n^{(2)}(k_i b) - (\Delta_1 - \hat{\imath}\Delta_2)H_n^{(1)}(k_i b) = 2\hat{\imath}M_2 \tag{2-A.14}$$

where

$$M_1 = \Delta_2 J_n(k_i b) - \Delta_1 Y_n(k_i b) \tag{2-A.15}$$

$$M_2 = \Delta_2 J_n'(k_i b) - \Delta_1 Y_n'(k_i b) \tag{2-A.16}$$

Then, eqns. (2-A.1) and (2-A.2) become

$$-\Delta H_n^{(1)}(k_m b)B_n + 2\hat{\imath}M_1 E_n = \Delta J_n(k_m b)A_n \tag{2-A.17}$$

$$-\mu_m k_m \Delta H_n^{(1)\prime}(k_m b)B_n + 2\hat{\imath}\mu_i k_i M_2 E_n = \mu_m k_m \Delta J_n'(k_m b)A_n \tag{2-A.18}$$

Solving these two equations gives

$$B_n = -\frac{N_1}{N_2}A_n \qquad E_n = \frac{\mu_m(\Delta_1 + \hat{\imath}\Delta_2)}{\pi b N_2}A_n \tag{2-A.19}$$

where

$$N_1 = \mu_m k_m M_1 J_n'(k_m b) - \mu_i k_i M_2 J_n(k_m b) \tag{2-A.20}$$

$$N_2 = \mu_m k_m M_1 H_n^{(1)\prime}(k_m b) - \mu_i k_i M_2 H_n^{(1)}(k_m b) \tag{2-A.21}$$

and the following Wronskian relation of Bessel functions

$$\mathcal{W}(J_n(z), H_n^{(1)}(z)) = J_n(z) H_n^{(1)\prime}(z) - J_n'(z) H_n^{(1)}(z) = \frac{2\hat{\imath}}{\pi z} \tag{2-A.22}$$

has been used. Thus, from eqn. (2-A.12)

$$C_n = -\frac{4\hat{\imath}\mu_i\mu_m}{\pi^2 a b N_2} A_n \qquad D_n = -\frac{\mu_m}{\pi b}\frac{\Delta_1 - \hat{\imath}\Delta_2}{N_2} A_n \tag{2-A.23}$$

Degenerated Cases

In the following, consider three degenerated cases in which the fiber-interphase-matrix model degenerates to the simpler fiber-matrix model in different ways.

Case 1: "Interphase = Matrix"

For this case, $\mu_i = \mu_m$, $k_i = k_m$; then,

$$\Delta_1 = \mu_f k_f J_n'(k_f a) J_n(k_m a) - \mu_m k_m J_n(k_f a) J_n'(k_m a) \tag{2-A.24}$$

$$\Delta_2 = \mu_f k_f J_n'(k_f a) Y_n(k_m a) - \mu_m k_m J_n(k_f a) Y_n'(k_m a) \tag{2-A.25}$$

$$M_1 = \Delta_2 J_n(k_m b) - \Delta_1 Y_n(k_m b) \tag{2-A.26}$$

$$M_2 = \Delta_2 J_n'(k_m b) - \Delta_1 Y_n'(k_m b) \tag{2-A.27}$$

$$N_1 = \frac{2\mu_m \Delta_1}{\pi b} = \frac{2\mu_m}{\pi b}\left[\mu_f k_f J_n'(k_f a) J_n(k_i a) - \mu_m k_m J_n(k_f a) J_n'(k_m a)\right] \tag{2-A.28}$$

$$N_2 = \frac{2\mu_m(\Delta_1 + \hat{\imath}\Delta_2)}{\pi b} = \frac{2\mu_m}{\pi b}\left[\mu_f k_f J_n'(k_f a) H_n^{(1)}(k_m a) - \mu_m k_m J_n(k_f a) H_n^{(1)\prime}(k_m a)\right] \tag{2-A.29}$$

where the following Wronskian relation

$$\mathcal{W}(Y_n(z), H_n^{(1)}(z)) \equiv Y_n(z) H_n^{(1)\prime}(z) - Y_n'(z) H_n^{(1)}(z) = -\frac{2}{\pi z} \tag{2-A.30}$$

and eqn. (2-A.22) have been used.

Therefore,

$$B_n = -\frac{\Delta_1 A_n}{\Delta_1 + \hat{\imath}\Delta_2} = -\frac{\mu_f k_f J_n'(k_f a) J_n(k_m a) - \mu_m k_m J_n(k_f a) J_n'(k_m a)}{\mu_f k_f J_n'(k_f a) H_n^{(1)}(k_m a) - \mu_m k_m J_n(k_f a) H_n^{(1)\prime}(k_m a)} A_n \tag{2-A.31}$$

$$C_n = -\frac{2\hat{\imath}\mu_m}{\pi a\left[\mu_f k_f J_n'(k_f a) H_n^{(1)}(k_m a) - \mu_m k_m J_n(k_f a) H_n^{(1)\prime}(k_m a)\right]} A_n \tag{2-A.32}$$

Furthermore,

$$D_n = -\frac{1}{2}\frac{\Delta_1 - \hat{\imath}\Delta_2}{\Delta_1 + \hat{\imath}\Delta_2} A_n \qquad E_n = \frac{1}{2} A_n \tag{2-A.33}$$

Substituting D_n and E_n into eqn. (2–88) gives the wave in the "interphase" as

$$\phi^{\mathrm{i}} = \sum_{n=-\infty}^{\infty} \left[D_n H^{(1)}(k_m r) + E_n H^{(2)}(k_m r)\right] \mathrm{e}^{\mathrm{i}n\theta} \tag{2-A.34}$$

$$= \sum_{n=-\infty}^{\infty} \left[(D_n + E_n) J_n(k_m r) + \hat{\imath}(D_n - E_n) Y_n(k_m r)\right] \mathrm{e}^{\mathrm{i}n\theta} \tag{2-A.35}$$

$$= \sum_{n=-\infty}^{\infty} \left[\frac{\hat{\imath}\Delta_2 A_n}{\Delta_1 + \hat{\imath}\Delta_2} J_n(k_m r) - \hat{\imath} \frac{\Delta_1 A_n}{\Delta_1 + \hat{\imath}\Delta_2} Y_n(k_m r) \right] e^{in\theta} \tag{2-A.36}$$

$$= \sum_{n=-\infty}^{\infty} [A_n J_n(k_m r) + B_n H^{(1)}(k_m r)] e^{in\theta} \tag{2-A.37}$$

which is the expression for the total wave in the field for the case of the elastic scatterer.

Case 2: "Interphase = Fiber"

For this case, $\mu_i = \mu_f$, $k_i = k_f$, and

$$\Delta_1 = 0 \qquad \Delta_2 = \frac{2\mu_f}{\pi a} \qquad M_1 = \frac{2\mu_f}{\pi a} J_n(k_f b) \qquad M_2 = \frac{2\mu_f}{\pi a} J_n'(k_f b) \tag{2-A.38}$$

$$N_1 = \frac{2\mu_f}{\pi a} [\mu_f k_f J_n'(k_f b) J_n(k_m b) - \mu_m k_m J_n(k_f b) J_n'(k_m b)] \tag{2-A.39}$$

$$N_2 = \frac{2\mu_f}{\pi a} \left[\mu_f k_f J_n'(k_f b) H_n^{(1)}(k_m b) - \mu_m k_m J_n(k_f b) H_n^{(1)\prime}(k_m b) \right] \tag{2-A.40}$$

where the following Wronskian relation

$$\mathcal{W}(J_n(z), Y_n(z)) \equiv J_n(z) Y_n'(z) - J_n'(z) Y_n(z) = \frac{2}{\pi z} \tag{2-A.41}$$

has been used.

Therefore,

$$B_n = -\frac{\mu_f k_f J_n'(k_f b) J_n(k_m b) - \mu_m k_m J_n(k_f b) J_n'(k_m b)}{\mu_f k_f J_n'(k_f b) H_n^{(1)}(k_m b) - \mu_m k_m J_n(k_f b) H_n^{(1)\prime}(k_m b)} A_n \tag{2-A.42}$$

$$C_n = -\frac{2\hat{\imath}\mu_m}{\pi b \left[\mu_f k_f J_n'(k_f b) H_n^{(1)}(k_m b) - \mu_m k_m J_n(k_f b) H_n^{(1)\prime}(k_m b) \right]} A_n \tag{2-A.43}$$

which are identical to the case for the elastic scatterer. Furthermore,

$$D_n = E_n = \frac{C_n}{2} = \frac{\hat{\imath}\mu_m A_n}{\pi b \left[\mu_f k_f J_n'(k_f b) H_n^{(1)}(k_m b) - \mu_m k_m J_n(k_f b) H_n^{(1)\prime}(k_m b) \right]} \tag{2-A.44}$$

Substituting D_n and E_n into eqn. (2–88) gives the wave in the "interphase" as

$$\phi^{\mathrm{i}} = \sum_{n=0}^{\infty} D_n [H_n^{(1)}(k_f r) + H_n^{(2)}(k_f r)] e^{in\theta} = \sum_{n=0}^{\infty} C_n J_n(k_f r) e^{in\theta} \tag{2-A.45}$$

which is exactly the expression for the refracted wave in the fiber for the case of the elastic scatterer of radius b.

Case 3: $b = a$

For this case,

$$\Delta_1 = \mu_f k_f J_n'(k_f a) J_n(k_i a) - \mu_m k_m J_n(k_f a) J_n'(k_i a) \tag{2-A.46}$$

$$\Delta_2 = \mu_f k_f J_n'(k_f a) Y_n(k_i a) - \mu_m k_m J_n(k_f a) Y_n'(k_i a) \tag{2-A.47}$$

Substituting eqns. (2-A.46) and (2-A.47) into eqns. (2-A.26) and (2-A.27) gives

$$M_1 = -\mu_i k_i J_n(k_f a) [J_n(k_i a) Y_n'(k_i a) - J_n'(k_i a) Y_n(k_i a)] = \frac{2\mu_i}{\pi a} J_n(k_f a) \tag{2-A.48}$$

$$M_2 = -\mu_f k_f J_n'(k_f a) [J_n(k_i a) Y_n'(k_i a) - J_n'(k_i a) Y_n(k_i a)] = \frac{2\mu_f k_f}{\pi k_i a} J_n(k_f a) \tag{2-A.49}$$

where the following Wronskian relation in eqn. (2-A.41) has been used. Thus,

$$N_1 = -\frac{2\mu_i}{\pi a}\left[\mu_f k_f J_n'(k_f a) J_n(k_m a) - \mu_m k_m J_n(k_f a) J_n'(k_m a)\right] \tag{2-A.50}$$

$$N_2 = \frac{2\mu_i}{\pi a}\left[\mu_f k_f J_n'(k_f a) H_n^{(1)}(k_m a) - \mu_m k_m J_n(k_f a) H_n^{(1)\prime}(k_m a)\right] \tag{2-A.51}$$

Therefore,

$$B_n = -\frac{\mu_f k_f J_n'(k_f a) J_n(k_m a) - \mu_m k_m J_n(k_f a) J_n'(k_m a)}{\mu_f k_f J_n'(k_f a) H_n^{(1)}(k_m a) - \mu_m k_m J_n(k_f a) H_n^{(1)\prime}(k_m a)} A_n \tag{2-A.52}$$

$$C_n = -\frac{2i\mu_m}{\pi b\left[\mu_f k_f J_n'(k_f a) H_n^{(1)}(k_m a) - \mu_m k_m J_n(k_f a) H_n^{(1)\prime}(k_m a)\right]} \tag{2-A.53}$$

$$D_n = -\frac{\mu_m}{2\mu_i}\frac{\mu_f k_f J_n'(k_f a) H_n^{(2)}(k_i a) - \mu_m k_m J_n(k_f a) H_n^{(2)\prime}(k_i a)}{\mu_f k_f J_n'(k_f a) H_n^{(1)}(k_m a) - \mu_m k_m J_n(k_f a) H_n^{(1)\prime}(k_m a)} A_n \tag{2-A.54}$$

$$E_n = \frac{\mu_m}{2\mu_i}\frac{\mu_f k_f J_n'(k_f a) H_n^{(1)}(k_i a) - \mu_m k_m J_n(k_f a) H_n^{(1)\prime}(k_i a)}{\mu_f k_f J_n'(k_f a) H_n^{(1)}(k_m a) - \mu_m k_m J_n(k_f a) H_n^{(1)\prime}(k_m a)} A_n \tag{2-A.55}$$

In this case, B_n and C_n are, again, identical to those in the case of the elastic scatterer. The coefficients D_n and E_n are irrelevant since the thickness of the interphase vanishes. The results ensure that no singularity occurs in the limiting case.

2-B Some Basic Formulas for 2-D P/SV Wave Scattering Problems

Displacements, Strains and Stresses in Terms of Displacement Potentials

From the definition of the displacement potentials,

$$u_r = \frac{\partial \varphi}{\partial r} + \frac{1}{r}\frac{\partial \psi}{\partial \theta} \tag{2-B.1}$$

$$u_\theta = \frac{1}{r}\frac{\partial \varphi}{\partial \theta} - \frac{\partial \psi}{\partial r} \tag{2-B.2}$$

It is noted that the problem is a plane-strain problem. The expressions for strains and stresses are

$$\varepsilon_{rr} = \frac{\partial^2 \varphi}{\partial r^2} + \frac{1}{r}\frac{\partial^2 \psi}{\partial r \partial \theta} - \frac{1}{r^2}\frac{\partial \psi}{\partial \theta}, \tag{2-B.3}$$

$$\varepsilon_{\theta\theta} = \frac{1}{r^2}\frac{\partial^2 \varphi}{\partial \theta^2} + \frac{1}{r}\frac{\partial \varphi}{\partial r} - \frac{1}{r}\frac{\partial^2 \psi}{\partial r \partial \theta} + \frac{1}{r^2}\frac{\partial \psi}{\partial \theta} \tag{2-B.4}$$

$$\gamma_{r\theta} = \frac{2}{r}\frac{\partial^2 \varphi}{\partial r \partial \theta} - \frac{2}{r^2}\frac{\partial \varphi}{\partial \theta} - \frac{\partial^2 \psi}{\partial r^2} + \frac{1}{r^2}\frac{\partial^2 \psi}{\partial \theta^2} + \frac{1}{r}\frac{\partial \psi}{\partial r} \tag{2-B.5}$$

$$\varepsilon_{zz} = \gamma_{rz} = \gamma_{zr} = \gamma_{\theta z} = \gamma_{z\theta} = 0 \tag{2-B.6}$$

$$\sigma_{rr} = \lambda \nabla^2 \varphi + 2\mu\left(\frac{\partial^2 \varphi}{\partial r^2} + \frac{1}{r}\frac{\partial^2 \psi}{\partial r \partial \theta} - \frac{1}{r^2}\frac{\partial \psi}{\partial \theta}\right) \tag{2-B.7}$$

$$\sigma_{\theta\theta} = \lambda \nabla^2 \varphi + 2\mu\left(\frac{1}{r^2}\frac{\partial^2 \varphi}{\partial \theta^2} + \frac{1}{r}\frac{\partial \varphi}{\partial r} - \frac{1}{r}\frac{\partial^2 \psi}{\partial r \partial \theta} + \frac{1}{r^2}\frac{\partial \psi}{\partial \theta}\right) \tag{2-B.8}$$

$$\sigma_{zz} = \lambda \nabla^2 \varphi \tag{2-B.9}$$

$$\sigma_{r\theta} = \mu \left(\frac{2}{r} \frac{\partial^2 \varphi}{\partial r \partial \theta} - \frac{2}{r^2} \frac{\partial \varphi}{\partial \theta} - \frac{\partial^2 \psi}{\partial r^2} + \frac{1}{r^2} \frac{\partial^2 \psi}{\partial \theta^2} + \frac{1}{r} \frac{\partial \psi}{\partial r} \right) \tag{2-B.10}$$

$$\sigma_{rz} = \sigma_{zr} = \gamma_{\sigma z} = \sigma_{z\theta} = 0 \tag{2-B.11}$$

Displacements, Strains and Stresses Due to a Single Term of Wave Expansions of Displacement Potentials

In the following, contributions to displacements, strains and stresses due to a single term of the wave expansion for each displacement potential are derived. Without loss of generality, the displacement potentials are assumed as

$$\varphi = \mathfrak{C}_n(\kappa r) e^{in\theta} \qquad \text{and} \qquad \psi = \mathfrak{C}_n(kr) e^{in\theta} \tag{2-B.12}$$

where $\mathfrak{C}_n$ is a formal notation for cylindrical functions, which can be any one of the following: $J_n(\cdot)$, $Y_n(\cdot)$, $H_n^{(1)}(\cdot)$ and $H_n^{(2)}(\cdot)$. Recall that φ and ψ must satisfy the following Helmholtz equations

$$\nabla^2 \varphi + \kappa^2 \varphi = 0 \qquad \nabla^2 \psi + k^2 \psi = 0 \tag{2-B.13}$$

Furthermore, the wave numbers are related to each other by material properties as

$$\left(\frac{\kappa}{k} \right)^2 = \frac{\mu}{\lambda + 2\mu} \tag{2-B.14}$$

In addition, the following recursive relations of the cylindrical functions will be used during the derivation

$$\mathfrak{C}_n'(z) = \mathfrak{C}_{n-1}(z) - \frac{n}{z} \mathfrak{C}_n(z) \tag{2-B.15}$$

$$\mathfrak{C}_n''(z) = \frac{1}{z^2} \left[\left(n^2 + n - z^2 \right) \mathfrak{C}_n(z) - z \mathfrak{C}_{n-1}(z) \right] \tag{2-B.16}$$

Displacements

—Contributions Due to φ

$\boxed{u_r}$

$$\frac{\partial \varphi}{\partial r} = \kappa \mathfrak{C}_n'(\kappa r) = \frac{1}{r} \left[-n \mathfrak{C}_n(\kappa r) + \kappa r \mathfrak{C}_{n-1}(\kappa r) \right] \tag{2-B.17}$$

where eqn. (2-B.15) has been used.

$\boxed{u_\theta}$

$$\frac{1}{r} \frac{\partial \varphi}{\partial \theta} = \frac{in}{r} \mathfrak{C}_n(\kappa r) = \frac{1}{r} \left[in \mathfrak{C}_n(\kappa r) \right] \tag{2-B.18}$$

—Contributions Due to ψ

$\boxed{u_r}$

$$\frac{1}{r} \frac{\partial \psi}{\partial \theta} = \frac{in}{r} \mathfrak{C}_n(kr) = \frac{1}{r} \left[in \mathfrak{C}_n(kr) \right] \tag{2-B.19}$$

$\boxed{u_\theta}$

$$-\frac{\partial \psi}{\partial r} = -k \mathfrak{C}_n'(kr) = \frac{1}{r} \left[n \mathfrak{C}_n(kr) - kr \mathfrak{C}_{n-1}(kr) \right] \tag{2-B.20}$$

Strain Components

—Contributions Due to φ

$\boxed{\varepsilon_{rr}}$

$$\frac{\partial^2\varphi}{\partial r^2} = \kappa^2\mathfrak{C}_n''(\kappa r) = \frac{1}{r^2}\left[\left(n^2+n-\kappa^2r^2\right)\mathfrak{C}_n(\kappa r) - \kappa r\mathfrak{C}_{n-1}(\kappa r)\right] \tag{2-B.21}$$

where eqn. (2-B.16) has been used.

$\boxed{\varepsilon_{\theta\theta}}$

$$\begin{aligned}\frac{1}{r^2}\frac{\partial^2\varphi}{\partial\theta^2} + \frac{1}{r}\frac{\partial\varphi}{\partial r} &= \frac{1}{r^2}\left[\left(-n^2\right)\mathfrak{C}_n(\kappa r) + \kappa r\mathfrak{C}_n'(\kappa r)\right] \\ &= \frac{1}{r^2}\left[\left(-n^2-n\right)\mathfrak{C}_n(\kappa r) + \kappa r\mathfrak{C}_{n-1}(\kappa r)\right]\end{aligned} \tag{2-B.22}$$

where eqn. (2-B.15) has been used.

$\boxed{\gamma_{r\theta}}$

$$\begin{aligned}\frac{2}{r}\frac{\partial^2\varphi}{\partial r\partial\theta} - \frac{2}{r^2}\frac{\partial\varphi}{\partial\theta} &= \frac{2}{r^2}\left[\hat{\imath}n\kappa r\mathfrak{C}_n'(\kappa r) - \hat{\imath}n\mathfrak{C}_n(\kappa r)\right] \\ &= \frac{2}{r^2}\hat{\imath}n\left[-(n+1)\mathfrak{C}_n(\kappa r) + \kappa r\mathfrak{C}_{n-1}(\kappa r)\right]\end{aligned} \tag{2-B.23}$$

where eqn. (2-B.15) has been used.

—Contributions Due to ψ

$\boxed{\varepsilon_{rr}}$

$$\begin{aligned}\frac{1}{r}\frac{\partial^2\psi}{\partial r\partial\theta} - \frac{1}{r^2}\frac{\partial\psi}{\partial\theta} &= \frac{1}{r^2}\left[\hat{\imath}nkr\mathfrak{C}_n'(kr) - \hat{\imath}n\mathfrak{C}_n(kr)\right] \\ &= \frac{1}{r^2}\hat{\imath}n\left[-(n+1)\mathfrak{C}_n(kr) + kr\mathfrak{C}_{n-1}(kr)\right]\end{aligned} \tag{2-B.24}$$

where eqn. (2-B.15) has been used.

$\boxed{\varepsilon_{\theta\theta}}$

$$\frac{1}{r^2}\frac{\partial\psi}{\partial\theta} - \frac{1}{r}\frac{\partial^2\psi}{\partial r\partial\theta} = \frac{1}{r^2}\hat{\imath}n\left[(n+1)\mathfrak{C}_n(kr) - kr\mathfrak{C}_{n-1}(kr)\right] \tag{2-B.25}$$

where it is noted that the left-hand side is the negation of the left-hand side of the ε_{rr} term in eqn. (2-B.24).

$\boxed{\gamma_{r\theta}}$

$$\begin{aligned}-\frac{\partial^2\psi}{\partial r^2} + \frac{1}{r}\frac{\partial\psi}{\partial r} + \frac{1}{r^2}\frac{\partial^2\psi}{\partial\theta^2} &= -k^2\mathfrak{C}_n''(kr) + \frac{\beta}{r}\mathfrak{C}_n'(kr) - \frac{n^2}{r^2}\mathfrak{C}_n(kr) \\ &= -\frac{1}{r^2}\left(n^2+n-k^2r^2\right)\mathfrak{C}_n(kr) + \frac{1}{r^2}kr\mathfrak{C}_{n-1}(kr) \\ &\quad + \frac{\beta}{r}\mathfrak{C}_{n-1}(kr) - \frac{\beta}{r}\frac{n}{kr}\mathfrak{C}_n(kr) - \frac{n^2}{r^2}\mathfrak{C}_n(kr) \\ &= \frac{2}{r^2}\left[-\left(n^2+n-\frac{1}{2}k^2r^2\right)\mathfrak{C}_n(kr) + kr\mathfrak{C}_{n-1}(kr)\right]\end{aligned} \tag{2-B.26}$$

where eqns. (2-B.15) and (2-B.16) have been used.

Stress Components

—Contributions Due to φ

$\boxed{\sigma_{rr}}$

$$\begin{aligned}\lambda\nabla^2\varphi + 2\mu\frac{\partial^2\varphi}{\partial r^2} &= -\lambda\kappa^2\varphi + 2\mu\frac{\partial^2\varphi}{\partial r^2}\\ &= -\lambda\kappa^2\mathfrak{C}_n(\kappa r) + \frac{2\mu}{r^2}\left[(n^2+n-\kappa^2r^2)\mathfrak{C}_n(\kappa r) - \kappa r\mathfrak{C}_{n-1}(\kappa r)\right]\\ &= \frac{2\mu}{r^2}\left[\left(n^2+n-\kappa^2r^2\frac{\lambda+2\mu}{2\mu}\right)\mathfrak{C}_n(\kappa r) - \kappa r\mathfrak{C}_{n-1}(\kappa r)\right]\\ &= \frac{2\mu}{r^2}\left[\left(n^2+n-\frac{1}{2}k^2r^2\right)\mathfrak{C}_n(\kappa r) - \kappa r\mathfrak{C}_{n-1}(\kappa r)\right] \qquad \text{(2-B.27)}\end{aligned}$$

where eqns. (2-B.13) and (2-B.21) have been used.

$\boxed{\sigma_{\theta\theta}}$

$$\begin{aligned}\lambda\nabla^2\varphi + 2\mu\left(\frac{1}{r^2}\frac{\partial^2\varphi}{\partial\theta^2} + \frac{1}{r}\frac{\partial\varphi}{\partial r}\right) &= -\lambda\kappa^2\varphi + 2\mu\left(\frac{1}{r^2}\frac{\partial^2\varphi}{\partial\theta^2} + \frac{1}{r}\frac{\partial\varphi}{\partial r}\right)\\ &= \frac{2\mu}{r^2}\left[\left(-n^2-n-\kappa^2r^2\frac{\lambda}{2\mu}\right)\mathfrak{C}_n(\kappa r) + \kappa r\mathfrak{C}_{n-1}(\kappa r)\right]\\ &= \frac{2\mu}{r^2}\left[\left(-n^2-n+\kappa^2r^2-\frac{1}{2}k^2r^2\right)\mathfrak{C}_n(\kappa r) + \kappa r\mathfrak{C}_{n-1}(\kappa r)\right] \qquad \text{(2-B.28)}\end{aligned}$$

where eqns. (2-B.13), (2-B.22) and (2-B.14) have been used.

$\boxed{\sigma_{zz}}$

$$\lambda\nabla^2\varphi = -\lambda\kappa^2\varphi = -\lambda\kappa^2\mathfrak{C}_n(\kappa r) = \frac{2\mu}{r^2}\left[\kappa^2r^2 - \frac{1}{2}k^2r^2\right]\mathfrak{C}_n(\kappa r) \qquad \text{(2-B.29)}$$

where eqns. (2-B.13) and (2-B.14) have been used.

$\boxed{\sigma_{r\theta}}$

$$2\mu\left(\frac{1}{r}\frac{\partial^2\varphi}{\partial r\partial\theta} - \frac{1}{r^2}\frac{\partial\varphi}{\partial\theta}\right) = \frac{2\mu}{r^2}\hat{\imath}n\left[-(n+1)\mathfrak{C}_n(\kappa r) + \kappa r\mathfrak{C}_{n-1}(\kappa r)\right] \qquad \text{(2-B.30)}$$

where eqn. (2-B.23) has been used.

—Contributions Due to ψ

$\boxed{\sigma_{rr}}$

$$2\mu\left(\frac{1}{r}\frac{\partial^2\psi}{\partial r\partial\theta} - \frac{1}{r^2}\frac{\partial\psi}{\partial\theta}\right) = \frac{2\mu}{r^2}\hat{\imath}n\left[-(n+1)\mathfrak{C}_n(kr) + kr\mathfrak{C}_{n-1}(kr)\right] \qquad \text{(2-B.31)}$$

where eqn. (2-B.24) has been used.

$\boxed{\sigma_{\theta\theta}}$

$$2\mu\left(\frac{1}{r^2}\frac{\partial\psi}{\partial\theta} - \frac{1}{r}\frac{\partial^2\psi}{\partial r\partial\theta}\right) = \frac{2\mu}{r^2}\hat{\imath}n\left[(n+1)\mathfrak{C}_n(kr) - kr\mathfrak{C}_{n-1}(kr)\right] \qquad \text{(2-B.32)}$$

where eqn. (2-B.25) has been used.

$\boxed{\sigma_{r\theta}}$

$$\mu\left(-\frac{\partial^2\psi}{\partial r^2} + \frac{1}{r}\frac{\partial\psi}{\partial r} + \frac{1}{r^2}\frac{\partial^2\psi}{\partial\theta^2}\right) = \frac{2\mu}{r^2}\left[-\left(n^2+n-\frac{1}{2}k^2r^2\right)\mathfrak{C}_n(kr) + kr\mathfrak{C}_{n-1}(kr)\right] \qquad \text{(2-B.33)}$$

where eqn. (2-B.26) has been used.

Displacements, Strains and Stresses in Terms of $\mathfrak{E}$-Functions

The contributions to any component of the displacement, stress and strain due to a single term of a displacement potential, as derived in eqns. (2-B.17) through (2-B.33), are complicated. To simplify the notation, a series of differential wave expansion basis functions, the $\mathfrak{E}$-functions, are defined in Appendix 2-C. With these $\mathfrak{E}$-functions, the expressions for the displacements, strains and stresses can be recast. Assuming the displacement potentials for the P and S waves are respectively expressible as

$$\varphi = \sum_{n=-\infty}^{\infty} A_n \mathfrak{C}_n(\kappa r) \mathrm{e}^{\mathrm{i}n\theta} \tag{2-B.34}$$

$$\psi = \sum_{n=-\infty}^{\infty} B_n \mathfrak{C}_n(k r) \mathrm{e}^{\mathrm{i}n\theta} \tag{2-B.35}$$

the expressions for the resulting displacements, strains and stresses can be written as

$$u_r = \frac{1}{r} \sum_{n=-\infty}^{\infty} \left[A_n \mathfrak{E}_{71n}(r) + B_n \mathfrak{E}_{72n}(r)\right] \mathrm{e}^{\mathrm{i}n\theta} \tag{2-B.36}$$

$$u_\theta = \frac{1}{r} \sum_{n=-\infty}^{\infty} \left[A_n \mathfrak{E}_{81n}(r) + B_n \mathfrak{E}_{82n}(r)\right] \mathrm{e}^{\mathrm{i}n\theta} \tag{2-B.37}$$

$$\varepsilon_{rr} = \frac{1}{r^2} \sum_{n=-\infty}^{\infty} \left[A_n \mathfrak{E}_{51n}(r) + B_n \mathfrak{E}_{52n}(r)\right] \mathrm{e}^{\mathrm{i}n\theta} \tag{2-B.38}$$

$$\varepsilon_{\theta\theta} = \frac{1}{r^2} \sum_{n=-\infty}^{\infty} \left[A_n \mathfrak{E}_{61n}(r) + B_n \mathfrak{E}_{62n}(r)\right] \mathrm{e}^{\mathrm{i}n\theta} \tag{2-B.39}$$

$$\varepsilon_{r\theta} = \frac{1}{r^2} \sum_{n=-\infty}^{\infty} \left[A_n \mathfrak{E}_{41n}(r) + B_n \mathfrak{E}_{42n}(r)\right] \mathrm{e}^{\mathrm{i}n\theta} \tag{2-B.40}$$

$$\sigma_{rr} = \frac{2\mu}{r^2} \sum_{n=-\infty}^{\infty} \left[A_n \mathfrak{E}_{11n}(r) + B_n \mathfrak{E}_{12n}(r)\right] \mathrm{e}^{\mathrm{i}n\theta} \tag{2-B.41}$$

$$\sigma_{\theta\theta} = \frac{2\mu}{r^2} \sum_{n=-\infty}^{\infty} \left[A_n \mathfrak{E}_{21n}(r) + B_n \mathfrak{E}_{22n}(r)\right] \mathrm{e}^{\mathrm{i}n\theta} \tag{2-B.42}$$

$$\sigma_{zz} = \frac{2\mu}{r^2} \sum_{n=-\infty}^{\infty} A_n \mathfrak{E}_{31n}(r) \mathrm{e}^{\mathrm{i}n\theta} \tag{2-B.43}$$

$$\sigma_{r\theta} = \frac{2\mu}{r^2} \sum_{n=-\infty}^{\infty} \left[A_n \mathfrak{E}_{41n}(r) + B_n \mathfrak{E}_{42n}(r)\right] \mathrm{e}^{\mathrm{i}n\theta} \tag{2-B.44}$$

Note that the shear strain in eqn. (2-B.40) is given as a tensor component. In the engineering form, the shear strain is

$$\gamma_{r\theta} = \frac{2}{r^2} \sum_{n=-\infty}^{\infty} \left[A_n \mathfrak{E}_{41n}(r) + B_n \mathfrak{E}_{42n}(r)\right] \mathrm{e}^{\mathrm{i}n\theta} \tag{2-B.45}$$

2-C $\mathfrak{E}$-Functions—Differential Wave Expansion Bases

The contributions to any component of the displacement, stress and strain due to a single term of a displacement potential, as eqns. (2-B.17) through (2-B.33) derived in Appendix 2-B, are complicated. Alternatively, they can be more concisely expressed in terms of a new series of functions—$\mathfrak{E}$-functions.

These functions were first introduced by Pao and Mow[4] and will be called *differential wave expansion basis functions* in this study. Their definitions are as follows:

$$\mathfrak{E}_{11n}(r) = \left(n^2 + n - \tfrac{1}{2}k^2r^2\right)\mathfrak{C}_n(\kappa r) - \kappa r\mathfrak{C}_{n-1}(\kappa r) \tag{2-C.1}$$

$$\mathfrak{E}_{21n}(r) = \left(-n^2 - n + \kappa^2r^2 - \tfrac{1}{2}k^2r^2\right)\mathfrak{C}_n(\kappa r) + \kappa r\mathfrak{C}_{n-1}(\kappa r) \tag{2-C.2}$$

$$\mathfrak{E}_{31n}(r) = \left(\kappa^2r^2 - \tfrac{1}{2}k^2r^2\right)\mathfrak{C}_n(\kappa r) \tag{2-C.3}$$

$$\mathfrak{E}_{41n}(r) = \hat{\imath}n\left[-(n+1)\mathfrak{C}_n(\kappa r) + \kappa r\mathfrak{C}_{n-1}(\kappa r)\right] \tag{2-C.4}$$

$$\mathfrak{E}_{51n}(r) = \left(n^2 + n - \kappa^2r^2\right)\mathfrak{C}_n(\kappa r) - \kappa r\mathfrak{C}_{n-1}(\kappa r) \tag{2-C.5}$$

$$\mathfrak{E}_{61n}(r) = \left(-n^2 - n\right)\mathfrak{C}_n(\kappa r) + \kappa r\mathfrak{C}_{n-1}(\kappa r) \tag{2-C.6}$$

$$\mathfrak{E}_{71n}(r) = -n\mathfrak{C}_n(\kappa r) + \kappa r\mathfrak{C}_{n-1}(\kappa r) \tag{2-C.7}$$

$$\mathfrak{E}_{81n}(r) = \hat{\imath}n\mathfrak{C}_n(\kappa r) \tag{2-C.8}$$

$$\mathfrak{E}_{12n}(r) = \hat{\imath}n\left[-(n+1)\mathfrak{C}_n(kr) + kr\mathfrak{C}_{n-1}(kr)\right] \tag{2-C.9}$$

$$\mathfrak{E}_{22n}(r) = \hat{\imath}n\left[(n+1)\mathfrak{C}_n(kr) - kr\mathfrak{C}_{n-1}(kr)\right] \tag{2-C.10}$$

$$\mathfrak{E}_{32n}(r) = 0 \tag{2-C.11}$$

$$\mathfrak{E}_{42n}(r) = -\left(n^2 + n - \tfrac{1}{2}k^2r^2\right)\mathfrak{C}_n(kr) + kr\mathfrak{C}_{n-1}(kr) \tag{2-C.12}$$

$$\mathfrak{E}_{52n}(r) = \hat{\imath}n\left[-(n+1)\mathfrak{C}_n(kr) + kr\mathfrak{C}_{n-1}(kr)\right] \tag{2-C.13}$$

$$\mathfrak{E}_{62n}(r) = \hat{\imath}n\left[(n+1)\mathfrak{C}_n(kr) - kr\mathfrak{C}_{n-1}(kr)\right] \tag{2-C.14}$$

$$\mathfrak{E}_{72n}(r) = \hat{\imath}n\mathfrak{C}_n(kr) \tag{2-C.15}$$

$$\mathfrak{E}_{82n}(r) = n\mathfrak{C}_n(kr) - kr\mathfrak{C}_{n-1}(kr) \tag{2-C.16}$$

In the above functions, the first subscript represents the component index number which is a little complicated as the result of attempting to scramble all the indices for displacements, strains and stresses into a single digit. The first subscript of value 1 to 4 is the stress index in the engineering (vector) notation; that is, σ_{rr}, $\sigma_{\theta\theta}$, σ_{zz} and $\sigma_{r\theta}$, respectively. The subscript of value 5 and 6 is the strain index for the first two strains in engineering notation; that is, ε_{rr} and $\varepsilon_{\theta\theta}$, respectively, and the rest of the strains share the same function as the stresses. The subscript of value 7 and 8 is for the displacements; that is, u_r and u_θ, respectively.

The second subscript signifies the contributing wave: 1 for P wave and 2 for S wave. It is noted that the functions having 1 as the second subscript always have κr as the arguments for the cylindrical functions involved, while the functions having 2 as the second subscript always have kr as the arguments.

These functions are invoked in a form such as $\mathfrak{E}^{1f}_{11n}(r)$ where the third subscript specifies the order of the cylindrical functions involved, the first superscript specifies the type of the cylindrical functions to be used, and the second superscript specifies the medium in which

the function is evaluated. The first superscript propagates into the cylindrical functions $\mathfrak{C}$ involved in the definitions of $\mathfrak{E}$, and the following conventions are adopted

$$\mathfrak{C}_n^1(z) = J_n(z) \qquad \mathfrak{C}_n^2(z) = Y_n(z) \tag{2-C.17}$$

$$\mathfrak{C}_n^3(z) = H_n^{(1)}(z) \qquad \mathfrak{C}_n^4(z) = H_n^{(2)}(z) \tag{2-C.18}$$

Without the first superscript, the function is taken as a formal notation of the entire class of the $\mathfrak{E}$-functions. When the second superscript is omitted, it is assumed that the medium is the infinite elastic problem domain outside the scatterer.

The following relation between $\mathfrak{E}$ functions can be observed

$$\mathfrak{E}_{12n}(r) = -\mathfrak{E}_{22n}(r) \tag{2-C.19}$$

$$\mathfrak{E}_{52n}(r) = \mathfrak{E}_{12n}(r) \tag{2-C.20}$$

$$\mathfrak{E}_{62n}(r) = \mathfrak{E}_{22n}(r) \tag{2-C.21}$$

$$\mathfrak{E}_{11n}(r) = \mathfrak{E}_{51n}(r) + \mathfrak{E}_{31n}(r) \tag{2-C.22}$$

$$\mathfrak{E}_{21n}(r) = \mathfrak{E}_{61n}(r) + \mathfrak{E}_{31n}(r) \tag{2-C.23}$$

and

$$\mathfrak{E}_{XX(-n)}(r) = (-1)^n \mathfrak{E}_{XXn}(r) \tag{2-C.24}$$

which is the direct consequence of the property of the cylindrical function $\mathfrak{C}_{(-n)}(z) = (-1)^n \mathfrak{C}_n(z)$, where XX is any of the appropriate subscripts.

There are cases when the following equivalent expressions for the $\mathfrak{E}$-functions are more convenient:

$$\mathfrak{E}_{11n}(r) = \left(n^2 - \tfrac{1}{2}k^2r^2\right)\mathfrak{C}_n(\kappa r) - \kappa r \mathfrak{C}_n'(\kappa r) \tag{2-C.25}$$

$$\mathfrak{E}_{12n}(r) = \hat{\imath}n\left[kr\mathfrak{C}_n'(kr) - \mathfrak{C}_n(kr)\right] \tag{2-C.26}$$

$$\mathfrak{E}_{41n}(r) = \hat{\imath}n\left[\kappa r\mathfrak{C}_n'(\kappa r) - \mathfrak{C}_n(\kappa r)\right] \tag{2-C.27}$$

$$\mathfrak{E}_{42n}(r) = \left(\tfrac{1}{2}k^2r^2 - n^2\right)\mathfrak{C}_n(kr) + kr\mathfrak{C}_n'(kr) \tag{2-C.28}$$

$$\mathfrak{E}_{71n}(r) = \kappa r\mathfrak{C}_n'(\kappa r) \tag{2-C.29}$$

$$\mathfrak{E}_{72n}(r) = \hat{\imath}n\mathfrak{C}_n(kr) \tag{2-C.30}$$

$$\mathfrak{E}_{81n}(r) = \hat{\imath}n\mathfrak{C}_n(\kappa r) \tag{2-C.31}$$

$$\mathfrak{E}_{82n}(r) = -kr\mathfrak{C}_n'(kr) \tag{2-C.32}$$

Note that the definitions given here are slightly different from those originally defined in [4]. The differences are due to the different wave expansion basis functions used. In [4], the wave expansion bases are those having different forms for symmetric and anti-symmetric waves, as in eqn. (2–37). The differences appear in the functions involving $\hat{\imath}$: $\mathfrak{E}_{12}$, $\mathfrak{E}_{22}$, $\mathfrak{E}_{41}$, $\mathfrak{E}_{72}$ and $\mathfrak{E}_{81}$. In [4], these functions do not include $\hat{\imath}$ in their definitions, but change signs for symmetric and anti-symmetric displacement potentials.

3

Concept of T-Matrix

Abstract: *The concept of the T-matrix is widely used in mathematical treatments of scattering problems. It also plays a vital role throughout this thesis. However, a simplistic definition given in the literature is often ambiguous. In this chapter, a clear and precise definition of the T-matrix is given, and its properties are examined in light of some fundamental physical principles.*

Contents:

Nomenclature

General Conventions

- Matrices are denoted by bold-faced symbols; symbols for column matrices are enclosed by flower brackets ({}); symbols for rectangular matrices are enclosed by square brackets ([]).
- When referring to a matrix entry, the entry's indicial number is to appear as subscript(s) *outside* the brackets. This distinguishes the indicial subscript(s) from the subscript(s), if any, associated with the entire matrix.

Symbols

$\{\boldsymbol{A}\}, \{\boldsymbol{B}\}, \cdots$	Wave expansion coefficient (column) matrices.
$\mathfrak{C}_n(x)$	Formal notation for cylindrical function at order n, which can be any one of the followings: $J_n(x)$, $Y_n(x)$, $H_n^{(1)}(x)$, or $H_n^{(2)}(x)$.
$\mathfrak{E}(r)$	Differential wave expansion basis function, as defined in Appendix 2-C.
$H_n^{(1)}(x), H_n^{(2)}(x)$	Hankel function of the first and second kinds, respectively, and order n.
$\{\boldsymbol{H}(r,\theta)\}$	Singular (Hankel) wave expansion basis matrix.
$\hat{\imath}$	Unit of imaginary number, $\hat{\imath} = \sqrt{-1}$.
Im	Imaginary part of a complex number.
$J_n(x)$	Bessel function of the first kind and order n.
$\{\boldsymbol{J}(r,\theta)\}$	Regular wave expansion basis matrix, same as $\{\Re\boldsymbol{H}(r,\theta)\}$.
κ, k	Wave numbers, for longitudinal and shear waves, respectively.
$\Re$	Regular counterpart of a singular function or functional basis. In this chapter, this means replacing Hankel functions of the first kind by Bessel functions of the first kind at the same order.
Re	Real part of a complex number.
$[\boldsymbol{T}]$	T-matrix for a scatterer.
$\boldsymbol{u}$	Displacement of a field point. Its components are u, v and w.
$\boldsymbol{v}$	Velocity of a field point.
$\boldsymbol{\varepsilon}$	Strain tensor. Components of engineering shear strain are denoted as γ.
λ, μ	Lamé constants of an elastic material.
Φ	Scalar displacement potential.
Ψ	The z-component of vector displacement potential.
ϕ	Spatial factor (complex amplitude) of displacement w for SH wave cases.
φ	Spatial factor (complex amplitude) of Φ, $\Phi(\boldsymbol{r},t) = \varphi(\boldsymbol{r})\mathrm{e}^{-\hat{\imath}\omega t}$.
ψ	Spatial factor (complex amplitude) of Ψ, $\Psi(\boldsymbol{r},t) = \psi(\boldsymbol{r})\mathrm{e}^{-\hat{\imath}\omega t}$.
$\boldsymbol{\sigma}$	Stress tensor. Components of shear stress are denoted as τ.
ω	Circular (angular) frequency of a time-harmonic wave.

Superscripts

inc, total, s	Quantities that belong to the incident, total and scattered waves, respectively.
P, S	Characteristic of or pertinent to P and S waves, respectively.
$*$	Conjugate transpose of a matrix: $[\boldsymbol{M}]^* = \overline{[\boldsymbol{M}]}^T = \overline{[\boldsymbol{M}]^T}$

Subscripts

m, f, i	Physical quantities that belong to the matrix, the fiber and the interphase.

3-1 Introduction

The concept of the T-matrix has been widely used in the mathematical treatments of scattering problems of a variety of types of waves.

The definition of the T-matrix is quite simple and is often stated as the matrix that relates the incident and the scattered waves. It represents the solution of the scattered wave for a scatterer subjected to any incident wave. In essence, the T-matrix contains all the mechanics regarding the scatterer when only the scattered waves are concerned.

The usefulness of the T-matrix lies in the fact that, once it is found, for *any* wave that incidents upon the scatterer, the scattered wave can be readily found, without the need of going back into detailed expressions for the displacements and stresses and solving the boundary value problem again. The advantage will be demonstrated to a larger extent in later chapters for problems involving multiple scatterers. In fact, it is a central concept in the multiple-scattering formulations throughout this thesis.

However, it has been found that a simplistic definition like the one above is often ambiguous. There are some unstated implications in the definition of the T matrix that must be explicitly specified.

Thus the objective of this chapter is to give a clear and precise definition of the T-matrix, to discuss these unstated implications of the definition, and to explore the properties of the T-matrix imposed by some fundamental physical requirements.

In this chapter, the matrix notation to be used in this thesis is introduced first in Section 3-2, then the definition for the T-matrix is followed in Section 3-3. Few example of the T-matrix for some simple scatterers, whose single-scatterer provblems have been solved in Chapter 2, are given in Section 3-4. The properties of T-matrix imposed by some physical principles are explored in Section 3-5. And finally some concluding remarks are noted Section 3-6.

3-2 Matrix Notation

As discussed in detail in Chapter 2, the complete solution for the Helmholtz equation using a polar coordinate system consists of linear combinations of *cylindrical wave functions* which is composed of Bessel or Hankel functions of various kinds as the radial factor and the simple harmonic as the azimuthal factor. Suppose, without loss of geneality, a generic wave is expressible as

$$\phi = \sum_{n=-\infty}^{\infty} A_n \mathfrak{C}_n(kr) e^{in\theta} \tag{3-1}$$

where $\mathfrak{C}_n(z)$ is a formal notation for cylindrical functions, which can be any of the following: $J_n(z)$, $Y_n(z)$, $H_n^{(1)}(z)$ and $H_n^{(2)}(z)$. In a matrix notation, ϕ is equivalently expressible as

$$\phi = \{\boldsymbol{A}\}^T\{\boldsymbol{\mathfrak{C}}(r,\theta)\} \tag{3-2}$$

where $\{\boldsymbol{A}\}$ and $\{\boldsymbol{\mathfrak{C}}(r,\theta)\}$ are two column matrices whose elements in the n-th row are

$$\{A\}_n = A_n \qquad \text{and} \qquad \{\mathfrak{C}(r,\theta)\}_n = \mathfrak{C}_n(kr)\mathrm{e}^{in\theta} \tag{3-3}$$

respectively. Obviously, the index n runs from $-\infty$ to ∞.

In general, $\{\boldsymbol{A}\}$ is called the *wave expansion coefficient matrix*, and $\{\boldsymbol{\mathfrak{C}}(r,\theta)\}$ is called the *wave expansion basis matrix*, or simply the *wave expansion basis*.

Two important wave expansion bases that are used extensively in scattering problems are:

$$\{\boldsymbol{J}(r,\theta)\} \qquad \text{with} \qquad \{J(r,\theta)\}_n = J_n(kr)\mathrm{e}^{in\theta} \tag{3-4}$$

$$\{\boldsymbol{H}(r,\theta)\} \qquad \text{with} \qquad \{H(r,\theta)\}_n = H_n^{(1)}(kr)\mathrm{e}^{in\theta} \tag{3-5}$$

Since $\{\boldsymbol{H}(r,\theta)\}$ is singular at the origin, it is called the *singular* wave expansion basis, whereas $\{\boldsymbol{J}(r,\theta)\}$ is called the *regular* (non-singular) wave expansion basis, and the following notation is used

$$\{\boldsymbol{J}(r,\theta)\} = \Re\{\boldsymbol{H}(r,\theta)\} \tag{3-6}$$

where the symbol $\Re$ is read as the *regular part* of the associated function, and denotes replacing the Hankel function of the first kind by the Bessel function of the first kind of the same order and the same argument.

In P/SV wave scattering problems, due to the different wave numbers of the two types of waves, it becomes necessary to include the wave number into the wave expansion basis, such as $\{\boldsymbol{J}(\kappa;r,\theta)\}$.

As seen in Chapter 2, there are other wave expansion bases, which can also be written in a similar form of matrix notation.

When using matrix notation, the following notational conventions are adopted: a bold-faced symbol, along with the appropriate brackets, denotes an entire matrix. A column matrix is enclosed by a pair of flower brackets ({ }), and a rectangular matrix by square brackets ([ ]). A super/subscript *inside* the brackets represents a modifier to the entire matrix. A subscript *outside* the brackets represents an indicial number for a matrix entry, which is denoted by the same but unbold symbol as the matrix.

3-3 Definition of T-matrix

With matrix notation, wave fields can be written in a more compact manner. For example, for SH wave singele-scatter problems, the incident wave can be expressed as

$$\phi^{\text{inc}} = \sum_{n=-\infty}^{\infty} A_n J_n(kr) \mathrm{e}^{in\theta} \tag{3-7}$$

and the corresponding scattered wave can be expresssed as

$$\phi^{\text{s}} = \sum_{n=-\infty}^{\infty} B_n H_n^{(1)}(kr) \mathrm{e}^{in\theta} \tag{3-8}$$

where A_n and B_n are wave expansion coefficients for the incident and the scattered waves, respectively. They can be equivalently expressed in matrix form as

$$\phi^{\text{inc}} = \{\boldsymbol{A}\}^T \{\boldsymbol{J}(r,\theta)\} \tag{3-9}$$

and

$$\phi^{\text{s}} = \{\boldsymbol{B}\}^T \{\boldsymbol{H}(r,\theta)\} \tag{3-10}$$

On the other hand, it is noted that the systems under consideration are linear. Mathematically, linearity implies that there exists a linear transformation between the inputs and the outputs in such a way that, for *any* input, applying the linear transformation to the input gives the corresponding output. Such a transformation is a characteristic of the system. In many simple mechanical systems, such a characteristic is also called the *transfer function(s)* of the system.

Specifically for scattering problems and using matrix notation, such a linear transformation would appear as a matrix that linearly relates the wave expansion coefficient matrices of the incident and the scattered waves. That is, taking eqns. (3–9) and (3–10) as an example, such a linear transformation appears to be

$$\{\boldsymbol{B}\} = [\boldsymbol{T}]\{\boldsymbol{A}\} \tag{3-11}$$

where $[\boldsymbol{T}]$ represents the transformation. Equations (3–9), (3–10) and (3–11) comprise *a* complete mathematical definition of the *T-matrix*, so named and denoted by convention. In words, the definition of the T-matrix can be stated as: *the matrix in a matrix notation that represents the linear transformation between the wave expansion coefficients of the incident and the scattered waves.*

The definition given above is quite broad in the sense that it only specifies a matrix notation. Other matrix notations, maybe along with other forms of wave expansions, could be used, resulting in different expressions or even different forms of the T-matrix for the same scatterer. Therefore, additional restrictions are needed to confine the context in which the T-matrix is defined.

Throughout this thesis, when the T-matrix for a scatterer is given or is said to be *known*, the following restrictions are implied. First, the problem configuration is that a single scatterer is embedded in an infinite medium. Second, a polar coordinate system, including its location and orientation, has been defined, and the origin of the coordinate system should fall within the region occupied by the scatterer. Third, the matrix notation of the form of eqns. (3–9) through (3–11) is assumed. Fourth, the incident wave is expressed in the *regular* wave expansion basis while the scattered wave is expressed in the *singular* wave expansion basis.

It must be noted that any change to these parameters will the cause the T-matrix to change. Thus it is necessary to have them explicitly specified.

3-4 T-Matrices of Some Simple Scatterers

For simple scatterers, the T-matrix can be obtained by solving the single-scatterer problem analytically and then re-express the result in the matrix form. In this section, expressions of T-matrices for several circular cylindrical scatterers, whose single-scattter problems have been solved in Chapter 2, are presented.

3-4.1 SH Waves

In Chapter 2, several single-scatterer SH wave scattering problems have been solved by assuming that the incident and the scattered waves are expressible as eqns. (3–7) and (3–8).

In all the solutions found in §2-3.1, there is a one-to-one correspondence between a pair of wave expansion coefficients A_n and B_n; that is, only the coefficients for the incident and the scattered waves of the same subscript are related to each other. This implies that, in all these cases, the T-matrices are diagonal. The element of a T-matrix at the n-th row and the n-th column is denoted as $[T]_n$, where the single subscript is purposefully used to signify that the matrix is diagonal. Then, by definition,

$$[T]_n = \frac{B_n}{A_n} \tag{3–12}$$

Specifically, for a circular rigid cylinder of radius a, from the solution found in §2-3.1,

$$[T]_n = -\frac{J_n(ka)}{H_n^{(1)}(ka)} \tag{3–13}$$

For a circular cylindrical void of radius a, from the solution found in §2-3.1,

$$[T]_n = -\frac{J_n'(ka)}{H_n^{(1)\prime}(ka)} \tag{3–14}$$

For a circular elastic cylinder of radius a, from the solution found in §2-3.1,

$$[T]_n = -\frac{\mu_f k_f J_n'(k_f a) J_n(k_m a) - \mu_m k_m J_n(k_f a) J_n'(k_m a)}{\mu_f k_f J_n'(k_f a) H_n^{(1)}(k_m a) - \mu_m k_m J_n(k_f a) H_n^{(1)\prime}(k_m a)} \tag{3-15}$$

where μ is the Lamé constant of the material, and the subscripts m and f denote the media of the matrix and the scatterer (fiber), respectively.

For a circular two-layer elastic cylinder, from the solution found in §2-3.1,

$$[T]_n = -\frac{\mu_m k_m M_1 J_n'(k_m b) - \mu_i k_i M_2 J_n(k_m b)}{\mu_m k_m M_1 H_n^{(1)\prime}(k_m b) - \mu_i k_i M_2 H_n^{(1)}(k_m b)} \tag{3-16}$$

where

$$\begin{aligned} M_1 = {} & \left[\mu_f k_f J_n'(k_f a) Y_n(k_i a) - \mu_i k_i J_n(k_f a) Y_n'(k_i a)\right] J_n(k_i b) \\ & - \left[\mu_f k_f J_n'(k_f a) J_n(k_i a) - \mu_i k_i J_n(k_f a) J_n'(k_i a)\right] Y_n(k_i b) \end{aligned} \tag{3-17}$$

$$\begin{aligned} M_2 = {} & \left[\mu_f k_f J_n'(k_f a) Y_n(k_i a) - \mu_i k_i J_n(k_f a) Y_n'(k_i a)\right] J_n'(k_i b) \\ & - \left[\mu_f k_f J_n'(k_f a) J_n(k_i a) - \mu_i k_i J_n(k_f a) J_n'(k_i a)\right] Y_n'(k_i b) \end{aligned} \tag{3-18}$$

a and b are the radii of the inner and the outer layers of the scatterer, respectively, and the subscript i denotes the medium of the outer layer (interphase) of the scatterer.

3-4.2 P/SV Waves

As discussed in Chapter 2, there are two types of waves could coexist in the case of P/SV scatterering. In general, the incident waves are expressble as

$$\varphi^{\text{inc}} = \sum_{n=-\infty}^{\infty} A_n J_n(\kappa r) e^{in\theta} \tag{3-19}$$

$$\psi^{\text{inc}} = \sum_{n=-\infty}^{\infty} a_n J_n(kr) e^{in\theta} \tag{3-20}$$

and the scattered waves are expressible as

$$\varphi^{\text{s}} = \sum_{n=-\infty}^{\infty} B_n H_n^{(1)}(\kappa r) e^{in\theta} \tag{3-21}$$

$$\psi^{\text{s}} = \sum_{n=-\infty}^{\infty} b_n H_n^{(1)}(kr) e^{in\theta} \tag{3-22}$$

where φ and ψ are the displacement potential fuctions for the P and S waves, respectively, and κ and k are the wave nunmbers for the P and S waves, respectively, A_n and a_n are the wave expansion coefficients for the incident P and S waves, respectively, and B_n and b_n are the expansion coefficients for the scattered P and S waves, respectively.

Due to mode conversions, a 2-D P/SV wave scattering problem involves four T-matrices: the scattered P wave due to a P incident wave, the scattered SV wave

due to a P incident wave, the scattered P wave due to an SV incident wave, and the scattered SV wave due to an SV incident wave; that is, two scattered waves due to an incident P wave and two scattered waves due to an incident SV wave. Denote these T-matrices as $[\boldsymbol{T}^{PP}]$, $[\boldsymbol{T}^{PS}]$, $[\boldsymbol{T}^{SP}]$ and $[\boldsymbol{T}^{SS}]$, respectively, where the first superscript denotes the type of incident wave and the second superscript denotes the type of scattered wave.

For all the simple single-scatterer problems solved in §2-3.2, the T-matrices are diagonal, and the expressions, by definition, are

$$[T^{PP}]_n = \frac{B_n}{A_n} \qquad [T^{PS}]_n = \frac{b_n}{A_n} \tag{3-23}$$

when $a_n = 0$, and

$$[T^{SP}]_n = \frac{B_n}{a_n} \qquad [T^{SS}]_n = \frac{b_n}{a_n} \tag{3-24}$$

when $A_n = 0$.

Specifically, for a rigid circular cylinder of radius a, from the solution found in §2-3.2,

$$[T^{PP}]_n = -\frac{\mathfrak{E}^1_{71n}(a)\mathfrak{E}^3_{82n}(a) - \mathfrak{E}^3_{72n}(a)\mathfrak{E}^1_{81n}(a)}{\mathfrak{E}^3_{71n}(a)\mathfrak{E}^3_{82n}(a) - \mathfrak{E}^3_{72n}(a)\mathfrak{E}^3_{81n}(a)} \tag{3-25}$$

$$[T^{PS}]_n = -\frac{\mathfrak{E}^3_{71n}(a)\mathfrak{E}^1_{81n}(a) - \mathfrak{E}^1_{81n}(a)\mathfrak{E}^3_{81n}(a)}{\mathfrak{E}^3_{71n}(a)\mathfrak{E}^3_{82n}(a) - \mathfrak{E}^3_{72n}(a)\mathfrak{E}^3_{81n}(a)} \tag{3-26}$$

$$[T^{SP}]_n = -\frac{\mathfrak{E}^1_{72}(a)\mathfrak{E}^3_{82n}(a) - \mathfrak{E}^3_{72n}(a)\mathfrak{E}^1_{82n}(a)}{\mathfrak{E}^3_{71n}(a)\mathfrak{E}^3_{82n}(a) - \mathfrak{E}^3_{72n}(a)\mathfrak{E}^3_{81n}(a)} \tag{3-27}$$

$$[T^{SS}]_n = -\frac{\mathfrak{E}^3_{71n}(a)\mathfrak{E}^1_{82n}(a) - \mathfrak{E}^1_{82n}(a)\mathfrak{E}^3_{81n}(a)}{\mathfrak{E}^3_{71n}(a)\mathfrak{E}^3_{82n}(a) - \mathfrak{E}^3_{72n}(a)\mathfrak{E}^3_{81n}(a)} \tag{3-28}$$

where $\mathfrak{E}(z)$'s are differential wave expansion basis functions defined in Appendix 2-C in Chapter 2.

For a circular cylindrical void of radius a, from the solution found in §2-3.2,

$$[T^{PP}]_n = -\frac{\mathfrak{E}^1_{11n}(a)\mathfrak{E}^3_{42n}(a) - \mathfrak{E}^3_{12n}(a)\mathfrak{E}^1_{41n}(a)}{\mathfrak{E}^3_{11n}(a)\mathfrak{E}^3_{42n}(a) - \mathfrak{E}^3_{12n}(a)\mathfrak{E}^3_{41n}(a)} \tag{3-29}$$

$$[T^{PS}]_n = -\frac{\mathfrak{E}^3_{11n}(a)\mathfrak{E}^1_{41n}(a) - \mathfrak{E}^1_{41n}(a)\mathfrak{E}^3_{41n}(a)}{\mathfrak{E}^3_{11n}(a)\mathfrak{E}^3_{42n}(a) - \mathfrak{E}^3_{12n}(a)\mathfrak{E}^3_{41n}(a)} \tag{3-30}$$

$$[T^{SP}]_n = -\frac{\mathfrak{E}^1_{12n}(a)\mathfrak{E}^3_{42n}(a) - \mathfrak{E}^3_{12n}(a)\mathfrak{E}^1_{42n}(a)}{\mathfrak{E}^3_{11n}(a)\mathfrak{E}^3_{42n}(a) - \mathfrak{E}^3_{12n}(a)\mathfrak{E}^3_{41n}(a)} \tag{3-31}$$

$$[T^{SS}]_n = -\frac{\mathfrak{E}^3_{11n}(a)\mathfrak{E}^1_{42n}(a) - \mathfrak{E}^1_{42n}(a)\mathfrak{E}^3_{41n}(a)}{\mathfrak{E}^3_{11n}(a)\mathfrak{E}^3_{42n}(a) - \mathfrak{E}^3_{12n}(a)\mathfrak{E}^3_{41n}(a)} \tag{3-32}$$

For the elastic and layered elastic cylinders, although no explicit analytical expressions are available, numerically solving the linear equation systems found in §2-3.2 (in eqns. (2-135) and (2-146)) should be straightforward. To calculate the T-matrices, first set $A_n = 1$ and $a_n = 0$ and solve the linear equation system; the

solutions for B_n and b_n correspond to $[T^{PP}]_n$ and $[T^{PS}]_n$, respectively. Then, set $A_n = 0$ and $a_n = 1$ and solve the system again. Now the solutions for B_n and b_n correspond to $[T^{SP}]_n$ and $[T^{SS}]_n$, respectively. The procedure must be repeated for every n.

3-5 Coordinate Transformations for T-matrix

In this section, coordinate transformation relations for a T-matrix are presented. In general for a two-dimensional problem, any coordinate transformation can be decomposed into a pure rotation (without moving the origin) and a pure translation (without changing the orientation). The two transformations are examined separately.

In the following, quantities in the new coordinate system are signified by a prime, such as (r', θ') for the coordinates. For brevity, only the case of SH wave scattering is considered. The extension to the case of P/SV wave scattering is straightforward.

3-5.1 Coordinate Rotation

Assume the new coordinate system is formed by rotating the original coordinate system about its origin counterclockwisely by an angle α. That is, a counterclockwise rotation is has a positive rotating angle. The relations between the new and the original coordinate systems can be found as

$$r = r' \qquad \theta = \theta' + \alpha \tag{3-33}$$

The incident wave in eqn. (3-9) can be written as

$$\phi^{\text{inc}} = \{\boldsymbol{A}\}^T\{\boldsymbol{J}(r,\theta)\} = \{\boldsymbol{A}'\}^T\{\boldsymbol{J}(r',\theta')\} \tag{3-34}$$

where $\{\boldsymbol{A}'\}$ denotes the wave expansion coefficient matrix for the incident wave in the new coordinate system. The expanded form can be written as

$$\phi^{\text{inc}} = \sum_{n=-\infty}^{\infty} A_n J_n(kr)\mathrm{e}^{in\theta} = \sum_{n=-\infty}^{\infty} A_n \mathrm{e}^{in\alpha} J_n(kr')\mathrm{e}^{in\theta'} \tag{3-35}$$

where eqns. (3-33) have been used. Comparing eqns. (3-34) and (3-35) gives

$$\{A'\}_n = \{A\}_n \mathrm{e}^{in\alpha} \tag{3-36}$$

Similarly, the scattered wave in eqn. (3-10) can be written as

$$\phi^{\text{s}} = \{\boldsymbol{B}\}^T\{\boldsymbol{H}(r,\theta)\} = \{\boldsymbol{B}'\}^T\{\boldsymbol{H}(r',\theta')\} \tag{3-37}$$

with

$$\{B'\}_n = \{B\}_n \mathrm{e}^{in\alpha} \tag{3-38}$$

The definition of the T-matrix in eqn. (3–11) gives

$$\{B\}_m = \sum_{m=-\infty}^{\infty} [T]_{mn}\{A\}_n \tag{3–39}$$

Rewriting in terms of $\{B'\}$ and $\{A'\}$ by using eqns. (3–36) and (3–38) gives

$$\{B'\}_m = \sum_{m=-\infty}^{\infty} e^{i(m-n)\alpha}[T]_{mn}\{A'\}_n \tag{3–40}$$

Thus, if the T-matrix in the new coordinate system is denoted as $[T']$, then

$$[T']_{mn} = e^{i(m-n)\alpha}[T]_{mn} \tag{3–41}$$

3-5.2 Coordinate Translation

Assume the origin of the new coordinate system is located at point o whose coordinates in the original coordinate system are (R, Θ), as sketched in Fig. 3–1. In

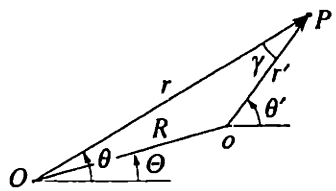

Fig. 3–1 The relation between the original and the new coordinate systems.

Fig. 3–1, P is an arbitrary field point which can be located by either the original coordinates (r, θ) or the new coordinate (r', θ'), and it can be found that

$$\theta' = \theta + \gamma \tag{3–42}$$

Recall *Graf's addition theorem* of Bessel functions[2]

$$H_m^{(1)}(\varpi) \begin{matrix}\cos\\ \sin\end{matrix} m\beta = \sum_{n=-\infty}^{\infty} H_{m+n}^{(1)}(Z) J_n(z) \begin{matrix}\cos\\ \sin\end{matrix} n\alpha \tag{3–43}$$

$$J_m(\varpi) \begin{matrix}\cos\\ \sin\end{matrix} m\beta = \sum_{n=-\infty}^{\infty} J_{m+n}(Z) J_m(z) \begin{matrix}\cos\\ \sin\end{matrix} n\alpha \tag{3–44}$$

where m and n are integers, and the geometrical relations among other parameters involved are sketched in Fig. 3–2. Equation (3–43) is valid only when $|Z| > |ze^{\pm i\alpha}|$;

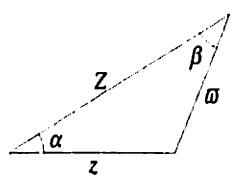

Fig. 3–2 Geometries of Graf's addition theorem.

whereas eqn. (3–44) is valid throughout the plane. For actual distances Z and z, the validity condition for eqn. (3–43) becomes $Z > z$.

Comparing the geometries in Figs. 3–1 and 3–2, with the following substitutions

$$z \to kR \qquad \varpi \to kr' \qquad Z \to kr \qquad \alpha \to \theta - \Theta \qquad \beta \to \gamma = \theta' - \theta$$

eqn. (3–43) can be written in complex notation as

$$H_m^{(1)}(kr')\mathrm{e}^{\mathrm{i}m(\theta'-\theta)} = \sum_{n=-\infty}^{\infty} H_{m+n}^{(1)}(kr)J_n(kR)\mathrm{e}^{\mathrm{i}n(\theta-\Theta)} \tag{3–45}$$

With slight rearrangements, it can be further written as

$$H_m^{(1)}(kr')\mathrm{e}^{\mathrm{i}m\theta'} = \sum_{n=0}^{\infty} \mathrm{e}^{-\mathrm{i}(m-n)\Theta}J_{m-n}(kR)H_n^{(1)}(kr)\mathrm{e}^{\mathrm{i}n\theta} \tag{3–46}$$

where eqn. (3–42) and the following relation of Bessel functions[2]

$$J_{-n}(z) = (-1)^n J_n(z) \tag{3–47}$$

have been used. In matrix form,

$$\{\boldsymbol{H}(r',\theta')\} = [\boldsymbol{Q}]\{\boldsymbol{H}(r,\theta)\} \tag{3–48}$$

where the element of the matrix $[\boldsymbol{Q}]$ at the m-th row and n-th column is

$$[Q]_{mn} = \mathrm{e}^{-\mathrm{i}(m-n)\Theta}J_{m-n}(kR) \tag{3–49}$$

and matrix $[\boldsymbol{Q}]$ is called the *coordinate translation matrix.*

By a similar procedure using eqn. (3–44), it can be shown that the coordinate translation for the regular wave expansion basis is

$$\{\boldsymbol{J}(r',\theta')\} = [\boldsymbol{Q}]\{\boldsymbol{J}(r,\theta)\} \tag{3–50}$$

Furthermore, since eqn. (3–50) is valid throughout the entire plane, and the origin O is located at the point $(R, \pi + \Theta)$ in the (r',θ') coordinate system, it can be readily shown that the inverse transformation of eqn. (3–50) is

$$\{\boldsymbol{J}(r,\theta)\} = [\boldsymbol{Q}]^{-1}\{\boldsymbol{J}(r',\theta')\} \tag{3–51}$$

where

$$\left([Q]^{-1}\right)_{mn} = (-1)^{m-n}[Q]_{mn} = \mathrm{e}^{\mathrm{i}(m-n)\Theta}J_{m-n}(kR) \tag{3–52}$$

and $([Q]^{-1})_{mn}$ denotes the m-th row and n-th column element of matrix $[\boldsymbol{Q}]^{-1}$; that is, the inverse of matrix $[\boldsymbol{Q}]$.

Using coordination translation relations in eqns. (3–48) and (3–50), the incident wave can be written as

$$\phi^{\mathrm{inc}} = \{\boldsymbol{A}'\}^T\{\boldsymbol{J}(r',\theta')\} = \{\boldsymbol{A}'\}^T[\boldsymbol{Q}]\{\boldsymbol{J}(r,\theta)\} \tag{3–53}$$

Similarly, the scattered wave can be written as

$$\phi^{\mathrm{s}} = \{\boldsymbol{B}'\}^T[\boldsymbol{Q}]\{\boldsymbol{J}(r,\theta)\} \tag{3–54}$$

Thus, coordinate translations for the wave expansion coefficient matrices are

$$\{A\} = [Q]^T\{A'\} \qquad \{B\} = [Q]^T\{B'\} \tag{3-55}$$

The definition of the T-matrix in eqn. (3-11) gives

$$[Q]^T\{B'\} = [T][Q]^T\{A'\} \tag{3-56}$$

Therefore,

$$[T'] = [Q]^{-T}[T][Q]^T \tag{3-57}$$

However, it must be noted that the condition imposed by Graf's addition theorem now requires that $r > R$. In other words, the above translation is only valid for expressing the scattered wave in the region $r > R$.

3-6 Properties of T-Matrix

In this section, some properties of T-matrices are examined. Known properties of the T-matrix fall into 2 categories. The first category are universal properties that must hold without exception is all cases. They are imposed by some basic physical principles. The second category is inherent from the geometrical and physical symmetry of the scatterer, thus they are specific to scatterers that possess the required symmetry.

3-6.1 Properties of T-Matrix Imposed By Physical Principles

In this subsection, some properties of T-matrices imposed by some physical principles of elastodynamics, specifically the principle of energy conservation and the principle of reprocity, are explored. Due to a distinct difference in the forms in which SH and P/SV scattering problems are formulated, these two cases are discussed separately.

Mathematical Expressions of Physical Principles

Expressions for the principle of energy conservation and the principle of reciprocity in general and the expressions particularized for the two-dimensional steady-state scattering problems using a polar coordinate system have beed derived in §2-4 in Chapter 2. For an easy reference, the expressions for the 2-D steady-state scattering problems are repeated here.

Principle of Energy Conservation

For the steady-state scattering problems in a two-dimensional space using a polar coordinate system, energy balance requirement, which is an alternative form of the principle of energy conservation, requires that the energy transmitted into a closed surface equals the energy emitted out of the surface. For simplicity, the closed surface is chosen as a circle of radius R centered at the origin of the coordinate system.

For the case of SH wave scattering, $U_r = U_\theta = 0$, $\Sigma_{rr} = \Sigma_{r\theta} = 0$,

$$\langle \dot{E} \rangle_{\mathrm{SH}} = \pi R \int_0^{2\pi} \left(Im\left\{ \Sigma_{rz} \overline{U}_z \right\} \right) \Big|_{r=R} d\theta = 0 \tag{3-58}$$

where U and Σ are the complex amplidutes of the displacement and stress components, respectively; $\langle \cdot \rangle$ denoted the time-average of a time-harmonic physical quantity over a complete period.

For the case of P/SV wave scattering, $U_z = 0$, $\Sigma_{rz} = 0$, and

$$\langle \dot{E} \rangle_{\mathrm{P/SV}} = \pi R \int_0^{2\pi} \left(Im\left\{ \Sigma_{rr} \overline{U}_r \right\} + Im\left\{ \Sigma_{r\theta} \overline{U}_\theta \right\} \right) \Big|_{r=R} d\theta = 0 \tag{3-59}$$

Principle of Reciprocity

Similarly, for problems in a two-dimenstional space using a polar coordinate system, the *Betti-Rayleigh Reciprocity Theorem* has been shown as, for the case of SH wave scattering, $U_r = U_\theta = 0$, $\Sigma_{rr} = \Sigma_{r\theta} = 0$, and for any two sets of time-harmonic loadings at the same frequency,

$$\int_0^{2\pi} \left[(\Sigma_{rz})_1 (U_z)_2 - (\Sigma_{rz})_2 (U_z)_1 \right] \Big|_{r=R} d\theta = 0 \tag{3-60}$$

and

$$\int_0^{2\pi} Re\left\{ (\Sigma_{rz})_1 (\overline{U}_z)_2 - (\overline{\Sigma}_{rz})_2 (U_z)_1 \right\} \Big|_{r=R} d\theta = 0 \tag{3-61}$$

where the subscripts 1 and 2 denote the quantities correspond to the first and second sets of loadings.

For the case of P/SV wave scattering, $U_z = 0$, $\Sigma_{rz} = 0$,

$$\int_0^{2\pi} \left\{ \left[(\Sigma_{rr})_1 (U_r)_2 + (\Sigma_{r\theta})_1 (U_\theta)_2 \right] - \left[(\Sigma_{rr})_2 (U_r)_1 + (\Sigma_{r\theta})_2 (U_\theta)_1 \right] \right\} \Big|_{r=R} d\theta = 0 \tag{3-62}$$

and

$$\int_0^{2\pi} Re\left\{ \left[(\Sigma_{rr})_1 (\overline{U}_r)_2 + (\Sigma_{r\theta})_1 (\overline{U}_\theta)_2 \right] - \left[(\overline{\Sigma}_{rr})_2 (U_r)_1 + (\overline{\Sigma}_{r\theta})_2 (U_\theta)_1 \right] \right\} \Big|_{r=R} d\theta = 0 \tag{3-63}$$

SH Waves

For this case, the total wave in the matrix can be written as

$$\phi^{\text{total}} = \phi^{\text{inc}} + \phi^{\text{s}} = \{A\}^T\{J(r,\theta)\} + ([T]\{A\})^T\{H(r,\theta)\} \tag{3-64}$$

where $\{A\}$ is the wave expansion coefficients of the incident wave. Also,

$$U_z = \phi^{\text{total}} \qquad \text{and} \qquad \Sigma_{rz} = 2\mu\frac{\partial\phi^{\text{total}}}{\partial r} \tag{3-65}$$

where μ is the Lamé constant for the matrix medium.

Energy Balance Requirement for SH Wave Scattering

Since the incident wave can be arbitrary, assume $\{A\}_n = 1$ and $\{A\}_p = 0$ when $p \neq n$. Then,

$$U_z = \phi^{\text{total}} = J_n(kr)e^{in\theta} + \sum_{p=-\infty}^{\infty}[T]_{pn}H_p^{(1)}(kr)e^{ip\theta} \tag{3-66}$$

$$\frac{1}{2\mu k}\Sigma_{rz} = \frac{\partial\phi^{\text{total}}}{\partial(kr)} = J_n'(kr)e^{in\theta} + \sum_{q=-\infty}^{\infty}[T]_{qn}H_q^{(1)\prime}(kr)e^{iq\theta} \tag{3-67}$$

$$\begin{aligned}\frac{1}{2\mu k}\Sigma_{rz}\overline{U}_z = {} & J_n(kr)\sum_{p=-\infty}^{\infty}[T]_{pn}H_n^{(1)\prime}(kr)e^{i(p-n)\theta} + J_n'(kr)\sum_{q=-\infty}^{\infty}\overline{[T]}_{qn}H_q^{(2)}(kr)e^{i(n-q)\theta} \\ & + J_n'(kr)J_n(kr) + \sum_{p=-\infty}^{\infty}\sum_{q=-\infty}^{\infty}[T]_{pn}\overline{[T]}_{qn}H_p^{(1)\prime}(kr)H_q^{(2)}(kr)e^{i(p-q)\theta}\end{aligned} \tag{3-68}$$

where in writing $\overline{U}_z$, it has been noted that

$$\overline{H_n^{(1)}(z)} = H_n^{(2)}(z) \qquad \text{and} \qquad \overline{H_n^{(1)\prime}(z)} = H_n^{(2)\prime}(z) \tag{3-69}$$

In performing the integration over θ, it is noted that

$$\int_0^{2\pi} e^{i(p-q)\theta}d\theta = \begin{cases} 0 & \text{when } p \neq q \\ 2\pi & \text{when } p = q, \end{cases} \tag{3-70}$$

Then,

$$\begin{aligned}\frac{1}{4\pi\mu k}\int_0^{2\pi}\Sigma_{rz}\overline{U}_z d\theta = {} & J_n(kr)[T]_{nn}H_n^{(1)\prime}(kr) + J_n'(kr)\overline{[T]}_{nn}H_n^{(2)}(kr) \\ & + J_n'(kr)J_n(kr) + \sum_{p=-\infty}^{\infty}|[T]_{pn}|^2 H_p^{(1)\prime}(kr)H_p^{(2)}(kr)\end{aligned} \tag{3-71}$$

Noting that

$$Im\{J_n'(kr)J_n(kr)\} = 0 \tag{3-72}$$

$$Im\left\{J_n(kr)[T]_{nn}H_n^{(1)\prime}(kr) + J_n'(kr)\overline{[T]}_{nn}H_n^{(2)}(kr)\right\} = \frac{1}{\pi kr}\left([T]_{nn} + \overline{[T]}_{nn}\right) \tag{3-73}$$

$$Im\left\{|[T]_{pn}|^2 H_p^{(1)\prime}(kr)H_p^{(2)}(kr)\right\} = \frac{2}{\pi kr}|[T]_{pn}|^2 \tag{3-74}$$

where the following Wronskian relations for Bessel/Hankel functions[1]

$$\mathcal{W}(J_n(z), H_n^{(1)}(z)) \equiv J_n(z)H_n^{(1)\prime}(z) - J_n'(z)H_n^{(1)}(z) = \frac{2\hat{\imath}}{\pi z} \tag{3-75}$$

$$\mathcal{W}(J_n(z), H_n^{(2)}(z)) \equiv J_n(z)H_n^{(2)\prime}(z) - J_n'(z)H_n^{(2)}(z) = -\frac{2\hat{\imath}}{\pi z} \tag{3-76}$$

$$\mathcal{W}(H_n^{(1)}(z), H_n^{(2)}(z)) \equiv H_n^{(1)}(z)H_n^{(2)\prime}(z) - H_n^{(1)\prime}(z)H_n^{(2)}(z) = -\frac{4\hat{\imath}}{\pi z} \tag{3-77}$$

have been used. Thus, by using eqns. (3–71) through (3–74), eqn. (3–58) becomes

$$\langle \dot{E} \rangle_{\text{SH}} = 4\pi\mu \left([T]_{nn} + \overline{[T]}_{nn} + 2 \sum_{p=-\infty}^{\infty} |[T]_{pn}|^2 \right) = 0 \tag{3-78}$$

Therefore, for any n,

$$Re\,\{[T]_{nn}\} = -\sum_{p=-\infty}^{\infty} |[T]_{pn}|^2 \tag{3-79}$$

Furthermore, squaring both sides of eqn. (3–79) gives

$$\left(\sum_{n=-\infty}^{\infty} |[T]_{pn}|^2 \right)^2 = (Re\,\{[T]_{nn}\})^2 \leq |[T]_{nn}|^2 \leq \sum_{n=-\infty}^{\infty} |[T]_{pn}|^2 \tag{3-80}$$

which means

$$\sum_{n=-\infty}^{\infty} |[T]_{pn}|^2 \leq 1 \tag{3-81}$$

Combining this property with eqn. (3–79) gives

$$-1 \leq \Re\{[T]_{nn}\} \leq 0 \tag{3-82}$$

For diagonal T-matrices, eqn. (3–79) becomes

$$Re\{[T]_n\} = -|[T]_n|^2 \tag{3-83}$$

It is observed that the expressions for T-matrices for various scatterers in §3-4.1 possess the form $[T]_n = -\frac{a}{a+ib}$ where both a and b are real. It can be readily verified that they satisfy eqn. (3–83).

Reciprocity for SH Wave Scattering

Assume that two sets of incident waves at the same frequency are represented by their respective wave expansion coefficient matrices $\{A_1\}$ and $\{A_2\}$ such that: $\{A_1\}_m = A_1$ and $\{A_1\}_p = 0$ when $p \neq m$; and $\{A_2\}_n = A_2$ and $\{A_2\}_q = 0$ when $q \neq n$, where A_1 and A_2 are arbitrary (complex) numbers. Then,

$$(U_z)_1 = A_1 J_m(kr)e^{im\theta} + A_1 \sum_{p=-\infty}^{\infty} [T]_{pm} H_p^{(1)}(kr)e^{ip\theta} \tag{3-84}$$

$$\frac{1}{2\mu k}(\Sigma_{rz})_1 = A_1 J_m'(kr)e^{im\theta} + A_1 \sum_{p=-\infty}^{\infty} [T]_{pm} H_p^{(1)\prime}(kr)e^{ip\theta} \tag{3-85}$$

$$(U_z)_2 = A_2 J_n(kr)\mathrm{e}^{in\theta} + A_2 \sum_{q=-\infty}^{\infty} [T]_{qn} H_q^{(1)}(kr)\mathrm{e}^{iq\theta} \tag{3-86}$$

$$\frac{1}{2\mu k}(\Sigma_{rz})_2 = A_2 J_n'(kr)\mathrm{e}^{in\theta} + A_2 \sum_{q=-\infty}^{\infty} [T]_{qn} H_q^{(1)\prime}(kr)\mathrm{e}^{iq\theta} \tag{3-87}$$

Thus,

$$\begin{aligned}
&\frac{1}{4\pi\mu k}\int_0^{2\pi} [(\Sigma_{rz})_1(U_z)_2 - (\Sigma_{rz})_2(U_z)_1]\, d\theta \\
&\quad = A_1 A_2 \left[J_m'(kr)[T]_{(-m)n} H_{-m}^{(1)}(kr) - J_n'(kr)[T]_{(-n)m} H_{-n}^{(1)}(kr)\right] \\
&\qquad + A_1 A_2 \left[J_n(kr)[T]_{(-n)m} H_{-n}^{(1)\prime}(kr) - J_m(kr)[T]_{(-m)n} H_{-m}^{(1)\prime}(kr)\right] \\
&\quad = \frac{2\hat{\imath} A_1 A_2}{\pi kr}\left[(-1)^n [T]_{(-n)m} - (-1)^m [T]_{(-m)n}\right]
\end{aligned} \tag{3-88}$$

$$\begin{aligned}
&\frac{1}{4\pi\mu k}\int_0^{2\pi} \left[(\Sigma_{rz})_1(\overline{U}_z)_2 - (\overline{\Sigma}_{rz})_2(U_z)_1\right] d\theta \\
&\quad = A_1 \overline{A}_2 \left[J_m'(kr)\overline{[T]}_{mn} H_m^{(2)}(kr) - J_n'(kr)[T]_{nm} H_n^{(1)}(kr)\right] \\
&\qquad + A_1 \overline{A}_2 \left[J_n(kr)[T]_{nm} H_n^{(1)\prime}(kr) - J_m(kr)\overline{[T]}_{mn} H_m^{(2)\prime}(kr)\right] \\
&\qquad + A_1 \overline{A}_2 \sum_{p=-\infty}^{\infty} [T]_{pm}\overline{[T]}_{pn} \left[H_p^{(1)\prime}(kr) H_p^{(2)}(kr) - H_p^{(1)}(kr) H_p^{(2)\prime}(kr)\right] \\
&\quad = \frac{2\hat{\imath} A_1 \overline{A}_2}{\pi kr}\left[\, [T]_{nm} + \overline{[T]}_{mn} + 2\sum_{p=-\infty}^{\infty} [T]_{pm}\overline{[T]}_{pn}\,\right]
\end{aligned} \tag{3-89}$$

where eqn. (3-70), the Wronskians in eqns. (3-75) through (3-77), and the following property of the cylindrical function $\mathfrak{C}_{-n}(z) = (-1)^n \mathfrak{C}_n(z)$ have been used.

From eqns. (3-60) and (3-88), it can be concluded

$$[T]_{mn} = (-1)^{m-n}[T]_{(-n)(-m)} \tag{3-90}$$

For eqn. (3-89), since both A_1 and A_2 are arbitrary complex numbers, it follows that reciprocity requires

$$\overline{[T]}_{mn} + [T]_{nm} + 2\sum_{p=-\infty}^{\infty} [T]_{pm}\overline{[T]}_{pn} = 0 \tag{3-91}$$

or, in matrix form,

$$\tfrac{1}{2}([\boldsymbol{T}]^* + [\boldsymbol{T}]) = -[\boldsymbol{T}]^*[\boldsymbol{T}] \tag{3-92}$$

where $*$ denotes the *conjugate transpose* of a matrix; that is, $[\boldsymbol{T}]^* \equiv \overline{[\boldsymbol{T}]}^T \equiv \overline{[\boldsymbol{T}]^T}$. It is noted that eqn. (3-79) is a special case of eqn. (3-92).

Conclusions for SH Wave Case

In conclusion, properties of a T-matrix for SH wave scattering imposed by the energy principle and the reciprocity principle are given in eqns. (3-90) and (3-92). Other properties can be derived from them and are summarized as follows:

- The magnitude of any element of a T-matrix is no larger than unity.
- The real part of any diagonal element of a T-matrix is always non-positive (negative or zero) but no smaller than -1.
- The sum of the magnitude squares of any entire column of a T-matrix is no larger than unity.

P/SV Waves

For P/SV wave scattering, the total displacement potential functions in the matrix can be written as

$$\varphi^{\text{total}} = \{\boldsymbol{A}\}^T\{\boldsymbol{J}(\kappa;r,\theta)\} + \left([\boldsymbol{T}^{PP}]\{\boldsymbol{A}\} + [\boldsymbol{T}^{SP}]\{\boldsymbol{a}\}\right)^T\{\boldsymbol{H}(\kappa;r,\theta)\} \quad (3\text{–}93)$$

$$\psi^{\text{total}} = \{\boldsymbol{a}\}^T\{\boldsymbol{J}(k;r,\theta)\} + \left([\boldsymbol{T}^{PS}]\{\boldsymbol{A}\} + [\boldsymbol{T}^{SS}]\{\boldsymbol{a}\}\right)^T\{\boldsymbol{H}(k;r,\theta)\} \quad (3\text{–}94)$$

where $\{\boldsymbol{A}\}$ and $\{\boldsymbol{a}\}$ are the wave expansion coefficients for the incident P and SV waves, respectively. The resulting complex amplitudes of displacement and stress components can be written as

$$U_r = \{\boldsymbol{A}\}^T\{\mathfrak{E}^1_{71}\} + \left([\boldsymbol{T}^{PP}]\{\boldsymbol{A}\}\right)^T\{\mathfrak{E}^3_{71}\} + \left([\boldsymbol{T}^{SP}]\{\boldsymbol{a}\}\right)^T\{\mathfrak{E}^3_{72}\} \quad (3\text{–}95)$$

$$U_\theta = \{\boldsymbol{A}\}^T\{\mathfrak{E}^1_{81}\} + \left([\boldsymbol{T}^{PP}]\{\boldsymbol{A}\}\right)^T\{\mathfrak{E}^3_{81}\} + \left([\boldsymbol{T}^{SP}]\{\boldsymbol{a}\}\right)^T\{\mathfrak{E}^3_{82}\} \quad (3\text{–}96)$$

$$\Sigma_{rr} = \{\boldsymbol{A}\}^T\{\mathfrak{E}^1_{11}\} + \left([\boldsymbol{T}^{PP}]\{\boldsymbol{A}\}\right)^T\{\mathfrak{E}^3_{11}\} + \left([\boldsymbol{T}^{SP}]\{\boldsymbol{a}\}\right)^T\{\mathfrak{E}^3_{12}\} \quad (3\text{–}97)$$

$$U_{r\theta} = \{\boldsymbol{A}\}^T\{\mathfrak{E}^1_{41}\} + \left([\boldsymbol{T}^{PP}]\{\boldsymbol{A}\}\right)^T\{\mathfrak{E}^3_{41}\} + \left([\boldsymbol{T}^{SP}]\{\boldsymbol{a}\}\right)^T\{\mathfrak{E}^3_{42}\} \quad (3\text{–}98)$$

where $\{\mathfrak{E}^i_{XY}\}$ are various differential wave expansion basis functions, whose elements in the n-th row is

$$\{\mathfrak{E}^i_{XY}\}_n = \mathfrak{E}^i_{XY}(r)e^{in\theta} \quad (3\text{–}99)$$

and functions $\mathfrak{E}^i_{XY}$ are defined in Appendix 2-C in Chapter 2.

Energy Balance Requirement for P/SV Wave Scattering

Since the incident waves can be arbitrary, it is assumed that $\{A\}_n = A$ and $\{A\}_p = 0$ when $p \neq n$, and $\{a\}_m = a$ and $\{a\}_q = 0$ when $q \neq m$, and A and a are arbitrary (complex) numbers, and m and n are arbitrary integers.

The complex amplidutes of displacement and stress components in the matrix are expressible as

$$\begin{aligned} rU_r = {} & A\mathfrak{E}^1_{71n}e^{in\theta} + \sum_{p=-\infty}^{\infty}\left(A[T^{PP}]_{pn} + a[T^{SP}]_{pm}\right)\mathfrak{E}^3_{71p}e^{ip\theta} \\ & + a\mathfrak{E}^1_{72m}e^{im\theta} + \sum_{p=-\infty}^{\infty}\left(A[T^{PS}]_{pn} + a[T^{SS}]_{pm}\right)\mathfrak{E}^3_{72p}e^{ip\theta} \end{aligned} \quad (3\text{–}100)$$

$$\begin{aligned} rU_\theta = {} & A\mathfrak{E}^1_{81n}e^{in\theta} + \sum_{p=-\infty}^{\infty}\left(A[T^{PP}]_{pn} + a[T^{SP}]_{pm}\right)\mathfrak{E}^3_{81p}e^{ip\theta} \\ & + a\mathfrak{E}^1_{82m}e^{im\theta} + \sum_{p=-\infty}^{\infty}\left(A[T^{PS}]_{pn} + a[T^{SS}]_{pm}\right)\mathfrak{E}^3_{82p}e^{ip\theta} \end{aligned} \quad (3\text{–}101)$$

$$\frac{r^2}{2\mu}\Sigma_{rr} = A\mathfrak{E}^1_{11n}e^{in\theta} + \sum_{p=-\infty}^{\infty}\left(A[T^{PP}]_{pn} + a[T^{SP}]_{pm}\right)\mathfrak{E}^3_{11p}e^{ip\theta}$$
$$+ a\mathfrak{E}^1_{12m}e^{im\theta} + \sum_{p=-\infty}^{\infty}\left(A[T^{PS}]_{pn} + a[T^{SS}]_{pm}\right)\mathfrak{E}^3_{12p}e^{ip\theta} \quad (3\text{–}102)$$

$$\frac{r^2}{2\mu}\Sigma_{r\theta} = A\mathfrak{E}^1_{41n}e^{in\theta} + \sum_{p=-\infty}^{\infty}\left(A[T^{PP}]_{pn} + a[T^{SP}]_{pm}\right)\mathfrak{E}^3_{41p}e^{ip\theta}$$
$$+a\mathfrak{E}^1_{42m}e^{im\theta} + \sum_{p=-\infty}^{\infty}\left(A[T^{PS}]_{pn} + a[T^{SS}]_{pm}\right)\mathfrak{E}^3_{42p}e^{ip\theta} \quad (3\text{–}103)$$

where it must be noted that the argument (r) for the $\mathfrak{E}$-functions has been suppressed for simplicity. Thus, constructing the energy flux density and performing the integration over θ, in which process eqn. (3–70) is used to reduce the expressions of energy flux density to a form that contains at most one summation, gives

$$\frac{r^3}{4\pi\mu}Im\left\{\int_0^{2\pi}\left(\Sigma_{rr}\overline{U}_r + \Sigma_{r\theta}\overline{U}_\theta\right)d\theta\right\}$$
$$= \frac{r^3}{8\hat{i}\pi\mu}\int_0^{2\pi}\left[\left(\Sigma_{rr}\overline{U}_r + \Sigma_{r\theta}\overline{U}_\theta\right) - \left(\overline{\Sigma}_{rr}U_r + \overline{\Sigma}_{r\theta}U_\theta\right)\right]d\theta$$
$$= |A|^2 f_1(n;1,1) + |a|^2 f_3(m;1,1) + A\overline{a}\delta_{mn}f_2(n;1,1) - \overline{A}a\delta_{mn}\overline{f_2(n;1,1)}$$
$$+ \overline{A}(A[T^{PP}]_{nn} + a[T^{SP}]_{nm})f_1(n;3,1) + A(\overline{A}[\overline{T^{PP}}]_{nn} + \overline{a}[\overline{T^{SP}}]_{nm})f_1(n;1,3)$$
$$+ A(\overline{A}[\overline{T^{PS}}]_{nn} + \overline{a}[\overline{T^{SS}}]_{nm})f_2(n;1,3) - \overline{A}(A[T^{PP}]_{nn} + a[T^{SP}]_{nm})\overline{f_2(n;1,3)}$$
$$+ \overline{a}(A[T^{PP}]_{mn} + a[T^{SP}]_{mm})f_2(n;3,1) + a(\overline{A}[\overline{T^{PP}}]_{mn} + \overline{a}[\overline{T^{SS}}]_{mm})f_2(n;1,3)$$
$$+ \overline{a}(A[T^{PS}]_{mn} + a[T^{SP}]_{mm})f_3(n;3,1) + a(\overline{A}[\overline{T^{PS}}]_{mn} + \overline{a}[\overline{T^{SS}}]_{mm})f_3(n;1,3)$$
$$\sum_{p=-\infty}^{\infty}|A[T^{PP}]_{pn} + a[T^{SP}]_{pm}|^2 f_1(p;3,3) + \sum_{p=-\infty}^{\infty}|A[T^{PS}]_{pn} + a[T^{SS}]_{pm}|^2 f_3(p;3,3)$$
$$+ \sum_{p=-\infty}^{\infty}(A[T^{PP}]_{pn}+a[T^{SP}]_{pm})(\overline{A}[\overline{T^{PS}}]_{pn}+\overline{a}[\overline{T^{SS}}]_{pm})f_2(p;3,3)$$
$$- \sum_{p=-\infty}^{\infty}(\overline{A}[\overline{T^{PP}}]_{pn}+\overline{a}[\overline{T^{SP}}]_{pm})(A[T^{PS}]_{pn}+a[T^{SS}]_{pm})\overline{f_2(p;3,3)} \quad (3\text{–}104)$$

where

$$f_1(n;i,j) \equiv \mathfrak{E}^i_{11n}\overline{\mathfrak{E}}^j_{71n} + \mathfrak{E}^i_{41n}\overline{\mathfrak{E}}^j_{81n} - \overline{\mathfrak{E}}^j_{11n}\mathfrak{E}^i_{71n} - \overline{\mathfrak{E}}^j_{41n}\mathfrak{E}^i_{81n} \quad (3\text{–}105)$$
$$f_2(n;i,j) \equiv \mathfrak{E}^i_{11n}\overline{\mathfrak{E}}^j_{72n} + \mathfrak{E}^i_{41n}\overline{\mathfrak{E}}^j_{82n} - \overline{\mathfrak{E}}^j_{12n}\mathfrak{E}^i_{71n} - \overline{\mathfrak{E}}^j_{42n}\mathfrak{E}^i_{81n} \quad (3\text{–}106)$$
$$f_3(n;i,j) \equiv \mathfrak{E}^i_{12n}\overline{\mathfrak{E}}^j_{72n} + \mathfrak{E}^i_{42n}\overline{\mathfrak{E}}^j_{82n} - \overline{\mathfrak{E}}^j_{12n}\mathfrak{E}^i_{72n} - \overline{\mathfrak{E}}^j_{42n}\mathfrak{E}^i_{82n} \quad (3\text{–}107)$$

and i and j can be either 1 or 3.

Substituting the expressions for $\mathfrak{E}$-functions in Appendix 2-C into eqns. (3–105) through (3–107) and using the Wronskian relations for cylindrical functions in

eqns. (3-75) through (3-77) give

$$f_2(n;i,j) = 0 \qquad f_1(n;i,j) = f_3(n;i,j) = \begin{cases} 0 & (i=1,\, j=1) \\ \frac{i}{\pi}k^2r^2 & (i=1,\, j=3) \\ \frac{i}{\pi}k^2r^2 & (i=3,\, j=1) \\ \frac{2i}{\pi}k^2r^2 & (i=3,\, j=3) \end{cases} \tag{3-108}$$

Therefore, combining eqns. (3-104) and (3-108), the energy balance requirement in eqn. (3-59) becomes

$$Re\left\{A^2[T^{PP}]_{nn} + \bar{a}A\left(\overline{[T^{SP}]_{nm}} + [T^{PS}]_{mn}\right) + a^2[T^{SS}]_{mm}\right\} + \sum_{p=-\infty}^{\infty}\left(\left|A[T^{PP}]_{pn} + a[T^{PS}]_{pm}\right|^2 + \left|A[T^{PS}]_{pn} + a[T^{SS}]_{pm}\right|^2\right) = 0 \tag{3-109}$$

Since the incident waves are arbitrary, consider the following two special cases. In the first, let $A = 1$ and $a = 0$. Equation (3-109) gives

$$Re\left\{[T^{PP}]_{nn}\right\} + \sum_{p=-\infty}^{\infty}\left(\left|[T^{PP}]_{pn}\right|^2 + \left|[T^{PS}]_{pn}\right|^2\right) = 0 \tag{3-110}$$

Next, let $A = 0$ and $a = 1$. Equation (3-109) gives

$$Re\left\{[T^{SS}]_{mm}\right\} + \sum_{p=-\infty}^{\infty}\left(\left|[T^{SP}]_{pm}\right|^2 + \left|[T^{SS}]_{pm}\right|^2\right) = 0 \tag{3-111}$$

Also note that

$$\left|A[T^{PP}]_{pn} + a[T^{SP}]_{pm}\right|^2 = |A|^2\left|[T^{PP}]_{pn}\right|^2 + |a|^2\left|[T^{SP}]_{pm}\right|^2 + 2Re\left\{A\bar{a}[T^{PP}]_{pn}\overline{[T^{SP}]_{pm}}\right\} \tag{3-112}$$

$$\left|A[T^{PS}]_{pn} + a[T^{SS}]_{pm}\right|^2 = |A|^2\left|[T^{PS}]_{pn}\right|^2 + |a|^2\left|[T^{SS}]_{pm}\right|^2 + 2Re\left\{A\bar{a}[T^{PS}]_{pn}\overline{[T^{SS}]_{pm}}\right\} \tag{3-113}$$

By using eqns. (3-110) through (3-113), eqn. (3-109) can be written as

$$Re\left\{A\bar{a}\left(\overline{[T^{SP}]_{nm}} + [T^{PS}]_{mn}\right)\right\} + 2\sum_{p=-\infty}^{\infty} Re\left\{A\bar{a}\left([T^{PP}]_{pn}\overline{[T^{SP}]_{pm}} + [T^{PS}]_{pn}\overline{[T^{SS}]_{pm}}\right)\right\} = 0 \tag{3-114}$$

Since both A and a are arbitrary complex numbers, it follows that

$$\overline{[T^{SP}]_{nm}} + [T^{PS}]_{mn} + 2\sum_{p=-\infty}^{\infty}\left([T^{PP}]_{pn}\overline{[T^{SP}]_{pm}} + [T^{PS}]_{pn}\overline{[T^{SS}]_{pm}}\right) = 0 \tag{3-115}$$

Or, in matrix form,

$$-\tfrac{1}{2}\left([\boldsymbol{T}^{SP}]^* + [\boldsymbol{T}^{PS}]\right) = [\boldsymbol{T}^{SP}]^*[\boldsymbol{T}^{PP}] + [\boldsymbol{T}^{SS}]^*[\boldsymbol{T}^{PS}] \tag{3-116}$$

Reciprocity for P/SV Wave Scattering

Consider three cases. In the first, assume the two sets of incident waves are all P waves and their respective wave expansion coefficient matrices are

$$\{\boldsymbol{A}_1\}\text{: } \{A_1\}_m = A_1,\ \{A_1\}_p = 0 \text{ when } p \neq m; \qquad \{\boldsymbol{a}_1\} = 0 \tag{3-117}$$

$$\{\boldsymbol{A}_2\}\text{: } \{A_2\}_n = A_2,\ \{A_2\}_q = 0 \text{ when } q \neq n; \qquad \{\boldsymbol{a}_2\} = 0 \tag{3-118}$$

where A_1 and A_2 are arbitrary (complex) numbers. The displacements and stresses due to $\{\boldsymbol{A}_1\}$ are

$$r(U_r)_1 = A_1 \mathfrak{E}^1_{71m} e^{im\theta} + A_1 \sum_{p=-\infty}^{\infty} \left([T^{PP}]_{pm} \mathfrak{E}^3_{71p} + [T^{PS}]_{pm} \mathfrak{E}^3_{72p} \right) e^{ip\theta} \tag{3-119}$$

$$r(U_\theta)_1 = A_1 \mathfrak{E}^1_{81m} e^{im\theta} + A_1 \sum_{p=-\infty}^{\infty} \left([T^{PP}]_{pm} \mathfrak{E}^3_{81p} + [T^{PS}]_{pm} \mathfrak{E}^3_{82p} \right) e^{ip\theta} \tag{3-120}$$

$$\frac{r^2}{2\mu}(\Sigma_{rr})_1 = A_1 \mathfrak{E}^1_{11m} e^{im\theta} + A_1 \sum_{p=-\infty}^{\infty} \left([T^{PP}]_{pm} \mathfrak{E}^3_{11p} + [T^{PS}]_{pm} \mathfrak{E}^3_{12p} \right) e^{ip\theta} \tag{3-121}$$

$$\frac{r^2}{2\mu}(\Sigma_{r\theta})_1 = A_1 \mathfrak{E}^1_{41m} e^{im\theta} + A_1 \sum_{p=-\infty}^{\infty} \left([T^{PP}]_{pm} \mathfrak{E}^3_{41p} + [T^{PS}]_{pm} \mathfrak{E}^3_{42p} \right) e^{ip\theta} \tag{3-122}$$

The displacements and stresses due to $\{\boldsymbol{A}_2\}$ are identical to those for $\{\boldsymbol{A}_1\}$ except that A_1 is replaced by A_2 and that m is replaced by n. It can be found that, for this case,

$$\begin{aligned}
&\frac{r^3}{4\pi\mu} \int_0^{2\pi} \left\{ \left[(\Sigma_{rr})_1 (\overline{U}_r)_2 + (\Sigma_{r\theta})_1 (\overline{U}_\theta)_2 \right] - \left[(\overline{\Sigma}_{rr})_2 (U_r)_1 + (\overline{\Sigma}_{r\theta})_2 (U_\theta)_1 \right] \right\} d\theta \\
&\quad = A_1 \overline{A_2} \Big\{ \delta_{mn} f_1(n;1,1) + \overline{[T^{PP}]}_{mn} f_1(m;1,3) + [T^{PP}]_{nm} f_1(n;3,1) \\
&\qquad + \overline{[T^{PS}]}_{mn} f_2(m;1,3) - [T^{PS}]_{nm} \overline{f_2(n;1,3)} \\
&\qquad + \sum_{p=-\infty}^{\infty} \Big([T^{PP}]_{pm} \overline{[T^{PP}]}_{pn} f_1(p;3,3) + [T^{PP}]_{pm} \overline{[T^{PS}]}_{pn} f_2(p;3,3) \\
&\qquad - [T^{PS}]_{pm} \overline{[T^{PP}]}_{pn} \overline{f_2(p;3,3)} + [T^{PS}]_{pm} \overline{[T^{PS}]}_{pn} f_3(p;3,3) \Big) \Big\}
\end{aligned} \tag{3-123}$$

Noting that both A_1 and A_2 are arbitrary complex numbers, $A_1\overline{A}_2$ can be purely real, purely imaginary or complex. Thus making the real part of the right-hand side of eqn. (3–123) vanish for *any* A_1 and A_2 requires the quantities in the flower brackets to vanish. Thus, the reciprocity requirement in eqn. (3–63) can be written for this case as

$$\overline{[T^{PP}]}_{mn} + [T^{PP}]_{nm} + 2 \sum_{p=-\infty}^{\infty} \left([T^{PP}]_{pm} \overline{[T^{PP}]}_{pn} + [T^{PS}]_{pm} \overline{[T^{PS}]}_{pn} \right) = 0 \tag{3-124}$$

where eqn. (3–108) has been used. Or, in matrix form,

$$-\tfrac{1}{2}([\boldsymbol{T}^{PP}]^* + [\boldsymbol{T}^{PP}]) = [\boldsymbol{T}^{PP}]^*[\boldsymbol{T}^{PP}] + [\boldsymbol{T}^{PS}]^*[\boldsymbol{T}^{PS}] \tag{3-125}$$

Like SH wave scattering case, eqn. (3-125) is a more general form than the one concluded from the energy balance requirement, eqn. (3-110).

In the second case, consider two SV incident waves as

$$\{\boldsymbol{A}_1\} = 0; \quad \{\boldsymbol{a}_1\} : \{a_1\}_m = a_1,\ \{a_1\}_p = 0 \text{ when } p \neq m \tag{3-126}$$

$$\{\boldsymbol{a}_2\} = 0; \quad \{\boldsymbol{a}_2\} : \{a_2\}_n = a_2,\ \{a_2\}_q = 0 \text{ when } q \neq n \tag{3-127}$$

where a_1 and a_2 are arbitrary (complex) numbers. The displacements and stresses due to $\{\boldsymbol{a}_1\}$ are

$$r(U_r)_1 = a_1 \mathfrak{E}^1_{72m} e^{im\theta} + a_1 \sum_{p=-\infty}^{\infty} \left([T^{SP}]_{pm} \mathfrak{E}^3_{71p} + [T^{SS}]_{pm} \mathfrak{E}^3_{72p} \right) e^{ip\theta} \tag{3-128}$$

$$r(U_\theta)_1 = a_1 \mathfrak{E}^1_{82m} e^{im\theta} + a_1 \sum_{p=-\infty}^{\infty} \left([T^{SP}]_{pm} \mathfrak{E}^3_{81p} + [T^{SS}]_{pm} \mathfrak{E}^3_{82p} \right) e^{ip\theta} \tag{3-129}$$

$$\frac{r^2}{2\mu}(\Sigma_{rr})_1 = a_1 \mathfrak{E}^1_{12m} e^{im\theta} + a_1 \sum_{p=-\infty}^{\infty} \left([T^{SP}]_{pm} \mathfrak{E}^3_{11p} + [T^{SS}]_{pm} \mathfrak{E}^3_{12p} \right) e^{ip\theta} \tag{3-130}$$

$$\frac{r^2}{2\mu}(\Sigma_{r\theta})_1 = a_1 \mathfrak{E}^1_{42m} e^{im\theta} + a_1 \sum_{p=-\infty}^{\infty} \left([T^{SP}]_{pm} \mathfrak{E}^3_{41p} + [T^{SS}]_{pm} \mathfrak{E}^3_{42p} \right) e^{ip\theta} \tag{3-131}$$

The displacements and stresses due to $\{\boldsymbol{a}_2\}$ are identical to those due to $\{\boldsymbol{a}_1\}$ except that a_1 is replaced by a_2 and that m is replaced by n. Then,

$$\begin{aligned}
&\frac{r^3}{4\pi\mu} \int_0^{2\pi} \left\{ \left[(\Sigma_{rr})_1 (\overline{U}_r)_2 + (\Sigma_{r\theta})_1 (\overline{U}_\theta)_2 \right] - \left[(\overline{\Sigma}_{rr})_2 (U_r)_1 + (\overline{\Sigma}_{r\theta})_2 (U_\theta)_1 \right] \right\} d\theta \\
&\quad = a_1 \overline{a}_2 \Big\{ \delta_{mn} f_3(n;1,1) - [\overline{T^{SP}}]_{mn} \overline{f_2(m;3,1)} + [\overline{T^{SS}}]_{mn} f_3(m;1,3) \\
&\qquad + [T^{SP}]_{nm} f_2(n;3,1) + [T^{SS}]_{nm} f_3(n;3,1) \\
&\qquad + \sum_{p=-\infty}^{\infty} \Big[[T^{SP}]_{pm} [\overline{T^{SP}}]_{pn} f_1(p;3,3) + [T^{SP}]_{pm} [\overline{T^{SS}}]_{pn} f_2(p;3,3) \\
&\qquad - [T^{SS}]_{pm} [\overline{T^{SP}}]_{pn} \overline{f_2(p;3,3)} + [T^{SS}]_{pm} [\overline{T^{SS}}]_{pn} f_3(p;3,3) \Big] \Big\}
\end{aligned} \tag{3-132}$$

Since both a_1 and a_2 are arbitrary complex numbers, the reciprocity requirement in eqn. (3-63) can be written for this case as

$$[\overline{T^{SS}}]_{mn} + [T^{SS}]_{nm} + 2 \sum_{p=-\infty}^{\infty} \left([T^{SS}]_{pm} [\overline{T^{SS}}]_{pn} + [T^{SP}]_{pm} [\overline{T^{SP}}]_{pn} \right) = 0 \tag{3-133}$$

where eqn. (3-108) has been used. Or, in matrix form,

$$-\tfrac{1}{2}([\boldsymbol{T}^{SS}]^* + [\boldsymbol{T}^{SS}]) = [\boldsymbol{T}^{SS}]^* [\boldsymbol{T}^{SS}] + [\boldsymbol{T}^{SP}]^* [\boldsymbol{T}^{SP}] \tag{3-134}$$

Again, eqn. (3-134) is a more general form than the similar one concluded from the energy balance requirement, eqn. (3-111).

In the third case, consider one P incident wave and one SV incident wave as

$$\{\boldsymbol{A}_1\}\text{: } \{A_1\}_m = A_1,\ \{A_1\}_p = 0 \text{ when } p \neq m; \qquad \{\boldsymbol{a}_1\} = 0 \tag{3-135}$$

$$\{\boldsymbol{A}_2\} = 0; \qquad \{\boldsymbol{a}_2\}\text{: } \{a_2\}_n = a_2,\ \{a_2\}_q = 0 \text{ when } q \neq n \tag{3-136}$$

where A_1 and a_2 are arbitrary (complex) numbers. The displacements and stresses due to $\{A_1\}$ are given in eqns. (3–119) through (3–122), and the displacements and stresses due to $\{a_2\}$ are given in eqns. (3–128) through (3–131), except that m is replaced by n, and the subscript 1 is replaced by 2.

It then follows that

$$\begin{aligned}
&\frac{r^3}{4\pi\mu}\int_0^{2\pi}\left\{\left[(\Sigma_{rr})_1(\overline{U}_r)_2+(\Sigma_{r\theta})_1(\overline{U}_\theta)_2\right]-\left[(\overline{\Sigma}_{rr})_2(U_r)_1+(\overline{\Sigma}_{r\theta})_2(U_\theta)_1\right]\right\}d\theta \\
&\quad= A_1\overline{a}_2\Big\{\delta_{mn}f_2(m;1,1)+\overline{[T^{SP}]}_{mn}f_1(m;1,3)+\overline{[T^{SS}]}_{mn}f_2(m;1,3) \\
&\qquad+[T^{PP}]_{nm}f_2(n;3,1)+[T^{PS}]_{nm}f_3(n;3,1) \\
&\qquad+\sum_{p=-\infty}^{\infty}\Big([T^{PP}]_{pm}\overline{[T^{SP}]}_{pn}f_1(p;3,3)+[T^{PS}]_{pm}\overline{[T^{SP}]}_{pn}f_2(p;3,3) \\
&\qquad-[T^{PP}]_{pm}\overline{[T^{SS}]}_{pn}\overline{f_2(p;3,3)}+[T^{PS}]_{pm}\overline{[T^{SS}]}_{pn}f_3(p;3,3)\Big)\Big\} \qquad (3\text{–}137)
\end{aligned}$$

Since both A_1 and a_2 are arbitrary complex numbers, the reciprocity requirement in eqn. (3–63) can be written for this case as

$$\overline{[T^{SP}]}_{mn}+[T^{PS}]_{nm}+2\sum_{p=-\infty}^{\infty}\left([T^{PP}]_{pm}\overline{[T^{SP}]}_{pn}+[T^{PS}]_{pm}\overline{[T^{SS}]}_{pn}\right)=0 \qquad (3\text{–}138)$$

where eqn. (3–108) has been used. Or, in matrix form,

$$-\tfrac{1}{2}([\boldsymbol{T}^{SP}]^*+[\boldsymbol{T}^{PS}])=[\boldsymbol{T}^{PS}]^*[\boldsymbol{T}^{PP}]+[\boldsymbol{T}^{SS}]^*[\boldsymbol{T}^{SP}] \qquad (3\text{–}139)$$

This time, eqn. (3–139) is identical to eqn. (3–116), the conclusion from the energy balance requirement. Taking the conjugate transpose of eqn. (3–139) gives

$$-\tfrac{1}{2}([\boldsymbol{T}^{PS}]^*+[\boldsymbol{T}^{SP}])=[\boldsymbol{T}^{PP}]^*[\boldsymbol{T}^{PS}]+[\boldsymbol{T}^{SP}]^*[\boldsymbol{T}^{SS}] \qquad (3\text{–}140)$$

Unfortunately, equations similar to eqn. (3–90) in the SH wave case were unable to be derived for the P/SV case.

Conclusions for P/SV Wave Case

In conclusion, eqns. (3–125), (3–134), (3–139) and (3–140) are the properties imposed by the reciprocity principle for the T-matrices of P/SV wave scattering. Other conclusion can be derived from these equations in a similar way as in the SH wave case, and can be summarized as follows:

- The magnitude of any element of any T-matrix is no larger than unity.
- The real part of any diagonal element of the $[\boldsymbol{T}^{PP}]$ and $[\boldsymbol{T}^{SS}]$ is non-positive but not smaller than -1.
- The sum of the magnitude squares of any entire column of any T-matrix is no larger than unity.
- The sum of the magnitude squares of any column of $[\boldsymbol{T}^{PP}]$ plus the sum of the same column of $[\boldsymbol{T}^{PS}]$ is no larger than unity.

- The sum of the magnitude squares of any column of $[\boldsymbol{T}^{SS}]$ plus the sum of the same column of $[\boldsymbol{T}^{SP}]$ is no larger than unity.
- For any column of the $[\boldsymbol{T}^{PP}]$ matrix, the real part of the diagonal term equals the negation of the total sum of the magnitude squares of the elements in the entire column and of the elements in the same column of the $[\boldsymbol{T}^{PS}]$ matrix.
- For any column of the $[\boldsymbol{T}^{SS}]$ matrix, the real part of the diagonal term equals the negation of the total sum of the magnitude squares of the elements in the entire column and of the elements in the same column of the $[\boldsymbol{T}^{SP}]$ matrix.

It is interesting to observe that, if the four T-matrices for P/SV scattering are assembled into the following *T-supermatrix*

$$[\mathfrak{T}] = \begin{bmatrix} [\boldsymbol{T}^{PP}] & [\boldsymbol{T}^{SP}] \\ [\boldsymbol{T}^{PS}] & [\boldsymbol{T}^{SS}] \end{bmatrix} \tag{3-141}$$

then eqns. (3–125), (3–134), (3–139) and (3–140) can be combined to give

$$\tfrac{1}{2}([\mathfrak{T}]^* + [\mathfrak{T}]) = -[\mathfrak{T}]^*[\mathfrak{T}] \tag{3-142}$$

which is identical in form to eqn. (3–92) in the SH wave case, and thus the properties concluded from eqn. (3–92) also hold for $[\mathfrak{T}]$. Furthermore, with similar construction of wave expansion coefficient supermatrices for various waves, such as the incident and the scattered waves as follows

$$\{\mathfrak{A}\} = \begin{Bmatrix} \{\boldsymbol{A}\} \\ \{\boldsymbol{a}\} \end{Bmatrix} \qquad \{\mathfrak{B}\} = \begin{Bmatrix} \{\boldsymbol{B}\} \\ \{\boldsymbol{b}\} \end{Bmatrix} \tag{3-143}$$

Then,

$$\{\mathfrak{B}\} = [\mathfrak{T}]\{\mathfrak{A}\} \tag{3-144}$$

That is, the T-matrix relation for the P/SV wave scattering is also identical in form to that of the SH wave case in eqn. (3–11).

3-6.2 Properties of T-Matrix Due to Scatterer Symmetries

In this subsection, the properties of the T-matrix imposed by scatterer symmetries are explored. By a symmetry, it is implied that both the geometry and relevant physical properties of the scatterer are symmetric. For brevity, considerations are restricted to the case of SH wave scattering. The extension to the case of P/SV wave scattering is straightforward.

Symmetry About $\theta = 0$ (x-Axis)

If the scatterer is symmetric about $\theta = 0$ (the x-axis), then for any incident wave that is symmetric about this axis, the resulting scattered wave must also be symmetric about this axis.

For an incident wave to be symmetric about $\theta = 0$ (the x-axis), the necessary and sufficient condition is $\phi^{\text{inc}}(r,\theta) = \phi^{\text{inc}}(r,-\theta)$; that is, for any r and θ,

$$\phi^{\text{inc}} = \sum_{n=-\infty}^{\infty} A_n J_n(kr)\mathrm{e}^{\mathrm{i}n\theta} = \sum_{n=-\infty}^{\infty} A_n J_n(kr)\mathrm{e}^{-\mathrm{i}n\theta} \tag{3-145}$$

which requires, for any $n > 0$,

$$\begin{aligned} &A_n J_n(kr)\mathrm{e}^{\mathrm{i}n\theta} + (-1)^n A_{-n} J_n(kr)\mathrm{e}^{-\mathrm{i}n\theta} \\ &\qquad = A_n J_n(kr)\mathrm{e}^{-\mathrm{i}n\theta} + (-1)^n A_{-n} J_n(kr)\mathrm{e}^{\mathrm{i}n\theta} \end{aligned} \tag{3-146}$$

where eqn. (3-47) has been used. Since both r and θ are arbitrary, eqn. (3-146) gives to

$$A_n = (-1)^n A_{-n} \tag{3-147}$$

Similarly, the scattered wave is symmetric about $\theta = 0$ (the x-axis), and hence

$$B_n = (-1)^n B_{-n} \tag{3-148}$$

From the definition of the T-matrix in eqn. (3-11),

$$\{B\}_m = [T]_{m0}\{A\}_0 + \sum_{n=1}^{\infty} \left[[T]_{mn} + (-1)^n [T]_{m(-n)}\right] \{A\}_n \tag{3-149}$$

$$\{B\}_{-m} = [T]_{(-m)0}\{A\}_0 + \sum_{n=1}^{\infty} \left[[T]_{(-m)n} + (-1)^n [T]_{(-m)(-n)}\right] \{A\}_n \tag{3-150}$$

where notational identities $\{A\}_n = A_n$ and $\{B\}_n = B_n$ and eqn. (3-147) has been used.

If $\{A\}_0 \neq 0$ and all other $\{A\}_n = 0$, according to eqn. (3-148),

$$[T]_{m0} = (-1)^m [T]_{(-m)0} \tag{3-151}$$

If $\{A\}_n \neq 0$ and all other $\{A\}_n = 0$, according to eqn. (3-148),

$$[T]_{mn} + (-1)^n [T]_{m(-n)} = (-1)^m \left[[T]_{(-m),n} + (-1)^n [T]_{(-m)(-n)}\right] \tag{3-152}$$

It is noted that eqn. (3-152) is inclusive of eqn. (3-151).

Thus, it can be concluded that, if the scatterer is symmetric about $\theta = 0$ (the x-axis), then, for any m and n,

$$[T]_{mn} + (-1)^n [T]_{m(-n)} = (-1)^m [T]_{(-m)n} + (-1)^{m+n} [T]_{(-m)(-n)} \tag{3-153}$$

Symmetry About $\theta = \pi/2$ (y-Axis)

If the scatterer is symmetric about $\theta = \pi/2$ (the y-Axis), then, by performing a coordinate rotation of $\pm\pi/2$, the scatterer would become symmetric about $\theta' = 0$ (the x'-axis) in the new (primed) coordinate system.

Using eqn. (3-41), the T-matrix in the rotated coordinate system is $[\boldsymbol{T}']$ with

$$[T']_{mn} = \mathrm{e}^{\pm\mathrm{i}(m-n)\frac{\pi}{2}} [T]_{mn} = (\pm\mathrm{i})^{m-n} [T]_{mn} \tag{3-154}$$

and since the scatterer is symmetric about $\theta' = 0$ (the x'-axis), eqn. (3-153) gives

$$[T']_{mn} + (-1)^n[T']_{m(-n)} = (-1)^m[T']_{(-m)n} + (-1)^{m+n}[T']_{(-m)(-n)} \qquad (3\text{-}155)$$

Combining eqns. (3-154) and (3-155) gives

$$\begin{aligned}(\pm\hat{\imath})^{m-n}[T]_{mn} + (-1)^n(\pm\hat{\imath})^{m+n}[T]_{m(-n)} \\ = (-1)^m(\pm\hat{\imath})^{-m-n}[T]_{(-m)n} + (-1)^{m+n}(\pm\hat{\imath})^{-m+n}[T]_{(-m)(-n)}\end{aligned} \qquad (3\text{-}156)$$

which can be readily reduced to

$$[T]_{mn} + [T]_{m(-n)} = [T]_{(-m)n} + [T]_{(-m)(-n)} \qquad (3\text{-}157)$$

Symmetries About Both $\theta = 0$ (x-Axis) And $\theta = \pi/2$ (y-Axis)

If the scatterer is symmetric about both $\theta = 0$ (the x-axis) and $\theta = \pi/2$ (the y-axis), the identical T-matrix should result if the coordinate system is rotated about its origin by an angle of $\pi/2$ or by an angle of $-\pi/2$. Thus, according to eqn. (3-41),

$$e^{i(m-n)\frac{\pi}{2}}[T]_{mn} = e^{-i(m-n)\frac{\pi}{2}}[T]_{mn} \qquad (3\text{-}158)$$

which gives

$$[T]_{mn} = e^{-i(m-n)\pi}[T]_{mn} = (-1)^{m-n}[T]_{mn} \qquad (3\text{-}159)$$

Therefore,

$$[T]_{mn} = 0 \qquad \text{when } (m-n) \text{ is odd} \qquad (3\text{-}160)$$

On the other hand, eqns. (3-153) and (3-157) hold simutaneously. Consider only the case when $(m-n)$ is even. For the case when both m and n are even, eqns. (3-153) and (3-157) become identical. For the case when both m and n are odd, eqn. (3-153) becomes

$$[T]_{mn} - [T]_{m(-n)} = -[T]_{(-m)n} + [T]_{(-m)(-n)} \qquad (3\text{-}161)$$

Combining eqns. (3-162) and (3-157) gives

$$[T]_{mn} = [T]_{(-m)(-n)} \qquad \text{and} \qquad [T]_{m(-n)} = [T]_{(-m)n} \qquad (3\text{-}162)$$

Note that the two equations in eqns. (3-162) is inclusive to each other of both m and n can be negative, any one suffices.

Therefore, properties of the T-matrix for this case can be concluded as follow:

- When $(m-n)$ is odd, $[T]_{mn} = 0$;
- When both m and n are odd, $[T]_{mn} = [T]_{(-m)(-n)}$;
- When both m and n are even,

$$[T]_{mn} + [T]_{m(-n)} = [T]_{(-m)n} + [T]_{(-m)(-n)}. \qquad (3\text{-}163)$$

Symmetries About Both $\theta = \pm\pi/4$

If the scatterer is symmetric about $\theta = \pm\pi/4$, then, by rotating the coordinate system about its origin by the angle $\pm\pi/4$, the scatterer would become symmetric about the $\theta' = 0$ (the x'-axis) and $\theta' = \pi/2$ (the y'-axis) in the new (primed) coordinate system, and the appropriate properties for these symmetries are applicable. Hence, from eqn. (3–160), $[T]_{mn} = 0$ when $(m-n)$ is odd.

When both m and n are odd, using eqn. (3–41) to apply the afore-mentioned coordinate rotation to eqn. (3–162) gives

$$e^{\pm i(m-n)\frac{\pi}{4}}[T]_{mn} = e^{\mp i(m-n)\frac{\pi}{4}}[T]_{(-m)(-n)} \tag{3–164}$$

or,

$$[T]_{mn} = (\mp\hat{\imath})^{m-n}[T]_{(-m)(-n)} = \hat{\imath}^{m-n}[T]_{(-m)(-n)} \tag{3–165}$$

where the $\mp$ sign has become immaterial as $(m-n)$ is even.

When both m and n are even, applying the coordinate transformation, eqn. (3–163) gives

$$\begin{aligned} &e^{\pm i(m-n)\frac{\pi}{4}}[T]_{mn} + e^{\pm i(m+n)\frac{\pi}{4}}[T]_{m(-n)} \\ &\quad = e^{\mp i(m+n)\frac{\pi}{4}}[T]_{(-m)n} + e^{\mp i(m-n)\frac{\pi}{4}}[T]_{(-m)(-n)} \end{aligned} \tag{3–166}$$

or,

$$[T]_{mn} + \hat{\imath}^{\pm n}[T]_{m(-n)} = \hat{\imath}^{\mp m}[T]_{(-m)n} + \hat{\imath}^{\pm(m-n)}[T]_{(-m)(-n)} \tag{3–167}$$

Therefore, the properties of the T-matrix for this case can be concluded as follow:

- When $(m-n)$ is odd, $[T]_{mn} = 0$;
- When when both m and n are odd, $[T]_{mn} = (-1)^{\frac{m-n}{2}}[T]_{(-m)(-n)}$;
- When when both m and n are even,

$$[T]_{mn} + (-1)^{\frac{n}{2}}[T]_{m(-n)} = (-1)^{\frac{m}{2}}[T]_{(-m)n} + (-1)^{\frac{m-n}{2}}[T]_{(-m)(-n)}. \tag{3–168}$$

Symmetries About $\theta = 0$ (x-Axis), $\theta = \pi/2$ (y-Axis) And $\theta = \pm\pi/4$

If the scatterer is symmetric about all the 4 axis, rotating the coordinate system about its origin by an angle of either $\pi/4$ or $-\pi/4$ generates the same T-matrix, although different from the original T-matrix. Thus, from eqn. (3–41),

$$e^{i(m-n)\frac{\pi}{4}}[T]_{mn} = e^{-i(m-n)\frac{\pi}{4}}[T]_{mn} \tag{3–169}$$

which gives

$$e^{i(m-n)\frac{\pi}{4}}[T]_{mn}(1 - e^{-i(m-n)\frac{\pi}{2}}) = e^{i(m-n)\frac{\pi}{4}}[T]_{mn}\left[1 - (-\hat{\imath})^{m-n}\right] = 0 \tag{3–170}$$

Thus, $[T]_{mn} \neq 0$ when $(m-n)$ is a multiple of 4, and $[T]_{mn} = 0$ for all other cases.

On the other hand, properties of the T-matrix for the symmetries about $\theta = \pm\pi/4$ and for the symmetries about $\theta = 0$ and $\theta = \pi/2$ must hold simultaneously.

When both m and n are odd, and $(m-n)$ is a multiple of 4, eqns. (3-162) and (3-165) identically give

$$[T]_{mn} = [T]_{(-m)(-n)} \qquad \text{and} \qquad [T]_{m(-n)} = [T]_{(-m)n} \tag{3-171}$$

When both m and n are even, eqn. (3-163) gives

$$[T]_{mn} + [T]_{m(-n)} = [T]_{(-m)n} + [T]_{(-m)(-n)} \tag{3-172}$$

and eqn. (3-168) gives

$$[T]_{mn} + (-1)^{\frac{n}{2}}[T]_{m(-n)} = (-1)^{\frac{m}{2}}[T]_{(-m)n} + (-1)^{\frac{m-n}{2}}[T]_{(-m)(-n)} \tag{3-173}$$

There are only two cases when when $(m-n)$ is a multiple of 4: when both m and n are multiples of 4, and when both m and n are multiples of 2 but not multiples 4. For the first case, eqns. (3-172) and (3-173) become identical. For the second case, eqn. (3-173) becomes

$$[T]_{mn} - [T]_{m(-n)} = -[T]_{(-m)n} + [T]_{(-m)(-n)} \tag{3-174}$$

Combining eqns. (3-174) and (3-172) gives

$$[T]_{mn} = [T]_{(-m)(-n)} \qquad \text{and} \qquad [T]_{m(-n)} = [T]_{(-m)n} \tag{3-175}$$

Therefore, the properties of the T-matrix for this case can be concluded as follow:

- when $(m-n)$ is not a multiple of 4, $[T]_{mn} = 0$;
- when both m and n are multiples of 4,

$$[T]_{mn} + [T]_{m(-n)} = [T]_{(-m)n} + [T]_{(-m)(-n)} \tag{3-176}$$

- For all other cases, $[T]_{mn} = [T]_{(-m)(-n)}$.

Axial Symmetry

If the scatterer is axially symmetric, then, by any amount of rotation, the T-matrix for the scatterer remains the same. Applying the coordinate transformation for a rotation of an arbitrary angle α, then,

$$[T]_{mn} = e^{i(m-n)\alpha}[T]_{mn} \tag{3-177}$$

Since α is arbitrary, it can be concluded that $[T]_{mn} \neq 0$ only when $m = n$. This implies, the T-matrix for an axially symmetric scatterer is a diagonal matrix.

3-7 Concluding Remarks

In the literature (*e.g.*, [3–5]), two widely known properties of the T-matrix, namely, the symmetry ($[\boldsymbol{T}]^T = [\boldsymbol{T}]$) and the unitarity ($Re\{[\boldsymbol{T}]\} = -[\boldsymbol{T}]^*[\boldsymbol{T}]$), are the conclusions drawn from these physical principles: the symmetry is derived from the reciprocity principle and the unitarity is derived from the energy balance requirement.

However, it is shown here that properties such as symmetry and unitarity do not necessarily hold in all cases, and more importantly, that such properties are particular to a specific context in which the T-matrix is defined. It can be further shown that eqn. (3–90) corresponds to the symmetry property in the literature, and that eqn. (3–92) corresponds to the unitarity property in the literature, had the wave expansion bases been chosen accordingly. In this sense, the properties for T-matrix in eqns. (3–90) and (3–92) are not new findings in this study.

The differences in the properties of T-matrices lie in the different choices of the wave expansion bases. The derivations in the literature are all based, although not explicitly stated, on the wave expansion basis that satisfies $\Re\{\text{Singular Basis}\} = Re\{\text{Singular Basis}\}$, where $\Re$ means replacing the singular basis function by the corresponding regular basis function. In a 2-D problem using polar coordinates, the singular bases that satisfy such a requirement are $H_n^{(1)}(kr)\begin{matrix}\sin\\ \cos\end{matrix} n\theta$. The basis $\{\boldsymbol{H}(r,\theta)\}$ used in §2-3 and §2-4 (the definition of T-matrix used in this thesis) does not satisfy this requirement.

On the other hand, the choice of any particular wave expansion basis should not be substantial, and the conversion from one basis to another is straightforward.

The choice of the uniform expansion is based solely on the consideration of the notational simplicity. With the choice of even-odd expansion, a simple SH scattering problem needs four T-matrices in order to completely relate the even (symmetric) and odd (skew-symmetric) waves, as the pairings in the P/SV wave case; and a P/SV scattering problem needs sixteen T-matrices. Such a form would make the multiple-scattering formulation much more intimidatingly complicated, which not only obscures the physics but also hinders the comprehension. On the other hand, it is noted that both expansions require the same number of unknowns and result in the same number of elements in the T-matrices if the same error tolerance is specified. That is, the choice of a particular wave expansion form simplifies only the notation, but not the numerical computation.

As far as the numerical computation is concerned, the uniform expansion form does have some minor advantages. For example, when the even-odd expansion is used, the wave expansion coefficient for the $n = 0$ term needs some special treatment. Typically a symbol ε_n, called the *Neumann factor*, is introduced with the definition

$\varepsilon_n = 1$ when $n = 0$ and $\varepsilon_n = 2$ otherwise. Also, some of the $\mathfrak{C}$-functions change signs for even and odd bases, as noted in Appendix 2-C in Chapter 2. These are minor differences, but could become potential sources of coding errors, and in some high-performance computer architectures, such special treatments could degrade the computer performace.

Historically, the term T-matrix is primarily due to Waterman's work [3] in which a new approach of solving scattering problems via integral equations was proposed. The approach is often arguably called the *T-matrix approach.* (Other names that do not bear the phrase T-matrix are probably more appropriate, such as the *extended boundary condition method* and the *null-field approach*, as it has been called.) There is extensive literature on the so-called T-matrix approach as exemplified by symposium proceedings [6].

It must be noted that the present work is *not* related to that approach. Only the concept of the T-matrix is used, and given a clarified definition. Such a clarification is necessary, as evidenced by the fact that different properties of T-matrices are concluded from the same physical principles.

References

[1] A. Erdélyi, *Higher Transcendental Functions, vol. 3.* McGraw Hill, N.Y., 1953.

[2] G.N. Watson, *Treaties of Theory of Bessel Functions,* 2nd edn., Cambridge University Press, London, 1945.

[3] P. C. Waterman, New formulation for acoustic scattering, *J. Acoust. Soc. Am.,* **45**, 1417–1429, 1969.

[4] V. Varatharajulu, Y.-H. Pao, Scattering matrix for elastic waves, I. Theory, *J. Acoust. Soc. Am.,* **59**, 1361–1371, 1976.

[5] P. C. Waterman, Matrix theory of elastic wave scattering, *J. Acoust. Soc. Am.,* **60**, 567–580, 1976.

[6] V. K. Varadan, V. V. Varadan, eds., *Acoustic, Electromagnetic and Elastic Wave Scattering — Focus on the T-Matrix Approach,* Pergamon, New York, 1980.

4

Multiple Scattering Solution

Abstract: *A solution for the two-dimensional multiple-scattering problem of elastic wave is presented. The solution follows the physical process envisioned as "ordered scattering" and arrives at a recursive solution procedure. Alternative forms are then derived. Using a matrix notation, the solution for the cases of SH waves and P/SV waves remains the same form. This solution is analytically exact and is capable of handling an arbitrary number of similar and/or dissimilar scatterers. Expressions for exterior and interior wave fields and for the stress and strain fields are given, and the validity condition of the solution is discussed.*

Contents:

Nomenclature

General Conventions

- Matrices are denoted by bold-faced symbols; symbols for column matrices are enclosed by flower brackets ({}); symbols for rectangular matrices are enclosed by square brackets ([]).
- When referring to a matrix entry, the entry's indicial number is to appear as subscript(s) *outside* the brackets. This distinguishes the indicial subscript(s) from the subscript(s), if any, associated with the entire matrix.
- Super-matrices are denoted by the same symbols as those for the corresponding matrices, but set in a calligraphic font.

Symbols

a_i	The radius of Scatterer i; that is, the radius of the smallest circumscribing circle of Scatterer i centered at the origin of local coordinate system.
$\{\boldsymbol{A}_i\}, \{\boldsymbol{B}_i\}, \cdots$	Wave expansion coefficient (column) matrices for Scatterer i
(d_{ij}, θ_{ij})	Coordinates of the origin of Scatterer j's local polar coordinate system in Scatterer i's local polar coordinate system.
$H_n(x)$	Hankel function of the first kind and n-th order.
$\{\boldsymbol{H}(r_i, \theta_i)\}$	Singular (Hankel) wave expansion basis of Scatterer i.
$\{\boldsymbol{H}_r(\cdot)\}, \{\boldsymbol{H}_\theta(\cdot)\}$	Singular differential wave expansion bases of Scatterer i for SH waves.
$\{\boldsymbol{H}_{\xi\eta}(r_i, \theta_i)\}$	Singular differential wave expansion bases of Scatterer i for P/SV waves.
$\hat{\imath}$	Unit of imaginary number, $\hat{\imath} = \sqrt{-1}$.
$J_n(x)$	Bessel function of the first kind and n-th order.
$\{\boldsymbol{J}(r_i, \theta_i)\}$	Regular wave expansion basis for Scatterer i, same as $\{\Re\boldsymbol{H}(r_i, \theta_i)\}$.
κ, k	Wave numbers, for longitudinal and shear waves, respectively.
$[\boldsymbol{K}_i^{(p)}]$	The p-th order scattering kernel of Scatterer i.
$[\boldsymbol{L}_{ij}]$	Inductance matrix of Scatterer i on Scatterer j.
N	Total number of scatterers.
$\Re$	Regular counterpart of a singular function or functional basis. In this chapter, this always implies replacing Hankel functions of the first kind by Bessel functions of the first kind at the same order.
$[\boldsymbol{R}_{ij}]$	Singular coordinate translation matrix.
$[\boldsymbol{T}_i]$	T-matrix of Scatterer i.
ϕ	Complex amplitude of displacement w for SH waves.
Φ, φ	Scalar displacement potential and its complex amplitude.
Ψ, ψ	The z-component of vector displacement potential and its complex amplitude.

Superscripts

$(1), (2), \cdots (p)$	Order of the wave; step number in an repetitive procedure
P, S	Characteristic of or pertinent to P and S waves, respectively.
ss	Scattered wave for the single-scatterer problem.
T	Matrix transposition.

Subscripts

i, j	Scatterer identifier.
m, n	Indicial number for a matrix entry.

4-1 Introduction

In general, the *multiple scattering* is referred to the process in which a *scattered wave* is subjected to further scattering by interfaces and/or boundaries.

In this thesis, considerations are restricted to situations in which no physical boundary present; that is, scatterers are embedded in an infinite medium, which is referred to as the *matrix*. Within such a context, there are at least two classes of situations in which the multiple scattering occurs.

The first class of situations is that the scatterer has some infra-structures, such as the layered cylindrical elastic scatterer considered in §2-3. Within such a scatterer, the wave scattered by the inner layer of the scatterer will be further scattered when it encounters the interface between the outer layer of the scatterer and the matrix. That is, the multiple scattering may occur in a single-scatterer problem.

The second class is the case when more than one scatterers are situated in the infinite medium. In such cases, the wave scattered by one scatterer will be further scattered by other scatterers. This is the situation with which this thesis is concerned. Unless otherwise noted, this is also the case the phrase "multiple scattering" in referred to.

In this chapter, a solution for the multiple scattering problem in a general multiple-scatterer situation is presented. The physical process is envisioned as the "ordered scattering" in which an observer follows a wave through its course of propagation. Then, following this process the solution is derived as a recursive solution procedure. Slight variations of the solution process lead to other more convenient solution forms. The solution thus obtained is analytically exact. It is further shown that the formal solution remains its form for both cases of SH and P/SV wave scattering.

In the remaining part of this section, a mathematical description of the problem is presented, followed by an examination of the physical process of multiple scattering in Section 4-2. The physical process leads to the mathematical structure of the solution procedure, which is derived in Sections 4-3 and 4-4 for SH and P/SV wave scattering problems, respectively. Finally, comparisons with other solutions that bear close resemblances to the present solution are made in Section 4-5.

4-1.1 Problem Specifications

The problem under consideration can be stated as follow:

Consider an arbitrary number of scatterers N situated in a host medium of infinite extent. The scatterers are not necessarily identical but are all infinitely long cylinders having known arbitrary cross sections. They are so

arranged that their axes are parallel to each other, and their locations are known deterministically. A time-harmonic incident wave propagates in a plane that is perpendicular to the axes of the scatterers. The steady-state responses at any location within the medium are sought.

Sets of local and global coordinate systems are defined, as sketched in Fig. 4–1. The global Cartesian coordinate system, whose coordinates are referred to as (x, y),

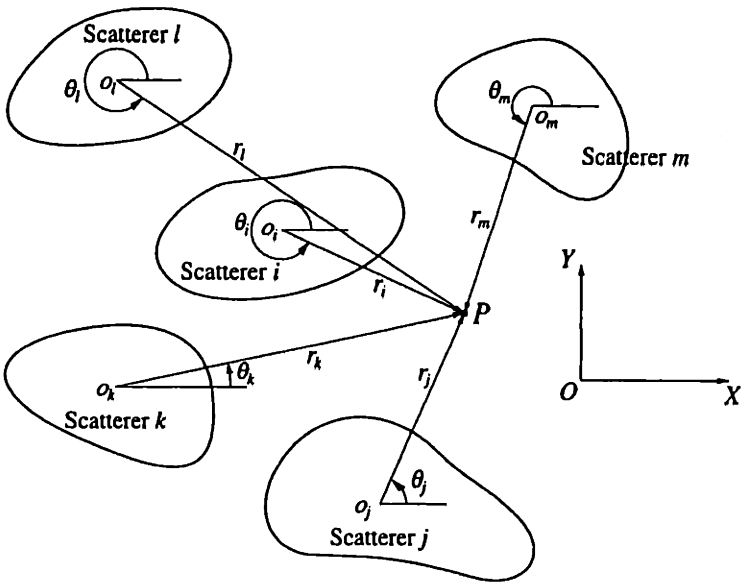

Fig. 4–1 Local and global coordinate systems.

is defined in such a way that the XY-plane is perpendicular to the axes of the scatterers. The problem is two-dimensional in the XY-plane.

One local polar coordinate system is fixed in each scatterer. Local coordinates are referred to as (r_i, θ_i) for scatterer i $(i = 1, 2, \cdots, N)$. The origin of scatterer i's local coordinate system, which in general is located within the region occupied by the scatterer, is located at point (X_i, Y_i) in the global coordinate system. All θ_i's are measured from the X-axis.

4-1.2 Assumptions

The problem statement given above represents a mathematical model for the physical situation. Several idealization assumptions lead to such a model. One of the assumptions is that, as mentioned earlier, there is no physical boundaries. This idealization eliminates the interactions of waves with physical boundaries. Thus the phenomena observed are entirely due to the scattering and multiple scattering effects. The mathematical model is built in a two-dimensional space by assuming that all scatterers are of infinite length and aligned parallelly with each other, and waves propagate within the plane normal to the axes of the scatterers.

These assumptions are essentially in the geometrical aspect of the problem. The following assumptions in the physical aspect of the problem are necessary for solving the problem.

First, it is assumed that the host medium is isotropic linearly elastic; the scatterers can be voids, or rigid and isotropic linearly elastic inclusions. In other words, the wave amplitude is very small compare with the linearity limit of elasticity of both the host medium and the scatterers.

Second, it is assumed that all relevant material properties are known. These properties include all mechanical, physical and geometrical properties of both the host medium and the scatterers that are necessary for solving the problem.

Third, it is assumed that the solution for the single-scatterer problem of every scatterer in the host medium is known for any time-harmonic incident wave. The single-scatterer problem is the problem in which a single scatterer is located at the origin of a coordinate system and is surrounded by the identical host medium of infinite extent. Each scatterer has an associated single-scatterer problem, and its solution is assumed to be known; that is, the T-matrix for every scatterer is known. As discussed in Chapter 3, the definition of a T-matrix specifies a problem, including its wave expansion bases.

As discussed in Chapter 3, the definition of a T-matrix specifies a problem, including its wave expansion bases. In the problem statement, it states that the locations of the scatterers are known. A clearer definition can be made by the following amendment: the location of a scatterer is represented by the location of the origin of the coordinate system within which the single-scatterer problem is solved, and the scatterer is oriented such that the $\theta = 0$ direction of its local coordinate system is in the $+X$ direction of the global coordinate system.

4-2 Physics of Multiple Scattering

In this section, the physical process of multiple scattering is presented. In this process, it is imagined that an observer follows an incident wave and traverses through the material as the incident wave encounters and interacts with the scatterers in the field.

Although the scope of consideration is restricted to SH waves in two dimensions, the process described herein is, in principle, applicable to all types of classical waves. In order to preserve this generality, generic mathematical notation is used. Waves are denoted by a generic symbol ϕ.

Suppose an incident wave ϕ^{inc}, originated at infinity, propagates towards the scatterers. Upon impinging a scatterer, say Scatterer j, and immediately afterwards, the incident wave is scattered by Scatterer j as if there were no other scatterer present. This scattered wave is called the *first order scattered wave*, or more

specifically, the *first order scattered wave scattered by Scatterer j* to signify the scatterer that causes the scattering. Every scatterer in the host medium generates a first order scattered wave. The excitation source of first order scattering is always the incident wave. The first order scattered wave scattered by Scatterer j is denoted as $\phi_j^{(1)}$.

Figure 4–2 depicts the incident wave and scattering at Scatterer j. The first

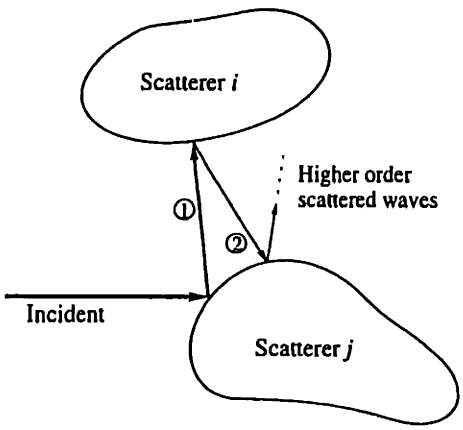

Fig. 4–2 Multiple scattering of a single wave between two scatterers.

order scattered wave $\phi_j^{(1)}$, denoted as wave ①, subsequently impinges a nearby Scatterer i, and then a *second order scattered wave*, denoted as wave ②, is generated. The scattered wave, scattered by Scatterer i with $\phi_j^{(1)}$ as the excitation source, is called the *second order scattered wave*, or more specifically, the *second order scattered wave scattered by Scatterer i due to $\phi_j^{(1)}$*. The second order scattered wave scattered by Scatterer i due to $\phi_j^{(1)}$ is denoted as $\phi^{(2)}_{i \text{ due to } \phi_j^{(1)}}$. This process is *second order scattering*. The term *order* signifies how many times an incident wave has encountered and been scattered by individual scatterers. Table 4–1 summarizes some of the terminologies involved in Fig. 4–2.

In the steady state, all the first order scattered waves, except the one scattered by Scatterer i itself, impinge upon Scatterer i. Figure 4–3 presents a global view of the first two orders of scattering. Therefore, in the steady state, it is possible to

Table 4–1 Summary of Some Terminologies in Fig. 4–2.

Wave	Order	Scattered by	Notation
Incident	—	—	ϕ^{inc}
①	First order	Scatterer j	$\phi_j^{(1)}$
②	Second order	Scatterer i	$\phi^{(2)}_{i \text{ due to } \phi_j^{(1)}}$

sum all the second order waves scattered by Scatterer i as

$$\phi_i^{(2)} = \sum_{\substack{j=1 \\ j\neq i}}^{N} \phi^{(2)}_{i \text{ due to } \phi_j^{(1)}} \tag{4-1}$$

which is called the *(total) second order scattered wave.*

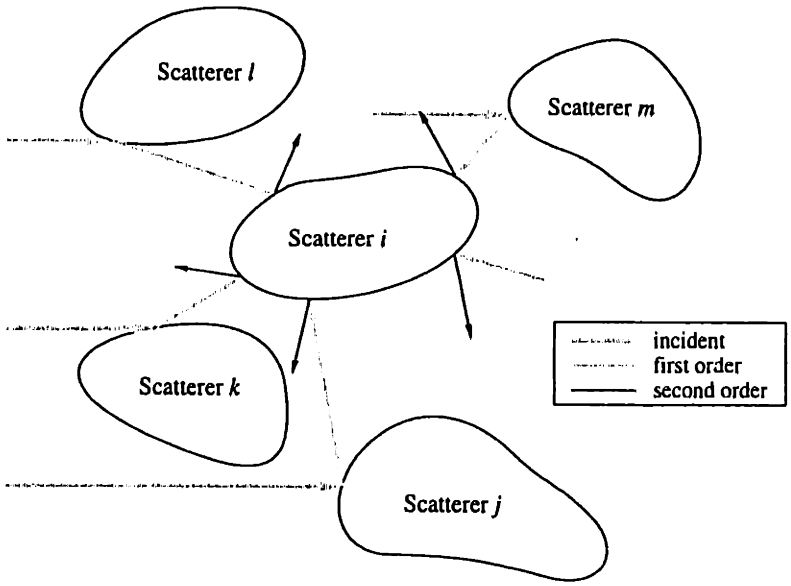

Fig. 4–3 The process of second order scattering. All the first order scattered waves, except the one scattered by Scatterer i itself, impinge onto Scatterer i. Each impinging first order wave generates a partial second order scattered wave.

Higher order scattered waves are generated in the same manner. Specifically, if $\phi_i^{(2)}$ is treated as a single wave, the process depicted in Fig. 4–3 also describes the third order scattering. Generalization to any higher order is straightforward, and the total p-th order scattered wave scattered by Scatterer i can be found as

$$\phi_i^{(p)} = \sum_{\substack{j=1 \\ j\neq i}}^{N} \phi^{(p)}_{i \text{ due to } \phi_j^{(p-1)}} \tag{4-2}$$

The process described above is inherently recursive. Physically, the higher the order of the scattered wave, the smaller the amplitude. Eventually, it dies out as the order becomes higher and higher.

The total wave in the host medium is the sum of the incident wave plus all the orders of the scattered waves;

$$\phi^{\text{total}} = \phi^{\text{inc}} + \sum_{i=1}^{N} \sum_{p=1}^{\infty} \phi_i^{(p)} \tag{4-3}$$

Alternatively, denote

$$\phi_i = \sum_{p=1}^{\infty} \phi_i^{(p)} \tag{4-4}$$

as the *total scattered wave* scattered by Scatterer i. Thus, the total wave in the host medium is

$$\phi^{\text{total}} = \phi^{\text{inc}} + \sum_{i=1}^{N} \phi_i \tag{4-5}$$

It is noted that the process described above is applicable only in the steady state. In a transient state, all the partial waves at all orders are not present in the medium since scattered waves of different orders will not have been generated at an arbitrary time.

4-3 Mathematics of Multiple Scattering—SH Waves

For a two-dimensional SH wave scattering problem, only the out-of-plane displacement w pertains and the governing equation is

$$\nabla^2 w = \frac{1}{c_s^2} \frac{\partial^2 w}{\partial t^2} \tag{4-6}$$

where $c_s = \sqrt{\mu/\rho}$ is the speed of the shear wave in the host medium, and μ and ρ are Lamè constant and the density, respectively, of the host medium. In the steady state, the governing equation becomes the following Helmholtz equation

$$\nabla^2 \phi + k^2 \phi = 0 \tag{4-7}$$

where

$$w = w(x, y, t) = \phi(x, y)\, e^{-i\omega t} \tag{4-8}$$

ω is the circular frequency of the time-harmonic input, k is the wave number $k = \omega/c_s = \omega\sqrt{\rho/\mu}$, i is the unit of imaginary numbers, $i = \sqrt{-1}$, and ϕ is the spatial distribution of the displacement w. Note that ϕ in the above equations is in general a complex quantity called the *complex amplitude* of w. The physical displacement w corresponds to the real part of the product of the spatial factor ϕ and the temporal factor $e^{-i\omega t}$.

As shown in Chapter 2, the general solution for eqn. (4-7) in a polar coordinates is a linear combination of the so-called *cylindrical wave functions*, or the *cylindrical wave expansion basis functions*. Each of the wave expansion basis functions is comprised of a Bessel function of various kinds (including Hankel functions) of order n as the radial factor and the simple harmonic $e^{in\theta}$ as the azimuthal factor, where n is an integer from $-\infty$ to ∞.

Furthermore, the incident wave is expressible, in matrix notation and Scatterer i's local polar coordinate system, as

$$\phi^{\text{inc}} = \{\boldsymbol{A}_i\}^T\{\boldsymbol{J}(r_i,\theta_i)\} \tag{4-9}$$

where $\{\boldsymbol{J}(r_i,\theta_i)\}$ is a column matrix whose n-th row entry ($n = -\infty,\cdots,\infty$) is

$$\{J(r_i,\theta_i)\}_n = J_n(kr_i)\mathrm{e}^{\mathrm{i}n\theta_i} \tag{4-10}$$

and $J_n(\cdot)$ is a Bessel function of the first kind. The matrix $\{\boldsymbol{J}(r_i,\theta_i)\}$ is called the *regular wave expansion basis matrix* of Scatterer i, and $\{\boldsymbol{A}_i\}$ is the wave expansion coefficient matrix of the incident wave. Although the incident wave is the same wave for all scatterers, it is expressed differently in different local coordinate systems.

The notation $\{\boldsymbol{A}_i\}$ does NOT refer to the i-th entry of a column matrix $\{\boldsymbol{A}\}$. Instead, here and henceforth, a bold-faced symbol, along with the appropriate brackets, signifies an entire matrix, such as $\{\boldsymbol{A}\}$. A subscript within the brackets is a modifier to the entire matrix. For this particular case, the subscript i signifies that the quantity belongs to Scatterer i. For clarity, the following conventions are adopted: A column matrix is always enclosed by a pair of curl brackets, and a rectangular/square matrix is enclosed by square brackets. When a specific matrix entry is referred to, it is denoted by the unbold-faced corresponding symbol, along with the accompanying super-/sub- scripts, if any, and the brackets, and the indicial number for the entry is placed *outside* the right bracket. For example, $\{A_i\}_n$ is the n-th entry (the entry at the n-th row) of column matrix $\{\boldsymbol{A}_i\}$.

4-3.1 Waves At Various Orders

First Order Waves

From the description of the physical process in the previous section, it is recognized that the first order scattered waves are the same as the scattered waves in the corresponding single-scatterer problem for each scatterer.

In a single-scatterer problem, for any incident wave, the scattered wave can be found from the T-matrix of the scatterer. According to the definition of the T-matrix in Chapter 3, the scattered wave is expressed in a singular wave expansion basis. For Scatterer i, the *singular wave expansion basis matrix* is denoted as $\{\boldsymbol{H}(r_i,\theta_i)\}$ whose n-th row entry is

$$\{H(r_i,\theta_i)\}_n = H_n^{(1)}(kr_i)\mathrm{e}^{\mathrm{i}n\theta_i} \tag{4-11}$$

where $H_n^{(1)}(\cdot)$ is a Hankel function of the first kind.

Denote the first order scattered wave scattered by Scatterer i as

$$\phi_i^{(1)} = \{\boldsymbol{C}_i^{(1)}\}^T\{\boldsymbol{H}(r_i,\theta_i)\} \tag{4-12}$$

Then, the T-matrix for Scatterer i gives

$$\{\boldsymbol{C}_i^{(1)}\} = [\boldsymbol{T}_i]\{\boldsymbol{A}_i\} \tag{4-13}$$

Second Order Waves

Without loss of generality, consider first the expression for $\phi^{(2)}_{j \text{ due to } \phi_i^{(1)}}$, the second order scattered wave scattered by Scatterer j due to $\phi_i^{(1)}$.

In general, as discussed in Chapter 2, an outgoing scattered wave is expressible in the singular wave expansion basis. Thus it can be assumed that

$$\phi^{(2)}_{j \text{ due to } \phi_i^{(1)}} = \{\boldsymbol{C}_{ji}^{(2)}\}^T \{\boldsymbol{H}(r_j, \theta_j)\} \tag{4-14}$$

Then, the *total* second order wave scattered by Scatterer j can be expressed as, according to eqn. (4–1),

$$\phi_j^{(2)} = \sum_{\substack{i=1 \\ i \neq j}}^{N} \left(\{\boldsymbol{C}_{ji}^{(2)}\}^T \{\boldsymbol{H}(r_j, \theta_j)\} \right) = \{\boldsymbol{C}_j^{(2)}\}^T \{\boldsymbol{H}(r_j, \theta_j)\} \tag{4-15}$$

where

$$\{\boldsymbol{C}_j^{(2)}\} = \sum_{\substack{i=1 \\ i \neq j}}^{N} \{\boldsymbol{C}_{ji}^{(2)}\} \tag{4-16}$$

Recall that in the single-scatterer case, a scattered wave is the *effect* that is *caused* by an incident wave, and this causality is embodied in the T-matrix. For a linear time-invariant system, a causality such as the T-matrix is a characteristic of the system. It specifies an incident wave expressed in the regular wave expansion basis as the "cause," and the corresponding scattered wave expressed in the singular wave expansion basis as the "effect." The generation of $\phi^{(2)}_{j \text{ due to } \phi_i^{(1)}}$ can be rephrased in light of such a "cause–effect" relation: $\phi^{(2)}_{j \text{ due to } \phi_i^{(1)}}$ is the "effect", due to the impingement of the "cause" $\phi_i^{(1)}$, and this "cause–effect" relation is described by Scatterer j's T-matrix $[\boldsymbol{T}_j]$.

In a causal relation such as eqn. (4–13), both "cause" and "effect" waves are expressed in the same coordinate system that is local to the scatterer to which the T-matrix belongs. This necessitates a coordinate transformation in order to express $\phi_i^{(1)}$ in eqn. (4–13) in terms of Scatterer j's local polar coordinates (r_j, θ_j).

Recall *Graf's addition theorem* of Bessel and Hankel functions[1] as

$$H_n^{(1)}(\varpi) \begin{matrix} \cos \\ \sin \end{matrix} n\beta = \sum_{m=-\infty}^{\infty} H_{n+m}^{(1)}(Z) J_m(z) \begin{matrix} \cos \\ \sin \end{matrix} m\alpha \tag{4-17}$$

and

$$J_n(\varpi) \begin{matrix} \cos \\ \sin \end{matrix} n\beta = \sum_{m=-\infty}^{\infty} J_{n+m}(Z) J_m(z) \begin{matrix} \cos \\ \sin \end{matrix} m\alpha \tag{4-18}$$

where both n and m are integers. Equation (4–17) is valid only when $|Z| > |ze^{\pm i\alpha}|$; whereas eqn. (4–18) is valid throughout the plane. When Z, z and ϖ are real and positive, the geometric relations of the parameters are as sketched in Fig. 4–4.

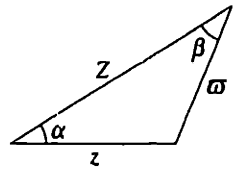

Fig. 4–4 Geometries of Graf's addition theorem.

Typical geometrical relations between two local coordinate systems are sketched in Fig. 4–5. An arbitrary field point P can be located by either (r_i, θ_i) or (r_j, θ_j), and (d_{ij}, θ_{ij}) is the location of o_j with respect to the coordinate system originating at o_i, and (d_{ji}, θ_{ji}) is the location of o_i with respect to the coordinate system originating at o_j. From Fig. 4–5,

$$d_{ij} = d_{ji} \qquad \text{and} \qquad \theta_{ij} = \pi + \theta_{ji} \tag{4-19}$$

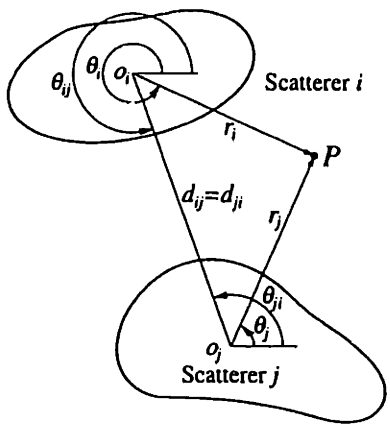

Fig. 4–5 Geometry for Graf's addition theorem adapted for a multiple-scattering problem setting.

Comparing the geometries in Figs. 4–4 and 4–5, after the following parameter substitutions

$$z \to r_j, \qquad \varpi \to r_i, \qquad Z \to d_{ji}, \qquad \alpha \to \theta_{ji} - \theta_j \qquad \text{and} \qquad \beta \to \theta_i - \theta_{ij},$$

eqn. (4–17) can be written as

$$H_n^{(1)}(r_i) \begin{matrix}\cos \\ \sin\end{matrix} n(\theta_i - \theta_{ij}) = \sum_{m=-\infty}^{\infty} H_{n+m}^{(1)}(d_{ji}) J_m(r_j) \begin{matrix}\cos \\ \sin\end{matrix} m(\theta_{ji} - \theta_j) \tag{4-20}$$

Or, in a more compact form using complex notations,

$$H_n^{(1)}(r_i) e^{in(\theta_i - \theta_{ij})} = \sum_{m=-\infty}^{\infty} H_{n+m}^{(1)}(d_{ji}) J_m(r_j) e^{im(\theta_{ji} - \theta_j)} \tag{4-21}$$

With some rearrangement, it can be further reduce to

$$H_n^{(1)}(r_i) e^{in\theta_i} = \sum_{m=-\infty}^{\infty} e^{i(n-m)\theta_{ij}} H_{n-m}^{(1)}(d_{ij}) J_m(r_j) e^{im\theta_j} \tag{4-22}$$

where the following relation of Bessel functions[2]

$$J_{-m}(r_j) = (-1)^m J_m(r_j) = e^{\pm i m\pi} J_m(r_j) \tag{4-23}$$

and the relation between θ_{ij} and θ_{ji} in eqns. (4–19) have been used. By a similar procedure, eqn. (4–18) can be reduced to

$$J_n(r_i)e^{in\theta_i} = \sum_{m=-\infty}^{\infty} e^{i(n-m)\theta_{ij}} J_{n-m}(d_{ij}) J_m(r_j) e^{im\theta_j} \tag{4-24}$$

Using the matrix notation, eqns. (4–22) and (4–24) can be rewritten as

$$\{\boldsymbol{H}(r_i,\theta_i)\} = [\boldsymbol{R}_{ij}]\{\boldsymbol{J}(r_j,\theta_j)\} \tag{4-25}$$

$$\{\boldsymbol{J}(r_i,\theta_i)\} = [\Re\boldsymbol{R}_{ij}]\{\boldsymbol{J}(r_j,\theta_j)\} \tag{4-26}$$

where the entries of matrices $[\boldsymbol{R}_{ij}]$ and $[\Re\boldsymbol{R}_{ij}]$ at the n-th row and the m-th column are

$$[R_{ij}]_{nm} = e^{i(n-m)\theta_{ij}} H^{(1)}_{n-m}(kd_{ij}) \tag{4-27}$$

$$[\Re R_{ij}]_{nm} = e^{i(n-m)\theta_{ij}} J_{n-m}(kd_{ij}) \tag{4-28}$$

and both n and m range from $-\infty$ to ∞. In writing eqns. (4–25) and (4–26), arguments for Bessel and Hankel functions have been scaled by a factor k, and the validity condition for eqn. (4–25) is $d_{ij} > r_j$. Matrices $[\boldsymbol{R}_{ij}]$ and $[\Re\boldsymbol{R}_{ij}]$ are called the singular and regular *coordinate translation matrices*, respectively.

One useful property of $[\Re\boldsymbol{R}_{ij}]$ can be obtained from the general validity of the eqn. (4–26). By switching the subscripts i and j, eqn. (4–26) can be written as

$$\{\boldsymbol{J}(r_j,\theta_j)\} = [\Re\boldsymbol{R}_{ji}]\{\boldsymbol{J}(r_i,\theta_i)\} \tag{4-29}$$

Replacing $\{\boldsymbol{J}(r_i,\theta_i)\}$ on the right-hand side of eqn. (4–29) by the right-hand side of eqn. (4–26) leads to

$$\{\boldsymbol{J}(r_j,\theta_j)\} = [\Re\boldsymbol{R}_{ji}][\Re\boldsymbol{R}_{ij}]\{\boldsymbol{J}(r_j,\theta_j)\} \tag{4-30}$$

which implies

$$[\Re\boldsymbol{R}_{ji}][\Re\boldsymbol{R}_{ij}] = [\boldsymbol{I}] \qquad \text{or} \qquad [\Re\boldsymbol{R}_{ji}] = [\Re\boldsymbol{R}_{ij}]^{-1} \tag{4-31}$$

where $[\boldsymbol{I}]$ is the identity matrix. It can be further verified that eqn. (4–31) is a special case of the following *Neumann's addition theorem*[2]

$$J_p(x-y) = \sum_{q=-\infty}^{\infty} J_{p+q}(x) J_q(y) \tag{4-32}$$

where x and y are any real numbers, and p and q are integers. Equations (4–31) and (4–32) become identical for the special case when $x = y = kd_{ij}$, and θ_{ij} is immaterial in such a special case.

With Graf's addition theorem, waves emanating from Scatterer i can be expressed in terms of Scatterer j's local coordinates. Specifically, substituting

eqn. (4–25) into eqn. (4–12) gives

$$\phi_i^{(1)} = \{C_i^{(1)}\}^T [R_{ij}]\{J(r_j, \theta_j)\} \tag{4–33}$$

Note that the "cause" wave as expressed in eqn. (4–33) is in terms of the regular wave expansion basis, while the "effect" wave in eqn. (4–14) is in terms of the singular wave expansion basis, and both are expressed in Scatterer j's local polar coordinate system. These expressions now conform to the causality embodied in $[T_j]$, the T-matrix of Scatterer j where the scattering occurs. Thus,

$$\{C_{ji}^{(2)}\} = [T_j][R_{ij}]^T\{C_i^{(1)}\} = [T_j][R_{ij}]^T[T_i]\{A_i\} \tag{4–34}$$

where eqn. (4–13) has been used.

Denote

$$[L_{ij}] = [T_j][R_{ij}]^T \tag{4–35}$$

and call it the *inductance matrix* of Scatterer j on Scatterer i, eqn. (4–34) can be further written as

$$\{C_{ji}^{(2)}\} = [L_{ij}]\{C_i^{(1)}\} = [L_{ij}][T_i]\{A_i\} \tag{4–36}$$

Next, recall that the incident wave is expressed differently in different local coordinate systems, *i.e.*,

$$\phi^{\text{inc}} = \{A_i\}^T\{J(r_i, \theta_i)\} = \{A_j\}^T\{J(r_j, \theta_j)\} \tag{4–37}$$

and since $\{J(r_j, \theta_j)\}$ can be transformed into $\{J(r_i, \theta_i)\}$ via Graf's addition theorem in eqn. (4–29), the incident wave can also be written as

$$\phi^{\text{inc}} = \{A_j\}^T[\Re R_{ji}]\{J(r_i, \theta_i)\} \tag{4–38}$$

Comparing eqns. (4–37) and (4–38) gives

$$\{A_i\} = [\Re R_{ji}]^T\{A_j\} \tag{4–39}$$

Substituting eqn. (4–39) into eqn. (4–36) gives

$$\{C_{ji}^{(2)}\} = [L_{ij}]\{C_i^{(1)}\} = [L_{ij}][T_i][\Re R_{ji}]^T\{A_j\} \tag{4–40}$$

Therefore, from eqn. (4–16), the coefficient matrix for the total second order scattered wave scattered by Scatterer j can be written as

$$\{C_j^{(2)}\} = \sum_{\substack{i=1 \\ i\neq j}}^{N}[L_{ij}]\{C_i^{(1)}\} = \sum_{\substack{i=1 \\ i\neq j}}^{N}[L_{ij}][T_i][\Re R_{ji}]^T\{A_j\} \tag{4–41}$$

Denote

$$[K_j^{(2)}] = \sum_{\substack{i=1 \\ i\neq j}}^{N}[L_{ij}][T_i][\Re R_{ji}]^T \tag{4–42}$$

then,

$$\{C_j^{(2)}\} = [K_j^{(2)}]\{A_j\} \tag{4–43}$$

and $[\boldsymbol{K}_j^{(2)}]$ is called the *second order multiple-scattering kernel matrix* of Scatterer j.

Third Order Waves

From the inherent recursive nature of the multiple scattering process, it is expected that the solution for a multiple-scatterer problem is also recursive. This is indeed true, as it can be seen by proceeding to derive the expressions for higher order waves in the same manner. In fact, the expressions for the third order waves have already shown clearly such a recursive structure. As the process is the same as for the second order waves, the derivation is opted to be brief.

Denote the third order scattered wave scattered by Scatterer j due to $\phi_i^{(2)}$ as

$$\phi^{(3)}_{j \text{ due to } \phi_i^{(2)}} = \{\boldsymbol{C}_{ji}^{(3)}\}^T \{\boldsymbol{H}(r_j, \theta_j)\} \tag{4-44}$$

and $\phi_i^{(2)}$ can be obtained simply by changing the subscript from j to i in eqn. (4–15) and then being re-expressed in Scatterer j's local coordinate system via a coordinate transformation of eqn. (4–25) as

$$\phi_i^{(2)} = \{\boldsymbol{C}_i^{(2)}\}^T \{\boldsymbol{J}(r_i, \theta_i)\} = \{\boldsymbol{C}_i^{(2)}\}^T [\boldsymbol{R}_{ij}] \{\boldsymbol{J}(r_j, \theta_j)\} \tag{4-45}$$

Using the T-matrix relation of Scatterer j gives

$$\{\boldsymbol{C}_{ji}^{(3)}\} = [\boldsymbol{T}_j] \left\{ \{\boldsymbol{C}_i^{(2)}\}^T [\boldsymbol{R}_{ij}] \right\}^T = [\boldsymbol{T}_j][\boldsymbol{R}_{ij}]^T \{\boldsymbol{C}_i^{(2)}\} = [\boldsymbol{L}_{ij}] \{\boldsymbol{C}_i^{(2)}\} \tag{4-46}$$

where eqn. (4–35) has been used. Writing eqn. (4–43) for Scatterer i, and substituting the resulting expression for $\{\boldsymbol{C}_i^{(2)}\}$ into eqn. (4–46) gives

$$\{\boldsymbol{C}_{ji}^{(3)}\} = [\boldsymbol{L}_{ij}] \{\boldsymbol{C}_i^{(2)}\} = [\boldsymbol{L}_{ij}][\boldsymbol{K}_i^{(2)}] \{\boldsymbol{A}_i\} = [\boldsymbol{L}_{ij}][\boldsymbol{K}_i^{(2)}][\Re \boldsymbol{R}_{ji}]^T \{\boldsymbol{A}_j\} \tag{4-47}$$

where eqn. (4–39) has been used.

Sum all the third order partial waves emanating from Scatterer j, and denote

$$\phi_j^{(3)} = \{\boldsymbol{C}_j^{(3)}\} \{\boldsymbol{H}(r_j, \theta_j)\} \tag{4-48}$$

then,

$$\{\boldsymbol{C}_j^{(3)}\} = \sum_{\substack{i=1 \\ i \neq j}}^{N} [\boldsymbol{L}_{ij}] \{\boldsymbol{C}_i^{(2)}\} = [\boldsymbol{K}_j^{(3)}] \{\boldsymbol{A}_j\} \tag{4-49}$$

where

$$[\boldsymbol{K}_j^{(3)}] = \sum_{\substack{i=1 \\ i \neq j}}^{N} [\boldsymbol{L}_{ij}][\boldsymbol{K}_i^{(2)}][\Re \boldsymbol{R}_{ji}]^T \tag{4-50}$$

and $[\boldsymbol{K}_j^{(3)}]$ is the *third order multiple-scattering kernel matrix* of Scatterer j.

General p-th Order Waves

Assume the $(p-1)$-st order $(p>1)$ waves scattered by every scatterer has been found, and denote the total p-th order wave scattered by Scatterer j as

$$\phi_j^{(p)} = \{C_j^{(p)}\}^T \{H(r_j, \theta_j)\} \tag{4-51}$$

Then, it can be shown that

$$\{C_j^{(p)}\} = \sum_{\substack{i=1 \\ i \neq j}}^{N} [L_{ij}]\{C_i^{(p-1)}\} = [K_j^{(p)}]\{A_j\} \tag{4-52}$$

where

$$[K_j^{(p)}] = \sum_{\substack{i=1 \\ i \neq j}}^{N} [L_{ij}][K_i^{(p-1)}][\Re R_{ji}]^T \tag{4-53}$$

and $[K_j^{(p)}]$ is the p-th order multiple-scattering kernel matrix of Scatterer j.

4-3.2 Solution Structures

In this subsection, expressions obtained thus far are collected and summarized into several compact and self-contained forms, and their comparative advantages and disadvantages are observed. The following solution structures are self-contained except the following common definitions: the singular wave expansion basis $\{H(r_i, \theta_i)\}$ defined in eqn. (4-11), the inductance matrix $[L_{ij}]$ defined in eqn. (4-35), and the coordinate translation matrices $[R_{ij}]$ and $[\Re R_{ij}]$ defined in eqns. (4-27) and (4-28), respectively. The T-matrix of each scatterer is assumed to be known externally.

Recursive Form I

Observing the first equalities in eqns. (4-41), (4-49) and (4-52), the following simple recursive form for the wave expansion coefficient matrices of the total p-th order scattered wave scattered by Scatterer j $(j = 1, 2, \cdots, N)$ can be obtained

$$\{C_j^{(p)}\} = \sum_{\substack{i=1 \\ i \neq j}}^{N} [L_{ij}]\{C_i^{(p-1)}\} \tag{4-54}$$

with the initialization condition

$$\{C_j^{(1)}\} = [T_j]\{A_j\} \tag{4-55}$$

Collecting eqns. (4-15), (4-48) and (4-51), the total wave in the host medium, according to eqn. (4-3), is

$$\phi^{\text{total}} = \phi^{\text{inc}} + \sum_{j=1}^{N} \sum_{p=1}^{\infty} \{C_j^{(p)}\}\{H(r_j, \theta_j)\} \tag{4-56}$$

This form of the formal solution is the simplest and most straightforward. But the shortcoming is that the solution obtained is particularized to a specific incident wave, *i.e.*, a particular set of $\{\boldsymbol{A}_j\}$.

Recursive Form II

Observing eqn. (4–43) and the last equalities in eqns. (4–49) and (4–52), the following recursive relation for Scatterer j's multiple-scattering kernel becomes obvious

$$[\boldsymbol{K}_j^{(p)}] = \sum_{\substack{i=1 \\ i\neq j}}^{N} [\boldsymbol{L}_{ij}][\boldsymbol{K}_i^{(p-1)}][\Re \boldsymbol{R}_{ji}]^T \qquad (\text{for } p > 1) \tag{4–57}$$

with the following initialization condition

$$[\boldsymbol{K}_j^{(1)}] = [\boldsymbol{T}_j] \tag{4–58}$$

The total wave in the host medium, according to eqn. (4–5), is

$$\phi^{\text{total}} = \phi^{\text{inc}} + \sum_{j=1}^{N} \phi_j, \tag{4–59}$$

where

$$\phi_j = \sum_{p=1}^{\infty} \phi_j^{(p)} = \{\boldsymbol{C}_j\}^T \{\boldsymbol{H}(r_j, \theta_j)\} \tag{4–60}$$

$$\{\boldsymbol{C}_j\} = [\boldsymbol{K}_j]\{\boldsymbol{A}_j\} \tag{4–61}$$

$$[\boldsymbol{K}_j] = \sum_{p=1}^{\infty} [\boldsymbol{K}_j^{(p)}] \tag{4–62}$$

$[\boldsymbol{K}_j]$ is called the *multiple-scattering kernel matrix*[1] of Scatterer j, and $\{\boldsymbol{C}_j\}$ is the wave expansion coefficient matrix of the total scattered wave scattered by Scatterer j.

Equations (4–58), (4–57) and (4–62) comprise the complete solution for the multiple-scattering kernel matrices. For a given incident wave, eqns. (4–59) through (4–61) complement to complete the solution.

In this solution form, the process of finding each scatterer's multiple-scattering kernel matrix does not require any knowledge of the incident wave. The incident wave is involved only when the scattered waves are to be calculated for a particular incident wave. In fact, these scattering kernel matrices characterize the multiple-scatterer system, just as the T-matrix characterizes a single-scatterer system. Once these matrices have been obtained, the system's response to any incident wave can be readily found by using eqns. (4–59) through (4–61).

[1] It is sometimes called the *multiple scattering T-matrix* of Scatterer i in observing the form of eqn. (4–61). However, to avoid possible confusion with another system characteristic matrix called *T-matrix for an assembly of scatterer*, to be introduced in Chapter 5, this name is avoided.

Implicit Form I

Denote

$$\{C_j\}^{(p)} = \sum_{q=1}^{p} \{C_j^{(q)}\} \tag{4-63}$$

where, as part of the notational convention in this thesis, the superscript (p) appearing *outside* the brackets on the left-hand side of eqn. (4–63) represents the partial sum of all the first p orders of the scattered waves; whereas the superscript (q) appearing *inside* the brackets on the right-hand side of eqn. (4–63) represents the q-th order scattered wave.

Making an exhaustive listing of all the first p orders of the scattered waves found via Recursive Form I gives

$$\begin{aligned}
\{C_j^{(p)}\} &= \sum_{\substack{i=1 \\ i\neq j}}^{N} [L_{ij}]\{C_i^{(p-1)}\} \\
\{C_j^{(p-1)}\} &= \sum_{\substack{i=1 \\ i\neq j}}^{N} [L_{ij}]\{C_i^{(p-2)}\} \\
\{C_j^{(p-2)}\} &= \sum_{\substack{i=1 \\ i\neq j}}^{N} [L_{ij}]\{C_i^{(p-3)}\} \\
&\vdots \\
\{C_j^{(1)}\} &= [T_j]\{A_j\}
\end{aligned} \tag{4-64}$$

Summing up each side of the above equations respectively gives

$$\{C_j\}^{(p)} = [T_j]\{A_j\} + \sum_{\substack{i=1 \\ i\neq j}}^{N} [L_{ij}]\{C_i\}^{(p-1)} \tag{4-65}$$

where eqn. (4–63) has been used.

Since the solution is to converge in theory; that is,

$$\lim_{p\to\infty} \{C_j\}^{(p)} = \lim_{p\to\infty} \{C_j\}^{(p-1)} = \{C_j\} \tag{4-66}$$

eqn. (4–65) effectively represents the following implicit equation system

$$\{C_j\} = [T_j]\{A_j\} + \sum_{\substack{i=1 \\ i\neq j}}^{N} [L_{ij}]\{C_i\} \tag{4-67}$$

and the total wave in the host medium, according to eqn. (4–5), is

$$\phi^{\text{total}} = \phi^{\text{inc}} + \sum_{j=1}^{N} \{C_j\}^T \{H(r_j, \theta_j)\} \tag{4-68}$$

It is noted that eqn. (4-65) can be viewed as an iterative solution procedure of prediction-correction type for eqn. (4-67).

In an iterative procedure, the choice for the *initialization condition*, which is also called the *initial guessed solution*, does not necessary conform with eqn. (4-64). In many cases, this extra freedom allows a better choice of initialization condition to achieve a converged solution in fewer iteration steps. When eqn. (4-64) is used as the initialization condition, the p-th approximation gives the partial sum of the first p orders of the scattered waves. However, when the chosen initialization condition is different from eqn. (4-64), the intermediate solution $\{\boldsymbol{C}_j\}^{(p)}$ no longer possess any physical meaning other than being an approximate solution.

When eqn. (4-65) is viewed as an iterative procedure for eqn. (4-67), and compared with eqn. (4-63), it noted that the meanings of the superscript (p) in eqn. (4-63) appearing *outside* the brackets are two-fold: the first is, as in eqn. (4-63), the partial sum of the first p orders of the scattered waves; and the second is, as in eqn. (4-65), the approximate solution at the p-th iteration.

It must also be noted that the words "recursive" and "iterative" are used for completely different meanings in this thesis: in a recursive process, the solution obtained in each step is a portion of the total solution; whereas in an iterative process, the solution obtained in each step is an approximation of the total solution.

Implicit Form II

Applying a similar procedure to the Recursive Form II gives the following implicit form for the multiple scattering kernel matrices

$$[\boldsymbol{K}_j] = [\boldsymbol{T}_j] + \sum_{\substack{i=1 \\ i\neq j}}^{N} [\boldsymbol{L}_{ij}][\boldsymbol{K}_i][\Re \boldsymbol{R}_{ji}]^T \tag{4-69}$$

and the following associated iterative solution procedure

$$[\boldsymbol{K}_j]^{(p)} = [\boldsymbol{T}_j] + \sum_{\substack{i=1 \\ i\neq j}}^{N} [\boldsymbol{L}_{ij}][\boldsymbol{K}_i]^{(p-1)}[\Re \boldsymbol{R}_{ji}]^T \tag{4-70}$$

For a given incident wave, the total wave in the host medium is, according to eqn. (4-5),

$$\phi^{\text{total}} = \phi^{\text{inc}} + \sum_{j=1}^{N} \{\boldsymbol{C}_j\}^T \{\boldsymbol{H}(r_j, \theta_j)\} \tag{4-71}$$

with

$$\{\boldsymbol{C}_j\} = [\boldsymbol{K}_j]\{\boldsymbol{A}_j\} \tag{4-72}$$

The advantage of this form is the extra freedom to choose the initialization solution, and that the solution is characteristic of the system which does not depend on the particularity of the incident wave.

Supermatrix Form

Define the following supermatrices:

$$\{\mathcal{C}\} = \begin{Bmatrix} \{C_1\} \\ \{C_2\} \\ \vdots \\ \{C_N\} \end{Bmatrix} \qquad \{\mathcal{A}\} = \begin{Bmatrix} [T_1]\{A_1\} \\ [T_2]\{A_2\} \\ \vdots \\ [T_N]\{A_N\} \end{Bmatrix} \tag{4-73}$$

$$[\mathcal{L}] = \begin{bmatrix} \mathbf{0} & [L_{21}] & \cdots & [L_{N1}] \\ [L_{12}] & \mathbf{0} & \cdots & [L_{N2}] \\ \cdots & \cdots & \cdots & \cdots \\ [L_{1N}] & \cdots & [L_{(N-1)N}] & \mathbf{0} \end{bmatrix} \tag{4-74}$$

Then, Implicit Form I can be equivalently written as

$$\{\mathcal{C}\} = \{\mathcal{A}\} + [\mathcal{L}]\{\mathcal{C}\} \tag{4-75}$$

or

$$[\mathcal{I} - \mathcal{L}]\{\mathcal{C}\} = \{\mathcal{A}\} \tag{4-76}$$

where $[\mathcal{I}]$ is the identity supermatrix. Equation (4–76) is a typical linear equation system.

The advantage of this form is that there are numerous well-established solution procedures and even computer program readily available for solving the linear equation system, which has been subjected to an extremely extensive study in the past few decades.

It is noted that none of the of the repetitive forms, either recursive of iterative, of the solution has been shown to have a guaranteed convergence. In such cases, the computation process has to be monitored closely. This Supermatrix Form can be directly solved thus avoids such problems in one hand, But on the hand, the solution obtained must be subjected to a further scrutiny in case the linear equation system is ill-conditioned.

Finally, it is noted that it is also possible to obtain a similar supermatrix form for *Implicit Form II*. However this case is not to be elaborated in this chapter.

4-3.3 Strains and Stresses

Since the out-of-plane w is the only non-vanishing displacement component, only the components of the shear strain and shear stress involving the z-coordinate exist. Furthermore, they are simply the sums of respective contributions from all waves in the medium. Without loss of generality, eqns. (4–59) and (4–60) can be used as the final form of the solution for ϕ^{total}. In eqn. (4–59), the total wave can be viewed as the incident wave plus N scattered waves, one emanating from each scatterer.

For the incident wave, in general, its expression in the global coordinate system is known, and its contribution to the strains can be readily obtained from the geometry relation as

$$\gamma_{xz}^{\text{inc}} = \gamma_{zx}^{\text{inc}} = \frac{\partial \phi^{\text{inc}}}{\partial x} \qquad \gamma_{yz}^{\text{inc}} = \gamma_{zy}^{\text{inc}} = \frac{\partial \phi^{\text{inc}}}{\partial y} \tag{4-77}$$

where γ^{inc}'s are the complex amplitudes of shear strain components contributed by the incident wave. All other strain components vanish.

For the scattered wave emanating from each scatterer, since it is much easier to express strains as polar components in each local coordinate system, the procedure taken here is to express the contributions from each scatterer in polar components in its own local polar coordinate system, and then transform them into the global Cartesian coordinate system. The coordinate transformations between a polar and a Cartesian coordinate systems for displacements, strains and stresses are given in Appendix 4-A.

Expressions for strain components for a point (x, y) in the global Cartesian coordinate system can thus be found as

$$\gamma_{xz} = \gamma_{zx} = \frac{\partial \phi^{\text{inc}}}{\partial x} + \sum_{i=1}^{N} (\gamma_{i r_i z} \cos\theta_i - \gamma_{i \theta_i z} \sin\theta_i) \tag{4-78}$$

$$\gamma_{yz} = \gamma_{zy} = \frac{\partial \phi^{\text{inc}}}{\partial y} + \sum_{i=1}^{N} (\gamma_{i r_i z} \sin\theta_i + \gamma_{i \theta_i z} \cos\theta_i) \tag{4-79}$$

where

$$\gamma_{i r_i z} = \frac{\partial \phi_i}{\partial r_i} \qquad \gamma_{i \theta_i z} = \frac{1}{r_i} \frac{\partial \phi_i}{\partial \theta_i} \tag{4-80}$$

are the complex amplitudes of respective shear strain components contributed by the scattered wave emanating from Scatterer i.

The local polar coordinates (r_i, θ_i) are related to the global Cartesian coordinates (x, y) by the following relations

$$x = X_i + r_i \cos\theta_i \qquad y = Y_i + r_i \sin\theta_i \tag{4-81}$$

and

$$r_i = \sqrt{(x - X_i)^2 + (y - Y_i)^2} \tag{4-82}$$

$$\theta_i = \begin{cases} \tan^{-1} \dfrac{y - Y_i}{x - X_i} & \text{for} \quad y > Y_i \text{ and } x \neq X_i \\ \pi + \tan^{-1} \dfrac{y - Y_i}{x - X_i} & \text{for} \quad y < Y_i \text{ and } x \neq X_i \\ \pi/2 & \text{for} \quad y > Y_i \text{ and } x = X_i \\ -\pi/2 & \text{for} \quad y < Y_i \text{ and } x = X_i \end{cases} \tag{4-83}$$

Introduce two column matrices $\{\boldsymbol{H}_r(r_i, \theta_i)\}$ and $\{\boldsymbol{H}_\theta(r_i, \theta_i)\}$, called *singular differential wave expansion bases*, whose entries at the n-th row are

$$\{H_r(r_i, \theta_i)\}_n = \frac{\partial \{H(r_i, \theta_i)\}_n}{\partial r_i} = k H_n'(k r_i) e^{\hat{\imath} n \theta_i} \tag{4-84}$$

$$\{H_\theta(r_i,\theta_i)\}_n = \frac{1}{r_i}\frac{\partial\{H(r_i,\theta_i)\}_n}{\partial\theta_i} = \frac{\hat{\imath}n}{r_i}H_n(kr_i)\mathrm{e}^{\hat{\imath}n\theta_i} \tag{4-85}$$

respectively. Then, eqn. (4–80) can be written as

$$\gamma_{ir_iz} = \{\boldsymbol{C}_i\}^T\{\boldsymbol{H}_r(r_i,\theta_i)\} \qquad \gamma_{i\theta_iz} = \{\boldsymbol{C}_i\}^T\{\boldsymbol{H}_\theta(r_i,\theta_i)\} \tag{4-86}$$

where eqn. (4–60) has been used.

Therefore, the expressions for the strains in the global Cartesian coordinate system are, from eqns. (4–78) and (4–79),

$$\gamma_{xz} = \gamma_{zx} = \frac{\partial\phi^{\text{inc}}}{\partial x} + \sum_{i=1}^{N}\{\boldsymbol{C}_i\}^T\left[\{\boldsymbol{H}_r(r_i,\theta_i)\}\cos\theta_i - \{\boldsymbol{H}_\theta(r_i,\theta_i)\}\sin\theta_i\right] \tag{4-87}$$

$$\gamma_{yz} = \gamma_{zy} = \frac{\partial\phi^{\text{inc}}}{\partial y} + \sum_{i=1}^{N}\{\boldsymbol{C}_i\}^T\left[\{\boldsymbol{H}_r(r_i,\theta_i)\}\sin\theta_i + \{\boldsymbol{H}_\theta(r_i,\theta_i)\}\cos\theta_i\right] \tag{4-88}$$

In the event that a global *polar* coordinate system, whose coordinates are referred to as (r,θ), has also been built such that $\theta = 0$ corresponds to the $+X$ direction and it shares the same origin as the global Cartesian coordinate system, and the strains in this coordinate system are desired, it can be found that, for a generic point (r,θ) in the global polar coordinate system,

$$\gamma_{rz} = \frac{\partial\phi^{\text{inc}}}{\partial r} + \sum_{i=1}^{N}\{\boldsymbol{C}_i\}^T\left[\{\boldsymbol{H}_r(r_i,\theta_i)\}\cos(\theta_i-\theta) - \{\boldsymbol{H}_\theta(r_i,\theta_i)\}\sin(\theta_i-\theta)\right] \tag{4-89}$$

$$\gamma_{\theta z} = \frac{\partial\phi^{\text{inc}}}{r\partial\theta} + \sum_{i=1}^{N}\{\boldsymbol{C}_i\}^T\left[\{\boldsymbol{H}_r(r_i,\theta_i)\}\sin(\theta_i-\theta) + \{\boldsymbol{H}_\theta(r_i,\theta_i)\}\cos(\theta_i-\theta)\right] \tag{4-90}$$

where the global polar coordinates (r,θ) are related to the global Cartesian coordinates (x,y) by

$$x = r\cos\theta \qquad y = r\sin\theta \tag{4-91}$$

which can be further related to the local coordinates (r_i,θ_i) by eqns. (4–81) through (4–83).

Finally, the calculation of the stress components has become trivial since

$$\sigma_{xz} = \mu\gamma_{xz} \qquad \sigma_{yz} = \mu\gamma_{yz} \tag{4-92}$$

and

$$\sigma_{rz} = \mu\gamma_{rz} \qquad \sigma_{\theta z} = \mu\gamma_{\theta z} \tag{4-93}$$

All other stress components vanish.

4-3.4 Discussions

Boundary Conditions

It is well known that a steady-state scattering problem in an infinite domain is a *boundary-value problem* for the governing partial differential equation(s). However, no boundary condition has ever been mentioned in the above exposition of the multiple-scattering solution. What happened to the boundary conditions?

In a strict sense, an application of a T-matrix relation is a process of applying the appropriate boundary condition(s), although this is not so obvious in the derivation process.

Recall that $[\boldsymbol{T}_i]$ matrix is obtained by applying the boundary condition(s) at the perimeter of Scatterer i and solving the associated single-scatterer problem. Examples of such processes are shown in Chapter 2. In the solution for a multiple-scatterer problem, at any order p, Graf's addition theorem is used to transform the wave emanating from Scatterer j, $\phi_j^{(p)}$, into Scatterer i's local coordinate system. The T-matrix relation for Scatterer i is then applied to obtain the wave expansion coefficient matrix of the resulting scattered wave. This effectively applies the boundary condition(s) at the perimeter of Scatterer i.

This is to say, as soon as the T-matrix is known, the boundary conditions have been taken care of. In fact, the disappearance of explicitly fixing the boundary conditions in the solution process is considered as one of the greatest advantages of the present formulation over many others. This formulation has exploited the fact that the T-matrix essentially contains all the mechanics of the scatterer when only the scattered waves are concerned.

In complementary to the present formulation, a similar multiple-scatterer problem is solved by Twersky[3] via the "ordered scattering" approach but the problem is treated strictly as a boundary-value problem. The similarity and the differences between the present formulation and that of Twersky's will be discussed in a greater detail later in §4-5.

Validity Condition

To facilitate discussions, it might be useful to define the *territory* of a scatterer. The territory of a scatterer is the smallest circle that is centered at the origin of the scatterer's local coordinate system and circumscribes the scatterer, as sketched in Fig. 4–6. The radius of the circumscribing circle, such as a_i and a_j in Fig. 4–6, is defined as the *radius of the scatterer.* These definitions are generalized from the case of circular scatterers.

Graf's addition theorem requires $d_{ij} > r_j$ when the wave expansion basis $\{\boldsymbol{H}(r_i, \theta_i)\}$ is expressed in terms of Scatterer j's local coordinates (r_j, θ_j). That is, the transformed expression is valid only within a circular region of radius d_{ij}

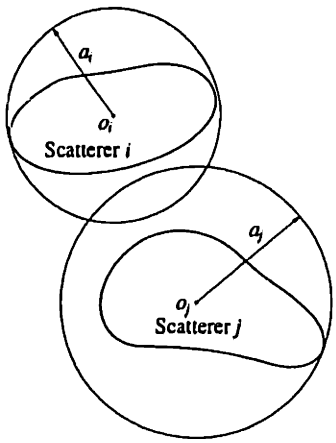

Fig. 4–6 Territories and radii of two neighboring scatterers. This is an example of overlapping territories that satisfy the validity condition.

centered at the origin of Scatterer j's local polar coordinate system, as illustrated by the shaded circular region, excluding the circle, in Fig. 4–7.

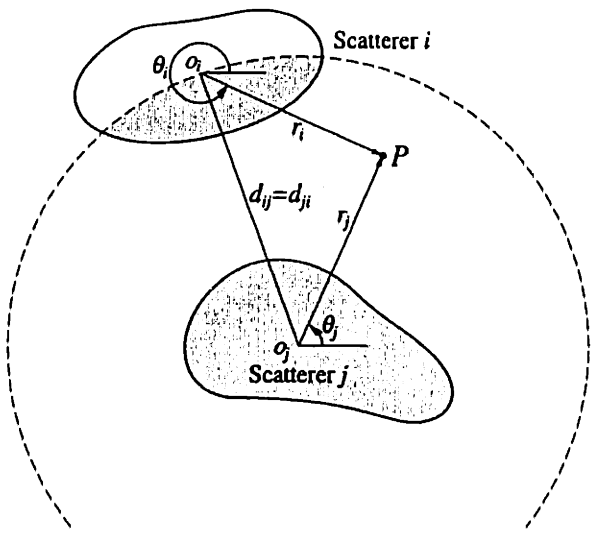

Fig. 4–7 The region shown as the shaded circular region, excluding the circle, is the validity region in which expression for wave expansion basis $\{\boldsymbol{H}(r_i, \theta_i)\}$ in terms of (r_j, θ_j) is valid.

In the solution process, after the coordinate transformation, the T-matrix relation of Scatterer j is then applied to obtain the resulting scattered wave scattered by Scatterer j. As applying the T-matrix relation is equivalently applying the boundary conditions at the interface between the scatterer and the matrix; that is, r_j runs through the entire perimeter of Scatterer j, the restriction of Graf's addition theorem requires that the entire Scatterer j remains within this shaded validity region in Fig. 4–7.

Since a similar restriction exists mutually between every pair of scatterers, the

overall validity condition for the present formal solution can be stated as: *for every scatterer, its territory should not enclose the origin of any other scatterer's local coordinate system.* For circular scatterers, this condition is naturally satisfied. But for scatterers of general cross-sectional geometries, this condition must be strictly observed.

In some literature[4,5], the validity condition is often stated as: the smallest circles that circumscribe individual scatterers (territories) should not overlap. This is simply an overstatement. For example, in Fig. 4–6 and assuming that there is no any other scatterers in the field, the territories of the two scatterers overlap, but they still satisfy the restriction condition since each territory does not enclose the other's origin. Also noted, in some literature[6,7], no such restriction was mentioned at all.

Interior Fields

The present formal solution assumes that every scatterer is composed of linearly elastic material(s), and the material properties are known. This allows the scatterers to have infra-structures such as cores, liners, *etc.* Therefore the wave fields inside a scatterer depends on the infra-structures of the scatterer and no general expression can be written. On the other hand, as long as the single-scatterer solution gives the interior fields, the interior fields in the multiple-scatterer setting can be obtained in a straightforward manner.

To illustrate the procedure, assume, as an example, that Scatterer i is homogeneous, and the single-scatterer solution gives the interior wave field as

$$\phi_i^{\text{ss interior}} = \{\boldsymbol{B}_i^{\text{interior}}\}^T \{\boldsymbol{J}(r_i, \theta_i)\} \tag{4–94}$$

Since the system is linear, the wave expansion coefficients of the interior wave can be related to the wave expansion coefficients of the incident wave by a characteristic matrix such that

$$\{\boldsymbol{B}_i^{\text{interior}}\} = [\boldsymbol{F}_i]\{\boldsymbol{A}_i\} \tag{4–95}$$

The characteristic matrix $[\boldsymbol{F}_i]$ is conceptually similar to the T-matrix and generally exist for a linear system, although the determination of such a matrix is beyond the scope of the multiple-scatterer solution. The wave expansion coefficients of the interior wave can be further related to the scattered wave as

$$\{\boldsymbol{B}_i^{\text{interior}}\} = [\boldsymbol{F}_i][\boldsymbol{T}_i]^{-1}\{\boldsymbol{B}_i\} \tag{4–96}$$

where the T-matrix relation has been used.

For the multiple-scatterer problem under consideration, the interior wave field inside Scatterer i is still expressible by the same wave expansion basis as in the single-scatterer case in eqn. (4–94), and its coefficient matrix is denoted as $\{\boldsymbol{D}_i\}$; that is,

$$\phi_i^{\text{interior}} = \{\boldsymbol{D}_i\}^T \{\boldsymbol{J}(r_i, \theta_i)\} \tag{4–97}$$

Then, since matrix $[\boldsymbol{F}_i][\boldsymbol{T}_i]^{-1}$ is the characteristic matrix that relates the wave expansion coefficients of the interior wave and the scattered wave, and in the multiple-scatterer problem, the coefficients of the scattered wave is $\{\boldsymbol{C}_i\}$, which can be obtained either directly or from the multiple scattering kernel matrix via eqn. (4–61), it follows that

$$\{\boldsymbol{D}_i\} = [\boldsymbol{F}_i][\boldsymbol{T}_i]^{-1}\{\boldsymbol{C}_i\} = [\boldsymbol{F}_i][\boldsymbol{T}_i]^{-1}[\boldsymbol{K}_i]\{\boldsymbol{A}_i\} \tag{4–98}$$

In fact, as long as the single-scatterer problem has been fully solved, for any interior field of interest, the characteristic matrix that relates the wave expansion coefficients of the wave of interest and the scattered wave, such as the $[\boldsymbol{G}_i] \equiv [\boldsymbol{F}_i][\boldsymbol{T}_i]^{-1}$ matrix, can be found directly without going through the matrix inversion, and be treated as a single matrix.

4-4 Formal Mathematics of Multiple Scattering —P/SV Waves

The case involving P and SV waves is much more complicated than the SH wave case due to mode conversions occurring at the material discontinuities and physical boundaries of the problem. For a two dimensional problem, coupling only occurs between P waves and the type of S waves that are polarized in the plane of the wave's propagation, known as *SV waves*. In general, at every interface/boundary, every impinging wave, containing either a purely P wave or a purely SV wave or the combined, generates two scattered waves, one P wave and one SV wave.

Despite this complication, the essence of the multiple scattering process in a multiple-scatterer situation as detailed in §4-2 is still the same, with the understanding that each imaginary wave depicted therein actually contains two components: one P wave and one SV wave.

Having explored the mathematical structure of the simpler SH wave case, this section deals with this more complicated case, and it is shown that, with some extensions and modifications, all the solution forms presented in the previous section still hold.

4-4.1 Basic Equations and Single-Scatterer Case

In terms of displacement potentials, the governing equations for elastic waves are

$$\nabla^2\Phi = \frac{1}{c_p^2}\frac{\partial\Phi}{\partial t^2} \qquad \nabla^2\boldsymbol{H} = \frac{1}{c_s^2}\frac{\partial\boldsymbol{H}}{\partial t^2} \tag{4–99}$$

where c_p and c_s are the speeds of the longitudinal and shear waves, respectively,

$$c_p = \sqrt{\frac{\lambda + 2\mu}{\rho}} \qquad c_s = \sqrt{\frac{\mu}{\rho}} \tag{4-100}$$

λ and μ are Lamè constants, ρ is the density, of the host medium, Φ is the *scalar displacement potential*, and $\boldsymbol{H}$ is the *vector displacement potential* which must satisfy an additional *gauge condition*

$$\nabla \cdot \boldsymbol{H} = 0 \tag{4-101}$$

The relation between the displacement $\boldsymbol{u}$ and the displacement potentials is

$$\boldsymbol{u} = \nabla\Phi + \nabla \times \boldsymbol{H} \tag{4-102}$$

As discussed in Chapter 2, for a two-dimensional plane-strain problem, such as a P/SV wave scattering problem, in the xy-plane, only the scalar displacement potential Φ and the z-component of the vector displacement potential $\boldsymbol{H}$, denoted as Ψ, contribute to the wave fields. The P and SV waves are solely associated with Φ and Ψ, respectively. In the steady state, the governing equations can be reduced to the following pair of Helmholtz equations

$$\nabla^2\phi + \kappa^2\phi = 0 \qquad \nabla^2\psi + k^2\psi = 0 \tag{4-103}$$

where φ and ψ are the complex amplitudes of Φ and Ψ, respectively, *i.e.*,

$$\Phi = \varphi(x,y)\mathrm{e}^{-i\omega t} \qquad \Psi = \psi(x,y)\mathrm{e}^{-i\omega t} \tag{4-104}$$

and κ and k are wave numbers of the P and SV waves in the medium, respectively, whose relations with the circular frequency ω are

$$\kappa = \frac{\omega}{c_p} = \omega\sqrt{\frac{\rho}{\lambda + 2\mu}} \quad \text{and} \quad k = \frac{\omega}{c_p} = \omega\sqrt{\frac{\rho}{\mu}} \tag{4-105}$$

As shown in Chapter 2, the complete general solution for the scattered waves in a 2-D problem using a polar coordinate system is a linear combination of the so-called wave functions or the wave expansion basis functions. For different types of waves, these wave expansion bases are different since the wave numbers are different. The incident waves are expressible as

$$\varphi_i^{\text{inc}} = \{\boldsymbol{A}_i\}^T\{\boldsymbol{J}(\kappa; r_i, \theta_i)\} \qquad \psi_i^{\text{inc}} = \{\boldsymbol{a}_i\}^T\{\boldsymbol{J}(k; r_i, \theta_i)\} \tag{4-106}$$

where $\{\boldsymbol{J}(\kappa; r_i, \theta_i)\}$ and $\{\boldsymbol{J}(k; r_i, \theta_i)\}$ are called the *regular wave expansion bases* for the P and SV waves, respectively, in Scatterer i's local polar coordinate system, and their elements at the n-th row are

$$\{J(\kappa; r_i, \theta_i)\}_n = J_n(\kappa r_i)\mathrm{e}^{\mathrm{i}n\theta_i} \qquad \{J(k; r_i, \theta_i)\}_n = J_n(k r_i)\mathrm{e}^{\mathrm{i}n\theta_i} \tag{4-107}$$

respectively. For the single-scatterer problem associated with Scatterer i, the scattered waves are expressible as

$$\varphi_i^{ss} = \{\boldsymbol{B}_i\}^T\{\boldsymbol{H}(\kappa; r_i, \theta_i)\} \qquad \psi_i^{ss} = \{\boldsymbol{b}_i\}^T\{\boldsymbol{H}(k; r_i, \theta_i)\} \tag{4-108}$$

where $\{\boldsymbol{H}(\kappa; r_i, \theta_i)\}$ and $\{\boldsymbol{H}(k; r_i, \theta_i)\}$ are called the *singular wave expansion bases* for the P and SV waves, respectively, in Scatterer i's local polar coordinate system, and their elements at the n-th row are

$$\{H(\kappa; r_i, \theta_i;)\}_n = H_n^{(1)}(\kappa r_i)\mathrm{e}^{in\theta_i} \qquad \{H(k; r_i, \theta_i)\}_n = H_n^{(1)}(k r_i)\mathrm{e}^{in\theta_i} \quad (4\text{–}109)$$

respectively.

It is noted that, as part of the notational conventions in this thesis, an upper case denomination of a wave expansion coefficient matrix such as $\{\boldsymbol{A}_i\}$ signifies a P wave, whereas a lower case denomination such as $\{\boldsymbol{a}_i\}$ signifies an SV wave.

For a single-scatterer P/SV wave scattering problem, the scattered waves are completely related to the incident waves by a set of four T-matrices, representing the scattered P waves due to a P incident wave, the scattered P wave due to an S incident wave, the scattered S wave due to a P incident wave and the scattered S wave due to an S incident wave, respectively. These T-matrices are denoted as $[\boldsymbol{T}^{PP}]$, $[\boldsymbol{T}^{SP}]$, $[\boldsymbol{T}^{PS}]$ and $[\boldsymbol{T}^{SS}]$, respectively, where the first superscript signifies the type of the incident wave and the second superscript signifies the type of the scattered waves. Furthermore, the *T-supermatrix* of Scatterer i can be constructed as

$$[\mathfrak{T}_i] = \begin{bmatrix} [\boldsymbol{T}_i^{PP}] & [\boldsymbol{T}_i^{SP}] \\ [\boldsymbol{T}_i^{PS}] & [\boldsymbol{T}_i^{SS}] \end{bmatrix} \quad (4\text{–}110)$$

and similarly the *wave expansion coefficient supermatrices* as

$$\{\mathfrak{B}_i\} = \begin{Bmatrix} \{\boldsymbol{B}_i\} \\ \{\boldsymbol{b}_i\} \end{Bmatrix} \quad \text{and} \quad \{\mathfrak{A}_i\} = \begin{Bmatrix} \{\boldsymbol{A}_i\} \\ \{\boldsymbol{a}_i\} \end{Bmatrix} \quad (4\text{–}111)$$

Then, the T-matrix relation for the case of P/SV wave scattering for Scatterer i can be written as

$$\{\mathfrak{B}_i\} = [\mathfrak{T}_i]\{\mathfrak{A}_i\} \quad (4\text{–}112)$$

This relation resembles in form the T-matrix relation for the case of SH wave scattering in eqn. (4–13).

Note that a wave expansion coefficient supermatrix is nothing more than a concatenation of the wave expansion coefficient matrices for a pair of P and SV waves and is used for formal simplicity. The convention for the concatenation is to place the P wave's expansion coefficient matrix first (on the top) and followed by the SV wave's. As such, when the wave expansion coefficient supermatrix for a pair of P and SV waves is known, the associated displacement potentials φ and ψ can be computed by splitting the supermatrix into two halves and performing an inner product for each half with the corresponding wave expansion basis.

4-4.2 Solution Structure of Multiple Scattering

Since the physical process of the multiple scattering for the multiple-scatterer setting described in §4-2 remains valid for the case of P/SV wave scattering, it is expected that the solution structures will be the same. The analogy can be readily found by finding the corresponding expressions for any of the second order scattered wave.

Without lost of generality, first, the expressions for the second order scattered waves scattered by Scatterer j due to the first order scattered waves scattered by Scatterer i are sought.

The waves that cause this scattering are

$$\phi_i^{(1)} = \{\boldsymbol{B}_i\}^T\{\boldsymbol{H}(\kappa; r_i, \theta_i)\} \tag{4-113}$$

$$\psi_i^{(1)} = \{\boldsymbol{b}_i\}^T\{\boldsymbol{H}(k; r_i, \theta_i)\} \tag{4-114}$$

In performing the coordinate transformation to express the wave expansion bases $\{\boldsymbol{H}(\kappa; r_i, \theta_i)\}$ and $\{\boldsymbol{H}(k; r_i, \theta_i)\}$ in Scatterer j's local coordinate system, it is noted that, in writing eqns. (4–25) and (4–26), the geometric distances shown in Fig. 4–5 are scaled by a factor k, the only wave number in the SH wave case. For the two different wave numbers κ and k in P/SV case, relations equivalent to eqns. (4–25) and (4–26) can be written as

$$\{\boldsymbol{H}(r_i, \theta_i; \kappa)\} = [\boldsymbol{R}_{ij}(\kappa)]\{\boldsymbol{J}(\kappa; r_j, \theta_j)\} \tag{4-115}$$

$$\{\boldsymbol{H}(k; r_i, \theta_i)\} = [\boldsymbol{R}_{ij}(k)]\{\boldsymbol{J}(k; r_j, \theta_j)\} \tag{4-116}$$

$$\{\boldsymbol{J}(\kappa; r_i, \theta_i)\} = [\Re\boldsymbol{R}_{ij}(\kappa)]\{\boldsymbol{J}(\kappa; r_j, \theta_j)\} \tag{4-117}$$

$$\{\boldsymbol{J}(k; r_i, \theta_i)\} = [\Re\boldsymbol{R}_{ij}(k)]\{\boldsymbol{J}(k; r_j, \theta_j)\} \tag{4-118}$$

where the entries at the n-th row and the m-th column of the singular coordinate translation matrices $[\boldsymbol{R}_{ij}(\kappa)]$ and $[\boldsymbol{R}_{ij}(k)]$ are

$$[R_{ij}(\kappa)]_{nm} = \mathrm{e}^{\mathrm{i}(n-m)\theta_{ij}} H_n^{(1)}(\kappa d_{ij}) \tag{4-119}$$

$$[R_{ij}(k)]_{nm} = \mathrm{e}^{\mathrm{i}(n-m)\theta_{ij}} H_n^{(1)}(k d_{ij}) \tag{4-120}$$

and the entries of regular coordinate translation matrices $[\Re\boldsymbol{R}_{ij}(\kappa)]$ and $[\Re\boldsymbol{R}_{ij}(k)]$ are identical to those of $[\boldsymbol{R}_{ij}(\kappa)]$ and $[\boldsymbol{R}_{ij}(k)]$, respectively, except that Hankel functions of the first kind are replaced by Bessel functions of the first kind at the same order. Thus, performing the coordinate transformation, eqns. (4–113) and (4–114) can be rewritten as

$$\phi_i^{(1)} = \Big([R_{ij}(\kappa)]^T\{\boldsymbol{B}_i\}\Big)^T\{\boldsymbol{J}(\kappa; r_j, \theta_j)\} \tag{4-121}$$

$$\psi_i^{(1)} = \Big([R_{ij}(k)]^T\{\boldsymbol{b}_i\}\Big)^T\{\boldsymbol{J}(r_j, \theta_j; k)\} \tag{4-122}$$

Denote the wave expansion coefficient supermatrix for these causing waves as

$\{\mathfrak{A}_j^{(2)}\}$, then,

$$\{\mathfrak{A}_j^{(2)}\} = \begin{Bmatrix} [R_{ij}(\kappa)]^T\{B_i\} \\ [R_{ij}(k)]^T\{b_i\} \end{Bmatrix} = [\mathfrak{R}_{ij}]^T\{\mathfrak{B}_i\} \tag{4-123}$$

where

$$[\mathfrak{R}_{ij}] = \begin{bmatrix} [R_{ij}(\kappa)] & 0 \\ 0 & [R_{ij}(k)] \end{bmatrix} \tag{4-124}$$

Thus, as implied by eqn. (4–112), the wave expansion coefficient supermatrix for the second order scattered waves scattered by Scatterer j due to the first order scattered waves scattered by Scatterer i, denoted as $\{\mathfrak{C}_{ji}^{(2)}\}$, is related to $\{\mathfrak{A}_j^{(2)}\}$ as

$$\{\mathfrak{C}_{ji}^{(2)}\} = [\mathfrak{T}_j]\{\mathfrak{A}_j^{(2)}\} = [\mathfrak{T}_j][\mathfrak{R}_{ij}]^T\{\mathfrak{B}_i\} \tag{4-125}$$

Or

$$\{\mathfrak{C}_{ji}^{(2)}\} = [\mathfrak{T}_j][\mathfrak{R}_{ij}]^T\{\mathfrak{C}_i^{(1)}\} = [\mathfrak{T}_j][\mathfrak{R}_{ij}]^T[\mathfrak{T}_i]\{\mathfrak{A}_i\} \tag{4-126}$$

where a notational convention $\{\mathfrak{B}_i\} \equiv \{\mathfrak{C}_i^{(1)}\}$ and the T-supermatrix relation for Scatterer i in eqn. (4–112) have been used. Performing another coordinate transformation to relate $\{\mathfrak{A}_i\}$ to $\{\mathfrak{A}_j\}$ leads to

$$\{\mathfrak{C}_{ji}^{(2)}\} = [\mathfrak{T}_j][\mathfrak{R}_{ij}]^T\{\mathfrak{C}_i^{(1)}\} = [\mathfrak{T}_j][\mathfrak{R}_{ij}]^T[\mathfrak{T}_i][\mathfrak{R}\mathfrak{R}_{ji}]^T\{\mathfrak{A}_j\} \tag{4-127}$$

Define the *inductance supermatrix* of Scatterer i on Scatterer j as

$$[\mathfrak{L}_{ij}] = [\mathfrak{T}_j][\mathfrak{R}_{ij}]^T = \begin{bmatrix} [T_j^{PP}][R_{ij}(\kappa)]^T & [T_j^{PS}][R_{ij}(\kappa)]^T \\ [T_j^{SP}][R_{ij}(k)]^T & [T_j^{SS}][R_{ij}(k)]^T \end{bmatrix} \tag{4-128}$$

then, eqn. (4–127) becomes

$$\{\mathfrak{C}_{ji}^{(2)}\} = [\mathfrak{L}_{ij}]\{\mathfrak{C}_i^{(1)}\} = [\mathfrak{L}_{ij}][\mathfrak{T}_i][\mathfrak{R}\mathfrak{R}_{ji}]^T\{\mathfrak{A}_j\} \tag{4-129}$$

which resembles eqn. (4–40) in form.

Summing up the contributions from all scatterers, except Scatterer j itself, for the total second order scattered waves scattered by Scatterer j gives

$$\{\mathfrak{C}_j^{(2)}\} = \sum_{\substack{i=1 \\ i\neq j}}^{N}[\mathfrak{L}_{ij}]\{\mathfrak{C}_i^{(1)}\} = \sum_{\substack{i=1 \\ i\neq j}}^{N}[\mathfrak{L}_{ij}][\mathfrak{T}_i][\mathfrak{R}\mathfrak{R}_{ji}]^T\{\mathfrak{A}_j\} = [\mathfrak{K}_j^{(2)}]\{\mathfrak{A}_j\} \tag{4-130}$$

where

$$[\mathfrak{K}_j^{(2)}] = \sum_{\substack{i=1 \\ i\neq j}}^{N}[\mathfrak{L}_{ij}][\mathfrak{K}_i^{(1)}][\mathfrak{R}\mathfrak{R}_{ji}]^T \tag{4-131}$$

and

$$[\mathfrak{K}_j^{(1)}] = [\mathfrak{T}_j] \tag{4-132}$$

$[\mathfrak{K}_j^{(2)}]$ is the *second order multiple-scattering kernel supermatrix* of Scatterer j.

Expressions for higher order waves can be obtained by following the same procedure and can be verified that they are all identical in form to those for the SH wave case in the previous section, except that matrices are replaced by the corresponding

Table 4–2 Analogy Between the Formulations for P/SV Wave Scattering and SH Wave Scattering Problems

SH Wave Formulation	P/SV Wave Formulation
$\{A_j\}$	$\{\mathfrak{A}_j\} = \begin{Bmatrix} \{A_j\} \\ \{a_j\} \end{Bmatrix}$
$\{C_j\}$	$\{\mathfrak{C}_j\} = \begin{Bmatrix} \{C_j\} \\ \{c_j\} \end{Bmatrix}$
$[T_j]$	$[\mathfrak{T}_j] = \begin{bmatrix} [T_j^{PP}] & [T_j^{SP}] \\ [T_j^{PS}] & [T_j^{SS}] \end{bmatrix}$
$[R_{ij}]$	$[\mathfrak{R}_{ij}] = \begin{bmatrix} [R_{ij}(\kappa)] & 0 \\ 0 & [R_{ij}(k)] \end{bmatrix}$
$[\Re R_{ij}]$	$[\Re\mathfrak{R}_{ij}] = \begin{bmatrix} [\Re R_{ij}(\kappa)] & 0 \\ 0 & [\Re R_{ij}(k)] \end{bmatrix}$
$[L_{ij}]$	$[\mathfrak{L}_{ij}] = \begin{bmatrix} [T_j^{PP}][R_{ij}(\kappa)]^T & [T_j^{PS}][R_{ij}(\kappa)]^T \\ [T_j^{SP}][R_{ij}(k)]^T & [T_j^{SS}][R_{ij}(k)]^T \end{bmatrix}$
$\{C_j\} = [K_j]\{A_j\}$	$\{\mathfrak{C}_j\} = [\mathfrak{K}_j]\{\mathfrak{A}_j\}$

supermatrices. For brevity, those derivations are not to be repeated. The analogy between the formulations for P/SV wave case and SH wave case is summarized in Table 4–2.

The total waves in the host medium can be written as, according to -eqn. (4–5),

$$\varphi^{\text{total}} = \varphi^{\text{inc}} + \sum_{j=1}^{N} \varphi_j = \varphi^{\text{inc}} + \sum_{j=1}^{N} \{C_j\}^T \{H(\kappa; r_j, \theta_j)\} \tag{4–133}$$

$$\psi^{\text{total}} = \psi^{\text{inc}} + \sum_{j=1}^{N} \psi_j = \psi^{\text{inc}} + \sum_{j=1}^{N} \{c_j\}^T \{H(k; r_j, \theta_j)\} \tag{4–134}$$

where $\{C_j\}$ and $\{c_j\}$ are obtained from the following wave expansion coefficient supermatrix

$$\{\mathfrak{C}_j\} = \begin{Bmatrix} \{C_j\} \\ \{c_j\} \end{Bmatrix} = \sum_{p=1}^{\infty} \{\mathfrak{C}_j^{(p)}\} = \sum_{p=1}^{\infty} \begin{Bmatrix} \{C_j^{(p)}\} \\ \{c_j^{(p)}\} \end{Bmatrix} \tag{4–135}$$

which, when necessary, can be related to the multiple scattering kernel supermatrix $[\mathfrak{K}_j]$ as

$$\{\mathfrak{C}_j\} = [\mathfrak{K}_j]\{\mathfrak{A}_j\} \qquad \text{and} \qquad \{\mathfrak{C}_j^{(p)}\} = [\mathfrak{K}_j^{(p)}]\{\mathfrak{A}_j\} \tag{4–136}$$

and

$$[\mathfrak{K}_j] = \sum_{p=1}^{\infty} [\mathfrak{K}_j^{(p)}] \tag{4–137}$$

Corresponding to the solution structures in the SH wave case, the following solution structures can be obtained, for either the wave expansion coefficient supermatrices or the multiple scattering kennel supermatrices:

Recursive Form I

$$\{\mathfrak{C}_j^{(p)}\} = \sum_{\substack{i=1 \\ i\neq j}}^{N} [\mathfrak{L}_{ij}]\{\mathfrak{C}_i^{(p-1)}\} \tag{4-138}$$

with

$$\{\mathfrak{C}_j^{(1)}\} = [\mathfrak{T}_j]\{\mathfrak{A}_j\} \tag{4-139}$$

Recursive Form II

$$[\mathfrak{K}_j^{(p)}] = \sum_{\substack{i=1 \\ i\neq j}}^{N} [\mathfrak{L}_{ij}][\mathfrak{K}_i^{(p-1)}][\mathfrak{R}\mathfrak{R}_{ji}]^T \tag{4-140}$$

with

$$[\mathfrak{K}_j^{(1)}] = [\mathfrak{T}_j] \tag{4-141}$$

Implicit Form I

$$\{\mathfrak{C}_j\} = [\mathfrak{T}_j]\{\mathfrak{A}_j\} + \sum_{\substack{i=1 \\ i\neq j}}^{N} [\mathfrak{L}_{ij}]^T\{\mathfrak{C}_i\} \tag{4-142}$$

Implicit Form II

$$[\mathfrak{K}_j] = [\mathfrak{T}_j] + \sum_{\substack{i=1 \\ i\neq j}}^{N} [\mathfrak{L}_{ij}][\mathfrak{K}_i][\mathfrak{R}\mathfrak{R}_{ji}]^T \tag{4-143}$$

Supermatrix Form

$$[\mathcal{I} - \mathcal{L}]\{\mathcal{C}\} = \{\mathcal{A}\} \tag{4-144}$$

where

$$\{\mathcal{C}\} = \begin{Bmatrix} \{\mathfrak{C}_1\} \\ \{\mathfrak{C}_2\} \\ \vdots \\ \{\mathfrak{C}_N\} \end{Bmatrix} \qquad \{\mathcal{A}\} = \begin{Bmatrix} [\mathfrak{T}_1]\{\mathfrak{A}_1\} \\ [\mathfrak{T}_2]\{\mathfrak{A}_2\} \\ \vdots \\ [\mathfrak{T}_N]\{\mathfrak{A}_N\} \end{Bmatrix} \tag{4-145}$$

$$[\mathcal{L}] = \begin{bmatrix} \mathbf{0} & [\mathfrak{L}_{21}] & \cdots & [\mathfrak{L}_{N1}] \\ [\mathfrak{L}_{12}] & \mathbf{0} & \cdots & [\mathfrak{L}_{N2}] \\ \cdots & \cdots & \cdots & \cdots \\ [\mathfrak{L}_{1N}] & \cdots & [\mathfrak{L}_{(N-1)N}] & \mathbf{0} \end{bmatrix} \tag{4-146}$$

4-4.3 Displacements, Strains and Stresses

As discussed in Chapter 2, a two-dimensional problem involving P and SV waves is a plain-strain problem, and the displacements, strains and stresses are expressible in terms of the $\mathfrak{E}$-functions defined in Appendix 2-C of Chapter 2.

From the formal solution in eqns. (4–133) and (4–134), the total wave field consists of the incident waves plus N pairs of scattered waves, with one pair emanating from each scatterer. Each pair consists of one P wave and one SV wave and their wave expansion coefficient matrices are $\{\boldsymbol{C}_j\}$ and $\{\boldsymbol{c}_j\}$, respectively, as expressed in eqns. (4–135) and (4–136). As the system is linear, the total displacements, strains and stresses are simply the sums of the respective contributions from each wave.

For the incident waves, in general their expressions are known, and their contributions to the displacements, strains and stresses can be directly written as, from the relation between the displacements, strains and stresses and the displacement potentials in Appendix 2-B in Chapter 2,

$$u_x^{\text{inc}} = \frac{\partial \varphi^{\text{inc}}}{\partial x} - \frac{\partial \psi^{\text{inc}}}{\partial y} \tag{4-147}$$

$$u_y^{\text{inc}} = \frac{\partial \varphi^{\text{inc}}}{\partial y} + \frac{\partial \psi^{\text{inc}}}{\partial x} \tag{4-148}$$

$$\varepsilon_{xx}^{\text{inc}} = \frac{\partial^2 \varphi^{\text{inc}}}{\partial x^2} - \frac{\partial \psi^{\text{inc}}}{\partial x \partial y} \tag{4-149}$$

$$\varepsilon_{yy}^{\text{inc}} = \frac{\partial^2 \varphi^{\text{inc}}}{\partial y^2} + \frac{\partial \psi^{\text{inc}}}{\partial x \partial y} \tag{4-150}$$

$$\gamma_{xy}^{\text{inc}} = 2\frac{\partial^2 \varphi^{\text{inc}}}{\partial x \partial y} + \frac{\partial \psi^{\text{inc}}}{\partial x^2} - \frac{\partial \psi^{\text{inc}}}{\partial y^2} \tag{4-151}$$

$$\sigma_{xx}^{\text{inc}} = -\lambda \kappa^2 \varphi^{\text{inc}} + 2\mu \left(\frac{\partial^2 \varphi^{\text{inc}}}{\partial x^2} - \frac{\partial \psi^{\text{inc}}}{\partial x \partial y} \right) \tag{4-152}$$

$$\sigma_{yy}^{\text{inc}} = -\lambda \kappa^2 \varphi^{\text{inc}} + 2\mu \left(\frac{\partial^2 \varphi^{\text{inc}}}{\partial y^2} + \frac{\partial \psi^{\text{inc}}}{\partial x \partial y} \right) \tag{4-153}$$

$$\sigma_{zz}^{\text{inc}} = -\lambda \kappa^2 \varphi^{\text{inc}} \tag{4-154}$$

$$\tau_{xy}^{\text{inc}} = \mu \left(2\frac{\partial^2 \varphi^{\text{inc}}}{\partial x \partial y} + \frac{\partial \psi^{\text{inc}}}{\partial x^2} - \frac{\partial \psi^{\text{inc}}}{\partial y^2} \right) \tag{4-155}$$

where the quantities on the left-hand sides are the *complex amplitudes* of the corresponding physical quantities, and the superscript "inc" denotes the contributions from the incident waves.

Introduce the following set of *singular differential wave expansion basis matrices*

$$\{\boldsymbol{H}_{\xi\eta}(r_i,\theta_i)\} \qquad \text{with} \qquad \{H_{\xi\eta}(r_i,\theta_i)\}_n = \mathfrak{E}^3_{\xi\eta n}(r_i)\mathrm{e}^{\mathrm{i}n\theta_i} \tag{4-156}$$

where ξ ranges from 1 to 8 and η ranges from 1 to 2, such that the subscripts of these differential wave expansion bases correspond to the first two subscripts of their respective $\mathfrak{E}$-functions.

Then, for any point (x,y) in the global Cartesian coordinate system, the contributions to the displacements, strains and stresses from each pair of scattered waves can be expressed in each scatterers's local polar coordinate system. For Scatterer i, they are

$$u_{i\,r_i} = \frac{1}{r_i}\left[\{\boldsymbol{C}_i\}^T\{\boldsymbol{H}_{71}(r_i,\theta_i)\} + \{\boldsymbol{c}_i\}^T\{\boldsymbol{H}_{72}(r_i,\theta_i)\}\right] \tag{4-157}$$

$$u_{i\,\theta_i} = \frac{1}{r_i}\left[\{\boldsymbol{C}_i\}^T\{\boldsymbol{H}_{81}(r_i,\theta_i)\} + \{\boldsymbol{c}_i\}^T\{\boldsymbol{H}_{82}(r_i,\theta_i)\}\right] \tag{4-158}$$

$$\varepsilon_{i\,r_ir_i} = \frac{1}{r_i^2}\left[\{\boldsymbol{C}_i\}^T\{\boldsymbol{H}_{51}(r_i,\theta_i)\} + \{\boldsymbol{c}_i\}^T\{\boldsymbol{H}_{52}(r_i,\theta_i)\}\right] \tag{4-159}$$

$$\varepsilon_{i\,\theta_i\theta_i} = \frac{1}{r_i^2}\left[\{\boldsymbol{C}_i\}^T\{\boldsymbol{H}_{61}(r_i,\theta_i)\} + \{\boldsymbol{c}_i\}^T\{\boldsymbol{H}_{62}(r_i,\theta_i)\}\right] \tag{4-160}$$

$$\gamma_{i\,r_i\theta_i} = \frac{2}{r_i^2}\left[\{\boldsymbol{C}_i\}^T\{\boldsymbol{H}_{41}(r_i,\theta_i)\} + \{\boldsymbol{c}_i\}^T\{\boldsymbol{H}_{42}(r_i,\theta_i)\}\right] \tag{4-161}$$

$$\sigma_{i\,r_ir_i} = \frac{2\mu}{r_i^2}\left[\{\boldsymbol{C}_i\}^T\{\boldsymbol{H}_{11}(r_i,\theta_i)\} + \{\boldsymbol{c}_i\}^T\{\boldsymbol{H}_{12}(r_i,\theta_i)\}\right] \tag{4-162}$$

$$\sigma_{i\,\theta_i\theta_i} = \frac{2\mu}{r_i^2}\left[\{\boldsymbol{C}_i\}^T\{\boldsymbol{H}_{21}(r_i,\theta_i)\} + \{\boldsymbol{c}_i\}^T\{\boldsymbol{H}_{22}(r_i,\theta_i)\}\right] \tag{4-163}$$

$$\sigma_{i\,zz} = \frac{2\mu}{r_i^2}\left[\{\boldsymbol{C}_i\}^T\{\boldsymbol{H}_{31}(r_i,\theta_i)\} + \{\boldsymbol{c}_i\}^T\{\boldsymbol{H}_{32}(r_i,\theta_i)\}\right] \tag{4-164}$$

$$\tau_{i\,r_i\theta_i} = \frac{2\mu}{r_i^2}\left[\{\boldsymbol{C}_i\}^T\{\boldsymbol{H}_{41}(r_i,\theta_i)\} + \{\boldsymbol{c}_i\}^T\{\boldsymbol{H}_{42}(r_i,\theta_i)\}\right] \tag{4-165}$$

where the relations between (x,y) and (r_i,θ_i) are given in eqns. (4-81) through (4-83).

Using the coordinate transformation relation between a polar and a Cartesian coordinate system given in Appendix 4-A to transform all the expressions in eqns. (4-157) through (4-165) into the global Cartesian coordinate system, the total displacement, strains and stresses can be expressed as the

$$u_x = u_x^{\text{inc}} + \sum_{i=1}^{N}\left(u_{i\,r_i}\cos\theta_i - u_{i\,\theta_i}\sin\theta_i\right) \tag{4-166}$$

$$u_y = u_y^{\text{inc}} + \sum_{i=1}^{N}\left(u_{i\,r_i}\sin\theta_i + u_{i\,\theta_i}\cos\theta_i\right) \tag{4-167}$$

$$\varepsilon_{xx} = \varepsilon_{xx}^{\text{inc}} + \sum_{i=1}^{N}\varepsilon_{i\,r_ir_i}\cos^2\theta_i - \tfrac{1}{2}\gamma_{i\,r_i\theta_i}\sin 2\theta_i + \varepsilon_{i\,\theta_i\theta_i}\sin^2\theta_i \tag{4-168}$$

$$\varepsilon_{yy} = \varepsilon_{yy}^{\text{inc}} + \sum_{i=1}^{N} \varepsilon_{i r_i r_i} \sin^2\theta_i + \tfrac{1}{2}\gamma_{i r_i \theta_i} \sin 2\theta_i + \varepsilon_{i \theta_i \theta_i} \cos^2\theta_i \tag{4-169}$$

$$\gamma_{xy} = \gamma_{xy}^{\text{inc}} + \sum_{i=1}^{N} \left[(\varepsilon_{i r_i r_i} - \varepsilon_{i \theta_i \theta_i}) \sin 2\theta_i + \gamma_{i r_i \theta_i} \cos 2\theta_i \right] \tag{4-170}$$

$$\sigma_{xx} = \sigma_{xx}^{\text{inc}} + \sum_{i=1}^{N} \left(\sigma_{i r_i r_i} \cos^2\theta_i - \sigma_{i r_i \theta_i} \sin 2\theta_i + \sigma_{i \theta_i \theta_i} \sin^2\theta_i \right) \tag{4-171}$$

$$\sigma_{yy} = \sigma_{yy}^{\text{inc}} + \sum_{i=1}^{N} \left(\sigma_{i r_i r_i} \sin^2\theta_i + \sigma_{i r_i \theta_i} \sin 2\theta_i + \sigma_{i \theta_i \theta_i} \cos^2\theta_i \right) \tag{4-172}$$

$$\sigma_{zz} = \sigma_{zz}^{\text{inc}} + \sum_{i=1}^{N} \sigma_{i zz} \tag{4-173}$$

$$\sigma_{xy} = \sigma_{xy}^{\text{inc}} + \sum_{i=1}^{N} \left[\tfrac{1}{2} (\sigma_{i r_i r_i} - \sigma_{i \theta_i \theta_i}) \sin 2\theta_i + \sigma_{i r_i \theta_i} \cos 2\theta_i \right] \tag{4-174}$$

In the event that a global *polar* coordinate system, whose coordinates are referred to as (r, θ), is also define such that $\theta = 0$ corresponds to the $+x$ direction and it shares the same origin as the global Cartesian coordinate system, it can be found that the total displacements, strains and stresses in this coordinate system for a generic field point (r, θ) are

$$u_r = \frac{\partial \varphi^{\text{inc}}}{\partial r} + \frac{\partial \psi^{\text{inc}}}{r \partial \theta} + \sum_{i=1}^{N} \left[u_{i r_i} \cos(\theta_i - \theta) - u_{i \theta_i} \sin(\theta_i - \theta) \right] \tag{4-175}$$

$$u_\theta = \frac{\partial \varphi^{\text{inc}}}{r \partial \theta} - \frac{\partial \psi^{\text{inc}}}{\partial r} + \sum_{i=1}^{N} \left[u_{i r_i} \sin(\theta_i - \theta) + u_{i \theta_i} \cos(\theta_i - \theta) \right] \tag{4-176}$$

$$\begin{aligned} \varepsilon_{rr} = {} & \frac{\partial^2 \varphi^{\text{inc}}}{\partial r^2} + \frac{\partial^2 \psi^{\text{inc}}}{r \partial r \partial \theta} - \frac{\partial \psi^{\text{inc}}}{r^2 \partial \theta} \\ & + \sum_{i=1}^{N} \left[\varepsilon_{i r_i r_i} \cos^2(\theta_i - \theta) - \tfrac{1}{2}\gamma_{i r_i \theta_i} \sin 2(\theta_i - \theta) + \varepsilon_{i \theta_i \theta_i} \sin^2(\theta_i - \theta) \right] \end{aligned} \tag{4-177}$$

$$\begin{aligned} \varepsilon_{\theta\theta} = {} & \frac{\partial^2 \varphi^{\text{inc}}}{r^2 \partial \theta^2} + \frac{\partial \varphi^{\text{inc}}}{r \partial r} - \frac{\partial^2 \psi^{\text{inc}}}{r \partial r \partial \theta} + \frac{\partial \psi^{\text{inc}}}{r^2 \partial \theta} \\ & + \sum_{i=1}^{N} \left[\varepsilon_{i r_i r_i} \sin^2(\theta_i - \theta) + \tfrac{1}{2}\gamma_{i r_i \theta_i} \sin 2(\theta_i - \theta) + \varepsilon_{i \theta_i \theta_i} \cos^2(\theta_i - \theta) \right] \end{aligned} \tag{4-178}$$

$$\begin{aligned} \gamma_{r\theta} = {} & 2\frac{\partial^2 \varphi^{\text{inc}}}{r \partial r \partial \theta} - 2\frac{\partial \varphi^{\text{inc}}}{r^2 \partial \theta} - \frac{\partial^2 \psi^{\text{inc}}}{\partial r^2} + \frac{\partial^2 \psi^{\text{inc}}}{r^2 \partial \theta^2} + \frac{\partial \psi^{\text{inc}}}{r \partial r} \\ & + \sum_{i=1}^{N} \left[(\varepsilon_{i r_i r_i} - \varepsilon_{i \theta_i \theta_i}) \sin 2(\theta_i - \theta) + \gamma_{i r_i \theta_i} \cos 2(\theta_i - \theta) \right] \end{aligned} \tag{4-179}$$

$$\sigma_{rr} = -\lambda\kappa^2\varphi^{\text{inc}} + 2\mu\left(\frac{\partial^2\varphi^{\text{inc}}}{\partial r^2} + \frac{\partial^2\psi^{\text{inc}}}{r\partial r\partial\theta} - \frac{\partial\psi^{\text{inc}}}{r^2\partial\theta}\right)$$
$$+ \sum_{i=1}^{N}\left[\sigma_{ir_ir_i}\cos^2(\theta_i-\theta) - \sigma_{ir_i\theta_i}\sin 2(\theta_i-\theta) + \sigma_{i\theta_i\theta_i}\sin^2(\theta_i-\theta)\right] \quad (4\text{–}180)$$

$$\sigma_{\theta\theta} = -\lambda\kappa^2\varphi^{\text{inc}} + 2\mu\left(\frac{\partial^2\varphi^{\text{inc}}}{r^2\partial\theta^2} + \frac{\partial\varphi^{\text{inc}}}{r\partial r} - \frac{\partial^2\psi^{\text{inc}}}{r\partial r\partial\theta} + \frac{\partial\psi^{\text{inc}}}{r^2\partial\theta}\right)$$
$$+ \sum_{i=1}^{N}\left[\sigma_{ir_ir_i}\sin^2(\theta_i-\theta) + \sigma_{ir_i\theta_i}\sin 2(\theta_i-\theta) + \sigma_{i\theta_i\theta_i}\cos^2(\theta_i-\theta)\right] \quad (4\text{–}181)$$

$$\sigma_{zz} = -\lambda\kappa^2\varphi^{\text{inc}} + \sum_{i=1}^{N}\sigma_{izz} \quad (4\text{–}182)$$

$$\sigma_{r\theta} = \mu\left(2\frac{\partial^2\varphi^{\text{inc}}}{r^2\partial r\partial\theta} - 2\frac{\partial\varphi^{\text{inc}}}{r^2\partial\theta} - \frac{\partial^2\psi^{\text{inc}}}{\partial r^2} + \frac{\partial^2\psi^{\text{inc}}}{r^2\partial\theta^2} + \frac{\partial\psi^{\text{inc}}}{r\partial r_i}\right)$$
$$+ \sum_{i=1}^{N}\left[\tfrac{1}{2}\left(\sigma_{ir_ir_i} - \sigma_{i\theta_i\theta_i}\right)\sin 2(\theta_i-\theta) + \sigma_{ir_i\theta_i}\cos 2(\theta_i-\theta)\right] \quad (4\text{–}183)$$

4-5 Comparison with Other Formalisms and Concluding Remarks

In the past few decades, several multiple-scatterer formulations have been developed, and all lead to the *exact* solution.

The idea of "ordered scattering" is probably due to Twersky[3] when a multiple-scatterer solution was given for scalar wave fields such as acoustic waves. Extension to the elastic wave was followed up by Cheng[8].

In this formulation, the multiple-scatterer problem is mathematically decomposed into different orders from the "boundary-value problem" point of view. In each order, the wave that excites one scatterer and the scattered wave due to that excitation form a boundary-values problem which is in turn solved. In this approach, the boundary value problems must be solved for every order of the scattering, and the solutions presented in both [3] and [8] are particularized to the case of identical rigid circular cylindrical scatterers subjected to a planar incident wave. Although the term "order" was not clearly defined or explained in [3], it essentially has the same meaning as the present formulation.

Compared with the present formulation, the formulation in [3] lacks the insight of the physical happenings at every order.

Another multiple-scatterer formulation that bears a close resemblance to the present one was developed by Varadan, Varadan and Pao[4]. This formulation

represents a different interpretation of the physical process of multiple scattering and yet gives the same solution as Implicit Form I.

The basic idea underlies [4] can be summarized as following. In a single-scatterer case, the scatterer is *excited* by the incident wave, and the scattered wave is then generated. The total wave in the field is the sum of the incident wave and the scattered wave. The coefficient matrices of the incident and the scattered waves are related by the T-matrix. In the multiple-scatterer case, each scatterer is *excited* by the incident wave plus the waves scattered by all other scatterers in the field. As such, the total wave in the field is the sum of the exciting wave and the scattered wave, from the point of view of any individual scatterer, and more importantly, the coefficient matrices of the exciting and the scattered waves are related by the same T-matrix of the scatterer in question. The analysis arrives at the same result as eqn. (4–67).

As the identical results are obtained both by the present formulation and that in [4], they can be regarded as complementary to each other. The present formulation gives a few more alternatives of obtaining the final result. Furthermore, the present formulation make it possible to track the detailed physics at each order of scattering. The detailed anatomy of the orders of scattering can be useful in the process of devising an approximate solution or investigating the influence of one scatterer on another.

In the past, the approach used in [4] and the approach of "ordered scattering" (or "orders of scattering", as sometimes being referred to in the literature) have been regarded as two different approaches. The present formulation not only bridges the two approaches, but also shows that results obtained are indeed identical, and the approach in [4] is one of the approaches to the final solution.

Not long after the so-called T-matrix approach, an integral equation approach for solving scattering problems, was proposed by Waterman[9] in 1969, Peterson and Ström[10] applied the approach to some multiple-scatterer problems in 1974. A two-scatterer problem is first solved by the T-matrix approach, which gives the total T-matrix for the assemblage. From this total T-matrix, contributions from each scatterer are then identified and interpreted in a way that is similar to the "orders of scattering" in the present formulation. Extension to the case of arbitrary number of scatterers then follows, and the explicit result is given only for the case of 3 scatterers, which is already quite mathematically involved.

Another approach was used by Bose and Mal[11, 12]. In this approach, all the wave fields are expressed in *every* scatterer's local coordinate system, and the direct application of the boundary conditions to the perimeter of every scatterer yields a system of equations for the wave expansion coefficients which is then solved to obtain the final results. This approach is purely mathematical.

The limitation which makes the multiple-scattering solutions in [3], [10] and [11, 12] difficult to extend to large numbers and dissimilar scatterers is the fact

that some kind of boundary value problems have to be solved, either at every order of scattering as in [3], or for the entire assemblage as in [10] and [11, 12]. In comparison, one of the clear advantages of the present formulation and of [4] is that the solution for the single-scatterer problem and the solution for the multiple-scatterer problem are cleanly separated as two problems. The use of the T-matrix notation lifts the burden of carrying out the mathematical manipulations in order to satisfy the boundary conditions, thus makes the formulation concise and yet versatile.

With the concept of the T-matrix, the present formulation can even be extended to consider abstract scatterers which may not be easily represented by a simple set of boundary conditions, as demonstrated by the developments in Chapter 6. This is the reason the current formulation is called a *formal* solution; it is not a complete solution without the single-scatterer solution; yet it remains the same form for different scatterers.

Another demonstrated advantage of the present formulation is that the solution forms remain unchanged for both the SH wave case and P/SV wave case. This greatly eases the implementation of the solution.

References

[1] G.N.Watson, *Treaties of Theory of Bessel Functions,* 2nd edn., Cambridge University Press, London, 1945.

[2] M. Abramowiz, I. Stegun, *Handbook of Mathematical Functions,* Dover, New York, 1965.

[3] V. Twersky, Multiple scattering of radiation by an arbitrary configuration of parallel cylinders *J. Acoust. Soc. Am.,* **24**, 42–46, 1952.

[4] V. K. Varadan, V. V. Varadan, Y.-H. Pao, Multiple scattering of elastic waves by cylinders of arbitrary cross section. I. SH waves, *J. Acoust. Soc. Am.,* **63**, 1310–1319, 1978.

[5] M. F. McCarthy, M. M. Carrol, Multiple scattering of SH waves by randomly distributed dissimilar scatterers, In *Wave Phenomena: Modern Theory and Applications,* C. Rogers, T. B. Moodie eds., pp. 433–451, Elisver-Science Publishers, North-Holland, 1984.

[6] V. V. Varadan, V. K. Varadan, Configurations with finite number of scatterers — A Self-Consistent T-Matrix Approach, *J. Acoust. Soc. Am.,* **70**, 213–217, 1981.

[7] V. K. Varadan, Y. Ma, V. V. Varadan, Multiple scattering of compressional and shear waves by fiber reinforced composite materials, *J. Acoust. Soc. Am.,* **80**, 333–339, 1986.

[8] S. L. Cheng, Multiple Scattering of elastic waves by parallel cylinders, *Trans. ASME, J. Appl. Mech.,* **36**, 523–527, 1969.

[9] P. C. Waterman, New formulation of acoustic scattering, *J. Acoust. Soc. Am.,* **45**, 1417–1429, 1969.

[10] B. Peterson, S. Ström, Matrix formulation of acoustic scattering from an arbitrary number of scatterers, *J. Acoust. Soc. Am.,* **56**, 771–780, 1974.

[11] S.K.Bose, A.K.Mal, Longitudinal Shear Waves in a Fiber-Reinforced Composite, *Int. J. Solids & Struct.,* **9**, 1075–1085, 1973.

[12] S.K.Bose, A.K.Mal, Elastic Waves in a Fiber-Reinforced Composite, *J. Mech. Phys. Solids,* **22**, 217–229, 1974.

Appendix

4-A Coordinate Transformation for Displacements, Stresses and Strains

Consider first a general coordinate transformation between two Cartesian coordinate systems $Oxyz$ and $Ox'y'z'$. The coordinate system $Ox'y'z'$ is generated by rotating the $Oxyz$ frame about the z axis counterclockwise by an angle α.

It can be found that such a coordinate transformation is represented by the following coordinate transformation matrix $[\alpha]$:

$$[\alpha] = \begin{bmatrix} \cos\alpha & -\sin\alpha & 0 \\ \sin\alpha & \cos\alpha & 0 \\ 0 & 0 & 1 \end{bmatrix} \quad \text{and} \quad [\alpha]^{-1} = [\alpha]^T \tag{4-A.1}$$

such that any vector $\{v\}$ in the $Oxyz$ is transformed into $\{v'\}$ in in the $Ox'y'z'$ coordinate system by

$$\{v\} = [\alpha]\{v'\} \quad \text{and} \quad \{v'\} = [\alpha]^T\{v\} \tag{4-A.2}$$

In such a context, a *transformation* means the relation between different expressions for the same physical quantity (vector). It can also be found that any tensor of second rank $[t]$, such as stress and strain tensors, in the $Oxyz$ frame is transformed into $[t']$ in the $Ox'y'z'$ frame according to

$$[t] = [\alpha][t'][\alpha]^T \quad \text{and} \quad [t'] = [\alpha]^T[t][\alpha] \tag{4-A.3}$$

Next, consider the coordinate transformation for displacements, stresses and strains between a polar coordinate system and a Cartesian coordinate system, whose coordinates are denoted as (r,θ) and (x,y), respectively. Assume the two coordinate systems shares the same origin, and $\theta = 0$ is along the $+x$ direction, as sketched in Fig. 4–8.

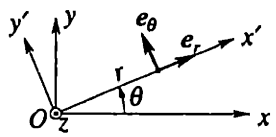

Fig. 4–8 Transformation between a Cartesian coordinate system and a polar coordinate system.

By definition, in a Cartesian coordinate system, the components of a displacement vector, u_x, u_y and u_z, represent the displacements at a point along the x, y and z axes, respectively. In a polar coordinate system, the displacement components u_r, u_θ and u_z are displacements along the radial, azimuthal and the z directions, respectively.

Note that the coordinate system is only referred for its directions in the definition for the displacement vector. The same is true for the definitions of the stress and the strain tensors.

Also note that polar coordinate system is a curvillinear coordinate system; that is, at every point (r,θ), unit vectors for each coordinate, such as e_r and e_θ in Fig. 4–8 representing the radial and the azimuthal directions, respectively, are perpendicular to each other.

When only the directions of the coordinates are concerned, in fact, the directions of the unit vectors of the polar coordinate system at point (r,θ) are the same as those of a Cartesian coordinate system, denoted as $Ox'y'z'$ in Fig. 4–8, which is formed by rotating the $Oxyz$ frame counterclockwise by an angle θ, the azimuthal coordinate. Furthermore, the transformations between the Cartesian coordinate system $Oxyz$ and the polar coordinate system for the point (r,θ) is represented by the matrix given in eqn. (4-A.1), except that α is replaced by θ.

Therefor, the following coordinate transformation relations for displacement, stresses and strains can be obtained, in analogy to eqns. (4-A.2) and (4-A.3):

$$\begin{Bmatrix} u_x \\ u_y \\ u_z \end{Bmatrix} = \begin{bmatrix} \cos\theta & -\sin\theta & 0 \\ \sin\theta & \cos\theta & 0 \\ 0 & 0 & 1 \end{bmatrix} \begin{Bmatrix} u_r \\ u_\theta \\ u_z \end{Bmatrix} \tag{4-A.4}$$

$$\begin{bmatrix} \sigma_{xx} & \tau_{xy} & \tau_{xz} \\ \tau_{yx} & \sigma_{yy} & \tau_{yz} \\ \tau_{zx} & \tau_{zy} & \sigma_{zz} \end{bmatrix} = \begin{bmatrix} \cos\theta & -\sin\theta & 0 \\ \sin\theta & \cos\theta & 0 \\ 0 & 0 & 1 \end{bmatrix} \begin{bmatrix} \sigma_{rr} & \tau_{r\theta} & \tau_{rz} \\ \tau_{\theta r} & \sigma_{\theta\theta} & \tau_{\theta z} \\ \tau_{zr} & \tau_{z\theta} & \sigma_{zz} \end{bmatrix} \begin{bmatrix} \cos\theta & \sin\theta & 0 \\ -\sin\theta & \cos\theta & 0 \\ 0 & 0 & 1 \end{bmatrix} \tag{4-A.5}$$

$$\begin{bmatrix} \varepsilon_{xx} & \varepsilon_{xy} & \varepsilon_{xz} \\ \varepsilon_{yx} & \varepsilon_{yy} & \varepsilon_{yz} \\ \varepsilon_{zx} & \varepsilon_{zy} & \varepsilon_{zz} \end{bmatrix} = \begin{bmatrix} \cos\theta & -\sin\theta & 0 \\ \sin\theta & \cos\theta & 0 \\ 0 & 0 & 1 \end{bmatrix} \begin{bmatrix} \varepsilon_{rr} & \varepsilon_{r\theta} & \varepsilon_{rz} \\ \varepsilon_{\theta r} & \varepsilon_{\theta\theta} & \varepsilon_{\theta z} \\ \varepsilon_{zr} & \varepsilon_{z\theta} & \varepsilon_{zz} \end{bmatrix} \begin{bmatrix} \cos\theta & \sin\theta & 0 \\ -\sin\theta & \cos\theta & 0 \\ 0 & 0 & 1 \end{bmatrix} \tag{4-A.6}$$

The expanded form of these transformations are

$$u_x = u_r\cos\theta - u_\theta\sin\theta \tag{4-A.7}$$

$$u_y = u_r\sin\theta + u_\theta\cos\theta \tag{4-A.8}$$

$$\sigma_{xx} = \sigma_{rr}\cos^2\theta - \tau_{r\theta}\sin 2\theta + \sigma_{\theta\theta}\sin^2\theta \tag{4-A.9}$$

$$\sigma_{yy} = \sigma_{rr}\sin^2\theta + \tau_{r\theta}\sin 2\theta + \sigma_{\theta\theta}\cos^2\theta \tag{4-A.10}$$

$$\sigma_{zz} = \sigma_{zz} \tag{4-A.11}$$

$$\tau_{xy} = \tau_{yx} = \tfrac{1}{2}(\sigma_{rr} - \tau_{\theta\theta})\sin 2\theta + \tau_{r\theta}\cos 2\theta \tag{4-A.12}$$

$$\tau_{xz} = \tau_{zx} = \tau_{rz}\cos\theta - \tau_{\theta z}\sin\theta \tag{4-A.13}$$

$$\tau_{yz} = \tau_{zy} = \tau_{rz}\sin\theta + \tau_{\theta z}\cos\theta \tag{4-A.14}$$

$$\varepsilon_{xx} = \varepsilon_{rr}\cos^2\theta - \varepsilon_{r\theta}\sin 2\theta + \varepsilon_{\theta\theta}\sin^2\theta \tag{4-A.15}$$

$$\varepsilon_{yy} = \varepsilon_{rr}\sin^2\theta + \varepsilon_{r\theta}\sin 2\theta + \varepsilon_{\theta\theta}\cos^2\theta \tag{4-A.16}$$

$$\varepsilon_{zz} = \varepsilon_{zz} \tag{4-A.17}$$

$$\varepsilon_{xy} = \varepsilon_{yx} = \tfrac{1}{2}(\varepsilon_{rr} - \varepsilon_{\theta\theta})\sin 2\theta + \varepsilon_{r\theta}\cos 2\theta \tag{4-A.18}$$

$$\varepsilon_{xz} = \varepsilon_{zx} = \varepsilon_{rz}\cos\theta - \varepsilon_{\theta z}\sin\theta \tag{4-A.19}$$

$$\varepsilon_{yz} = \varepsilon_{zy} = \varepsilon_{rz}\sin\theta + \varepsilon_{\theta z}\cos\theta \tag{4-A.20}$$

For strains, sometimes engineering strains are used. These two set of strains differ at the shear strain components, with the engineering shear strains being twice the corresponding shear strain components of the tensor strain. Conventionally, the engineering shear strains are denoted by γ while the components of the strain tensor are denoted as ε. Engineering strain is not a tensor and thus cannot be transformed using the relation is eqn. (4-A.6). But the transformation can be derived from the transformation relation for the strain tensor as following:

$$\varepsilon_{xx} = \varepsilon_{r_ir}\cos^2\theta - \tfrac{1}{2}\gamma_{r\theta}\sin 2\theta + \varepsilon_{\theta\theta}\sin^2\theta \tag{4-A.21}$$

$$\varepsilon_{yy} = \varepsilon_{rr}\sin^2\theta + \tfrac{1}{2}\gamma_{r\theta}\sin 2\theta + \varepsilon_{\theta\theta}\cos^2\theta \tag{4-A.22}$$

$$\varepsilon_{zz} = \varepsilon_{zz} \tag{4-A.23}$$

$$\gamma_{xy} = \gamma_{yx} = (\varepsilon_{rr} - \varepsilon_{\theta\theta})\sin 2\theta + \gamma_{r\theta}\cos 2\theta \tag{4-A.24}$$

$$\gamma_{xz} = \gamma_{zx} = \gamma_{rz}\cos\theta - \gamma_{\theta z}\sin\theta \tag{4-A.25}$$

$$\gamma_{yz} = \gamma_{zy} = \gamma_{rz}\sin\theta + \gamma_{\theta z}\cos\theta \tag{4-A.26}$$

The inverse transformations are

$$u_r = u_x\cos\theta + u_y\sin\theta \tag{4-A.27}$$

$$u_\theta = -u_x\sin\theta + u_y\cos\theta \tag{4-A.28}$$

$$\sigma_{rr} = \sigma_{xx}\cos^2\theta + \tau_{xy}\sin 2\theta + \sigma_{yy}\sin^2\theta \tag{4-A.29}$$

$$\sigma_{\theta\theta} = \sigma_{xx}\sin^2\theta - \tau_{xy}\sin 2\theta + \sigma_{yy}\cos^2\theta \tag{4-A.30}$$

$$\sigma_{zz} = \sigma_{zz} \tag{4-A.31}$$

$$\tau_{r\theta} = \tau_{\theta r} = \tfrac{1}{2}(\sigma_{yy} - \sigma_{xx})\sin 2\theta + \tau_{xy}\cos 2\theta \tag{4-A.32}$$

$$\tau_{rz} = \tau_{zr} = \tau_{xz}\cos\theta + \tau_{yz}\sin\theta \tag{4-A.33}$$

$$\tau_{\theta z} = \tau_{z\theta} = -\tau_{xz}\sin\theta + \tau_{yz}\cos\theta \tag{4-A.34}$$

$$\varepsilon_{rr} = \varepsilon_{xx}\cos^2\theta + \varepsilon_{xy}\sin 2\theta + \varepsilon_{yy}\sin^2\theta \tag{4-A.35}$$

$$\varepsilon_{\theta\theta} = \varepsilon_{xx}\sin^2\theta - \varepsilon_{xy}\sin 2\theta + \varepsilon_{yy}\cos^2\theta \tag{4-A.36}$$

$$\varepsilon_{zz} = \varepsilon_{zz} \tag{4-A.37}$$

$$\varepsilon_{r\theta} = \varepsilon_{\theta r} = \tfrac{1}{2}(\varepsilon_{yy} - \varepsilon_{xx})\sin 2\theta + \varepsilon_{xy}\cos 2\theta \tag{4-A.38}$$

$$\varepsilon_{rz} = \varepsilon_{zr} = \varepsilon_{xz}\cos\theta + \varepsilon_{yz}\sin\theta \tag{4-A.39}$$

$$\varepsilon_{\theta z} = \varepsilon_{z\theta} = -\varepsilon_{xz}\sin\theta + \varepsilon_{yz}\cos\theta \tag{4-A.40}$$

$$\varepsilon_{rr} = \varepsilon_{xx}\cos^2\theta + \tfrac{1}{2}\gamma_{xy}\sin 2\theta + \varepsilon_{yy}\sin^2\theta \tag{4-A.41}$$

$$\varepsilon_{\theta\theta} = \varepsilon_{xx}\sin^2\theta - \tfrac{1}{2}\gamma_{xy}\sin 2\theta + \varepsilon_{yy}\cos^2\theta \tag{4-A.42}$$

$$\varepsilon_{zz} = \varepsilon_{zz} \tag{4-A.43}$$

$$\gamma_{r\theta} = \gamma_{\theta r} = (\varepsilon_{yy} - \varepsilon_{xx})\sin 2\theta + \gamma_{xy}\cos 2\theta \tag{4-A.44}$$

$$\gamma_{rz} = \gamma_{zr} = \gamma_{xz}\cos\theta + \gamma_{yz}\sin\theta \tag{4-A.45}$$

$$\gamma_{\theta z} = \gamma_{z\theta} = -\gamma_{xz}\sin\theta + \gamma_{yz}\cos\theta \tag{4-A.46}$$

Next, consider the coordinate transformation between a Cartesian coordinate system and a polar coordinate system, but the two do not share the same origin. The origin of the polar coordinate system is located at point (X, Y) in the cartesian coordinate system, as sketched in Fig. 4–9. It can be observed from Fig. 4–9, as long θ is measured from the $+x$ direction, the location of the origin of the polar coordinate system actually does not matter. Therefore, the coordinate transformations given in eqns. (4-A.4) through (4-A.46) are still valid for such case.

Lastly, consider the coordinate transformation for two polar coordinate systems that do not share the same origin, as sketched in Fig. 4–10. The coordinates for the two polar coordinate systems are denoted as (r_1, θ_1) and (r_2, θ_2). Denote the origin of the coordinate system (r_2, θ_2) is located at point (R, Θ) in the coordinate system (r_1, θ_1).

For this case, it can be observed from Fig. 4–10 that the angle between e_{r_1} and e_{r_2} is $\theta_2 - \theta_1$. More precisely, rotating e_{r_1} in the counterclockwise direction by the amount $\theta_2 - \theta_1$ gives the direction of e_{r_2}. Therefore, the coordinate transformation between these two polar

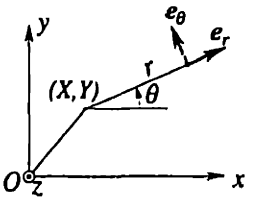

Fig. 4–9 Relation between a Cartesian coordinate system and a polar coordinate system that do not share the same origin.

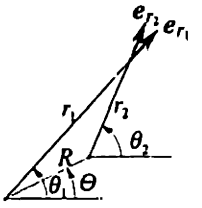

Fig. 4–10 Relation between two polar coordinate systems that do not share the same origin.

coordinate systems is obtained by replacing θ with $\theta_2 - \theta_1$ for the previous cases and taking the polar coordinate system (r_1, θ_1) as an analogy to the $Oxyz$ frame in the previous case. That is, for the displacement, for example, the relation is

$$\begin{Bmatrix} u_{r_1} \\ u_{\theta_1} \\ u_z \end{Bmatrix} = \begin{bmatrix} \cos(\theta_2 - \theta_1) & -\sin(\theta_2 - \theta_1) & 0 \\ \sin(\theta_2 - \theta_1) & \cos(\theta_2 - \theta_1) & 0 \\ 0 & 0 & 1 \end{bmatrix} \begin{Bmatrix} u_{r_2} \\ u_{\theta_2} \\ u_z \end{Bmatrix} \tag{4-A.47}$$

Transformations for the stress and strain tensors, which are similar to eqns. (4-A.5) and (4-A.6), respectively, and are omitted for brevity.

5

Implementation of Multiple-Scattering Solution

Abstract: *The implementation of the multiple-scattering solution is discussed in detail. Error estimates, truncation and convergence criteria are established, implementation strategies are devised, computer programs are developed, and computational characteristics are examined. Computer programs are then verified via the physical requirement of energy balance.*

Contents:

Nomenclature

General Conventions

- Matrices are denoted by bold-faced symbols; symbols for column matrices are enclosed by flower brackets ({}); symbols for rectangular matrices are enclosed by square brackets ([]).
- When referring to a matrix entry, the entry's indicial number is to appear as subscript(s) *outside* the brackets. This distinguishes the indicial subscript(s) from the subscript(s), if any, associated with the entire matrix.
- Super-matrices are denoted by the same symbols as those for the corresponding matrices, but set in a calligraphic font.

Symbols

a_i	The radius of Scatterer i; that is, the radius of the smallest circumscribing circle of Scatterer i centered at the origin of local coordinate system.
$\{\boldsymbol{A}_i\}, \{\boldsymbol{B}_i\}, \cdots$	Wave expansion coefficient (column) matrices for Scatterer i
d_{ij}	Distance between Scatterers i and j.
$H_n^{(1)}(x)$	Hankel function of the first kind and n-th order.
$\{\boldsymbol{H}(r_i, \theta_i)\}$	Singular (Hankel) wave expansion basis of Scatterer i.
$\hat{\imath}$	Unit of imaginary number, $\hat{\imath} = \sqrt{-1}$.
$J_n(x)$	Bessel function of the first kind and n-th order.
$\{\boldsymbol{J}(r_i, \theta_i)\}$	Regular wave expansion basis for Scatterer i, same as $\{\Re\boldsymbol{H}(r_i, \theta_i)\}$.
k	Wave number for the shear wave.
$[\boldsymbol{K}_i^{(p)}]$	The p-th order scattering kernel of Scatterer i.
$[\boldsymbol{L}_{ij}]$	Inductance matrix of Scatterer i on Scatterer j.
M	Truncation term of wave expansions.
N	Total number of scatterers.
$[\boldsymbol{R}_{ij}]$	Coordinate transformation matrix for expressing $\{\boldsymbol{H}(r_j, \theta_j)\}$ in Scatterer i's local coordinate system.
$[\boldsymbol{T}_i]$	"T-matrix" of Scatterer i.
(X_i, Y_i)	Global coordinates of the origin of Scatterer i's local coordinate system.
θ_{ij}	Azimuthal coordinate of o_j measured in the polar coordinate system local to Scatterer i (d_{ij} is the corresponding radial coordinate).

Superscripts

$(1), (2), \cdots (p)$	Order of the wave; step number of iteration for a variable solved by an iterative procedure
P	Characteristic of or pertinent to a longitudinal wave.
S	Characteristic of or pertinent to a shear wave.
ss	Scattered wave for the single scatterer case.
T	Matrix transposition.

Subscripts

i, j	Scatterer identifier.
m, n	Indicial number for a matrix entry.

5-1 Introduction

Beginning with this chapter, the considerations of this thesis are restricted to the case of SH wave scattering due to its simplicity. The case of SH wave scattering is simpler than the P/SV wave case the physical processes do not involve mode conversions and because the wave field ϕ that enters the multiple-scattering formulation is directly related to the displacement field.

This simplicity, however, does not trivialize the SH wave scattering problem. SH wave scattering is appropriate for modeling anti-plane wave scattering in solids; and the wave equation that describes SH wave scattering is mathematically identical to that for acoustic waves, which by themselves constitute an active area of research. In addition, as the formulations for SH and P/SV waves are almost identical, it is expected that once the computational structure for this simpler case has been explored, the close resemblance between the two formulations will be directly beneficial in establishing the computational structure of the P/SV wave case.

In this chapter, issues concerning the computer implementation of the multiple-scattering solution are addressed and some numerical examples are presented.

In the first part of this chapter, truncation errors of various solution components are estimated in Section 5-2, which leads to the establishment of the truncation and convergence criteria for the implementation. Some computational characteristics of the various solution forms presented in Chapter 4 are examined in Section 5-3. The programs implementing these solution forms are verified in Section 5-4. Verifications are based on the fundamental physical principle of energy conservation. Numerical examples are presented in the second part of this chapter. In Section 5-5, two approximate solutions are derived and numerical results are compared with exact solutions. In Section 5-6, a series of examples is used to demonstrate an interesting geometrical resonance phenomenon due to multiple-scatterering effects.

5-2 Error Analyses

In this section, order-of-magnitude estimates for errors incurred by truncating various matrices of infinite dimension are established. For brevity, mathematical notations defined in Chapter 4 are used without repeating their definitions. Based on these estimates, the truncation and the convergence criteria are then derived.

In the following error analyses, the O-notation is used in which $O(\phi)$ denotes the order of magnitude of the quantity ϕ. The O-notation allows replacing a complicated expression by a simpler one but having the same order of magnitude.

5-2.1 Truncation Errors

Definition and Assumptions

In the form of wave expansion, wave fields are expressed as infinite series. In order to perform a numerical computation, these series have to be truncated to a finite number of terms, thus *truncation errors* occur. Suppose a wave expansion is expressed as

$$\phi = \sum_{n=-\infty}^{\infty} \alpha_n \tag{5-1}$$

then, a *truncation at the M-th term* means using the partial sum from $n = -M$ up to M to approximate the exact value; that is,

$$\phi \approx \sum_{n=-M}^{M} \alpha_n \tag{5-2}$$

and M is called the *truncation term.* A generally accepted *order-of-magnitude* estimate of the truncation error is

$$\mathcal{E}(\phi; M) = O\left(\frac{|\alpha_{-M-1} + \alpha_{M+1}|}{\left|\sum_{n=-M}^{M} \alpha_n\right|}\right) \tag{5-3}$$

where $\mathcal{E}(\phi; M)$ denotes the order of magnitude of the truncation error incurred in computing the field quantity ϕ by truncating its wave expansion at the M-th term. If $O(\phi) = 1$, the above definition can be simplified as

$$\mathcal{E}(\phi; M) = O\left(|\alpha_{-M-1} + \alpha_{M+1}|\right) \tag{5-4}$$

With the matrix notation used in the solution, it is necessary to extend the above definition as follow: for a wave field ϕ having $O(\phi) \leq 1$,

$$\mathcal{E}(\phi; M) = O\left(\left\| \begin{bmatrix} \text{Result obtained with} \\ \text{matrices truncated at} \\ \text{size } M+1 \end{bmatrix} - \begin{bmatrix} \text{Result obtained with} \\ \text{matrices truncated at} \\ \text{size } M \end{bmatrix} \right\|\right) \tag{5-5}$$

where a *matrix truncated at size M* means that, for a square matrix, both row and column indices run from $-M$ to M, and for a column matrix, the row index runs from $-M$ to M.

In general, the field quantity ϕ varies from point to point throughout the plane, and so does $\mathcal{E}(\phi; M)$. It is assumed that the cross-sectional dimension of a scatterer does not vary significantly in any direction in the plane. Hence, the value of ϕ and its error evaluated at a scatterer's perimeter have the same order of magnitude as their corresponding values evaluated at the perimeter of the scatterer's territory (defined in Chapter 4). Furthermore, since the amplitude of a scattered wave in general decreases with distance from the scatterer, it suffices to estimate the error of a scattered wave at the perimeter of the territory of the scatterer. That is, if ϕ_i is a wave scattered by Scatterer i of radius a_i, it is assumed that at any field point,

$$O(\phi_i(r_i)) \leq O(\phi_i(a_i)) \qquad \text{and} \qquad \mathcal{E}(\phi_i(r_i); M) \leq \mathcal{E}(\phi_i(a_i); M) \tag{5-6}$$

where the field point is located at (r_i, θ) in the matrix medium.

Another necessary assumption concerns with the incident wave. For the plane incident wave of unit amplitude, the wave expansion is[1]

$$\phi = e^{ikx} = e^{ikr\cos\theta} = \sum_{n=-\infty}^{\infty} i^n J_n(kr) e^{in\theta} \tag{5-7}$$

which satidifes $|\{A_i\}_n| = 1$. For a general case, it is assumed that the incident wave can always be normalized such that

$$O(|\{A_i\}_n|) \leq 1 \tag{5-8}$$

Error of First Order Wave

The expression for the first order wave scattered by Scatterer i has been derived in Chapter 4 as

$$\phi_i^{(1)} = \{\boldsymbol{C}_i^{(1)}\}^T \{\boldsymbol{H}(r_i, \theta_i)\} = ([\boldsymbol{T}_i]\{\boldsymbol{A}_i\})^T \{\boldsymbol{H}(r_i, \theta_i)\} \tag{5-9}$$

This is the same as the single-scattering problem associated with Scatterer i.

Consider first a special case of the single-scatterer problem in which the wave expansion coefficients of the incident wave are: $\{A\}_n = 1$ and $\{A\}_m = 0$ when $m \neq n$, where n is an arbitrary integer; that is,

$$\phi_i^{ss \text{ inc}} = J_n(ka_i) e^{in\theta_i} \tag{5-10}$$

where the superscript ss denotes the *s*ingle-*s*catterer case. The corresponding scattered wave is

$$\phi_i^{ss \text{ s}} = \sum_{m=-\infty}^{\infty} [T_i]_{mn} \{H(r_i, \theta_i)\}_m \tag{5-11}$$

Since the amplitude of the scattered wave generally does not exceed that of the incident wave,

$$O\left(\sum_{m=-\infty}^{\infty} [T_i]_{mn} \{H(a_i, \theta_i)\}_m \right) \leq J_n(ka_i) \tag{5-12}$$

Next, consider the scatterer subjected to a general incident wave. By the definition in eqn. (5–5), the truncation error in computing the first order scattered wave as given in eqn. (5–9) is

$$\mathcal{E}(\phi_i^{(1)}(a_i); M) \leq O\left(\left| \sum_{m=-(M+1)}^{M+1} \sum_{n=-(M+1)}^{M+1} [T_i]_{mn} \{H(a_i, \theta_i)\}_m - \sum_{m=-M}^{M} \sum_{n=-M}^{M} [T_i]_{mn} \{H(a_i, \theta_i)\}_m \right| \right) \tag{5-13}$$

where eqn. (5–8) has been used. Combining eqns. (5–12) and (5–13) gives

$$\mathcal{E}(\phi_i^{(1)}(a_i); M) \leq O\left(J_{M+1}(ka_i)\right) \tag{5-14}$$

However, this estimate cannot be accurate when ka_i is near one of the zero points of the Bessel function $J_{M+1}(z)$. It is known (see, *e.g.*, [26] or [10]) that, for a fixed argument z, as the order n increases and exceeds the value of its argument ($n > z$), $J_n(z)$ approaches zero rapidly, and $Y_n(z)$ diverges at essentially the same rate such that $O(J_n(z)Y_n(z)) \approx 1$. This means, for a broad range of values of z,

$$O\left(J_n(z)\right) = O\left(\frac{1}{M_n(z)}\right) \tag{5-15}$$

where $M_n(z)$ is the modulus of the Hankel function $H_n^{(1)}(z)$ defined as

$$M_n(z) = \left|H_n^{(1)}(z)\right| = \sqrt{J_n^2(z) + Y_n^2(z)} \tag{5-16}$$

and it is known that $M_n(z)$ has no zero point. Thus, combining eqns. (5-6), (5-14) and (5-15) gives

$$\mathcal{E}(\phi_i^{(1)}; M) \leq O\left(\frac{1}{M_{M+1}(ka_i)}\right) \tag{5-17}$$

Error of Second Order Wave

Consider the truncation error in computing $\phi^{(2)}_{j \text{ due to } \phi_i^{(1)}}$, whose expression is given in Chapter 4 as

$$\phi^{(2)}_{j \text{ due to } \phi_i^{(1)}} = \left([\boldsymbol{L}_{ij}][\boldsymbol{T}_i]\{\boldsymbol{A}_i\}\right)^T \{\boldsymbol{H}(r_j, \theta_j)\} \tag{5-18}$$

By the definition of truncation error in eqn. (5-5),

$$\mathcal{E}\left(\phi^{(2)}_{j \text{ due to } \phi_i^{(1)}}(a_j); M\right) = O\left(\left| \sum_{m=-(M+1)}^{M+1} \sum_{n=-(M+1)}^{M+1} ([L_{ij}][T_i])_{mn}\{A_i\}_n\{H(a_j,\theta_j)\}_m \right.\right.$$
$$\left.\left. - \sum_{m=-M}^{M} \sum_{n=-M}^{M} ([L_{ij}][T_i])_{mn}\{A_i\}_n\{H(a_j,\theta_j)\}_m \right|\right) \tag{5-19}$$

In the order-of-magnitude sense, each term under the summation can be replaced by its respective modilus, and due to eqn. (5-8),

$$\mathcal{E}\left(\phi^{(2)}_{j \text{ due to } \phi_i^{(1)}}(a_j); M\right) = O\left(\sum_{m=-(M+1)}^{M+1} \sum_{n=-(M+1)}^{M+1} |[L_{ij}][T_i]|_{mn} M_m(ka_j) \right.$$
$$\left. - \sum_{m=-M}^{M} \sum_{n=-M}^{M} |[L_{ij}][T_i]|_{mn} M_m(ka_j) \right) \tag{5-20}$$

where $M_n(z)$ is the modulus of the Hankel function $H_n^{(1)}(z)$.

Define the following operator $S_j([\boldsymbol{P}]; M)$ for Scatterer j as

$$S_j([\boldsymbol{P}]; M) = \sum_{n=-(M+1)}^{M+1} \left[\left|[P]_{(M+1)n}\right| + \left|[P]_{(-M-1)n}\right|\right] M_{M+1}(ka_j)$$
$$+ \sum_{n=-M}^{M} \left[\left|[P]_{n(M+1)}\right| + \left|[P]_{n(-M-1)}\right|\right] M_n(ka_j) \tag{5-21}$$

Then eqn. (5–20) becomes

$$\mathcal{E}\left(\phi^{(2)}_{j \text{ due to } \phi_i^{(1)}}; M\right) \leq O\left(\mathcal{S}_j([\boldsymbol{L}_{ij}][\boldsymbol{T}_i]; M)\right) \tag{5-22}$$

According to Chapter 4, the total second order wave scattered by Scatterer j is

$$\phi_i^{(2)} = \sum_{\substack{j=1 \\ j\neq i}}^{N} \phi^{(2)}_{j \text{ due to } \phi_i^{(1)}} \tag{5-23}$$

Thus, from eqn. (5–22)

$$\mathcal{E}(\phi_j^{(2)}; M) \leq (N-1) \max_{\substack{j=1 \\ j\neq i}}^{N} O\left(\mathcal{S}_j([\boldsymbol{L}_{ij}][\boldsymbol{T}_i]; M)\right) \tag{5-24}$$

Error of Incident Wave via Graf's Addition Theorem

Form II of the solution involves an additional operation using Graf's addition theorem to transform $\{\boldsymbol{A}_j\}$ into Scatterer i's coordinates, such as

$$\phi^{\text{inc}} = \{\boldsymbol{A}_j\}^T \{\boldsymbol{H}(r_j, \theta_j)\} = \left([\Re \boldsymbol{R}_{ij}]\{\boldsymbol{A}_i\}\right)^T \{\boldsymbol{H}(r_i, \theta_i)\} \tag{5-25}$$

where the elements of $[\Re \boldsymbol{R}_{ij}]$ are, according to Chapter 4,

$$[\Re R_{ij}]_{nm} = \mathrm{e}^{i(n-m)\theta_{ij}} J_{n-m}(kd_{ij}) \tag{5-26}$$

According to eqn. (5–5), the truncation error for this operation can be written, for any incident wave that satisfies eqn. (5–8), as

$$\mathcal{E}(\phi^{\text{inc}}(a_i); M) = O\left(\sum_{m=-(M+1)}^{M+1} \sum_{n=-(M+1)}^{M+1} [\Re R_{ij}]_{mn} J_n(ka_i) - \sum_{m=-M}^{M} \sum_{n=-M}^{M} [\Re R_{ij}]_{mn} J_n(ka_i) \right) \tag{5-27}$$

Since $|J_n(z)|$ never exceeds unity and decreases as n increases, in an order-of-magnitude sense, the leading term of the difference of the sumations in eqn. (5–27) is

$$\mathcal{E}(\phi^{\text{inc}}(a_i); M) = O\left([\Re R_{ij}]_{0M} J_0(ka_i)\right) = O\left(J_M(kd_{ij})\right) \tag{5-28}$$

where eqn. (5–26) has been used. Combining eqns. (5–15) and (5–28) gives

$$\mathcal{E}(\phi^{\text{inc}}; M) = O\left(\frac{1}{M_M(kd_{ij})}\right) \tag{5-29}$$

5-2.2 Truncation Criteria

In Chapter 4, two solution forms have been given that are referred to as Form I and Form II. Within each form, a *recursive form* and an *implicit form* are given, with the addition of a *supermatrix form* in Form I. A recursive form follows the physical process of "ordered scattering". Implicit forms of the solution can be implemented as iterative solution procedures of the prediction–correction type.

Form I

Define the error tolerance for the total scattered wave in each order of the scattering as ϵ. Then, for each of the first two orders of waves not to exceed the error tolerance, from eqns. (5–17) and (5–24), the following respective conditions must be satisfied:

$$\max_{i=1}^{N} \frac{N}{M_{M+1}(ka_i)} < \epsilon \qquad \text{(First Order)} \qquad (5\text{–}30)$$

and

$$N(N-1)\left[\max_{\substack{i,j=1 \\ j\neq i}}^{N} \mathcal{S}_i\left([\boldsymbol{L}_{ij}][\boldsymbol{T}_i]; M\right)\right] < \epsilon \qquad \text{(Second Order)} \qquad (5\text{–}31)$$

Physically, since there are N scatterers and thus N first order scattered waves, the sum of all the first order scattered waves should not have an error that exceeds the error tolerance, and thus eqn. (5–30). Since there are $N(N-1)$ second order scattered waves such as $\phi^{(2)}_{j \text{ due to } \phi^{(1)}_i}$, eqn. (5–31) guarantees that the total second order scattered wave will not exceed the error tolerance.

Furthermore, recall that the generation of the second order waves is by the excitation of all first order waves, and the generation of all the higher order waves is by the same mechanism. Equation (5–31) also effectively ensures that, as long as the error in the excitation wave does not exceed the error tolerance, the error in the resulting higher order waves will not exceed the error tolerance.

Therefore, eqns. (5–30) and (5–31) comprise the truncation criteria for the recursive Form I of the solution. The implicit and the supermatrix forms of Form I are simply rearrangements of the recursive form, hence the same truncation criteria apply.

Form II

Form II of the solution involves an additional step to express the incident wave in different local coordinate systems via Graf's addition theorem, in which instance a truncation error is introduced. For the error not to exceed the error tolerance, according to the error estimate in eqn. (5–29), it is necessary that

$$\max_{\substack{i,j=1 \\ j\neq i}}^{N} \frac{1}{M_M(kd_{ij})} < \epsilon \qquad (5\text{–}32)$$

Therefore, eqns. (5–30), (5–31) and (5–32) comprise the truncation criteria for Form II of the solution, either recursive or implicit.

Supermatrix Form

The Supermatrix Form is simply a rearrangement of Implicit Form I, thus eqns. (5–30) and (5–31) are its truncation criteria.

5-2.3 Convergence Criteria

There are two types of convergence behaviors for repetitive solution forms. In a recursive solution procedure, waves in each order of scattering are calculated until at some order the amplitudes of the waves are less than the pre-established error tolerance. In an iterative procedure, the total wave is repeatedly calculated until the difference between two successive calculations is less then the pre-established error tolerance. Correspondingly, there are two types of convergence criteria.

Recursive Form I

If a recursive solution procedure is terminated at step P, the "ordered scattering" process is truncated at the P-th order of scattering. For N scatterers, the recursion can be said to have converged at the P-th step if the amplitude of the P-th order scattered wave scattered by any scatterer, say Scatterer j, is negligible; that is,

$$O\left(\phi_j^{(P)}\right) \leq O\left(\{\boldsymbol{C}_j^{(P)}\}^T\{\boldsymbol{H}(a_j,\theta_j)\}\right) \leq \frac{\epsilon}{N} \tag{5–33}$$

Since the elements of the singular wave expansion basis $\{H(a_j,\theta_j)\}_n$ are of order unity for small n, and diverge as n increases and exceeds ka_i, assuming the wave expansion converges, the following is used as an order-of-magnitude estimate of this wave:

$$O\left(\phi_j^{(P)}\right) = \left\|\{\boldsymbol{C}_j^{(P)}\}\right\|_\infty \tag{5–34}$$

where $\|\cdot\|_\infty$ denotes the *infinite norm* of a vector, which is the maximum modulus among all its elements (see, *e.g.*, SCHEID, 1968). Therefore, the convergence criterion for this solution form is

$$N\left\|\{\boldsymbol{C}_j^{(P)}\}\right\|_\infty \leq \epsilon \tag{5–35}$$

Recursive Form II

In this form, the computation is performed over multiple-scattering kernel matrices of various orders, from which the wave expansion coefficients can be obtained as

$$\{\boldsymbol{C}_j^{(p)}\} = [\boldsymbol{K}_j^{(p)}]\{\boldsymbol{A}_j\} \tag{5–36}$$

for any given incident wave. If the incident wave can be normalized to satisfy eqn. (5–8), according to eqn. (5–36), the convergence criterion for this solution form is

$$N \left\| [\overline{K}_j^{(P)}] \right\|_\infty \leq \epsilon \tag{5–37}$$

where the infinite norm for a matrix is defined as (see, *e.g.*, [7]) the maxmium value of the sum of the modulus of all the elements in any single row of the matrix.

Implicit Forms

For the implicit forms of the solution, the difference between the solutions at the P-th and the $(P-1)$-st steps essentially represents the P-th order scattering. Thus this difference can be used in place of the corresponding P-th order quantities for the respective recursive procedures. Specifically, for Implicit Form I,

$$N \left\| \{C_j\}^{(P)} - \{C_j\}^{(P-1)} \right\|_\infty \leq \epsilon \tag{5–38}$$

and for Implicit Form II,

$$N \left\| [K_j]^{(P)} - [K_j]^{(P-1)} \right\|_\infty \leq \epsilon \tag{5–39}$$

5-3 Computational Characteristics of Solutions

All the various solution forms presented in Chapter 4 are implemented. Programs are designed for computing a segment of the response spectrum, with a user-specified but presumed small frequency interval. In an iterative solution procedure (for an implicit solution form), the solution for the previous frequency is used as the initial prediction. In the event there is no previous result, the first order scattering is used as the initial prediction, in which case, an iterative solution procedure is effectively the same as a recursive procedure.

Algorithms for the current implementation are given in Appendix 5-A. Programs are written in C^{++} programming language. One of the advantages of this particular programming language is that two basic classes (data types), representing complex numbers and matrices, respectively, along with a large assortment of arithmetic operators for each class, can be built to facilitate the implementation..

Computations are performed on a Sun Microsystem Inc.'s SparcStation 5, with a 115 MHz CPU and an on-board memory size of 64 M (megabytes). Programs are compiled by Free Software Foundation's Gnu g^{++} compiler. The entire implementation is then ported to a Silicon Graphics Inc.'s (SGI's) Indigo^2 WorkStation, with a 150 MHz CPU and 64 M on-board memory, using SGI's standard C^{++} compiler.

In this section, some basic computational characteristics are examined through numerical examples. Since modeling fiber reinforced composites is the focus of this series, only cases involving identical scatterers are considered.

In particular, consider the two configurations that are the most commonly used micromechanics models for fiber reinforced composites — the 4-fiber square arrangement and the 7-fiber hexagonal arrangement, as shown in Figs. 5–1. Both

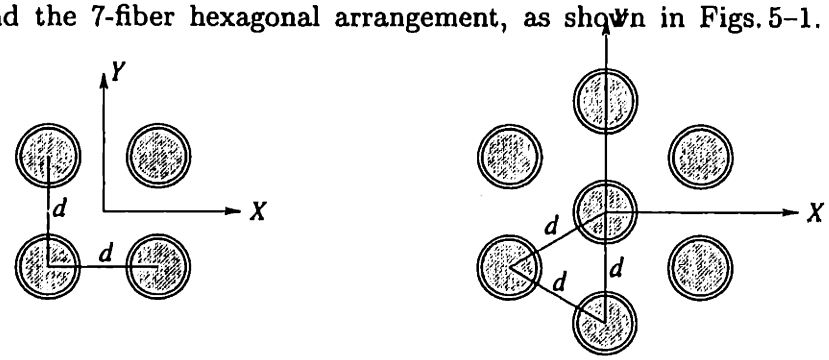

(*a*) Four-fiber square arrangement. (*b*) Seven-fiber hexagonal arrangement.

Fig. 5–1 Two types of arrangements to be considered in the following numerical results.

arrangements require only one parameter d, called the *fiber spacing*, to characterize their respective configuration.

The fibers are modeled as layered circular elastic cylinders in which the inner core represents the fiber and the outer layer represents the interphase between the fiber and the matrix. The single-scatterer problem for such a scatterer has been studied Chapter 2 in which a closed form analytical solution has been found. This solution, with minor rearrangements, gives the expression for the T-matrix according to the definition given in Chapter 3.

In the numerical examples, the same material properties as in Chapter 2, which correspond to a ceramic-fiber reinforced metal-matrix composite system, are used. For convenience, these data, as listed in Table 2–1, are repeated here in Table 5–1. Similar to Chapter 2, the fiber radius can be assumed as $a = 10\mu\text{m}$[3] when a specific value is desired. The correspondence between frequency, nondimensional frequency ka and wave lengths in different media is listed in Table 5–2. The fiber

Table 5–1: Constituent Material Properties for a Metal-Matrix Ceramic-Fiber Composite System[3]

Property	Matrix (AA520 Aluminium)	Fiber (Alumina, Al_2O_3)	Interphase (Zirconia, ZrO_2)
Density (kg/m^3)	2600	3700	6300
Young's Modulus (GPa)	66	360	97
Poisson's Ratio	0.31	0.25	0.33
Lamé Constant λ (GPa)	41	144	71
Lamé Constant μ (GPa)	25	144	37
P Wave Speed (m/s)	5920	10800	4800
S Wave Speed (m/s)	3100	6240	2420

Table 5–2: Correspondence Between Frequency, Nondimensional Frequency and Wavelengths for Composite System in Table 5–1 ($a = 10\mu$m).

ka	Frequency (MHz)	Wavelength λ (μm)	λ/a	λ_f/a	λ_i/a
1	49.35	62.83	6.283	12.64	3.838
2	98.70	31.42	3.142	6.320	1.919
5	246.8	12.57	1.257	2.528	0.7675
10	493.5	6.283	0.6283	1.264	0.3838
20	987.0	3.142	0.3142	0.6320	0.1919

radius is denoted as a, the outer radius of the interphase is assumed as $b = 1.1a$, and the nondimensionalized frequency ka is used throughout.

The incident wave is assumed as a plane wave of unit magnitude traveling in the $+X$ direction. The expression for the incident wave is given in eqn. (5–7). By writing the incident wave in the nondimensional form of eqn. (5–7), it is implied that all the field quantities ϕ have been normalized by the amplitude of the incident wave.

5-3.1 Truncation Term

Due to the difference in the truncation criteria, the truncation size M is different for Form I and Form II. They are denoted as M_I and M_{II}, respectively.

Figures 5–2 and 5–3 show the truncation terms M_I and M_{II}, respectively, for the 4-fiber square arrangement for various fiber spacings in the frequency range from $ka = 0.05$ to 10 with an interval of 0.05. The goal error tolerance is set as $\epsilon = 10^{-3}$. Figures 5–4 and 5–5 show simlar data for the 7-fiber hexagonal arrangement.

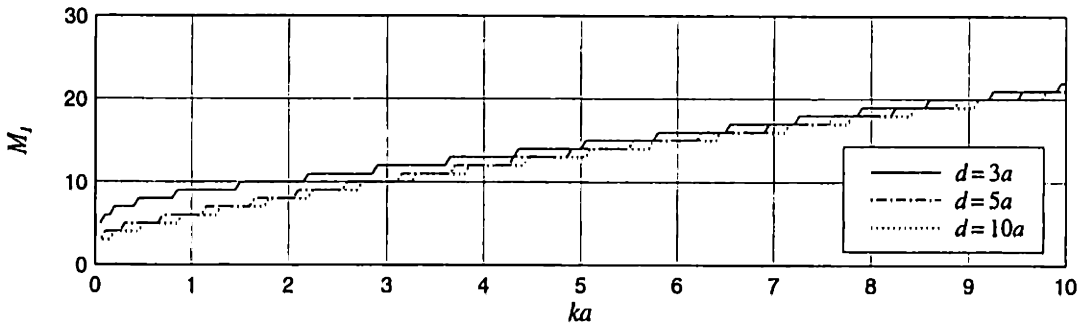

Fig. 5–2 Truncation term for Form I's, M_I, for the 4-fiber square arrangement at three different fiber spacings.

It is observed from Figs. 5–2 through 5–5 that, for a given problem configuration, the truncation size M for either Form I or Form II increases monotonically with increasing frequency.

The computations for the truncation sinzes M in Figs. 5–2 through 5–5 is slightly different from what has been described in the algorithms. In these computations,

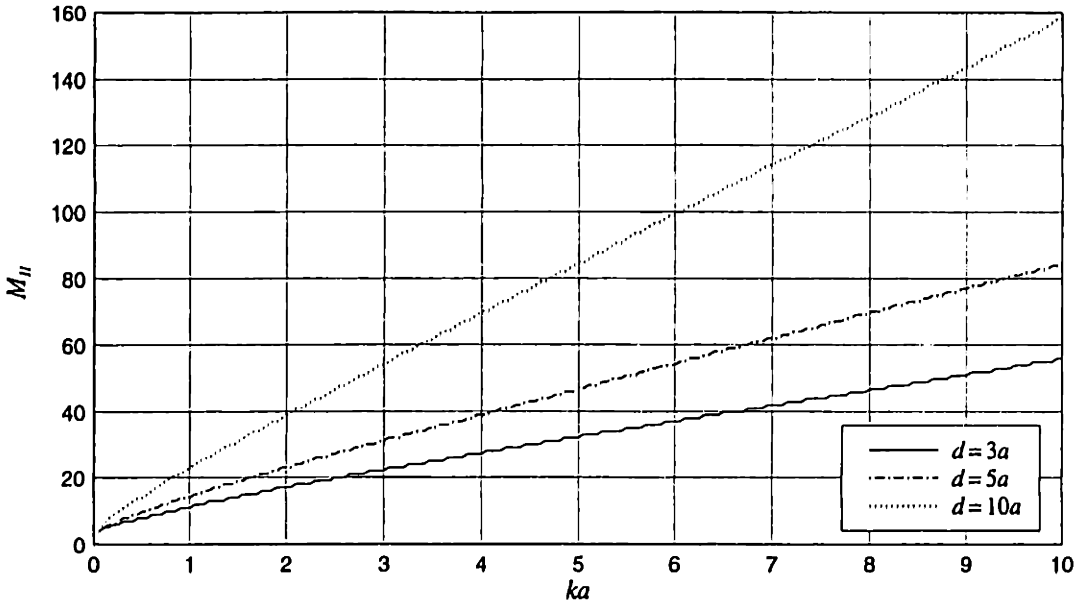

Fig. 5–3 Truncation term for Form II's, M_{II}, for the 4-fiber square arrangement at three different fiber spacings.

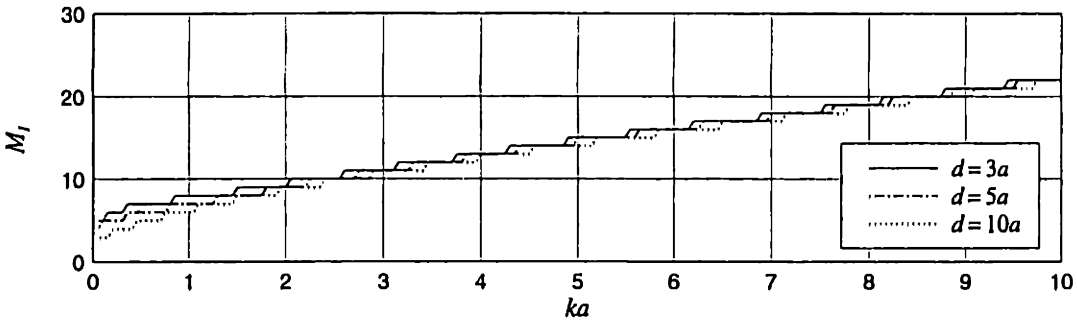

Fig. 5–4 Truncation term for Form I's, M_I, for the 7-fiber hexagonal arrangement at three different fiber spacings.

a small preset value of M is given for every frequency. The results in all cases show that, for a given problem configuration, the truncation term M increases monotonically as the frequency increases monotonically. This observation has been incorporated into the algorithms in the previous section, in which the value of M for the previous computation is taken as the preset value for the next computation.

For Form I, the normalized frequency ka plays the dominant role. Figures 5–2 and 5–4 show that the truncation size M_I increases almost linearly as the frequency increases in the range shown, and

$$M_I \approx 8 + 1.4ka \tag{5–40}$$

appears to be a good approximation, except in the low frequency range $ka < 1$. The effects of both the fiber spacing d and the number of fibers in the assemblage N are minimal. An increase in fiber spacing results in a slight decrease in M_I; and an

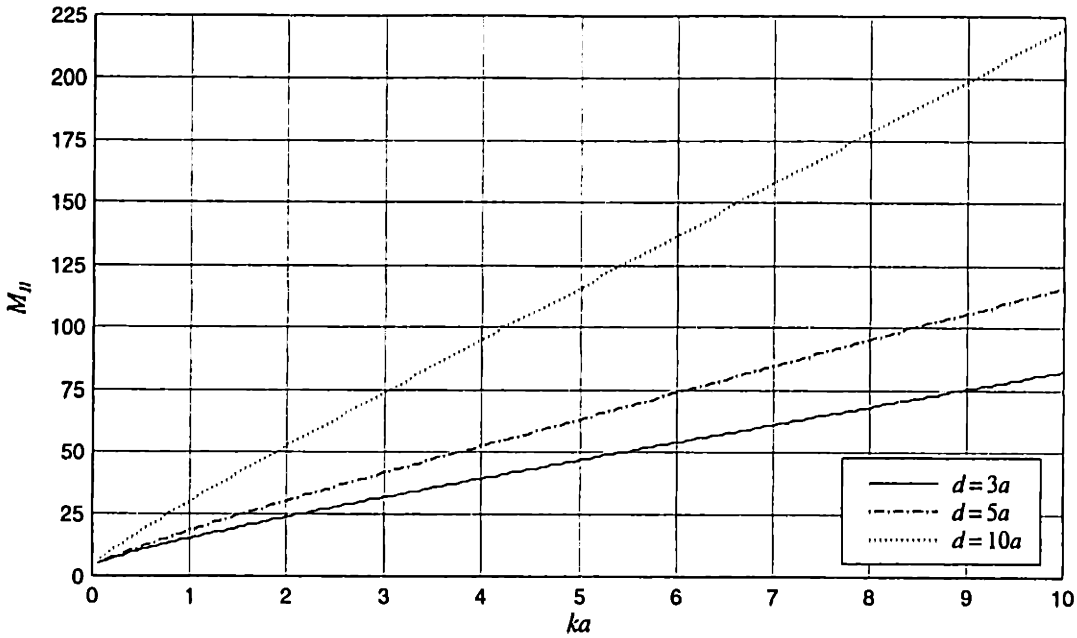

Fig. 5–5 Truncation term for Form II's, M_{II}, for the 7-fiber hexagonal arrangement at three different fiber spacings.

increase in the number of scatterers results in a slight increase in M_I.

The truncation sizes for Form II in Figs. 5–3 and 5–5 are substantially different from those for Form I in Figs. 5–2 and 5–4. This indicates that eqn. (5–32) solely determines the truncation size for Form II, with the possible exception in the low frequency range.

Equation (5–32) requires that $M_{M_{II}}(kD)$ be sufficiently large at the truncation size M_{II}, where D is the maximum distance between any two fibers throughout the configuration. It is known that, for a fixed argument z, when $n < z$, $O(M_n(z)) = 1$. As n increases and exceeds its argument ($n > z$), $M_n(z)$ diverges rapidly. The curves in Figs. 5–3 and 5–5 agree with this behavior: the values of M_{II} are always slightly larger than kD, namely

$$M_{II} \approx 10 + kD \tag{5–41}$$

5-3.2 Error Behaviors

There are two types of errors involved in most solution forms. One is associated with the truncation criteria and is thus referred to as the *truncation error*. The other is associated with the convergence criteria and is thus referred to as the *convergence-truncation error*.

Accurate Solutions

Since there are no exact numerical results available for the problems under consideration, prior to assessing any type of computational error, a set of accurate results must be established against which others are compared. Results obtained by the Supermatrix Form are chosen as candidates since they do not contain convergence-truncation errors.

In the Supermatrix Form, the following linear equation system

$$([\mathcal{I}] - [\mathcal{L}])\{\mathcal{C}\} = \{\mathcal{A}\} \tag{5-42}$$

is solved by some well established solvers, where $\{\mathcal{A}\}$, $\{\mathcal{C}\}$ and $[\mathcal{L}]$ are the supermatrices defined in Chapter 4. The following solvers have been implemented: Gaussian elimination solver, fully pivoted Gaussian elimination solver[4], LU-decomposition solver, and fully pivoted LU-decomposition solver (also called LUP-decomposition solver[4]). All these solvers belong to a class in which errors are entirely due to the computer's round-off errors. Note that all these solvers belong to a class of *direct method* in which the errors are entirely due to the computer's round-off errors. Among these solvers, pivoting is a technique to control and minimize the computer's round-off errors[4].

Table 1 lists the computed amplitudes of the total wave $|\phi^{\text{total}}|$ at an arbitrarily chosen point $(x, y) = (-1.5d, 0)$ and the associated errors, for both the 4-fiber and the 7-fiber configurations at $ka = 3$ for various fiber spacings. Errors are computed according to

$$\text{Error} = \left\| \{\mathcal{A}\} - ([\mathcal{I}] - [\mathcal{L}])\{\mathcal{C}\} \right\|_2 \tag{5-43}$$

where $\|\cdot\|_2$ denotes the *2-norm* (or *length*) of a vector, which is defined as the square root of the sum of the squares of the moduli of all its elements (see, *e.g.*, SCHEID, 1968).

Table 5–3 lists the computed amplitudes of the total wave $|\phi^{\text{total}}|$ at an arbitrarily chosen point $(x, y) = (-1.5d, 0)$ and the associated errors, for both the 4-fiber and the 7-fiber configurations at $ka = 3$ for various fiber spacings. Errors are computed according to

$$\text{Error} = \left\| \{\mathcal{A}\} - [\mathcal{I} - \mathcal{L}]\{\mathcal{C}\} \right\|_2 \tag{5-44}$$

where $\|\cdot\|_2$ denotes the *second norm* of a matrix, which is defined as, for a column matrix $\{v\}$, the square root of the sum of the squares of the moduli of all its elements (see, *e.g.*, R5:FS68):

$$\|\{v\}\|_2 = \sum_{n=-M}^{M} |\{v\}_n|^2 \tag{5-45}$$

It is observed from Table 5–3 that in every case, the results obtained by using different solvers are identical for all 6 significant figures. The errors are of order 10^{-14} to 10^{-15}, which are satisfactorily small, considering that the computer used in these computations is capable of producing only 15 significant figures.

Table 5–3: Comparison of Results Obtained by Using Different Linear Equation System Solvers in Supermatrix Form at $ka = 3$

Solver [a]	Fiber spacing	4-Fiber Arrangement		7-Fiber Arrangement	
		$\lvert\phi^{\text{total}}\rvert$	Error	$\lvert\phi^{\text{total}}\rvert$	Error
GE	$d = 3a$	0.799039	4.85335×10^{-15}	0.888485	1.86652×10^{-14}
	$d = 5a$	0.965366	2.26681×10^{-15}	0.885394	6.23928×10^{-15}
	$d = 10a$	0.995827	2.55399×10^{-15}	0.867470	5.69610×10^{-15}
PGE	$d = 3a$	0.799039	4.45122×10^{-15}	0.888485	1.36505×10^{-14}
	$d = 5a$	0.965366	1.82491×10^{-15}	0.885394	5.16508×10^{-15}
	$d = 10a$	0.995827	1.41674×10^{-15}	0.867470	6.75156×10^{-15}
LU	$d = 3a$	0.799039	2.75933×10^{-15}	0.888485	6.69867×10^{-15}
	$d = 5a$	0.965366	1.82500×10^{-15}	0.885394	5.39283×10^{-15}
	$d = 10a$	0.995827	2.31243×10^{-15}	0.867470	5.42291×10^{-15}
LUP	$d = 3a$	0.799039	4.25540×10^{-15}	0.888485	1.50270×10^{-14}
	$d = 5a$	0.965366	1.82500×10^{-15}	0.885394	5.39283×10^{-15}
	$d = 10a$	0.995827	2.31243×10^{-15}	0.867470	5.42291×10^{-15}

[a] GE: Gaussian elimination solver; PGE: fully pivoted Gaussian elimination solver; LU: LU-decomposition solver; LUP: fully pivoted LU-decomposition solver.

Therefore, with a sufficiently large truncation size, the results obtained via the Supermatrix Form can be considered as the accurate results for the resulting linear equation system, and contain only truncation errors.

It is often stated that Gaussian elimination and LU-decomposition methods should never be used without pivoting[4]. However, the results in Table 5–3, as well as the results from extensive computations performed for this study, demonstrated that the linear equation system in the Supermatrix Form, eqn. (5–42), in general is very well-behaved, as non-pivoted solvers do not degrade the solution accuracy in any significant way. In fact, for the cases of $d = 5a$ and $d = 10a$ solved by the LU-solver and the pivoted LU-solver, Table 5–3 lists not only identical results, but also identical errors for both solvers, suggesting that no benefit is obtained in the fully pivoted solution process. Since pivoting may significantly increase the time needed to solve an equation system, pivoting appears not to be necessary for such well-behaved systems.

Truncation Errors and Convergence-Truncation Errors

Suppose the truncation criteria require a truncation size of M for a given frequency and problem configuration, then three computations are performed that correspond to truncation sizes of $M/2$, M and $2M$. It is assumed that the wave expansions converge, and the larger the truncation size, the smaller the truncation error.

Tables 5–4 and 5–5 list the computed total wave field $|\phi^{\text{total}}|$ at the point $(-1.5d, 0)$ for the 4-fiber and the 7-fiber configurations, respectively, for various

Table 5–4: Comparison of Results Computed at Different Truncation Terms for Four-Fiber Square Arrangements at Different Fiber Spacings.

Solution Form	Fiber Spacing	Value of M	Computed $\lvert\phi^{\text{total}}(-1.5d, 0)\rvert$		
			$M/2$	M	$2M$
Recursive Form I	$d = 3a$	12	0.799003	0.799004	0.799004
Recursive Form II		21	0.912510	0.798868	0.798871
Implicit Form I		12	0.799007	0.799008	0.799008
Implicit Form II		21	0.912566	0.798952	0.798955
Supermatrix Form		12	0.799037	0.799039	0.799039
Recursive Form I	$d = 5a$	10	0.965208	0.965372	0.965372
Recursive Form II		31	0.966133	0.965379	0.965372
Implicit Form I		10	0.965202	0.965366	0.965366
Implicit Form II		31	0.966115	0.965361	0.965355
Supermatrix Form		10	0.965202	0.965366	0.965366

Table 5–5: Comparison of Results Computed At Different Truncation Terms for Seven-Fiber Hexagonal Arrangements at Different Fiber Spacings.

Solution Form	Fiber Spacing	Value of M	Computed $\lvert\phi^{\text{total}}(-1.5d, 0)\rvert$		
			$M/2$	M	$2M$
Recursive Form I	$d = 3a$	14	0.888351	0.888490	0.888490
Recursive Form II		30	0.865142	0.888498	0.888493
Implicit Form I		14	0.888342	0.888481	0.888481
Implicit Form II		30	0.865161	0.888524	0.888518
Supermatrix Form		14	0.888346	0.888485	0.888485
Recursive Form I	$d = 5a$	11	0.884871	0.885393	0.885393
Recursive Form II		42	0.954015	0.885392	0.885393
Implicit Form I		11	0.884874	0.885391	0.885391
Implicit Form II		42	0.954025	0.885395	0.885396
Supermatrix Form		11	0.884873	0.885394	0.885394

fiber spacings at the frequency $ka = 3$. Results for implicit forms are obtained by computing a small segment of a spectrum, from $ka = 2.95$ to 3 with an interval of 0.05, in which the result for $ka = 2.95$ is used as the initial prediction for the computation for $ka = 3$.

Tables 5–4 and 5–5 can be interpreted as follows. Results obtained by the Supermatrix Form with truncation size $2M$ are taken as the *accurate results*. For Form I, the two types of errors can be separated. Truncation errors are represented by the differences between the results obtained by the Supermatrix Form and the accurate results. The differences between the results of Form I and those of the Supermatrix Form using the same truncation sizes represent the convergence-truncation errors. For Form II, the two types of errors cannot be easily separated. But since the convergence criteria are the same for different truncation sizes, the differences between

Table 5–6: Memory Usages by Major Constituents in Different Solution Forms (Unit: size of a complex number in computer representation)

	Form I's	Form II's
$[\boldsymbol{L}_{ij}]$	$N(N-1)(2M_I+1)^2$	$N(N-1)(2M_{II}+1)^2$
$[\Re\boldsymbol{R}_{ij}]$	N/A	$N(N-1)(2M_{II}+1)^2$
$[\boldsymbol{T}_j]$	$N(2M_I+1)^2$	$N(2M_{II}+1)^2$
$\{\boldsymbol{A}_j\}$	$N(2M_I+1)$	—
$\{\boldsymbol{C}_j\}$	$N(2M_I+1)$	—
Other Intermediate Variables	$2N(2M_I+1)$	$3N(2M_{II}+1)^2$
Total (Approximate)	$\sim 4N^2M_I^2$	$\sim 8N(N+1)M_{II}^2$

N/A: The variable is not used in the solution form.

—: The variable is only need when some other variables that overall take a larger amount of memory can be freed, therefore the variable does not contribute the calculation of the problem size.

the results obtained by Form II at truncation size $2M$ and the accurate results represent the convergence-truncation errors. Thus, the differences between the results obtained by Form II and those of the Supermatrix Form using the same truncation sizes are primarily the truncation errors.

Tables 5–4 and 5–5 show that the truncation criteria for both Form I and Form II are sufficiently accurate. For Form I, results obtained by halving the truncation size are in general still accurate to the specified error tolerance. For Form II, results obtained by halving the truncation size do not always yield results that are satisfactorily accurate.

The convergence-truncation errors for all three truncation sizes are within the error tolerance. Therefore, the established convergence criteria for both Form I and Form II are adequate.

5-3.3 Problem Size and Solution Time

The *problem size* refers to the size of the computer memory required to solve the problem. Table 5–6 lists the sizes of the primary computer program constituents in each solution procedure. They represent the leading factors of the memory usage in the programs.

In Table 5–6, the "other intermediate variables" are those temporary matrices used in the core solution procedure. Specifically, for recursive forms, they include $\{\boldsymbol{C}_j^{\text{new}}\}$ and $\{\boldsymbol{C}_j^{\text{old}}\}$, and for implicit forms, they include $[\boldsymbol{K}_j]$, $[\boldsymbol{K}_j^{\text{new}}]$ and $[\boldsymbol{K}_j^{\text{old}}]$. The table lists the cases in which the T-matrices ares square matrices (not diagonal). In the summations to calculate the "total" line, smaller terms are dropped, and $(2M+1)$ is approximated as $2M$. Also note that, in terms of memory usage, the Supermatrix Form is a mere rearranged Recursive Form I and hence not listed.

Table 5–7: Problem Size for Four-Fiber Square Arrangement at $ka = 2$ and $d = 3a$ (Unit: size of a complex number in computer representation)

	Four-Fiber Square Arrangement		Seven-Fiber Square Arrangement	
	Form I's	Form II's	Form I's	Form II's
Truncation Term	$M_I = 12$	$M_{II} = 21$	$M_I = 14$	$M_{II} = 30$
$[L_{ij}]$	7,500	22,188	35,322	156,282
$[\Re R_{ij}]$	N/A	22,188	N/A	156,282
$[T_j]$	2,500	7,396	5,887	26,047
$\{A_j\}$	100	—	203	—
$\{C_j\}$	100	—	203	—
Other	200	22,188	406	78,141
Total	10,400	73,960	42,021	416,752

Table 5–7 lists the numerical values corresponding to Table 5–6 for both the 4-fiber and the 7-fiber arrangements at $ka = 3$ and $d = 3a$.

The truncation sizes M_I and M_{II} can be related to the problem parameters as, according to eqns. (5–40) and (5–41),

$$M_I \sim k \qquad M_{II} \sim kD \tag{5–46}$$

where "$\sim$" denotes the rate of growth when k or kD is very large. If the scatterers are clustered uniformaly in a region around the origin of the global coordinate system, then $D \sim \bar{d}\sqrt{N}$ where $\bar{d}$ represents the average distance between two neighboring scatterers. For such cases, according to Table 5–6, the problem sizes can be approximated as $\sim k^2N^2$ for Form I, and $\sim k^2N^3$ for Form II.

For the solution time, since there are many influencing variables, it is only fair to compare the net CPU time needed to perform one single step of the repetitive solution procedures. From the algorithms, within each repetitive step, Form I's only need to perform $N(N-1)$ products of a square matrix with a column matrix; whereas Form II's need to perform $2N(N-1)$ products of two square matrices.

Denote the time for an elementary manipulation, such as an addition or a multiplication, of real numbers as τ. A product of a square matrix with a column matrix requires $(2M+1)^2$ additions and $(2M+1)^2$ multiplications of complex numbers. It is estimated that a multiplication of two complex numbers takes about 6τ time and an addition of two complex numbers takes about 2τ. Thus, the total time for a product of a square matrix with a column matrix is roughly $8(2M_I+1)^2\tau \approx 32M_I^2\tau$. Similarly, a product of two square matrices requires $(2M+1)^3$ multiplications and $(2M+1)^3$ additions of complex numbers; that is, roughly $8(2M_{II}+1)^3\tau \approx 64M_{II}^3\tau$.

This implies that the computation time for each step in the Form I's and Form II's are $\sim N^2M_I^2$ and $\sim N^2M_{II}^3$, respectively. Again, in terms of the apparent physical parameters of the problem, they are roughly $\sim k^2N^2$ and $\sim k^3N^{4.5}$, respectively.

For the Supermatrix Form, the resulting linear equation system is of the size

Table 5–9: CPU Time for Every Step of Repetitive Solution Procedure for $ka = 2$ and $d = 3a$ for Different Fiber Arrangement (Unit: second)

Solution Form	Four-Fiber Square Arrangement	Seven-Fiber Hexagonal Arrangement
Recursive Form I	0.007	0.018
Implicit Form I	0.007	0.018
Recursive Form II	0.917	13.708
Implicit Form II	0.936	14.849
Supermatrix Form	0.760	2.970

$N(2M_I + 1) \times N(2M_I + 1)$ and the typical solution time is $\sim N^3 M_I^3$. In terms of apparent physical parameters, the solution time is $\sim k^3 N^3$.

Table 5–9 lists the time needed to perform one step of the repetitive solution procedure for various solution forms. The data shown are the computer's CPU time on the SGI's Indigo^2 averaged over 20 repetitive steps.

For comparison, the CPU time for the Supermatrix Form is also listed in Table 5–9. It is noted the times listed for this case have different meanings: they are the total times required to solve the linear equation system; whereas for all other cases, the times listed are for each step of repetition, and a typical computation may take from 10 to 200 repetitions.

Due to the structural similarity between two Form I's, the times for Form I's are identical. The times for the two Form II's are also very close. The difference is due to the fact that the Implicit Form II takes a little extra effort to perform a matrix subtraction in order to check the convergence criterion. Although a similar operation is also necessary for Implicit Form I, the difference between Implicit Form I and Recursive Form I is not observable.

In general, from Table 5–9 and from extensive computations performed for this study, differences in the CPU times between the Form I's and Form II's are huge. Overall, the times for the Supermatrix Form is comparable with the Form I's.

5-3.4 Convergence Behavior

Figures 5–6 and 5–7 show the numbers of steps needed for various repetitive solution procedures to achieve a converged solution for the 4-fiber square arrangement at $d = 3a$ and $5a$, respectively. The computations are performed at a frequency interval of 0.05. Figures 5–8 and 5–9 show the similar data for the 7-fiber hexagonal arrangement for the cases $d = 3a$ and $5a$, respectively.

Figures 5–6 and 5–7 show the numbers of steps needed for various repetitive solution procedures to achieve a converged solution for the 4-fiber configuration at $d = 3a$ and $d = 5a$, respectively. The computations are performed with a ka interval of 0.05. Figures 5–8 and 5–9 show the corresponding data for the 7-fiber

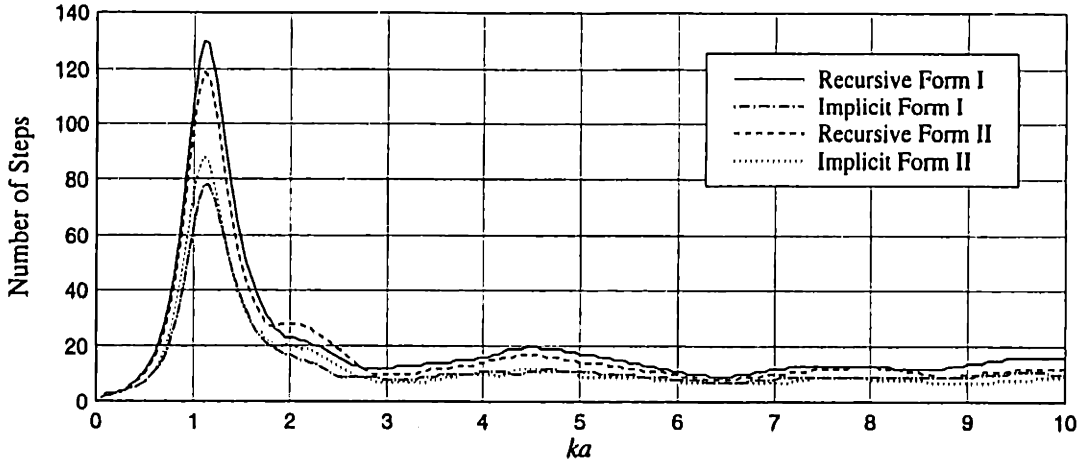

Fig. 5–6 Numbers of steps needed in repetitive solution procedures to achieve a converged solution for the case of 4-fiber square arrangement with fiber spacing $d = 3a$.

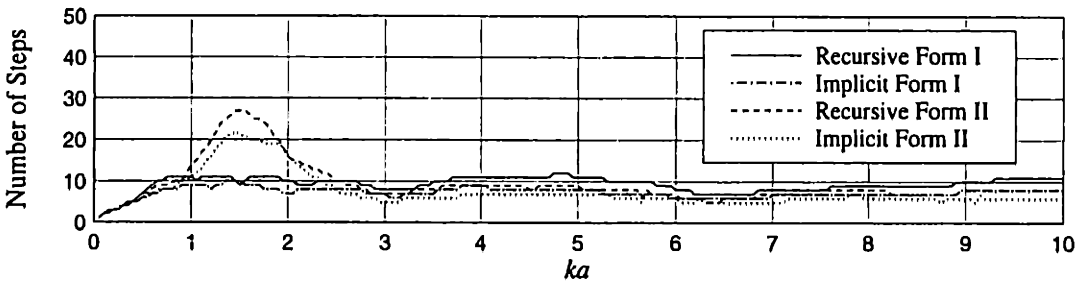

Fig. 5–7 Numbers of steps needed in repetitive solution procedures to achieve a converged solution for the case of 4-fiber square arrangement with fiber spacing $d = 5a$.

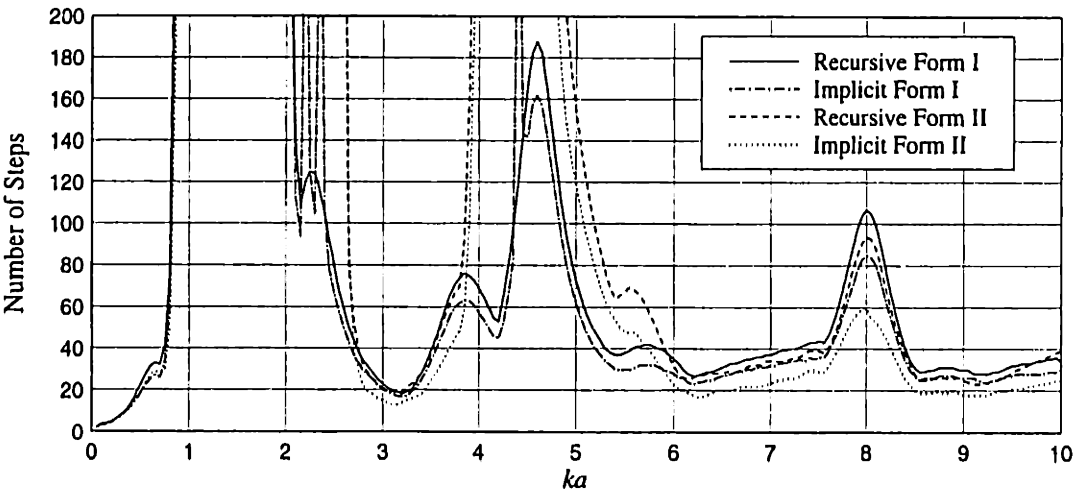

Fig. 5–8 Numbers of steps needed in repetitive solution procedures to achieve a converged solution for the case of 7-fiber hexagonal arrangement with fiber spacing $d = 3a$.

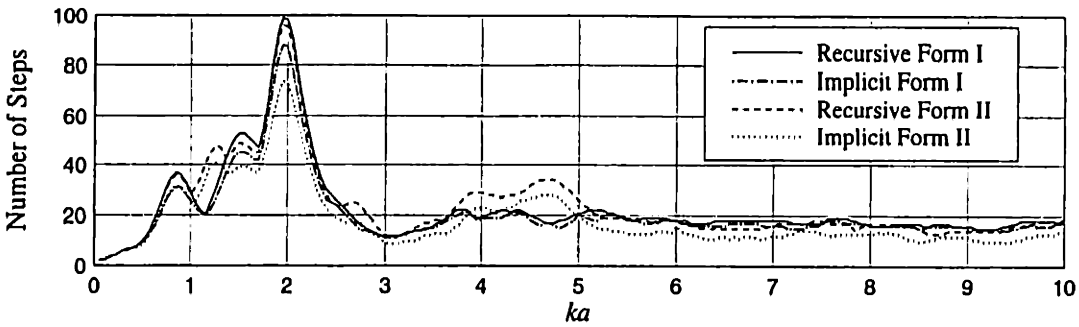

Fig. 5–9 Numbers of steps needed in repetitive solution procedures to achieve a converged solution for the case of 7-fiber hexagonal arrangement with fiber spacing $d = 5a$.

configuration for $d = 3a$ and $d = 5a$, respectively. It can be observed from Figs. 5–6 through 5–9 that the two recursive forms converge in nearly the same numbers of steps, and so do the two implicit forms. Also, in all repetitive solution forms, convergence is reached in fewer steps when the scatterers are located farther apart.

Unfortunately, it is also observed, for example, in Fig. 5–8 for the 7-fiber configuration with $d = 3a$, that there are ranges of frequencies in which repetitive procedures diverge. For Form I, the recursive form diverges in the frequency range $ka = 0.9$ to 2.05. The implicit form also diverges in this range, and additionally at $ka = 4.35$. For Form II, both recursive and implicit forms diverge in exactly the same ranges, $ka = 0.9$ to 2.7, and $ka = 3.95$ to 4.8.

Recall that the Supermatrix Form is obtained by a rearrangement of Implicit Form I. Hence, Implicit Form I as well as Recursive Form I, since they are structurally similar, are variants of the following iterative solution procedure:

$$\{\mathcal{C}\}^{(p)} = \{\mathcal{A}\} + [\mathcal{L}]\{\mathcal{C}\}^{(p-1)} \tag{5-47}$$

Equation (5–47) is the Jacobi method (see, *e.g.*, [5]) for solving the linear equation system in eqn. (5–42). The necessary and sufficient condition for the Jacobi method to converge is that the modulus of the dominant eigenvalue of the (super)matrix $[\mathcal{L}]$ must be smaller than unity.

The *dominant eigenvalue* λ, the eigenvalue of the largest modulus, and its associated eigenvector $\{\Lambda\}$ of matrix $[\mathcal{L}]$ can be determined by the *power method*[7]. In this method, for an almost arbitrary vector $\{v\}$ and a sufficiently large p, the vector $\{\Lambda\}^{(p)}$ as calculated according to

$$\{\Lambda\}^{(p)} = [\mathcal{L}]^p\{v\} \tag{5-48}$$

gives an approximation for $\{\Lambda\}$, and an approximation for λ is given by the following *Rayleigh's quotient*:

$$\lambda^{(p)} = \frac{\{\Lambda\}^{(p)^T}[\mathcal{L}]\{\Lambda\}^{(p)}}{\{\Lambda\}^{(p)^T}\{\Lambda\}^{(p)}} \tag{5-49}$$

The approximations become exact in the limit $p \to \infty$.

The power method can be implemented as following[6]. Select an arbitrary vector $\{v\}$ such that the largest modulus of its elements equals unity. Let $\{\Lambda\}^{(1)} = \{v\}$. Repeat the following computations

$$\{y\}^{(p+1)} = [\mathcal{L}]\{\Lambda\}^{(p)} \tag{5-50}$$

$$\{\Lambda\}^{(p+1)} = \frac{\{y\}^{(p+1)}}{||\{y\}^{(p+1)}||_\infty} \tag{5-51}$$

In the limit,

$$|\lambda| = \lim_{p\to\infty} \left|\left|\{y\}^{(p+1)}\right|\right|_\infty \qquad \{\Lambda\} = \lim_{p\to\infty} \{y\}^{(p+1)} \tag{5-52}$$

and λ is given by the element of $\{y\}^{(p+1)}$ that is of the largest moduluse. The computation can be terminated when the computed $|\lambda|$ converges within the prescribed error tolerance.

Although the choice for the starting vector $\{v\}$ is not completely arbitrary, this method almost always yields the correct dominant eigenvalue. The restriction for the choice of $\{v\}$ is that it should not be orthogonal to $\{\Lambda\}$. However, in most cases, even with an unfortunate choice of $\{v\}$ such that it is orthogonal to $\{\Lambda\}$, in the computation process, the computer's round-off errors will provide the non-orthogonal components that are vital for the computation to converge to the dominant eigenvalue. On the other hand, for a successful computation, a small error tolerance must be specified, since the convergence rate might be very slow, especially when the next-dominant eigenvalue has a very close modulus to the dominant eigenvalue.

Figures 5–10 and 5–11 show the modulus of the computed dominant eigenvalues $|\lambda|$ for the 4-fiber and the 7-fiber configurations, respectively. In the computations, the computation is terminated when the difference between $||\{y\}^{(p+1)}||_\infty$ and $||\{y\}^{(p)}||_\infty$ is smaller than 2×10^{-5}. It is observed that the computed dominant eigenvalues seem to be unaffected by the change of the truncation term M, as long as the truncation is accurate enough.

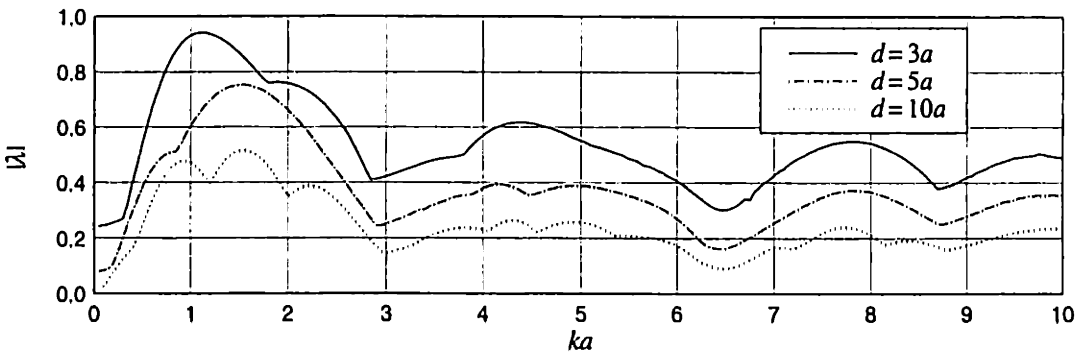

Fig. 5–10 Modulus of the computed dominant eigenvalue of the system matrix $[\mathcal{L}]$ for the 4-fiber square arrangement.

Comparing Figs. 5–8 and 5–11, a clear correlation between the condition $|\lambda| > 1$ and the divergence of Form II can be observed. The frequency ranges in which

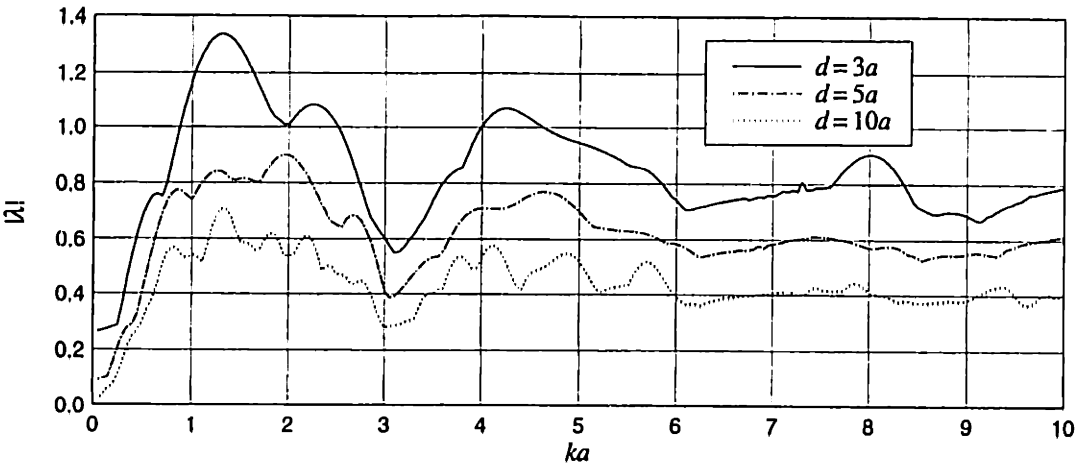

Fig. 5–11 Modulus of the computed dominant eigenvalue of the system matrix $[\mathcal{L}]$ for the 7-fiber hexagonal arrangement.

Form I diverges fall within the ranges in which $|\lambda| > 1$. But, interestingly, in some ranges, Form I converges though $|\lambda| > 1$. Comparing Figs. 5–6 through 5–9 and Figs. 5–10 and 5–11 shows that there is a clear correspondence between the number of repetitive steps needed to achieve convergence and the modulus of the dominant eigenvalue.

5-3.5 Summary

The characteristics of the computational structures observed in this section can be summarized as following:

- For a given problem configuration, the truncation size for Form I increases monotonically as the frequency increases and can be approximated as $M_I \approx 8 + 1.4ka$ when $ka > 1$. The truncation size for Form II also increases monotonically as the frequency increases, and can be approximated as $M_{II} \approx 10 + kD$ when $ka > 1$, where D is the maximum distance between any two scatterers in the configuration.
- The truncation and convergence criteria established are adequate.
- The growth rate of the problem size is $\sim N^2M^2$ where N is the number of scatterers and M is the truncation size. For a cluster of uniformly distributed scatterers, the problem size can be approximated as $\sim k^2N^2$ for Form I, and $\sim k^2N^3$ for Form II.
- For all the repetitive solution procedures, a converged solution is reached in fewer steps when the scatterers are located further apart. Unfortunately there are cases where repetitive solution procedures diverge.

- In general, the Supermatrix Form can be used even when all the repetitive solution forms fail. The linear equation system of the Supermatrix Form is generally well-behaved and can be solved by many well-established solvers. In many cases, pivoting can be avoided without significant errors.

5-4 Program Verifications

In this section, the computer programs for implementing the multiple-scattering solution are verified by performing various computations of energy conservation.

One of forms of the energy conservation principle that is frequently used in scattering problems is called the *energy balance requirement.* It requires that, for a closed surface (a closed path for a 2-dimensional problem) that encloses neither a source nor a sink, the total energy transmitted into the surface equals the total energy emitted from the surface. The mathematical expression for this requirement has been derived in Chapter 2. For a circular integration path of radius R centered at the origin of the global polar coordinate system, the energy balance requires

$$\int_{\mathcal{A}} \langle \dot{E} \rangle d\mathcal{A} = \frac{\omega R}{2} \int_0^{2\pi} Im \left\{ \Sigma_{rz} \overline{U}_z \right\}_{r=R} d\theta = 0 \tag{5-53}$$

where Σ_{rz} and U_z are the complex amplitudes of the stress component and the displacement component, respectively, the overbar denotes a complex conjugate, and $\langle \dot{E} \rangle$ is the time-averaged energy flux density function. Furthermore,

$$U_z = \phi^{\text{total}} \qquad \Sigma_{rz} = \sigma_{rz} = \mu \gamma_{rz} \tag{5-54}$$

where expressions for ϕ^{total} and γ_{rz} have been derived in Chapter 4.

Since the incident wave is given in normalized form in eqn. (5–7), the following normalized time-averaged energy flux density function

$$\langle \dot{e} \rangle = \frac{\langle \dot{E} \rangle}{\mu \left| \phi^{\text{inc}} \right|^2} = \frac{1}{\left| \phi^{\text{inc}} \right|^2} Im\{ \gamma_{rz} \overline{\phi^{\text{total}}} \} \tag{5-55}$$

is defined. Then, the energy balance requirement becomes

$$\int_0^{2\pi} \langle \dot{e} \rangle \Big|_{r=R} d\theta = 0 \tag{5-56}$$

where eqns. (5–54) and (5–55) have been used.

The integration is performed numerically as follows. The entire circular path is divided into a predetermined number of subdivisions S. Within each subdivision, it is assumed that both γ_{rz} and ϕ^{total} are constant, and the values at the center of the subdivision are taken as the respective average values for that subdivision. Thus,

the integration process is conducted in accordance with

$$I(R,\theta) = \frac{1}{|\phi^{\text{inc}}|}\int_0^{\theta} Im\left\{\gamma_{rz}\overline{\phi^{\text{total}}}\right\}_{r=R} d\theta$$

$$\approx \frac{2\pi}{S|\phi^{\text{inc}}|}\sum_{n=0}^{[\frac{\theta}{2\pi}S]} Im\left\{\gamma_{rz}\left(R,\frac{(2n+1)\pi}{S}\right)\overline{\phi^{\text{total}}}\left(R,\frac{(2n+1)\pi}{S}\right)\right\} \quad (5\text{–}57)$$

from $\theta = 0$ toward 2π. The energy balance requires $I(R, 2\pi) = 0$. The final non-zero value of $I(R, 2\pi)$ represents the cumulative error of the entire computation, from solving the multiple-scattering problem to the numerical integration.

Consider 4 examples. Unless otherwise noted, the multiple-scattering problem is solved via the Supermatrix Form, in which the linear equation system is solved by the LU-decomposition solver. The integration of eqn. (5–57) is performed over 720 intervals unless otherwise specified.

First, consider the 4-fiber configuration with a fiber spacing $d = 3a$ at the frequency $ka = 2$. Three integration paths, of radii $R = a$, $10a$ and $50a$, are chosen, as sketched in Fig. 5–12. The path with $R = a$ falls entirely within an area surrounded by the fibers. The paths with radii $10a$ and $50a$ represent the near-field and the far-field, respectively.

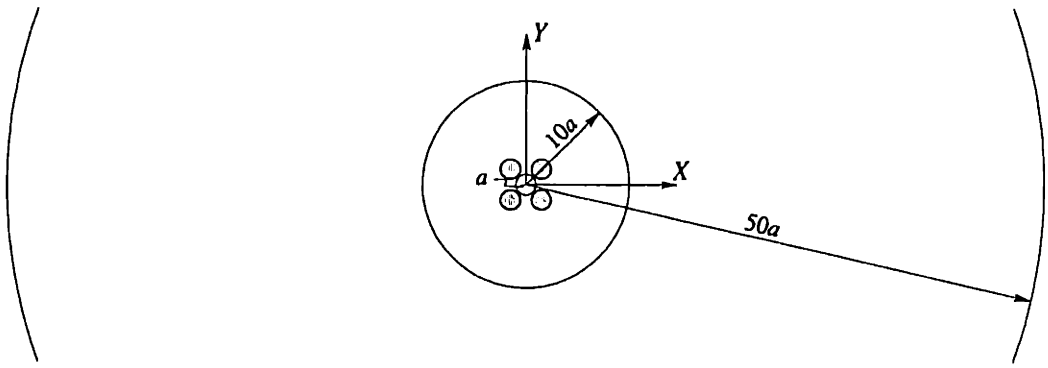

Fig. 5–12 Energy integration paths for the 4-fiber square arrangement.

Figure 5–13*a* shows the normalized time-averaged energy flux density function $\langle \dot{e} \rangle$ along the three integration paths, called the angular distributions of $\langle \dot{e} \rangle$. Figure 5–13*b* shows the corresponding integration processes along these paths. Since the problem is symmetric about the X-axis, only the results for the upper half plane, from $\theta = 0$ to π, are shown.

The computed final values of $|I(R, 2\pi)|$ are 1.76248×10^{-15}, 1.44624×10^{-14} and 1.51355×10^{-15} for the paths of radii $R = a$, $10a$ and $50a$, respectively. Since the computer used in this computation has only 15 significant figures, the small magnitudes of $|I(R, 2\pi)|$ mean that the errors are at the level of the computer's round-off errors. In other words, these computations are as accurate as the computer is capable of obtaining.

Table 5–10 shows the numerical values of $|I(R, 2\pi)|$ at the end of integration as

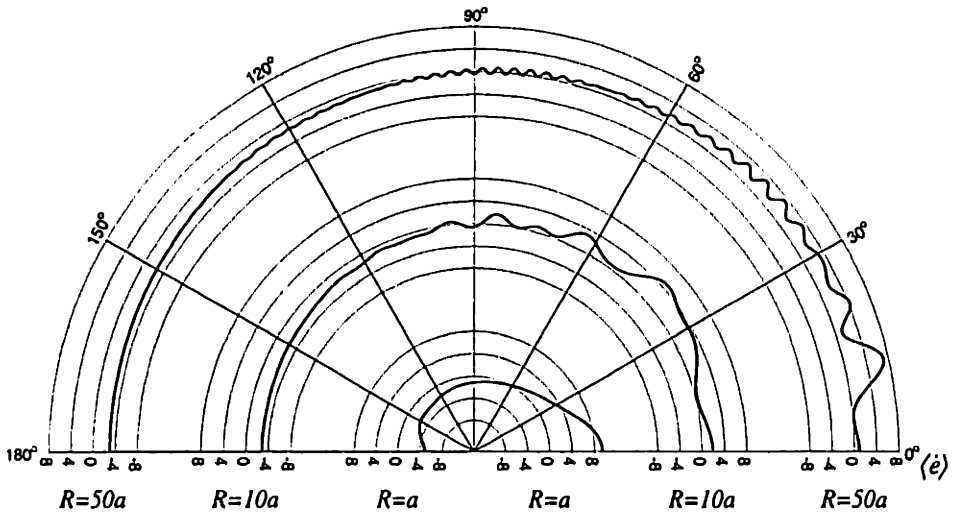

(*a*) Angular distributions of normalized time-averaged energy flux density function $\langle \dot{e} \rangle$.

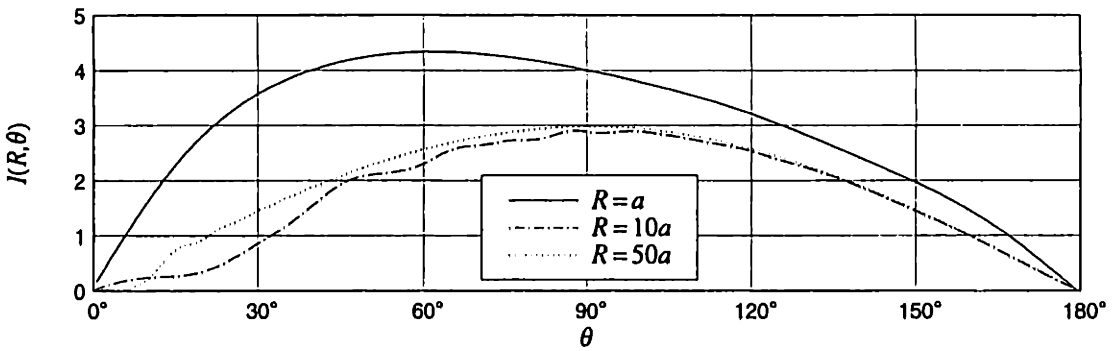

(*b*) Numerical integration progresses.

Fig. 5–13 Energy integration for 4-fiber square arrangement at frequency $ka = 2$ along three paths, of radii: $R = a$, $10a$ and $50a$, respectively.

compared to the maximum value of $|I(R,\theta)|$ reached during the integration process, $|I(R,\theta)|_{\max}$, for various numbers of subdivisions.

Since the computer used in this computation has only 15 significant figures, the small magnitudes of $|I(R,2\pi)|$ mean that the errors are at the level of the computer's round-off errors. In other words, these computations are as accurate as the computer is capable of obtaining.

The error ($|I(R,2\pi)|$) for $R = 50a$ computed by 180 subdivisions is large compared to other cases. Note that the energy balance computation is performed along different paths for different number of subdivisions based on the same set of $\{C_j\}$'s. The error dramatically decreases as the number of subdivisions is increased to 360.

This means that the large error is caused by using 180 subdivisions and can be further attributed to the assumption that both ϕ^{total} and γ_{rz} are constant within each subdivision. At larger radii, wave field changes significantly in a 2° arc angle

Table 5–10: Comparison of Energy Integrations at Different Numbers of Subdivisions for 4-Fiber Square Arrangement at $d = 3a$ and $ka = 3$

Integration Path	Subdivision	$\|I(R,\theta)\|_{max}$	$\|I(R,2\pi)\|$
$R = a$	180	4.34233	6.60583×10^{-15}
	360	4.34220	3.66374×10^{-14}
	720	4.34220	1.76248×10^{-15}
$R = 10a$	180	2.90034	4.88956×10^{-13}
	360	2.89893	3.39805×10^{-13}
	720	2.98056	1.44624×10^{-14}
$R = 50a$	180	2.99020	7.98483×10^{-6}
	360	2.89944	2.42882×10^{-13}
	720	2.97982	1.51355×10^{-15}

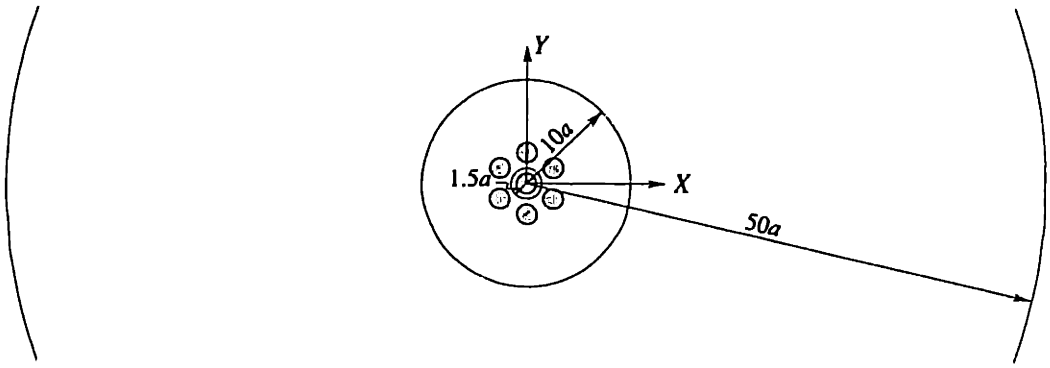

Fig. 5–14 Energy integration paths for 7-fiber hexagonal arrangement.

(the angle of one subdivision when the entire circle of 360° is divided by 180). In such cases, it is necessary to have finer angular subdivisions.

Second, consider the 7-fiber hexagonal configuration with $d = 3a$, at the frequency $ka = 2$. This is the case in which all the repetitive solution procedures have failed. Similarly, three integration paths are chosen, of radii $R = 1.5a$, $10a$ and $50a$, respectively, as sketched in Fig. 5–14. Again, the path of radius $R = 1.5$ falls entirely within an area surrounded by the fibers, and the paths of radii $10a$ and $50a$ represent the near-field and the far-field, respectively.

Figure 5–15*a* shows angular distributions of the normalized time-averaged energy flux density function $\langle \dot{e} \rangle$ along the three integration paths. Figure 5–15*b* shows the corresponding integration processes along these paths.

The computation using 720 subdivisions gives the final errors $|I(R,2\pi)|$ as 1.24623×10^{-14}, 1.04951×10^{-14} and 6.43582×10^{-15} for the paths of radii $R = 1.5a$, $10a$ and $50a$. All these results are at the level of the computer's round-off errors.

Third, again consider the 7-fiber hexagonal configuraion with fiber spacing $d = 3a$, but at the frequency $ka = 4.3$. As seen in Figs. 5–8 and 5–11, this is the case in which the computed dominant eigenvalue has a modulus larger than unity and yet the repetitive (recursive and implicit) solution procedures of Form I converge.

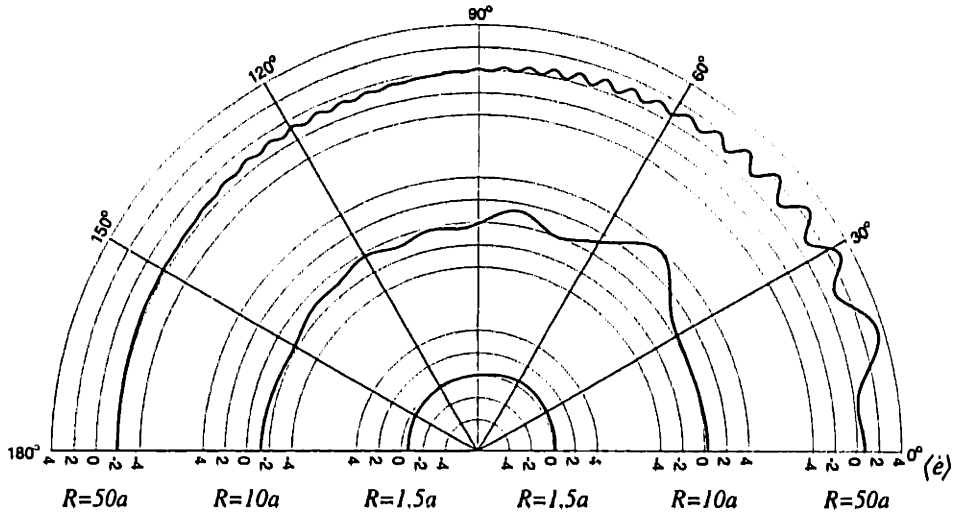

(*a*) Angular distributions of normalized time-averaged energy flux density function $\langle \dot{e} \rangle$.

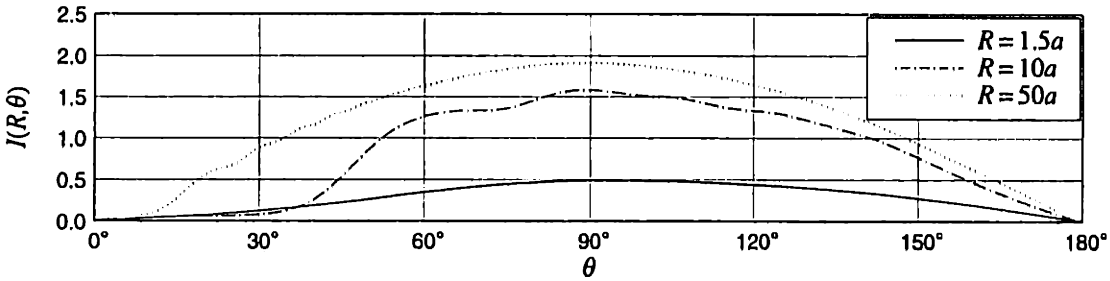

(*b*) Numerical integration progresses.

Fig. 5–15 Energy integration for 7-fiber hexagonal arrangement at frequency $ka = 2$ along three paths, of radii: $R = 1.5a$, $10a$ and $50a$, respectively.

For this case, the multiple-scattering problem is solved twice: by Recursive Form I and by the Supermatrix Form. Then energy computations are performed based on these two sets of solutions. For each set of solutions, three integration paths, of radii $R = 1.5a$, $10a$ and $50a$, are chosen. Table 5–11 lists the numerical results of the final errors of $|I(R, 2\pi)|$, as compared with the largest modulus of $|I(R, \theta)|$ during the process, $|I(R, \theta)|_{\max}$.

Results in Table 5–11 indicate that both solutions are correct. The solution obtained by the Supermatrix Form is accurate to the accuracy capability of the computer; and the converged solution obtained by Recursive Form I is accurate to the desired accuracy, notwithstanding the fact that the dominant eigenvalue of the system is larger than unity, which generally results in divergence.

So far, all problem configurations considered are symmetric about the X-axis. As the last example, consider a non-symmetric 4-fiber problem configuration as shown in Fig. 5–16. This is part of the 7-fiber hexagonal configuration with 3 fibers

Table 5–11: Comparison of Final Errors During Energy Integrations Based on Different Multiple-Scattering Solutions for 7-Fiber Hexagonal Arrangement at $d = 3a$ and $ka = 4.3$

Path radius	Supermatrix Form		Recursive Form I	
	$\|I(R,\theta)\|_{\max}$	$\|I(R,2\pi)\|$	$\|I(R,\theta)\|_{\max}$	$\|I(R,2\pi)\|$
$R = 1.5a$	1.71527	9.21138×10^{-16}	1.71529	1.00230×10^{-5}
$R = 10a$	3.70991	7.49574×10^{-15}	3.70992	4.47507×10^{-5}
$R = 50a$	4.17806	1.68737×10^{-14}	4.17806	8.95014×10^{-6}

removed.

The same three integration paths as for the case of 7-fiber arrangement are chosen. The angular distributions of the normalized time-averaged energy flux density function $\langle \dot{e} \rangle$ along these integration paths are shown in Fig. 5–17*a*, and the integration processes are shown in Fig. 5–17*b*.

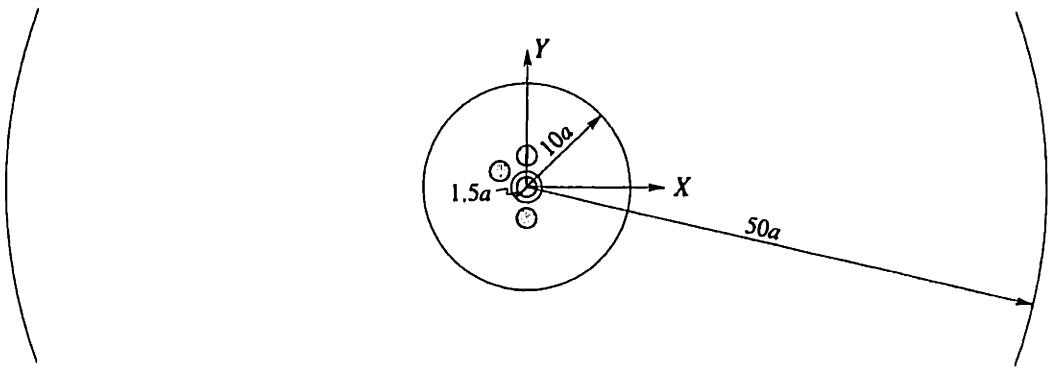

Fig. 5–16 Geometry of a non-symmetric 4-fiber problem configuration, and energy integration paths.

Using 720 subdivisions, the computed final errors $|I(R,2\pi)|$ are 1.02570×10^{-14}, 1.72223×10^{-14}, and 4.68375×10^{-16} for the paths of radii $R = 1.5a$, $10a$ and $50a$, respectively.

For this non-symmetric case, it is observed that the upper half plane of the angular distributions of the normalized time-averaged energy flux density function $\langle \dot{e} \rangle$ are very similar to the corresponding distribution for the 7-fiber hexagonal distribution at the same frequency, in Fig. 5–15. Distributions in the lower half plane are quite different, but the asymmetry tends to diminish as the radius increases.

In conclusion, for all the four examples, when using 720 subdivisions, the final errors $|I(R,2\pi)|$ are all within the order of 10^{-14} when the multiple-scattering problems is solved via Supermatrix Form. These examples verify that the programs used for all the computations, from solving the multiple-scattering problem via the Supermatrix Form to computing the total wave and the resulting displacements and stains, are correct. Furthermore, even if the resulting system is theoretically unstable when using the repetitive solution procedures, if the computation yields a

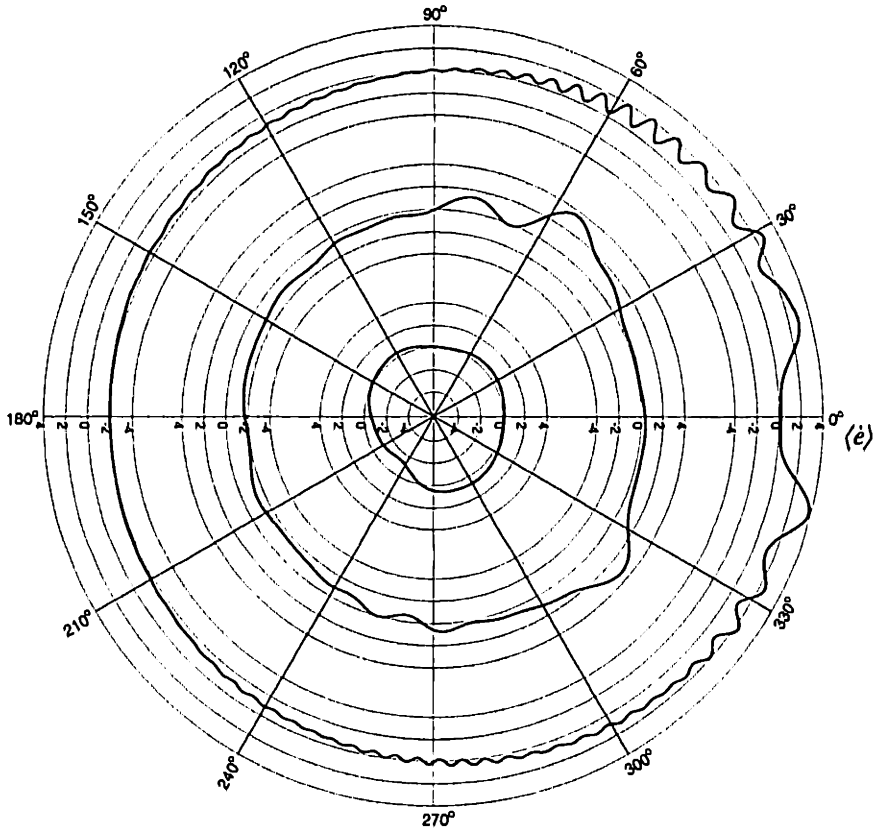

(*a*) Angular distributions of normalized time-averaged energy flux density function $\langle \dot{e} \rangle$.

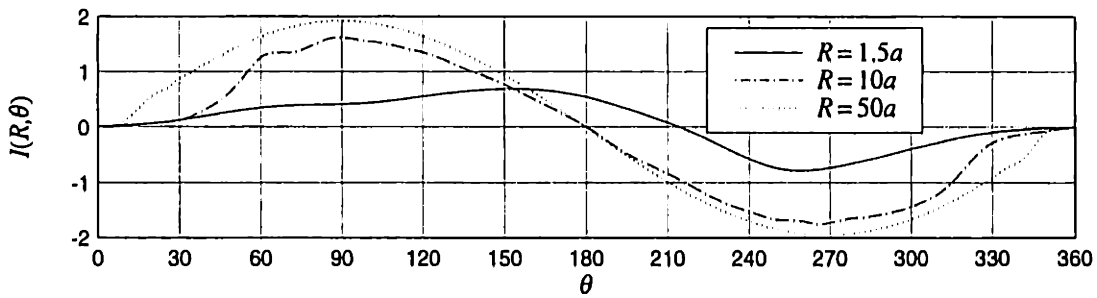

(*b*) Numerical integration progresses.

Fig. 5–17 Energy integration for non-symmetric 4-fiber configuration at frequency $ka = 2$ along three paths, of radii: $R = 1.5a$, $10a$ and $50a$, respectively.

converged solution, the solution will satisfy the energy balance requirement, and is further verified to be accurate to the desired accuracy.

5-5 Concluding Remarks

In this chapter, details concerning the implementation of the various forms of the the multiple-scattering solution given in Chapter 4 are discussed, and the computer programs developed for this study are verified. The computational structures and the characteristics of the various forms are discussed in great detail and summarized in §5-3.5.

In the numerical computation aspect, at some particular frequencies or a range of frequencies, various repetitive solution procedures may fail. But no particular numerical difficulties has been encountered using the Supermatrix Form. Therefore this form is suitable for computing a response spectrum of a multiple-scattering system.

These examples show that the multiple-scattering solution is capable of handling large numbers of scatterers. The limitation of its capability is set by the amount of available computer memory, which unfortunately grows at a rate of $\sim N^2M^2$ as the number of scatterers N increases, where M is truncation size which. With this growth rate, increasing the memory size is not the way to realize the goal of "full-scale" simulation. This necessitates the developments of the next chapter which seeks to reduces the growth rate of the problem size so to extend the computability of the multiple-scattering solution.

References

[1] Y.-H. Pao, C.-C. Mow, *Diffraction of Elastic Waves and Dynamic Stress Concentrations,* Crane Russak, Co., New York, 1971.

[2] H. Yim, J. H. Williams, Jr, Formulation and its energy balance verification for ultrasonic non-destructive characterization of a single fiber composite interphase, *Ultrasonics,* **33**, 377–387, 1995.

[3] H. Yim, J. H. Williams, Jr, Database generation and parametric study for ultrasonic non-destructive characterization of a single fiber composite interphase, *Ultrasonics,* **33**, 389–401, 1995.

[4] W. H. Press, B. P. Flannery, S. A. Teukolsky, W. T. Vetterling, *Numerical Recipes: The Art of Scientific Computing, C/FORTRAN/Pascal Versions,* Cambridge University Press, Cambridge, UK, 1986.

[5] D. M. Young, *Iterative Solution of Large Linear Systems,* Academic Press, New York, 1971.

[6] A. R. Gourlay, G. A. Watson, *Computational Methods for Matrix Eigenproblems,* John Wiley & Sons, Chichester (UK), 1973.

[7] F. Scheid, *Schaum's Outline Series: Theory and Problems of Numerical Analysis,* McGrall-Hill Book Co., New York, 1968.

[8] R. H. Hackman, Acoustic scattering from elastic solids, *Physical Acoustics, Vol. XXII: Underwater Scattering and Radiation,* A. D. Pierce, R. N. Thurston, ed., pp. 1–193, Academic Press, Boston, 1993.

[9] T. H. Cormen, C. E. Leiserson, R. L. Rivest, *Introduction to Algorithms,* MIT Press, Cambridge, Massachusetts & McGraw-Hill Book Co., New York, 1990.

[10] M. Abramowiz, I. Stegun, *Handbook of Mathematical Functions,* Dover, New York, 1965.

[11] W. J. Cody, SPECFUN—A portable FORTRAN package of special function routines and test drivers, *ACM Trans. Math. Software,* **19**, 22–32, 1993.

[12] J. F. Hart, E. W. Cheney, E. W., *et al, Computer Approximations,* John-Weley & Sons, New York, 1968.

[13] F. W. J. Olver, D. J. Sookne, Note on backward recurrence algorithms, *Math. of Comput.,* **26**, 941–947, 1972.

[14] D. J. Sookne, Bessel functions of real argument and integer order, *J. of Res. of Nat. Bureau of Standards, Series B,* **77A**, 125–132, 1973.

[15] D. J. Sookne, Certification of an algorithm for Bessel functions of real argument, *J. of Res. of Nat. Bureau of Standards, Series B,* **77A**, 115–124, 1973.

[16] J. B. Campbell, Bessel functions $J_\nu(x)$ and $Y_\nu(x)$ of real order and real argument, *Comp. Phys. Comm.,* **18**, 133–142, 1979.

[17] N. M. Temme, On the numerical evaluation of the ordinary Bessel function of the second kind, *J. Comp. Phys.,* **21**, 343–350, 1976

[18] L. W. Fullerton, Portable special function routines, *Lecture Notes in Computer Science, Vol. 57: Portability of Numerical Software,* W. Cowell ed., 452–483, Springer-Verlag, 1976.

[19] R. F. Boisvert, B. V. Saunders, Portable vectorized software for Bessel function evaluation, *ACM Trans. Math. Software,* **18**, 456–469, 1992.

[20] L. Baker, *C Mathematical Function Handbook,* McGraw-Hill, New York, 1992.

[21] D. E. Amos, S. L. Daniel, M. K. Weston, CDC 6600 subroutines IBESS and JBESS for Bessel functions $I_\nu(x)$ and $J_\nu(x)$, $x \geq 0$, $\nu \geq 0$, *ACM Trans. Math. Software,* **3**, 96–103, 1977.

[22] D. E. Amos, A portable package for Bessel functions of a complex argument and nonnegative order, *ACM Trans. Math. Software,* **12**, 265–273, 1986.

[23] IMSL, Inc., *IMSL User's Manual: FORTRAN Subroutines for Mathematical Applications, MATH/LIBRARY Special Functions, Version 2.0* IMSL, Inc., Houston, 1991.

[24] NAG Ltd., *NAG FORTRAN Library Manual, Mark 15,* Vol. **10**, NAG Ltd, Oxford, U.K., 1991.

[25] The MathWorks, Inc., MATLAB: *High-Performance Numeric Computation and Visualization Software, Reference Guide,* The MathWorks, Inc., Natick, MA, 1992.

[26] G. N. Watson, *Treaties of Theory of Bessel Functions,* 2nd edn., Cambridge University Press, London, 1945.

[27] G. Blanch, Numerical evaluations of continued fractions, *SIAM Rev.,* **6**, 383–421, 1964.

Appendix

5-A Algorithms

In this appendix, algorithms for implementing the multiple-scattering solution are given in a form of pseudo-codes. The style for the pseudo-codes essentially follows that in [9], with some modifications. The main stylistic conventions include:

- A routine/function name is denoted by small-capitals, and a multi-word name is hyphenated between words, such as FUNCTION-NAME;
- A keyword in a computational structure is emphasized by a bold typeface;
- A variable name is denoted by an italic typeface, and a multi-word name is connected by underscore(s), such as *variable_name*;
- A block structure is indicated by an appropriate amount of indentation and the cumulative amount of the indentation indicates the level of nesting of blocks;
- An assignment is indicated by an arrow (←);
- An entry of an array is denoted by the index number placed in a pair of sqare brackets ([]).

These pseudo-codes do not specify variables for a routine. It is up to the programmer to decide the types and scopes of necessary variables. Instead, the symbols used in the mathematical formulation are used in these pseudo-codes. Minor procedures are described only literally without further elaboration in order to keep the pseudo-codes concise and yet self-explanatory.

The present implementation is designed for computating a segment of a response spectrum of the system. Routine MAIN-PROGRAM represents the main computational structure.

The central task in Routine MAIN-PROGRAM (Routine 5-A.1) is the determination of the truncation term M by a trial-and-error approach. The procedure starts with a preset trial value of M. It first checks whether the first truncation criterion in eqn. (5-30) is satisfied; adjust M by increasing it by one at a time until this criterion is satisfied, or the preset $M_{\max}$ is reached. $M_{\max}$ is the maximum value of M beyond which the problem cannot be handled by the computer. The routine then proceeds to satisfy the second truncation criterion in eqn. (5-31) in the same manner.

It is noted that a complete evaluation of eqn. (5-31) involves a significant amount of computation, and yet at this stage of computation, only a rough order-of-magnitude estimates suffices. Reduction is achieved by estimating only the pair of i and j that gives the largest error during the first trial. In Routine 5-A.1, this pair is identified as I and J. In later trials within the **while** loop, only this particular pair is checked against eqn. (5-31). Satisfying the third criterion in eqn. (5-32) is left out of this routine since it is not necessary for some of the solution forms.

In the entire computation for a response spectrum, the preset M value is specified only once, before entering the loop over the wave number k. In the computations that follow, M determined for the previous k value is used as the preset value. This design is based on the

observation (see §5-3.1) that, for a given problem configuration, M increases monotonically as k increases monotonically.

Whenever M is increased during the trial-and-error, it is necessary to *augment* $[\boldsymbol{L}_{ij}]$ matrices. To *augment* a matrix means to enlarge its size, and fill the newly created elements with appropriate values by performing necessary computations.

It may be argued that it is computationally efficient to initialize $[\boldsymbol{L}_{ij}]$ to a large enough size at the beginning and then reduce their size in later steps. But the disadvantage of this approach is that, since $[\boldsymbol{L}_{ij}]$ take a dominant portion of computer memory for the computation, a large size would exceed the memory capacity of the computer for a problem which may otherwise be accommodated.

On the other hand, T-matrices are indeed initialized to a large size, based on the efficiency consideration. Since the computations for the T-matrices are outside of the multiple-scattering solution, and there may not exist convenient formulas that can be used for the computation.

The core of the multiple-scattering computation is done in the routine represented by CORE-SOLUTION-PROCEDURE. This is a collective name for routines that correspond to various solution forms. The name for each of these routines corresponds to one of the solution forms; namely, RECURSIVE-FORM-I (Routine 5–A.2), RECURSIVE-FORM-II (Routine 5–A.3), IMPLICIT-FORM-I (Routine 5–A.4), IMPLICIT-FORM-I (Routine 5–A.5), and

Routine 5–A.1: Main Program Structure for the Multiple-Scattering Solution for Computation of a Response Spectrum

```
MAIN-PROGRAM
    setup geometry of problem
    preset a truncation term M, and its upper limit M_max
    for every frequency k (k increases monotonically)
        build T-matrix for each scatterer at size M_max
        e ← from left-hand side of eqn. (5–30)
        while ( e > tolerance )
            M ← M + 1
            if M > M_max
                then terminate computation
                else e → from left-hand side eqn. (5–30)
        build [L_ij] matrices at size M
        e ← 0
        for every i and j from 1 to N
            e' ← from left-hand side eqn. (5–31) for i and j
            if e' > e
                then e ← e', I ← i, J ← j
        while ( e > tolerance )
            M ← M + 1
            if M > M_max
                then terminate computation
                else augment [L_ij] matrices
                    e ← from left-hand side eqn. (5–31) for i = I and j = J
        CORE-SOLUTION-PROCEDURE (various)
        if {C_j} exist
            then compute field quantities as desired
```

Routine 5–A.2: Core Solution Procedure for Recursive Form I

```
RECURSIVE-FORM-I
    for every j from 1 to N
        initialize {A_j} to size M
        resize [T_j] to size M
        {C_j^old} ← {C_j} ← [T_j]{A_j}
    e ← a large value
    while e > tolerance
        e ← 0
        for every j from 1 to N
            {C_j^new} ← 0
            for every i from 1 to N
                if i ≠ j
                    then {C_j^new} ← {C_j^new} + [L_ij]{C_i^old}
            {C_j} ← {C_j} + {C_j^new}
            e ← THE-LARGER-OF(e, ||{C_j^new}||_∞)
        if e > preset large value (diverges)
            then erase all {C_j} and EXIT
            else for every j from 1 to N
                    {C_j^old} ← {C_j^new}
```

SUPERMATRIX-FORM (Routine 5–A.6). Such a routine performs the designated solution procedure, and, unless the procedure fails, computes the wave expansion coefficients matrices of the scattered waves $\{C_j\}$ as the final results.

In Routine RECURSIVE-FORM-I, the variables $\{C_j^{\text{new}}\}$ and $\{C_j^{\text{old}}\}$ store the scattered wave coefficients of the present and the previous order, respectively, and $\{C_j\}$ store the summation of all orders of the scattered waves.

The function THE-LARGER-OF() takes two arguments and returns the larger as the result. The function EXIT simply terminates the execution of the routine and returns to the main program, which is what naturally happens at the end of any routine. To *resize* a matrix means to change its size, and fill the newly created elements with zeros if the new size is larger then the original.

In the event that the recursive procedure diverges, all the computed $\{C_j\}$ are destroyed. This is the mechanism to notify MAIN-PROGRAM not to compute any wave fields for a diverged case, and for the next frequency in the computation, everything is started anew.

The first portion of RECURSIVE-FORM-II is to continue the task of determining the truncation term M by the third criterion, eqn. (5–32). Again, this is done by the trial-and-error approach while increasing M by one at a time. Afterwards, the structure of Routine RECURSIVE-FORM-II is very similar to RECURSIVE-FORM-I. At the end, if a converged result is reached, RECURSIVE-FORM-II also computes the wave expansion coefficient matrices of the scattered waves $\{C_j\}$ before it exits.

Routines IMPLICIT-FORM-I and IMPLICIT-FORM-II are similar to routines RECURSIVE-FORM-I and RECURSIVE-FORM-II, respectively. Besides the obvious, there is a subtle difference in the initialization process. In the implicit routines, the results of the previous computation, $\{C_j\}$ for IMPLICIT-FORM-I and $[K_j]$ for IMPLICIT-FORM-II, are inherited as the initial guessed solution for the present computation unless there is no previous solution available, which can happen in two situations. One is during the first loop over k, and the

Routine 5–A.3: Core Solution Procedure for Recursive Form II

```
RECURSIVE-FORM-II
    e ← from left-hand side of eqn. (5–32)
    while e > criterion
        M ← M + 1
        augment [L_ij] matrices
        e ← from left-hand side of eqn. (5–32)
    build [ℜR_ij] matrices at size M
    for every j from 1 to N
        resize [T_j] to size M
        [K_j] ← [K_j^old] ← [T_j]
    e ← a large value
    while e > tolerance
        e ← 0
        for every j from 1 to N
            [K_j^new] ← 0
            for every i from 1 to N
                if i ≠ j
                    then [K_j^new] ← [K_j^new] + [L_ij][K_i^old][ℜR_ji]
            [K_j] ← [K_j] + [K_j^new]
            e ← THE-LARGER-OF(e, ||[K_j^new]||∞)
        if e > preset large value (diverges)
            then destroy all [K_j] and EXIT
            else for every j from 1 to N
                    [K_j^old] ← [K_j^new]
    for every j from 1 to N
        initialize {A_j} at size M
        {C_j} ← [K_j]{A_j}
```

other is when the previous computation fails (diverges). In such cases, the initial guessed solution is assumed as that of the first order scattering.

Routine SUPERMATRIX-FORM is straightforward. After the determination of the truncation term M, all the matrices are assembled into supermatrices. The resulting linear equation system can then be solved by many well-established solution algorithms, and many of them are readily available. Numerous computations performed for this study have not encountered any particular numerical difficulties, and virtually any established algorithm for the linear equation system can be used.

Finally, it is noted that the computation for a 2-D multiple-scattering problem requires a reliable and highly accurate numerical library for Bessel functions of various kinds. Computation for high accuracy Bessel functions is not trivial. In this study, such a set of high accuracy Bessel functions has been built; algorithms and other related issues are documented in Appendix 5-B.

Routine 5–A.4: Core Solution Procedure for Implicit Form I

```
IMPLICIT-FORM-I
    for every j from 1 to N
        resize [T_j] to size M
        initialize {A_j} to size M
        if {C_j} exists
            then resize {C_j} to size M
            else {C_j} ← [T_j]{A_j}
        {C_j^old} ← {C_j}
    error e ← a large value
    while e > tolerance
        e ← 0
        for every j from 1 to N
            {C_j^new} ← [T_j]{A_j}
            for every i from 1 to N
                if i ≠ j
                    then {C_j^new} ← {C_j^new} + [L_ij]{C_i^old}
            e ← THE-LARGER-OF(e, ||{C_j^new} − {C_j^old}||_∞)
        if e > preset large value (diverges)
            then destroy all {C_j} and EXIT
            else for every j from 1 to N
                    {C_j^old} = {C_j^new}
```

5-B On Computation of Bessel Functions of Real Arguments and Integer Orders

Bessel functions of various kinds, especially the first and the second kinds with real arguments and integer order, are primitive in some engineering applications such as wave motions and mechanical vibrations. From an engineering perspective, the "number of significant figures" is one of the most important measures on the accuracy of a numerical evaluation. However, computations for Bessel functions with such a relative accuracy have never been easy. The difficulties are mostly due to the fact that Bessel functions are not analytic functions and there is no single all-purpose formula readily available, although there is an astonishingly large number of related formulas can be used. A naive endeavor will likely see the failures of those formulas one after another, for the reasons ranging from lost of accuracy to numerical over- and/or under-flows.

This appendix summarizes the efforts in the present study to build such routines. The goal of the present implementation is to obtain Bessel functions as accurate as the hardware is capable of giving, for orders no larger than 1000, or whatever restricted by the computer (due to underflows and overflows).

Routine 5–A.5: Core Solution Procedure for Implicit Form II

```
IMPLICIT-FORM-II
    e ← from left-hand side of eqn. (5–32)
    while e > criterion
        M ← M + 1
        augment [L_ij] matrices
        e ← from left-hand side of eqn. (5–32)
    build [ℜR_ij] matrices at size M
    for every j from 1 to N
        resize [T_j] to size M
        if [K_j] exists
            then resize [K_j] to size M
            else [K_j] ← [T_j]
        [K_j^old] ← [K_j]
    e ← a large value
    while e > tolerance
        e ← 0
        for every j from 1 to N
            [K_j^new] ← [T_j]
            for every i from 1 to N
                if i ≠ j
                    then [K_j^new] ← [K_j^new] + [L_ij][K_i^old][ℜR_ji]
            e ← THE-LARGER-OF(e, |||[K_j^new] − [K_j^old]|||∞)
        if e > preset large value (diverges)
            then destroy all [K_j] and EXIT
            else for every j from 1 to N
                    [K_j^old] = [K_j^new]
    for every j from 1 to N
        initialize {A_j} at size M
        {C_j} ← [K_j]{A_j}
```

Routine 5–A.6: Core Solution Procedure for Supermatrix Form

```
SUPERMATRIX-FORM
    for every j from 1 to N
        resize [T_j] to size M
        initialize {A_j} to size M
    construct supermatrix {𝒜}
    construct supermatrix [ℐ − ℒ]
    solve the linear system [ℐ − ℒ]{𝒞} = {𝒜}
    for every j from 1 to N
        extract {C_j} from {𝒞}
```

Brief Summary of Some Available Routines[1]

Classical computational methods for Bessel functions have been summarized in [10]. Some of currently available computer programs are briefly summarized in the following.

SPECFUN[11] is a special function package which contains several routines for Bessel functions. It has separate routines for the zero, first and arbitrary integer orders. The routines for the zero and first orders are based on the author's unpublished minimax rational approximations for $x \leq 8$ and the approximation given in [12] for $x > 8$. The routine for the arbitrary integer order is based on a general three-term recurrence algorithm discovered by Olver and Sookne[13–15]. The routine for $Y_n(x)$ is adapted from those by Campbell[16] and Temme[17]. Unlike routines for the first kind, this routine is for real orders. The entire SPECFUN package is publicly available in NetLib[2].

FNLIB[18] is also a special function package which is also available in NetLib. The limitation of this package is that it has only the zero and first orders of Bessel functions. It uses truncated Chebyshev series, generated by other routines in the same package, to interpolate some precalculated highly accurate values at several points. VFNLIB[19] is the vectorized version of FNLIB and is also available on NetLib.

Reference [20] and [4] also have routines for computing Bessel functions of various kinds. However, both provide no error information.

Several Bessel function routines are available in the Association for Computer Machinery (ACM) Algorithm Collection, also obtainable from NetLib. Algorithm 511[21] is for Bessel function of the first kind, with real argument and real order. Algorithm 644[22] is another complete set of Bessel functions, which is capable of computing Bessel functions of various kinds with complex arguments and real orders with absolute accuracy. Algorithm 713[19] is the same as VFNLIB. Algorithm 715[11] is a duplication of SPECFUN.

For commercial mathematical software packages, IMSL's routines[23] are essentially the same as those in SPECFUN, but no specific accuracy information is given; NAG's routines[24] are based on ACM's Algorithm 644[22]. MATLAB routines[25] use a similar strategy.

Fundamental Formulas

The series expressions for Bessel function of both the first and second kinds with real arguments and integer orders are[10]

$$J_n(x) = \sum_{k=0}^{\infty} (-1)^k \frac{\left(\frac{1}{2}x\right)^{n+2k}}{k!(n+k)!} \tag{5-B.1}$$

---

[1] Sincere thanks to the following individuals who have pointed out some of available routines and algorithms: Brent Carruth of University of Louisville, Kentucky, Stan Kerr of University of Illinois at Urbana-Champaign, Dave Cawlfield of National Supercomputing Center for Energy and the Environment at University of Nevada, Las Vegas, Robert S. Cargill II of University of Pennsylvania and Herman Rubin of Purdue University.

[2] NetLib is a repository of a large pool of high-quality mathematical softwares. The main purpose of its establishment, sponsored by several academic institutions, is to electronically distribute those public-domain softwares in an automated, fast, easy and efficient way on an as-needed basis. NetLib is acessable via "anonymous ftp" from the following sites: `research.att.com` (AT&T Bell Laboratory, Murray Hill, New Jersey) and `netlib@ornl.gov` (Oak Ridge National Laboratory, Oak Ridge, Tennessee).

$$\pi Y_n(x) = -\sum_{k=0}^{n-1} \frac{(n-k-1)!}{k!} \left(\tfrac{1}{2}x\right)^{-n+2k} + \sum_{k=0}^{\infty} (-1)^k \frac{\left(\frac{1}{2}x\right)^{n+2k}}{k!(n+k)!} \left[2\ln\left(\tfrac{1}{2}x\right) - \psi(k+1) - \psi(n+k+1)\right] \quad (5\text{-B.2})$$

where

$$\psi(k+1) = -\gamma + 1 + \frac{1}{2} + \cdots + \frac{1}{k} \quad (5\text{-B.3})$$

and $\gamma = 0.57721566490153286060606512\cdots$ is the *Euler constant*. When $n = 0$, the first summation in eqn. (5-B.2) should not appear. Equations (5-B.1) and (5-B.2) are sometimes called the *ascending series*.

When x is large and much greater than n, the following asymptotic expansions[10] can be used

$$J_n(x) \approx \sqrt{\frac{2}{\pi x}} \left[P_n(x)\cos\xi_n(x) - Q_n(x)\sin\xi_n(x)\right], \quad (5\text{-B.4})$$

$$Y_n(x) \approx \sqrt{\frac{2}{\pi x}} \left[P_n(x)\sin\xi_n(x) + Q_n(x)\cos\xi_n(x)\right], \quad (5\text{-B.5})$$

where

$$\xi_n(x) = x - \frac{\pi}{4} - \frac{n\pi}{2}, \quad (5\text{-B.6})$$

$$P_n(x) = 1 - \frac{(4n^2-1)(4n^2-9)}{2!(8x)^2} + \frac{(4n^2-1)(4n^2-9)(4n^2-25)(4n^2-49)}{4!(8x)^4} - \cdots, \quad (5\text{-B.7})$$

$$Q_n(x) = \frac{(4n^2-1)}{8x} - \frac{(4n^2-1)(4n^2-9)(4n^2-25)}{3!(8x)^3} + \cdots. \quad (5\text{-B.8})$$

Equations (5-B.4) and (5-B.5) are often called the *Hankel uniform asymptotic expansions* or the *descending series*.

The following properties of Bessel functions, known as the *recurrence relations*, are often used in computations of Bessel functions[10]:

$$C_{n+1}(x) = \frac{2n}{x} C_n(x) - C_{n-1}(x), \quad (5\text{-B.9})$$

which can also be written in backward direction as

$$C_{n-1}(x) = \frac{2n}{x} C_n(x) - C_{n+1}(x), \quad (5\text{-B.10})$$

where $C_n(x)$ can be either $J_n(x)$ or $Y_n(x)$. They are called the *forward recurrence* and the *backward recurrence*, respectively.

Observations

Equation (5-B.1) is theoretically accurate for any n and x but only computationally works well when both x and n are small or when n is very large, and it fails in other regions.

The main reason for the failure of eqn. (5-B.1) is the so-called cancellation error, which occurs when a subtraction of two numbers cancels the first several significant figures. When $(x/2)^2 > n+1$, the magnitude of each term under the summation in eqn. (5-B.1) grows by a factor of $\frac{(x/2)^2}{k(k+n)}$ until some value of k is reached. (This is probably the reason the series are called ascending series.) Then, the magnitude of each term decreases as k increases. The increase of the magnitude indicates a possible loss of significant figures during the summation. If the maximum magnitude of some term in the series is $\sim 10^p$, while the final

result of $J_n(x)$ is $\sim 10^q$ $(q < 0)$, then, $p - q - 1$ significant figures may have been eventually lost. At this point, eqn. (5-B.1) fails due to the loss of too many significant figures.

If after losing those significant figures, the result may still be possibly acceptable, sufficiently large k should be taken to ensure that the truncation error does not contribute to any further loss of significant figures. However, when n is large, an underflow often occurs before such a term is reached.

The behavior of eqn. (5-B.2) is very similar to that of eqn. (5-B.1). In addition, it is observed that, for a small x, say $x < 50$, the computation for $Y_n(x)$ with various n using eqn. (5-B.2) retains the largest number of significant figures when n is roughly around $[1.2x]$, where the square brackets denote the largest integer no larger than the number enclosed.

Equations (5-B.4) and (5-B.5) are valid only for large x and comparatively small n. Although no particular numerical difficulty is expected, and the asymptotic theory guarantees that if the approximations are accurate enough for argument X, they should be accurate enough for any $x > X$, quantifying the validity region, such as the minimum X for a given n, or the maximum n for a given x, has to be done with great care.

Using recurrence relations is a way to span the computability over the gap. It is generally regarded that, for computation of $J_n(x)$, the forward recurrence is unstable while the backward recurrence is stable. For computation of $Y_n(x)$, the forward recurrence is stable while the backward is not.

Extensive observations in this study have concluded that the stability of a recurrence formula depends very little on the formula itself but largely on the property of Bessel function. If the value of Bessel function outgrows, or at least grows at a same rate as, the error, the recurrence is stable, otherwise it is unstable.

Furthermore, a generally stable recurrence does not guarantee a desired accuracy, since the error still grows as it recurses. It has been encountered such a case in which the computed $J_{100}(70)$ and $J_{99}(70)$, via eqn. (5-B.1), had 14 significant figures, $J_0(70)$ computed by the backward recurrence retained only 2 significant figures. This catastrophic case occurred because at a few occasions in the course of recurrence, the cancellation errors are significant, and these errors then propagate and may even be magnified to the end.

To suppress the propagation of such cancellation errors, an alternative two-step backward recurrence formula[27] can be used

$$C_{n-2}(x) = \left[\frac{4n(n-1)}{x^2} - 1\right] C_n(x) - \frac{2(n-1)}{x} C_{n+1}(x) \qquad \text{(5-B.11)}$$

when it is suspected that the cancelation error in the computed $C_{n-1}(z)$ using eqn. (5-B.10) is severe. Similarly, the two-step forward recurrence is

$$C_{n+2}(x) = \left[\frac{4n(n+1)}{x^2} - 1\right] C_n(x) - \frac{2(n+1)}{x} C_{n-1}(x) \qquad \text{(5-B.12)}$$

Since severe cancellation error tends to occur when x is close to one of the zeros of Bessel functions, and it is known that the zeros of Bessel function are interlaced[26]; that is, $J_{n\pm1}(z)$ and $J_n(z)$ do not reach their zeros at the same time, the use of these alternative recurrence formulas substantially reduces the chance a severe cancellation error being propagated to the very end of a recurrence.

It is also observed that when using the backward recurrence, say, starting with $J_M(x)$ and $J_{M-1}(x)$, the larger the M is, the more accurate the $J_0(x)$ will be.

Implementation Considerations

The present implementation is aimed at the application in solving problems of multiple-scattering of elastic waves. In such a problem, Bessel functions of all orders up to some predetermined maximum order $N_{\max}$ are all need for a given argument. For such a problems nature, the use of the recurrence formulas is generally preferred.

Since each of $J_n(x)$ and $Y_n(x)$ takes a considerable amount of effort to compute, in which process all $J_n(x)$ and $Y_n(x)$ from $n = 0$ to $N_{\max}$ are likely to have been computed, it is computationally efficient to keep the entire series in the compute's memory for possible later uses. In fact, several such series should be kept since in an application program, there might be a simultaneous need for Bessel functions of a few different arguments.

In the present implementation, two parameters are configurable by the users: the maximum order of Bessel functions needed, $N_{\max}$, and the number of series of Bessel functions to be kept in the memory simultaneously. In the following discussions, such a series of Bessel functions is called a *table*. That is, a table contains Bessel functions for the same argument from orders from $n = 0$ up to $N_{\max}$.

The infra-structure of the present implementation of Bessel functions consists of three levels of routines. The top level is an administrative routine which actually only manages a number of tables of Bessel functions. This is also the front-end routine to be called by the user. The next level is a table-generation routine which generates table entries as directed by the administrative routine. The bottom level is the routines that actually implement eqns. (5-B.1) and (5-B.4) or eqns. (5-B.2) and (5-B.5) and to be called by the generation routine to generate the seeds for a recurrence.

Routines 5–B.1 (Routines $\mathrm{J}(n,x)/\mathrm{Y}(n,x)$) represent such a infra-structure. Note that Routines 5–B.1 contain two routines, $\mathrm{J}(n,x)$ and $\mathrm{Y}(n,x)$ for Bessel functions of the first and the second kinds, respectively. When the user invokes the function, by providing the values of x and n, the administrative routine first checks if the requested argument has been computed previously. If the table for this argument has been computed, it simply looks up the table and returns the value at the requested order. If the requested argument is a new one, it then calls the appropriate generation routine to generate a new table, and finally the administrative routine looks up the table and returns the value.

An administrative routine manages two lists: *argument_list*, which is an array that contains the arguments of the Bessel function that have been previously computed, and *table_list*, which locates the tables of Bessel functions for the arguments in the *argument_list*.

An administrative routine also dispatches two subroutines, as shown in Routine 5–B.2. Subroutine LOOK-UP-ENTRY(x) searches the *argument_list* for a specified argument x, and returns the corresponding table. Subroutine CREATE-NEW-TABLE(x) creates a new

Routine 5–B.1 Top Level Administrative Routines for Bessel Functions

```
J(n,x)/Y(n,x)
    table ← LOOK-UP-ENTRY(x)
    if ( not found )
        then table ← CREATE-NEW-TABLE(x)
            GENERATE-J-TABLE(x, table)/GENERATE-Y-TABLE(x, table)
    if ( n < 0 )
        then return (−1)^n × table[|n|]
        else return table[n]
```

Routine 5–B.2 Administrative Subroutines

```
LOOK-UP-ENTRY(x)
    for every i from N_max to 1 in descending order
        if ( x = argument_list[i] )
            then return table_list[i]
    return not found

CREATE-NEW-TABLE(x)
    count ← 0
    for every i from 1 to N_max
        if ( table_list[i] is occupied )
            then count ← count + 1
    if ( count = N_max )
        then for every i from 2 to N_max
            argument_list[i − 1] ← argument_list[i]
            table_list[i − 1] ← table_list[i]
        else table_list[count] ← allocate memory
        argument_list[count] ← x
    return table_list[count]
```

table for the specified argument. This subroutine also performs the house-cleaning for the administrative routine. When CREATE-NEW-TABLE(x) is called, it first counts the number of arguments enlisted in the *argument_list*. When it locates the first vacant table slot, the table slot is returned to the administrative routine. If all the configured table slots have been occupied, it then discards the oldest table to make room for the new one.

The administrative routine then passes the table slot to the second level routine to generate Bessel functions to fill in the assigned table slot. Generations of Bessel functions are different for the first and the second kinds. They are discussed separately in the following two subsections.

Generation of $J_n(x)$

For a very large x ($x > 1000$), only the forward recurrence is used to compute all orders up to the highest desired order, with seeds being $J_0(x)$ and $J_1(x)$ computed by eqn. (5-B.1).

For a small to moderately large argument, the backward recurrence is used. However, a direct use of eqn. (5-B.10) requires accurate seeds, which many not be readily computable to the desired accuracy by using eqn. (5-B.1). Sookne's three-term recurrence algorithm[13-14] avoids the needs for accurate seeds, and thus is adopted.

Theoretically, Sookne's algorithm can be used to obtain Bessel function of the first kind of virtually any accuracy[14]. The algorithm works as follow. For a given argument x, choose a high enough order M, and set $j_{M+1}(x) = 0$ and $j_M(x) = 1$. Repeatedly use the backward recurrence to compute $j_n(x)$ until $n = 0$. Then normalizing the entire series $j_n(x)$ by a normalizing factor Δ gives a series of Bessel functions of the first kind. That is

$$J_n(x) = \frac{j_n(x)}{\Delta} \qquad \Delta = 2 \sum_{n=0}^{[M/2]} j_{2n}(x) - j_0(x) \tag{5-B.13}$$

This algorithm is based on the following identity of Bessel functions[10] of the first kind

$$J_0(x) + 2\sum_{n=1}^{\infty} J_{2n}(x) = 1 \tag{5-B.14}$$

Sookne[14] has described a method to choose the particular value of M for a desired accuracy. Since the higher the starting order M, the more accurate the results, for simplicity, in the present implementation, M is chosen as large as possible with the only criterion that no overflow should occur.

Furthermore, in order to take full advantage of computer's capability, Sookne's original algorithm is slightly modified as follow: suppose the smallest positive floating number (in double precision) can be represented by the implementing computer is 10^{-K}, then the seeds for the recurrence are set as $j_{M+1}(x) = 0$ and $j_M(x) = 10^{-K}$. This modification allows a larger M to be used to achieve a higher accuracy.

The starting order M is determined such that during the course of the recurrence, the maximum value of Δ is about 10^K, which is the largest positive floating number (in double precision) can be represented by the implementing computer. This way, after the normalization, $O(J_M(x)) = 10^{-2K}$. An underflow will certainly occur in such a normalization process, which need to be watched for. On the other hand, this also ensures that for all the computed $J_n(x)$ before the underflow occurs, the values are accurate to the best of the computers capability.

Since in general $M >> x$, the leading term in the ascending series expression gives a very good order-of-magnitude approximation of $J_M(x)$. Thus, let 10^{-2K} equal the leading term approximation for $J_M(x)$, that is

$$\left(\frac{x}{2}\right)^M \frac{1}{M!} \approx \frac{1}{\sqrt{2\pi M}} \left(\frac{ex}{2M}\right)^M = 10^{-2K} \tag{5-B.15}$$

where Sterling formula for large M,

$$M! \approx \sqrt{2\pi M} M^M \mathrm{e}^{-M} \tag{5-B.16}$$

has been used. As only a rough estimate of M is needed, the factor $\sqrt{2\pi M}$ can be simply ignored, and the approximation can be written as an equation. Taking the logarithms of base 10 on both sides of eqn. (5-B.15) gives

$$M\left[\log\left(\frac{ex}{2}\right) - \log M\right] + 2K = 0 \tag{5-B.17}$$

Next, Newton's iteration is used to obtain an approximation for M, which gives

$$M^{(m+1)} = \frac{0.4343M^{(m)} + 2K}{\log M^{(m)} - \log x + 0.30103} \tag{5-B.18}$$

where the superscript (m) denotes the iteration step. In the present implementation, the initial value $M^{(0)}$ is empirically chosen as $x + K$, and Newton's iteration is performed only once.

Since no-overflow is a crucial condition to ensure the accuracy, the computation process has to be closely monitored for overflows. When the recursion reaches an order n' such that the summation Δ is very close to 10^K, the recurrence is terminated, and M is decreased by n' and the entire process is restarted over.

For further reduction of possible errors, especially the propagation of cancellation errors, during the recurrence, the result of each recurrence step is compared with $J_n(x)$ and $J_{n+1}(x)$.

If the result is small compare with either of the two, which predicts a severe cancellation error, this result will not be used in the next recurrence, the alternative two-step recurrence relation in eqn. (5-B.11) is used instead.

Routine GENERATE-J-TABLE(x, *table*) summarizes the above process. In this routine, when the argument x is large, it calls the third level routines to compute the seeds a and b, and then dispatches Subroutine FORWARD-RECURRENCE(a, b, *start_n*, x, *table*) to perform the recurrence. When the argument is small, it first estimates M and dispatches Subroutine BACKWARD-RECURRENCE(a, b, *start_n*, x, *table*) to perform the recurrence. Since it is known that $|J_0(x)| \leq 1$, when the recurrence fails (overflow occurs), the table entry that corresponds to $J_0(x)$ records $n' + 2$ where n' is the order at which the overflow occurs, then M is reduced by this number and the recurrence subroutine called again. The process is repeated until no overflow occurs. Note that recording the overflow is done in the recurrence subroutine.

Both Subroutines FORWARD-RECURRENCE(a, b, *start_n*, x, *table*) and BACKWARD-RECURRENCE(a, b, *start_n*, x, *table*) have the same invocation form, in which a and b are the recurrence seeds, *start_n* is the starting order, x is the argument of the Bessel functions to be generated, and *table* is the assigned table slot to store the results.

Within both recurrence routines, detecting a severe cancellation error is performed in each step. Whenever it is suspected that the cancellation may be large, the alternative two-step recursions is performed. However, two-step recurrence is only used as a temporary substitute. For the next step, the normal single-step recurrence is resumed.

At the end of Subroutine BACKWARD-RECURRENCE, the normalization is performed if the recurrence is successful. Otherwise, the subroutine records the order at which the overflow occurs and exits. Also note that the normalization is only performed when the starting order *start_n* is greater than 40. This is a mechanism to enable the routine to be used as a regular recurrence for use in generating Bessel functions of the second kind, which will be discussed later.

Subroutine STORE(v, n, *table*) checks if the order n is within the desired range. If it is, the value v is stored in to the assigned *table*. The value v is discarded if it is not within the desired orders. Thus it is necessary to compute Δ within Subroutine BACKWARD-RECURRENCE.

Generation of $Y_n(x)$

Computation for Bessel functions of the second kind is much simpler. As mentioned before, forward recurrence is stable for computation of $Y_n(x)$. However, as a precautionary

Routine 5–B.3 Routine for Generating Bessel Function of the First Kind

```
GENERATE-J-TABLE(x, table)
    if ( x < 1000 )
        then a ← J_0(x) according to eqn. (5-B.1)
             b ← J_1(x) according to eqn. (5-B.1)
             FORWARD-RECURRENCE(a, b, 1, x, table)
        else M ← according to eqn. (5-B.18)
             BACKWARD-RECURRENCE(0, 10^-K, M, x, table)
             while ( table[0] > 1 )
                 M ← M − table[0]
                 BACKWARD-RECURRENCE(0, 10^-K, M, x, table)
```

Routine 5–B.4 Subroutine for Forward Recurrence

```
FORWARD-RECURRENCE(a, b, start_n, x, table)
    STORE(a, start_n − 1, table)
    STORE(b, start_n, table)
    n ← start_n
    while ( n < N_max )
        c ← (2n/x) b − a
        STORE(c, n + 1, table)
        if ( c < 0.1a or c < 0.1b )
            then d ← (4n(n+1)/x²) b − (2(n+1)/x) a
                STORE(d, n + 2, table)
                a ← c;   b ← d;   n ← n + 2
            else a ← b;   b ← c;   n ← n + 1
```

Routine 5–B.5 Subroutine for Backward Recurrence

```
BACKWARD-RECURRENCE(a, b, start_n, x, table)
    Δ ← 0
    n ← start_n
    while ( n ≤ 0 )
        c ← (2n/x) b − a
        STORE(c, n − 1, table)
        if ( n is odd )
            then Δ ← Δ + c
        if ( c < 0.1a or c < 0.1b )
            then d ← (4n(n−1)/x²) b − (2(n−1)/x) a
                STORE(d, n − 2, table)
                if ( n is even )
                    then Δ ← Δ + d
                a ← c;   b ← d;   n ← n − 2
            else a ← b;   b ← c;   n ← n − 1
        if ( Δ > 10^K )
            then table[0] ← n + 2
                EXIT
    if ( start_n > 40 )      bf then Δ ← 2Δ − table[0]
            for every n from 0 to N_max
                table[n] ← table[n]/Δ
```

Routine 5–B.6 Subroutine for Storing Computed Results

```
STORE(v, n, table)
    if ( 0 ≤ n ≤ N_max )
        then table[n] ← v
```

Routine 5–B.7 Routine for Generating Bessel Function Of The Second Kind

GENERATE-Y-TABLE(x, *table*)
  if ($x < 30$)
    then $n \leftarrow [1.2x]$
      $a \leftarrow Y_n(x)$ *according to eqn. (5-B.2)*
      $b \leftarrow Y_{n+1}(x)$ *according to eqn. (5-B.2)*
      BACKWARD-RECURRENCE($b, a, n-1, x$, *table*)
      FORWARD-RECURRENCE(a, b, n, x, *table*)
    else $a \leftarrow Y_0(x)$ *according to eqn. (5-B.2)*
      $b \leftarrow Y_1(x)$ *according to eqn. (5-B.2)*
      FORWARD-RECURRENCE($a, b, 0, x$, *table*)

measure, when the argument is small, backward recurrence is used to take the advantage that the largest number of significant figures are retained at orders roughly $[1.2x]$.

In the present implementation, when x is small, ($x \leq 30$), the seeds are chosen as $Y_N(x)$ and $Y_{N+1}(x)$ and generated by eqn. (5-B.2), where $N = [1.2x]$. Then, the backward recurrence is used to span to the orders from 0 to $N-1$ and the forward recurrence is used in the range from $N+2$ to $N_{\max}$. When x is large ($x > 30$) the seeds are $Y_0(x)$ and $Y_1(x)$ generated by eqn. (5-B.5), and only the forward recurrence is used. Accordingly, Routine GENERATE-Y-TABLE(x, *table*) is straightforward.

In order to maintain the best efficiency of the computer programs, many of the subroutines and the third level routines (whose algorithms are not given since they simply implement the designated equations) are shared by GENERATE-J-TABLE and GENERATE-Y-TABLE. A minor problem arises in the backward recurrence routine: Routine GENERATE-Y-TABLE does not need a normalization to be performed, whereas Routine GENERATE-J-TABLE does. In GENERATE-Y-TABLE, the backward recurrence is only used when $x \leq 30$, in which range the starting order is $[1.2x]$. On the other hand, the backward recurrence used in GENERATE-J-TABLE has a starting order of roughly K, which is usually about 300 in most computers. Therefore, a mechanism is set up in Subroutine BACKWARD-RECURRENCE such that the normalization will be performed only when the starting order *start_n* is larger than 40.

Verification

The computed Bessel functions have been verified by computing the following Wronskian relation[10]

$$J_{n+1}(x)Y_n(x) - J_n(x)Y_{n+1}(x) = \frac{2}{\pi x} \tag{5-B.19}$$

The verification is based on the assumption that if the result of the left-hand side of eqn. (5-B.19) has S significant figures that match those in the result in the right-hand side of eqn. (5-B.19), then all values involved in the left-hand side are said to have at least S significant figures.

All the integer values of both n and x in the range $1 \leq x \leq 100$ and $0 \leq n \leq 100$ have been tested. The verification shows that the largest and the smallest number of significant figures among the computer Bessel functions are 15 and 11 respectively, and the number of significant figures averaged over all 10100 results is 14.51.

6

Scatterer Polymerization

Abstract: *The methodology of scatterer polymerization is proposed, implemented and verified. This is a scatterer-building process that constructs abstract scatterers to be used in general multiple-scattering solution. The purpose of building such an abstract scatterer is to reduce the number of scatterers that enters the multiple-scattering solution while maintaining a large number of actual scatterers. This is a way to expand the computability of the multiple-scattering solution.*

Contents:

Nomenclature

General Conventions

- Matrices are denoted by bold-faced symbols; symbols for column matrices are enclosed by flower brackets ({}); symbols for rectangular matrices are enclosed by square brackets ([]).
- When referring to a matrix entry, the entry's indicial number is to appear as subscript(s) *outside* the brackets. This distinguishes the indicial subscript(s) from the subscript(s), if any, associated with the entire matrix.

Symbols

a	Radius of the fiber in the fiber-interphase-matrix micromechanics model for fiber reinforced composites.
a_c	Core radius of a molecule; that is, the radius of the circle that passes through the origin of the local coordinate systems farthest away from the origin of the global coordinate system.
a_s	Radius of a scatterer: the radius of the smallest circle that circumscribes the entire scatterer or all scatterers that make up the molecule.
$\{\boldsymbol{A}_i\}, \{\boldsymbol{B}_i\}, \cdots$	Wave expansion coefficient (column) matrices for Scatterer i
b	Outer radius of the interphase in a fiber-interphase-matrix micromechanics model for fiber reinforced composites.
(d_i, θ_{iO})	Global polar coordinates of the origin of Scatterer i's local coordinate system.
e_1, e_2	T-matrix comformity errors.
$\{\boldsymbol{H}(r,\theta)\}$	Singular wave expansion basis in the global coordinate system.
$\{\boldsymbol{H}(r_i,\theta_i)\}$	Singular wave expansion basis of Scatterer i.
$H_n^{(1)}(z)$	Hankel function of the first kind and the n-th order.
$\hat{\imath}$	Unit of imaginary numbers, $\hat{\imath} = \sqrt{-1}$.
$\{\boldsymbol{J}(r,\theta)\}$	Regular wave expansion basis in global coordinate system.
$\{\boldsymbol{J}(r_i,\theta_i)\}$	Regular wave expansion basis for Scatterer i.
$J_n(z)$	Bessel function of the first kind and the n-th order.
k	Wave number of SH waves.
$[\boldsymbol{K}_i]$	The multiple-scattering kernel matrix of Scatterer i.
M	Truncation term (truncation size) for infinite series and matrices.
N	Total number of *elements* in a multiple-scatterer configuration.
$\mathcal{N}$	Total number of *scatterers* in a multiple-scatterer configuration. A scatterer can be an element or a molecule.
$[\boldsymbol{Q}_i]$	Global coordinate translation matrix for Scatterer i.
$[\boldsymbol{T}_i]$	T-matrix of Scatterer i.
$[\boldsymbol{T}^{\text{total}}]$	T-matrix of an assemblage of scatterers.
ϕ	Complex amplitude of displacement w for SH waves.
Σ	The first norm of matrix $[\boldsymbol{T}^{\text{total}}]$, $\Sigma = \|[\boldsymbol{T}^{\text{total}}]\|$.

Superscripts

T	Matrix transposition.
$*$	Matrix conjugate transposition.

Subscripts

i, j	Scatterer identifier.
m, n	Indicial number for a matrix entry.

6-1 Introduction

In Chapter 4, a formal solution for general multiple-scattering problems is formulated. The formal solution is analytically exact and in theory is capable of handling arbitrary numbers of similar or dissimilar scatterers. However, in Chapter 5, it is observed that the main limitation of its capability is the amount of computer memory available for the computation. The examples in Chapter 5 indicate that the computer used in the present study can only accommodate problems having roughly 30 fibers.

Furthermore, it is shown in Chapter 5 that even in an optimal situation in which scatterers are evenly distributed around a clustered area, the *problem size*, the size of computer memory required to solve the problem, grows at least at a rate of $\sim N^2$. With such a high growth rate, even if the computer memory were doubled, the computer could only accommodate a problem having about 45 fibers. These numbers of fibers are far too limiting for the goal of "full-scale simulation" of this thesis.

Simply expanding the computer memory is not an economical way, if feasible at all, to expand the computability of the multiple-scattering solution. Alternative ways must be sought. A computational methodology called the *scatterer polymerization* is developed in this chapter as an attempt to reduce the growth rate of the problem size.

The central concept in the multiple-scattering formulation is the T-matrix. The T-matrix of a scatterer is the transformation matrix that relates the wave expansion coefficients of the scattered and the incident waves. The complete definition of the T-matrix is given in Chapter 3. In essence, T-matrices of all the scatterers involved are all that are necessary for solving a multiple-scattering problem.

The basic idea of the scatterer polymerization methodology is to exploit this fact further to represent an assemblage of a number of scatterers by a single T-matrix, thus effectively reduce the entire assemblage to a single but abstract scatterer. This way, an assemblage of a large number of scatterers can be treated as consisting only a few abstract scatterers but each abstract scatterer contains of a fair number of actual scatterers. The effect is that the number of scatterers involved in the multiple-scattering formulation is significantly reduced, thus the problem size.

In Section 6-2, this idea is explained in detail, including examples illustrating the reduction of the problem size growth rate. A full mathematical formulation for the methodology of scatterer polymerization is presented in Section 6-3, and verifications through numerical examples are presented in Section 6-4. Finally, some computational behaviors of the methodology are explored via numerical examples in Section 6-5.

6-2 Idea of Scatterer Polymerization

In this section, the idea of scattered polymerization is explained with the postulation that it is possible to treat an assemblage of scatterers as a *single* but somewhat abstract scatterer. To treat an assemblage as a single scatterer means the *T-matrix for the assemblage* can be found. This postulation will be proved, by providing the mathematical formulation for the T-matrix for the assemblage, in the next section.

Consider, for example, the consecutive computations depicted in Fig. 6–1 in which different numbers of fibers are assembled during different stages of the computation.

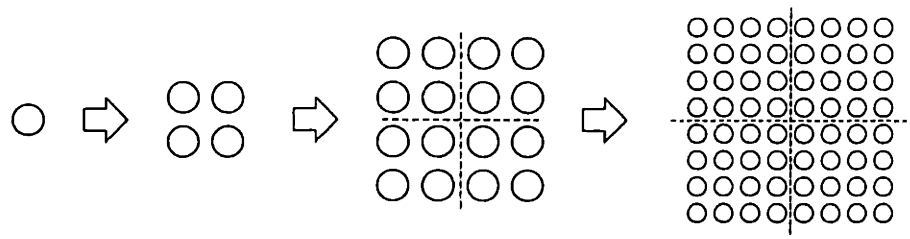

Fig. 6–1 An example of scatterer polymerization.

In the first stage as indicated by the left-most hollow arrow, 4 individual scatterers, single fibers as shown to the left of the arrow, are used in the assemblage, as shown to the right of the arrow. The multiple-scattering solution can be applied to the assemblage. Instead of finding the response in the steady state, the T-matrix for the 4-fiber assemblage is found. In this process, a single fiber is called an *element* and the assemblage is called a *molecule.*

In the second stage as indicated by the center hollow arrow, 4 individual scatterers, molecules generated from the previous stage as shown to the left of the arrow, are used in the assemblage, as shown to the right of the arrow. Since the T-matrix for an individual scatterer (molecule) has been found in the previous stage, the multiple-scattering solution can be applied to the assemblage and the T-matrix for the 16-fiber assemblage is found. The assemblage is called a *polymerized molecule.*

Similarly, in the third stage as indicated by the right-most hollow arrow, the individual scatterers in this stage are polymerized molecules whose T-matrix has been found the the previous stage. The assemblage is yet another polymerized molecule, whose T-matrix is to be found in this stage.

The entire process, or any stage of it, is called the *scatterer polymerization* in analogy to common material structures. Briefly, it can be summarized as that the *scatterer polymerization* is a scatterer-building process in which a number of scatterers are assembled and analyzed; and as the result, the T-matrix for the assemblage

Table 6–1: Comparison of Problem Sizes of Scatterer Polymerization Methodology and Multiple-Scattering Solution

	Scatterer Polymerization			Multiple-Scattering	
	$\mathcal{N}$	N	Size ($\sim\mathcal{N}^2M^2$)	N	Size ($\sim N^2M^2$)
Stage 1	4	4	$\sim 16M^2$	4	$\sim 16M^2$
Stage 2	4	16	$\sim 16M^2$	16	$\sim 256M^2$
Stage 3	4	64	$\sim 16M^2$	64	$\sim 4096M^2$

is found, which can be used to represent the assemblage as a single scatterer in later computations.

In future discussions, it might be beneficial to make several terminological distinctions. The term *scatterer* is used to inclusively refer to either an actual scatterer or an abstract scatterer built by a scatterer polymerization process. The abstract scatterer built by a scatterer polymerization process is called a *molecule*. A polymerized molecule is also called a molecule for simplicity. A single actual scatterer is an *element*, and for the particular considerations in this thesis, it is more often called a *fiber*. For example in Fig. 6–1, there are 4 scatterers in every stage; the assemblage consists of 4 fibers in the first stage, 4 molecules or 16 fibers in the second stage and 4 molecules or 64 fibers in the third stage.

Recall briefly the analysis of the problem size in §5-4.3 in Chapter 5. In the formal multiple-scattering solution, the problem size growth rate is $\sim N^2M^2$, where N is the number of fibers, M is the truncation size of the problem, and $\sim$ denotes the asymptotic behavior when all other problem parameters remain the same.

By using the scatterer polymerization methodology, the problem size now can be denoted as $\sim\mathcal{N}^2M^2$ where $\mathcal{N}$ is the number of scatterers. Although both N and $\mathcal{N}$ denote the number of scatterers, they have different meanings where lies the difference in problem sizes. More precisely, N denotes the number of fibers; whereas $\mathcal{N}$ denotes the number of molecules.

Assume that the configurations shown in Fig. 6–1 are to be analyzed side-by-side by using the scatterer polymerization and by directly using the multiple-scattering solution, and assume that the same truncation size M is used in both approaches, Table 6–1 lists the corresponding memory requirements in each stage. From Table 6–1, it becomes obvious that the problem size is tremendously reduced by using the scatterer polymerization process.

It must be noted that Fig. 6–1 is merely an example which happens to have the same number of identical scatterers in each stage. There is no such limitation inherent of the scatterer polymerization methodology, as with the formal multiple-scattering solution. In fact, even molecules of different degrees of polymerization can be combined, which entails great flexibilities to tailor the polymerization process at will.

6-3 Mathematics of Scatterer Polymerization

As stated earlier, to treat an assemblage of scatterers as a single scatterer is to represent the assemblage, in analogy to a single scatterer, by a single T-matrix for the assemblage for later computations. Thus it is necessary to begin the mathematical formulation for the scatterer polymerization with a brief review of the definition of the T-matrix for a scatterer, which has been discussed in great detail in Chapter 3. Considerations are restricted to the case of SH wave (horizontally polarized shear wave) scattering problems.

6-3.1 T-Matrix for Single Scatterer

As discussed in Chapter 3, the T-matrix for a scatterer specifies a single-scatterer problem configuration, a coordinate system and a set of wave expansion bases. In the single-scatterer problem configuration, a single scatterer is located at the origin of a coordinate system, and throughout this thesis, a polar coordinate system is used, whose coordinates are denoted as (r, θ).

Within the definition of the T-matrix, the incident wave is expressed as, in matrix notation,

$$\phi^{\text{inc}} = \{\boldsymbol{A}\}^T \{\boldsymbol{J}(r,\theta)\} \tag{6-1}$$

where $\{\boldsymbol{A}\}$ is the wave expansion coefficient matrix for the incident wave, and $\{\boldsymbol{J}(r,\theta)\}$ is the *regular* wave expansion basis, whose element in the n-th column $(n = -\infty, \cdots, -1, 0, 1, \cdots, \infty)$ is

$$\{J(r,\theta)\}_n = J_n(kr)\mathrm{e}^{\mathrm{i}n\theta} \tag{6-2}$$

where k is the wave number, $J_n(z)$ is the Bessel function of the first kind at order n, and i denotes the unit of imaginary numbers, $\mathrm{i} = \sqrt{-1}$.

The scattered wave is expressed as

$$\phi^{\text{s}} = \{\boldsymbol{B}\}^T \{\boldsymbol{H}(r,\theta)\} \tag{6-3}$$

where $\{\boldsymbol{B}\}$ is the wave expansion coefficient matrix for the scattered wave, and $\{\boldsymbol{H}(r,\theta)\}$ is the *singular* wave expansion basis, whose element in the n-th column $(n = -\infty, \cdots, -1, 0, 1, \cdots, \infty)$ is

$$\{H(r,\theta)\}_n = H_n^{(1)}(kr)\mathrm{e}^{\mathrm{i}n\theta} \tag{6-4}$$

where $H_n^{(1)}(z)$ is the Hankel function of the first kind at order n.

The total wave in the host medium can be written as

$$\phi^{\text{total}} = \phi^{\text{inc}} + \phi^{\text{s}} = \{\boldsymbol{A}\}^T \{\boldsymbol{J}(r,\theta)\} + \{\boldsymbol{B}\}^T \{\boldsymbol{H}(r,\theta)\} \tag{6-5}$$

In other words, the total wave consists of two wave: the incident wave expressed in the regular wave expansion basis and the scattered wave expressed in the singular wave expansion basis.

The T-matrix for the scatterer relates the wave expansion coefficients of the scattered and the incident waves such that

$$\{\boldsymbol{B}\} = [\boldsymbol{T}]\{\boldsymbol{A}\}. \tag{6-6}$$

6-3.2 T-Matrix for Assemblage

Recall the formal solution for a multiple-scattering problem involving N scatterers. The solution gives the total wave in the host medium as

$$\phi^{\text{total}} = \phi^{\text{inc}} + \sum_{i=1}^{N} \phi_i = \phi^{\text{inc}} + \sum_{i=1}^{N} \{\boldsymbol{C}_i\}^T \{\boldsymbol{H}(r_i, \theta_i)\} \tag{6-7}$$

where ϕ_i is the total scattered wave scattered by Scatterer i, (r_i, θ_i) denotes Scatterer i's local polar coordinate system, and $\{\boldsymbol{C}_i\}$ is the wave expansion coefficient matrix for ϕ_i, which can be solved according to the following

$$\{\boldsymbol{C}_j\} = [\boldsymbol{T}_j]\{\boldsymbol{A}_j\} + \sum_{\substack{i=1 \\ i \neq j}}^{N} [\boldsymbol{L}_{ij}]\{\boldsymbol{C}_i\} \tag{6-8}$$

$$[\boldsymbol{L}_{ij}] = [\boldsymbol{T}_j][\boldsymbol{R}_{ij}]^T \tag{6-9}$$

where $[\boldsymbol{T}_j]$ is the T-matrix of Scatterer j, $[\boldsymbol{R}_{ij}]$ is the *coordinate translation matrix* between Scatterers i and j and

$$[R_{ij}]_{mn} = \mathrm{e}^{\mathrm{i}(m-n)\theta_{ij}} H^{(1)}_{m-n}(kd_{ij}) \tag{6-10}$$

and (d_{ij}, θ_{ij}) is the coordinates of the origin of Scatterer i's local coordinate system in Scatterer j's local coordinate system.

Assume a global polar coordinate system has been built, whose coordinates are referred to as (r, θ). The geometrical relation between the global coordinate system and Scatterer i's local coordinate system is depicted in Fig. 6–2.

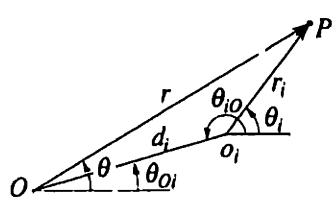

Fig. 6–2 Geometries of local and global polar coordinate systems.

In Fig. 6–2, P is an arbitrary field point which can be located by either the global polar coordinates (r, θ) or Scatterers i's local polar coordinates (r_i, θ_i). The global coordinates (d_i, θ_{iO}) locate the origin of Scatterer i's local coordinate system o_i. The

coordinates (d_i, θ_{Oi}) in Scatterer i's local coordinate system locate the origin of the global coordinate system O. It can be found that

$$\theta_{Oi} = \theta_{iO} - \pi \tag{6-11}$$

Also, recall *Graf's addition theorem* of Bessel functions[1]

$$H_m^{(1)}(\varpi) \begin{matrix}\cos\\ \sin\end{matrix} m\beta = \sum_{n=-\infty}^{\infty} H_{m+n}^{(1)}(Z) J_n(z) \begin{matrix}\cos\\ \sin\end{matrix} n\alpha \tag{6-12}$$

$$J_m(\varpi) \begin{matrix}\cos\\ \sin\end{matrix} m\beta = \sum_{n=-\infty}^{\infty} J_{m+n}(Z) J_m(z) \begin{matrix}\cos\\ \sin\end{matrix} n\alpha \tag{6-13}$$

where m and n are integers. Equation (6–12) is valid only when $|Z| > |ze^{\pm i\alpha}|$; whereas eqn. (6–13) is valid throughout the plane. For actual distances (meaning Z, z and ϖ are real and positive), the geometrical relations of the parameters involved are sketched in Fig. 6–3, and the validity condition for eqn. (6–12) reduces to $Z > z$.

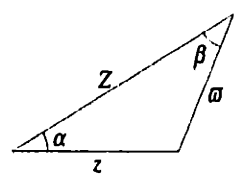

Fig. 6–3 Geometries of Graf's addition theorem.

Comparing the geometries in Figs. 6–2 and 6–3, with the following substitutions

$$z \to kd_i \qquad \varpi \to kr_i \qquad Z \to kr \qquad \alpha \to \theta - \theta_{Oi} \qquad \beta \to \theta_i - \theta$$

eqn. (6–12) can be written in complex notation as

$$H_m^{(1)}(kr_i)e^{im(\theta_i-\theta)} = \sum_{n=-\infty}^{\infty} H_{m+n}^{(1)}(kr) J_n(kd_i) e^{in(\theta-\theta_{Oi})} \tag{6-14}$$

With slight rearrangements, it can be further written as

$$H_m^{(1)}(kr_i)e^{im\theta_i} = \sum_{n=-\infty}^{\infty} e^{i(m-n)\theta_{iO}} J_{m-n}(kd_i) H_n^{(1)}(kr) e^{in\theta} \tag{6-15}$$

where the following relation of Bessel functions[2]

$$J_{-n}(z) = (-1)^n J_n(z) = e^{in\pi} J_n(z) \tag{6-16}$$

and the relation between θ_{iO} and θ_{Oi} in eqn. (6–11) have been used. In matrix form,

$$\{\boldsymbol{H}(r_i, \theta_i)\} = [\boldsymbol{Q}_i]\{\boldsymbol{H}(r, \theta)\} \tag{6-17}$$

where the element of matrix $[\boldsymbol{Q}_i]$ at the m-th row and the n-th column is

$$[Q_i]_{mn} = e^{i(m-n)\theta_{iO}} J_{m-n}(kd_i) \tag{6-18}$$

and $[\boldsymbol{Q}_i]$ is called the *global coordinate translation matrix* of Scatterer i.

By a similar procedure using eqn. (6–13), it can be shown that the transformation for the regular wave expansion basis is

$$J_m(kr_i)e^{im\theta_i} = \sum_{n=-\infty}^{\infty} e^{i(m-n)\theta_{iO}} J_{m-n}(kd_i) J_n(kr) e^{in\theta} \tag{6–19}$$

or, in matrix form

$$\{\boldsymbol{J}(r_i, \theta_i)\} = [\boldsymbol{Q}_i]\{\boldsymbol{J}(r, \theta)\} \tag{6–20}$$

Note that eqn. (6–19) is valid throughout the plane, and can be interpreted as translating the coordinate system to the one that is originated at point (d_i, θ_{iO}). The same relation can be applied to translate the global coordinate system to scatterer i's local coordinate system by nothing that the new origin is at (d_i, θ_{Oi}). That is,

$$J_m(kr)e^{im\theta} = \sum_{n=-\infty}^{\infty} e^{i(m-n)\theta_{Oi}} J_{m-n}(kd_i) J_n(kr_i) e^{in\theta_i} \tag{6–21}$$

On the other hand, eqn. (6–20) can be rewritten as

$$\{\boldsymbol{J}(r, \theta)\} = [\boldsymbol{Q}_i]^{-1}\{\boldsymbol{J}(r_i, \theta_i)\} \tag{6–22}$$

Comparing eqns. (6–21) and (6–22) gives

$$\left([Q_i]^{-1}\right)_{mn} = e^{i(m-n)\theta_{Oi}} J_{m-n}(kd_i) \tag{6–23}$$

where $\left([Q_i]^{-1}\right)_{mn}$ denotes the m-th row and the n-th column element of $[\boldsymbol{Q}_i]^{-1}$; that is, the inverse of $[\boldsymbol{Q}_i]$. Combining eqns. (3–49), (6–23) and (6–11), it can be further shown that

$$\left([Q_i]^{-1}\right)_{mn} = (-1)^{m-n}[Q_i]_{mn} \tag{6–24}$$

which can alternatively be derived from the following *Neumann's addition theorem* of Bessel functions[2]

$$J_m(x - y) = \sum_{n=-\infty}^{\infty} J_{m+n}(x) J_n(y) \tag{6–25}$$

by letting $x = y = kd_i$.

With the coordinate transformation, all the scattered waves can be re-expressed in the global coordinate system. The total wave in the host medium then becomes

$$\phi^{\text{total}} = \phi^{\text{inc}} + \sum_{i=1}^{N} \{\boldsymbol{C}_i\}^T [\boldsymbol{Q}_i]\{\boldsymbol{H}(r, \theta)\} \tag{6–26}$$

Denote

$$\{\boldsymbol{B}^{\text{total}}\} = \sum_{i=1}^{N} [\boldsymbol{Q}_i]^T \{\boldsymbol{C}_i\} \tag{6–27}$$

then, eqn. (6–26) becomes

$$\phi^{\text{total}} = \{\boldsymbol{A}\}^T \{\boldsymbol{J}(r, \theta)\} + \{\boldsymbol{B}^{\text{total}}\}^T \{\boldsymbol{H}(r, \theta)\} \tag{6–28}$$

where the incident wave has been written in its wave expansion form as in eqn. (6–1).

Comparing eqns. (6–5) and (6–28), it is noted that the two equations are in the identical form: the total wave in the host medium consists of the incident wave plus the scattered wave. Since the system under consideration is linear, in analogy to eqn. (6–6), the *T-matrix for the assemblage* can be defined such that

$$\{\boldsymbol{B}^{\text{total}}\} = [\boldsymbol{T}^{\text{total}}]\{\boldsymbol{A}\} \tag{6–29}$$

That is, the T-matrix for the assemblage is the matrix that relates the wave expansion coefficients of the incident and the total scattered wave of the assemblage of scatterers expressed in a common polar coordinate system.

6-3.3 Computation of T-Matrix for Assemblage

Recall that there are two forms of formal solutions for the multiple-scattering problems presented in Chapter 4. Correspondingly, there are two forms of computational methods for the T-matrix for the assemblage.

Form I

This is the form in which the definition of the T-matrix for the assemblage is given in §6-3.1. There is no readily available analytical expressions for $[\boldsymbol{T}^{\text{total}}]$. Rather, a computational method is described below.

Note that, from eqn. (6–29), if $\{\boldsymbol{A}\}$ is set up in such a way that only one element of $\{\boldsymbol{A}\}$, say $\{A\}_n$ is non-zero and all the others are zero, the resulting $\{\boldsymbol{B}^{\text{total}}\}$ equals a column of $[\boldsymbol{T}^{\text{total}}]$ multiplied by the common factor $\{A\}_n$. This suggests the following computational method:

For every value of n, set $\{A\}_n = 1$ and all other elements of $\{\boldsymbol{A}\}$ to zero. From this, compute a set of $\{\boldsymbol{A}_i\}$, and solve the multiple-scattering problem of the assemblage subjected to the hypothetical incident wave represented by this set of $\{\boldsymbol{A}_i\}$. This multiple-scattering solution gives a set of wave expansion coefficient matrices of the scattered waves $\{\boldsymbol{C}_i\}$. Assemble this set of matrices according to eqn. (6–27), then the resulting matrix $\{\boldsymbol{B}^{\text{total}}\}$ is the n-th column of $[\boldsymbol{T}^{\text{total}}]$. The complete matrix $[\boldsymbol{T}^{\text{total}}]$ is obtained after n has run through the desired index range.

In computing $\{\boldsymbol{A}_i\}$ from $\{\boldsymbol{A}\}$, it is noted that they represent the same incident wave expressed in different coordinate systems. That is

$$\phi^{\text{inc}} = \{\boldsymbol{A}\}^T\{\boldsymbol{J}(r,\theta)\} = \{\boldsymbol{A}_i\}^T\{\boldsymbol{J}(r_i,\theta_i)\} \tag{6–30}$$

By using the coordinate transformation in eqn. (6–20), the last equation can be rewritten as

$$\{\boldsymbol{A}_i\}^T\{\boldsymbol{J}(r_i,\theta_i)\} = \{\boldsymbol{A}_i\}^T[\boldsymbol{Q}_i]\{\boldsymbol{J}(r,\theta)\} \tag{6–31}$$

which gives

$$\{\boldsymbol{A}_i\} = [\boldsymbol{Q}_i]^{-T}\{\boldsymbol{A}\} \tag{6–32}$$

Routine 6–1: Routine for Computing T-Matrix for an Assemblage

```
COMPUTE-T-TOTAL
    setup multiple-scattering problem geometry
    preset truncation term M
    for every n from −M to M
        {A}_n ← 1; {A}_m ← 0 when m ≠ n
        for every i from 1 to N
            compute {A_i} from {A} according to eqn. (6–32)
        solve multiple-scattering problem with {A_i} as incident
        assemble {B^total} according to eqn. (6–27)
        put {B^total} as n-th column of [T^total]
```

where $[\boldsymbol{Q}_i]^{-T} = ([\boldsymbol{Q}_i]^{-1})^T$ and the expression for elements of $[\boldsymbol{Q}_i]^{-1}$ has been given in eqn. (6–23).

The computational procedure described above resembles a direct matrix inversion algorithm[3]. This procedure is summarized as the pseudo-code in Routine 6–1.

Form II

Recall Form II's of the multiple-scattering solution in Chapter 4. In these solution forms, a multiple-scattering system's characteristic matrix, called the *multiple-scattering kernel matrix* is found such that

$$\{\boldsymbol{C}_i\} = [\boldsymbol{K}_i]\{\boldsymbol{A}_i\} \tag{6–33}$$

Thus, eqn. (6–27) can be written as

$$\{\boldsymbol{B}^{\text{total}}\} = \sum_{i=1}^{N} [\boldsymbol{Q}_i]^T \{\boldsymbol{C}_i\} = \sum_{i=1}^{N} [\boldsymbol{Q}_i]^T [\boldsymbol{K}_i]\{\boldsymbol{A}_i\} \tag{6–34}$$

Substituting eqns. (6–34) and (6–32) into eqn. (6–27) gives

$$\{\boldsymbol{B}^{\text{total}}\} = \sum_{i=1}^{N} [\boldsymbol{Q}_i]^T [\boldsymbol{K}_i][\boldsymbol{Q}_i]^{-T}\{\boldsymbol{A}\} \tag{6–35}$$

Comparing eqns. (6–27) and (6–35) gives

$$[\boldsymbol{T}^{\text{total}}] = \sum_{i=1}^{N} [\boldsymbol{Q}_i]^T [\boldsymbol{K}_i][\boldsymbol{Q}_i]^{-T} \tag{6–36}$$

However, since it has been observed in Chapter 5 that the repetitive solution forms can be problematic, due to resonance of the system, the application of Form II for computing $[\boldsymbol{T}^{\text{total}}]$ is not to be discussed further.

6-3.4 Discussions

Core Region and Territory of Molecule

The validity condition for transforming Scatterer i's local singular wave expansion basis $\{\boldsymbol{H}(r_i, \theta_i)\}$ to the global singular wave expansion basis $\{\boldsymbol{H}(r, \theta)\}$ is $r > d_i$. That is, the transformed expression is valid outside a circular region of radius d_i and centered at the origin of the global coordinate system.

In deriving $[\boldsymbol{T}^{\text{totla}}]$, such a transformation is applied to every scatterer in the assemblage. Thus, the total scattered wave scattered by the assemblage as expressed in eqn. (6–28) is only valid outside a circle region centered at the origin of the global coordinate system and having the radius that equals the largest d_i, *i.e.*, the farthest distance from the origin of the global coordinate system to the origins of the local coordinate systems. Define

$$a_c = \max_{i=1}^{N} (d_i) \tag{6–37}$$

then, eqn. (6–28) is valid in the region $r > a_c$. The region $r \leq a_c$ is called the *core* of a molecule in which eqn. (6–28) becomes invalid, and a_c is called the *core radius* of a molecule. In essence, the core of a molecule becomes a part of the molecule and distinghushes itself from being the host medium.

When the assemblage, or the molecule, is treated as a single scatterers, the definitions of its territory and radius, which have been given in Chapter 4 for an element, still apply and it is worth repeating here with the adaption for the concept of a molecule. The *territory* of a molecule is the smallest circle that circumscribes all the elements that make up the molecule. The radius of its territory is called the *radius* of the molecule.

Figure 6–4 illustrates the core region and the territory of a molecule consisting of three elements. In Fig. 6–4, o_i, o_j and o_k denote the origins of local coordinate systems, and O denotes the origin of the global coordinate system. Among all the origins of local coordinate systems, o_k is located the farthest away from O and thus determines the core radius of the molecule a_c. However, a portion of Scatterer j is the farthest away from O and thus determines the radius of the molecule a_s. In general, $a_s > a_c$.

The same definitions of the core, the territory and their radii apply to polymerized molecules. Figure 6–5 shows such an example. In Fig. 6–5, the assemblage consists of 3 molecules shown in Fig. 6–4, o_i, o_j and o_k are the origins of local coordinate systems and O is the origin of the global coordinate system. The core region is represented by the gridded circular region, which is dictated by the location of o_k. The territory is marked by the outer-most circle, which is dictated by one of the elements in molecule k.

In the multiple-scattering solution, Graf's addition theorem requires that the territory of a scatterer should not enclose the origin of any other scatterer's local

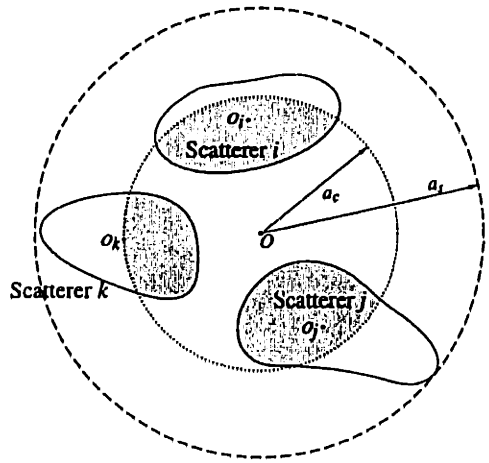

Fig. 6–4 The core, defined as the shaded circular region of radius a_c, of a molecule made up of 3 elements. The territory of the molecule is marked by the outer-most circle of radius a_s.

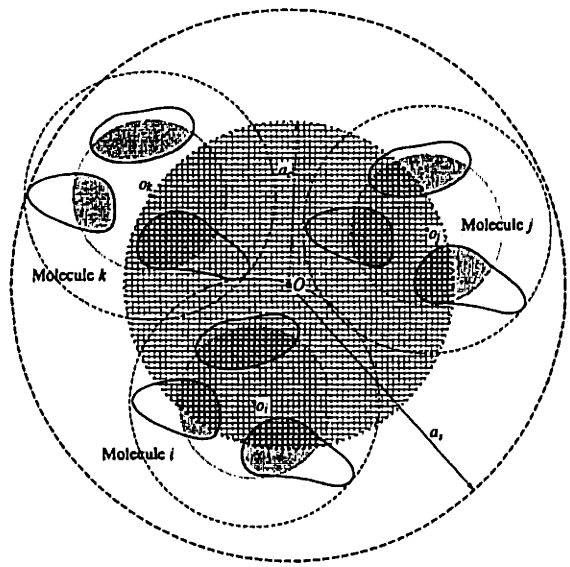

Fig. 6–5 Polymerized molecule made up of 3 molecules shown in Fig. 6–4. Its core is marked by the gridded circular region of radius a_c, and its territory is marked by the outer-most circle of radius a_s.

coordinate system. For a molecule or a polymerized molecule, the definition of its territory conforms with that for a scatterer. The core region of a molecule is smaller than its territory in general. Therefore, no additional restriction is introduced by the scatterer polymerization regarding the arrangements of the scatterers.

Interior Fields

Unfortunately, some information is lost in the scatterer polymerization process. For example, there are no longer readily available formulas for the wave fields interior of each element. And so are the wave fields within the core region of each molecule.

In theory, those lost information can all be recovered. For example, it is possible to track the interior fields. For Form I, the recovery requires maintaining the multiple-scattering solution $\{C_i\}$ for every set of hypothetical incident wave $\{A\}$. These solutions, if properly arranged, are in fact the same as the multiple-scattering kernel matrix $[K_i]$ used in Form II. However, such a recovering process would soon become extremely tedious within just a few stages of polymerization.

Implementation Considerations

The implementation of Routine 6–1 is straightforward. Recall that in implementing the multiple-scattering solutions, truncation and convergence criteria must be established prior to the implementation. For a scatterer polymerization process, such criteria become unnecessary.

The ultimate goal of scatterer polymerization is to construct a molecule and and to find its T-matrix. The thus-found T-matrix will be used in later computations, such as further polymerization or used to find a particular solution of the molecule, either in a single- or multiple-scatterer configuration. The truncation size is only need to be determined in the latter case. During a scatterer polymerization process, the truncation size is simply determined *a priori*.

In a computation, the multiple-scattering problem is solved by using Supermatrix Form. As shown in Chapter 5, this solution form can be used as an all-around form which has not encountered any particular numerical difficulty so far, and virtually any established solvers for linear equation system can be used to solve the resulting linear equation system. Whereas other repetitive solution forms have failed to reach converged solutions under some circumstances. Furthermore, in computing $[\boldsymbol{T}^{\text{total}}]$, the multiple-scattering problem for the same configuration is solved multiple times, with a different incident wave each time but the system matrix for the resulting linear equation system remains the same. For such computations, LU-decomposition solver is efficient for solving the resulting linear equation system since the LU-decomposition only need to be performed once.

6-4 Verifications

In this section, a small-scale example is studies numerically to verify that both the formulation and the computer implementation of the scatterer polymerization methodology are correct. The example is chosen such that the problem configuration is also computable by directly using the multiple-scattering solution, whose computer programs have been verified in Chapter 5. Three independent verifications will be performed.

6-4.1 Verification Methods

The first verification is the *T-matrix property conformity verification.* It has been shown in Chapter 3 that some properties inherent of a T-matrix are imposed by some basic physical principles. In particular, for SH wave scattering, any T-matrix should possess the following properties:

$$[T]_{mn} = (-1)^{m-n}[T]_{(-n)(-m)} \tag{6-38}$$

$$\tfrac{1}{2}([\boldsymbol{T}]^* + [\boldsymbol{T}]) = -[\boldsymbol{T}]^*[\boldsymbol{T}] \tag{6-39}$$

where $*$ denotes the conjugate transpose of a matrix; that is, $[\boldsymbol{T}]^* = [\overline{\boldsymbol{T}}]^T = \overline{[\boldsymbol{T}]^T}$, and the overbar denotes the complex conjugate. Without exception, any T-matrix for an assemblage of scatterers as computed by the scatterer polymerization process should possess the above properties.

Define the following error measurements, called *T-matrix property conformity errors*:

$$e_1 = \sum_{m=0}^{M} \sum_{n=-M}^{M} \left| [T^{\text{total}}]_{mn} - (-1)^{m-n}[T^{\text{total}}]_{(-n)(-m)} \right| \tag{6-40}$$

$$e_2 = \left\| [\tau] \right\|_1 = \sum_{m=-M}^{M} \sum_{n=-M}^{M} |[\tau]_{mn}| \tag{6-41}$$

where $\|\cdot\|_1$ denotes the *first norm* of a matrix, and

$$[\tau] = \tfrac{1}{2}\left([\boldsymbol{T}^{\text{total}}]^* + [\boldsymbol{T}^{\text{total}}]\right) + [\boldsymbol{T}^{\text{total}}]^*[\boldsymbol{T}^{\text{total}}] \tag{6-42}$$

According to eqns. (6–38) and (6–39), if the T-matrix for the assemblage is exact, e_1 vanishes, and e_2 represents a truncation error. Non-vanishing e_1 represents other errors incurred during the computation. Relative errors can be observed by comparing the errors e_1 and e_2 against the first norm of the T-matrix denoted as $\Sigma = \|[\boldsymbol{T}^{\text{total}}]\|_1$.

Since eqns. (6–38) and (6–39) are derived from the energy conservation principle and the reciprocity principle of elastodynamics, this verification is equivalent of performing verifications for the requirements set forth by these principles.

The second verification is the *wave field computation verification* in which the wave fields at some arbitrarily chosen points are checked. In the first, the assemblage of scatterers is treated as a single scatterer, and the T-matrix for the assemblage is used to compute the wave fields in the host medium according to eqn. (6–28). Next, as a comparison, the same wave fields are computed by directly using the multiple-scattering solution. In both cases, the incident wave is assumed as a plane wave of unit amplitude propagating along $\theta = 0$ direction, whose expressions is known as[4]

$$\phi^{\text{inc}} = \mathrm{e}^{ikr\cos\theta} = \sum_{n=-\infty}^{\infty} i^n J_n(kr)\mathrm{e}^{in\theta} \tag{6-43}$$

Note that by assuming a *unit-amplitude* incident wave in the nondimensional form as in eqn. (6–43), it is equivalent of assuming that the wave field ϕ has been *normalized* and *nondimensionalized* by the amplitude of the incident wave.

The third verification is the *consistency verification* in which the same assemblage is polymerized differently in the intermediate stage(s) of the computation, and the consistency of the resulting T-matrix for the assemblage is checked. Theoretically, as long as the final configuration remains the same, different polymerization processes should yield the same results.

6-4.2 Example of Four-Fiber Configuration

Consider a configuration consisting of 4 identical 2-layer circular cylinders in a square arrangement as sketched in Fig. 6–6. The origin of the global coordinate system is located at the geometrical center of the configuration.

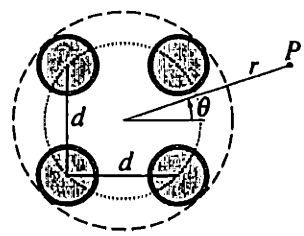

Fig. 6–6 Configuration of a molecule consisting of 4 fibers arranges in square. Dashed circle shows the territory of the molecule. Dotted circle shows its core region.

This configuration is an extension of a fiber-interphase-matrix micromechanics model for fiber reinforced composites, in which the inner layer of the cylinder represents a fiber and the outer layer represents the interphase between the fiber and the matrix. The single-scatterer case for such a fiber-interphase-matrix model has been studies in [6] for P/SV wave scattering and in Chapter 2 for SH wave scattering. Some SH wave multiple-scattering examples have been presented in Chapter 5.

The constituent materials in the configuration correspond to a ceramic-fiber reinforced metal-matrix composite system. Material properties, taken from [6], are listed in Table 6–2. The fiber radius can be assumed as $a = 10\,\mu\text{m}$[6] when specific values are desired. More often, a is taken as a unit of length, and the nondimensionalized frequency ka is used. For all the cases considered, the outer radius of the interphase is assumed to be $b = 1.1a$, and the fiber spacing is $d = 3a$.

In the first two verifications, the entire 4-fiber assemblage is considered, and the T-matrix of the assemblage is computed at various frequencies. Truncation term is chosen *a priori* as $M = 25$.

Figure 6–7 shows the profiles of the T-matrix for the assemblage at various frequencies. In these figures, each block represents an element of the $[\boldsymbol{T}^{\text{total}}]$ matrix,

Table 6–2: Constituent Material Properties for a Metal-Matrix Ceramic-Fiber Composite System[6]

Property	Matrix (AA520 Aluminium)	Fiber (Alumina, Al_2O_3)	Interphase (Zirconia, ZrO_2)
Density (kg/m^3)	2600	3700	6300
Young's Modulus (GPa)	66	360	97
Poisson's Ratio	0.31	0.25	0.33
Lamé Constant λ (GPa)	41	144	71
Lamé Constant μ (GPa)	25	144	37
P Wave Speed (m/s)	5920	10800	4800
S Wave Speed (m/s)	3100	6240	2420

Table 6–3: T-Matrix Property Conformity Errors

ka	Σ	e_1	e_2
1	4.03127	2.74607×10^{-15}	4.27984×10^{-15}
2	15.8350	1.49163×10^{-14}	3.45528×10^{-14}
3	24.8127	4.39922×10^{-14}	1.69416×10^{-13}
4	37.0132	8.56002×10^{-14}	3.16655×10^{-13}
5	46.0868	1.37187×10^{-13}	2.55943×10^{-9}
6	60.5736	1.85996×10^{-13}	9.28128×10^{-6}

with the upper-left corner being $[T^{\text{total}}]_{(-M)(-M)}$ and the lower-right corner being $[T^{\text{total}}]_{MM}$. The height of each block represents the modulus of the element.

From these figures, it is observed that blocks of substantial moduli (observable heights) are concentrated around the central element $[T^{\text{total}}]_{00}$. As the frequency ka increases, the size of the concentration area increases accordingly. The size of the area essentially represents the necessary truncation sizes for the multiple-scattering computations.

It is also observed that, in all the profiles of the T-matrix for the assemblage in Fig. 6–7, only the elements located on the lines parallel to the major diagonal of the matrix and at distances of multiples of 4 have observable heights. This agrees with the properties of T-matrix imposed by scatterer symmetries. The molecule is symmetric about the axes of $\theta = 0, \pm\pi/4$ and $\pi/2$. From Chapter 3, these symmetries require $[T]_{mn} = 0$ if $(m-n)$ is not a multiple of 4. These symmetry properties are not used in the verification since they are not common features for a general molecule.

Table 6–3 lists the numerical values of T-matrix property conformity errors e_1 and e_2, as compared with the first norm of $[T^{\text{total}}]$, Σ. Noting that the computer used in the computation, a Silicon Graphics Inc.'s Indigo^2 workstation with an R4400 CPU and 64 M core memory, has 15 significant figures, the error e_1 is comparable with the computer's round-off errors.

The error e_2 is in the same order as e_1 at low frequencies, but increases significantly at higher frequencies. This is primarily due to insufficient truncation terms,

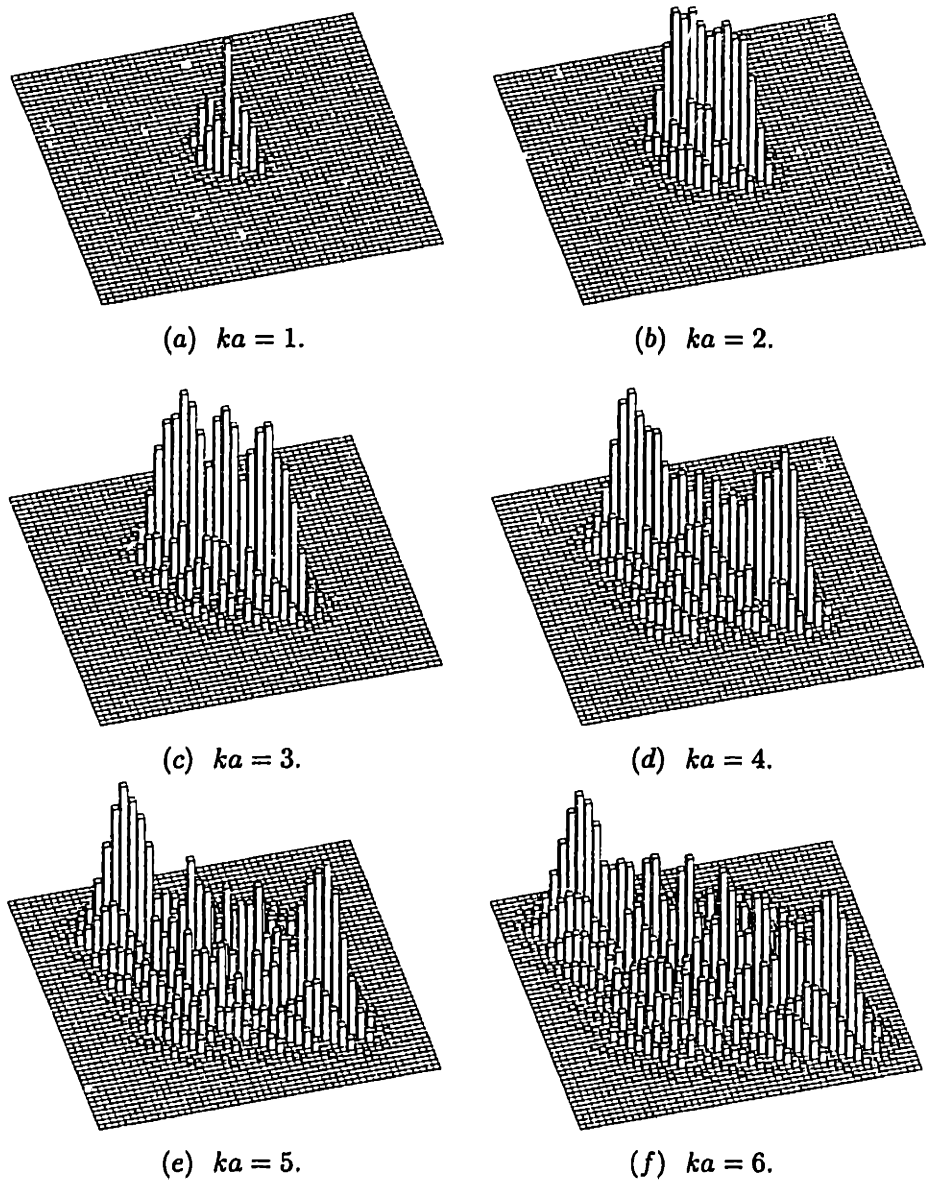

(a) $ka = 1.$ (b) $ka = 2.$

(c) $ka = 3.$ (d) $ka = 4.$

(e) $ka = 5.$ (f) $ka = 6.$

Fig. 6–7 Profiles of the T-matrix for the assemblage of 4 fibers shown in Fig. 6–6 at various frequencies.

as can be observed from the T-matrix profiles in Fig. 6–7. For instance in Fig. 6–7f, the area where blocks of observable heights concentrate has almost reached the boundary of the matrix, suggesting too small an M has been used in the computation. In a separate computation for the case of $ka = 6$ with $M = 50$, the computed errors e_1 and e_2 are 1.84170×10^{-13} and 7.05534×10^{-13}, respectively.

As the second verification, Table 6–4 lists the amplitudes of the scattered wave $|\phi^s(r, \theta)|$ at various field points, compared with the same quantities computed by directly using the multiple-scattering solution. Results obtained by multiple-scattering solution are assumed to be accurate for all the significant figures shown since exactly

Table 6–4: Comparison of Amplitudes of Scattered Wave $|\phi^s(r,\theta)|$ Computed by Scatterer Polymerization Process (SPP) and Multiple-Scattering Solution (MSS)

ka	Method	$\lvert\phi^s(20a,0)\rvert$	$\lvert\phi^s(20a,\pi)\rvert$	$\lvert\phi^s(200a,0)\rvert$	$\lvert\phi^s(200a,\pi)\rvert$
1	SPP	0.360118	0.456544	0.117171	0.143859
	MSS	0.360118	0.456544	0.117171	0.143859
2	SPP	0.917414	0.282906	0.304424	0.0845778
	MSS	0.917414	0.282906	0.304424	0.0845778
3	SPP	1.24655	0.115426	0.421966	0.0357060
	MSS	1.24655	0.115426	0.421966	0.0357060
4	SPP	1.34055	0.143890	0.465138	0.0440317
	MSS	1.34055	0.143890	0.465138	0.0440317
5	SPP	1.41403	0.202894	0.499946	0.0658883
	MSS	1.41402	0.202893	0.499945	0.0658877
6	SPP	1.30483	0.246864	0.478956	0.0757723
	MSS	1.30456	0.246989	0.478968	0.0758204

the same configuration has been studied and verified extensively in Chapter 5.

Table 6–5 shows that both methods yield almost identical results. Results for frequencies up to $ka = 4$ are identical up to all 6 significant figures shown. At $ka = 5$, discrepancies appear at the order of $1-^{-6}$; and at $ka = 6$, discrepancies are relatively large, but still acceptably small at the order of 10^{-4}.

Again, these errors are primarily due to insufficient truncation terms used in the scatterer polymerization process. In the computation for the case of $ka = 6$ and using $M = 50$, the results are identical, up to all 6 significant figures shown, to the corresponding values obtained by directly using the multiple-scattering solution.

As the third verification, the same configuration is computed by 3 different polymerization procedures referred to as Procedures A, B and C. In *Procedure A*, the entire assemblage is treated in unity, as in the previous two verifications. In *Procedure B*, two fibers are assembled first and the T-matrix for the 2-fiber assemblage is found; then two such molecules are assembled to form the (2×2)-fiber configuration, as shown in Fig. 6–8*a*. *Procedure C* is similar to Procedure B except that the 2-fiber assemblage has a different orientation, as shown in Fig. 6–8*b*.

Computations are performed for the case of $ka = 3$ using a truncation size $M = 25$. Table 6–5 compares the numerical values of various elements of the resulting matrix $[\boldsymbol{T}^{\text{total}}]$ for the final 4-fiber assemblage. These elements are chosen such that they are non-zero elements having moduli that are representative of the elements of substantial moduli of the T-matrix. Table 6–6 compares the T-matrix property conformity errors e_1 and e_2 during the computation for the 4-fiber assemblage (the second stage for Procedures B and C), along with amplitudes of the scattered wave $|\phi^s(r,\theta)|$ at various field points for the 4-fiber assemblage subjected to the incident

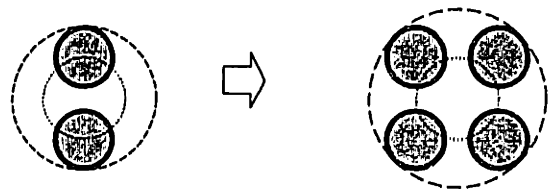

(*a*) Procedure B.

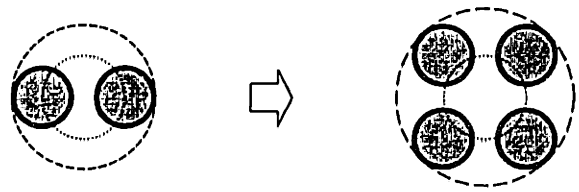

(*b*) Procedure C.

Fig. 6–8 Two alternative procedures for forming an assemblage of 4-fiber square arrangement. Dashed circles represent the territories of molecules; dotted circles represent their core regions.

wave in eqn. (6–43).

From Tables 6–5 and 6–6, it is observed that the three procedures yield essentially the same numerical results with numerical errors in an acceptable level. More detailed analyses of the error behaviors of the scatterer polymerization process are deferred until next section.

At this point, it can be concluded that the 3 verifications performed so far are all successful. Therefore, both the mathematical formulation and implemented computer programs for the scatterer polymerization methodology are correct.

6-5 Error Behaviors

The verifications in the previous section, although successful, indicate that some errors incurred in computations could be noticeably large, such as the errors during the second stage of computations in Procedures B and C. In this section, error behaviors of the scatterer polymerization process are examined systematically via numerical examples.

6-5.1 Error Measurements

Beside providing a numerical proof that both the formulation and the computer program of scatterer polymerization are theoretically correct, the examples in the previous section also provide opportunities to observed the sensitivities of the error measurements e_1 and e_2 defined therein.

Table 6–5: Computed Values of Various T-Matrix Elements at $ka = 3$.

Element	Part	Procedure A	Procedure B	Procedure C
$[T]_{00}$	*Re*	−0.955658	−0.955703	−0.955623
	Im	0.0511269	0.0511070	0.0510387
$[T]_{04}$	*Re*	−0.00132178	−0.0012663	−0.00180594
	Im	−0.139746	−0.139455	−0.139838
$[T]_{08}$	*Re*	0.0162467	0.0160304	0.0162237
	Im	−0.00610270	−0.00600950	−0.00661598
$[T]_{40}$	*Re*	−0.00132178	−0.00122970	−0.00127159
	Im	0.139746	−0.139689	−0.139721
$[T]_{44}$	*Re*	−0.894429	−0.894643	−0.894767
	Im	0.158467	0.158066	0.158320
$[T]_{48}$	*Re*	0.0456451	0.0458015	0.0455413
	Im	−0.0574435	−0.057638	−0.0575182
$[T]_{80}$	*Re*	0.0162467	0.0162527	0.0163504
	Im	−0.00610270	−0.00606144	−0.00607827
$[T]_{84}$	*Re*	0.0456451	0.0458528	0.0454153
	Im	−0.0574435	−0.0575032	−0.0580142
$[T]_{88}$	*Re*	−0.360752	−0.360459	−0.360294
	Im	−0.470712	−0.470555	−0.471042

Table 6–6: T-Matrix Property Conformity Errors and Amplitudes of Scattered Waves at $ka = 3$. (Truncation Term $M = 25$.)

	Procedure A	Procedure B	Procedure C
Σ	24.8127	24.8873	24.9387
e_1	$4.3^{4}922\times10^{-14}$	0.0457748	0.116856
e_2	1.69416×10^{-13}	0.0579395	0.116067
$\lvert\phi^s\rvert$ at $(20a, 0)$	1.24655	1.24646	1.24652
$\lvert\phi^s\rvert$ at $(20a, \pi)$	0.115426	0.115355	0.115484
$\lvert\phi^s\rvert$ at $(200a, 0)$	0.421966	0.421804	0.421949
$\lvert\phi^s\rvert$ at $(200a, \pi)$	0.0357060	0.0356756	0.0357218

From Tables 6–3 and 6–4, it is observed that in most cases, e_1 and e_2 are in the same order, with e_2 being slightly larger. When they are not in the same order, usually e_2 is larger than e_1, and this happens only when the truncation size M is too small. This indicates that the error e_2 is more sensitive to the truncation size.

Errors e_1 and e_2, when they are in the same order, appear as a good measures of the overall error level of the computation. More specifically, the ratios e_1/Σ and e_2/Σ accurately describe the relative errors of individual elements of the T-matrix for the assemblage. For instance, in Table 6–5, both e_1/Σ and e_2/Σ in both Procedures B and C are of the order of $O(10^{-3})$. Relative errors in individual elements of T-matrix ranges from 2×10^{-4} to 2×10^{-3} for Procedure B, and from 4×10^{-5} to

5×10^{-3} for Procedure C. Furthermore, it is comforting to observe that the errors in the computed amplitudes of the scattered wave are much smaller than these ratios, as seen from the data in Table 6–6.

From definitions of e_1 and e_2 in eqns. (6–40) and (6–41), the computation of e_1 only involves direct comparisons of individual elements of the T-matrix for the assemblage. The type of symmetry embodied in eqn. (6–40) is inherent, regardless of truncation size, of the formulation, which is primarily due to the symmetry of the wave expansion basis; that is $|\{H(r,\theta)\}_n| = |\{H(r,\theta)\}_{-n}|$, and the satisfaction of eqn. (6–38) by the T-matrix of each element. Therefore, e_1 is primarily a measurement of computer's round-off errors incurred during the computation.

On the other hand, the computation of e_2 involves a matrix product, which essentially represents the energy in the wave field. Physically, the property in eqn. (6–39) is derived from both the energy balance requirement and the reciprocity principle. Therefore, e_2 is primarily a measurement for the overall accuracy of the T-matrix for the assemblage. This is also the reason that e_2 is more sensitive to the truncation errors, and that e_2 is in general larger than e_1, since the computer's round-off errors are also compounded into e_2.

With this understanding, e_1 and e_2 can be effectively and almost exclusively used in the following observations of various error behaviors of the scatterer polymerization process. They can also be used to determine whether a computed T-matrix for an assemblage is accurate enough. Numerical values of e_1 and e_2 can be interpreted as follows: if both are in the same order, they represent the overall level of error incurred in the computations. If they are in the different order, e_2 should in general be larger then e_1. In such cases, e_1 represent the computer's round-off errors, and e_2 represents the truncation errors.

6-5.2 Generational Errors

One of the most striking observations can be made from Tables 6–5 and 6–6 is that the numerical accuracy deteriorates drastically in 2-stage procedures. In both Procedures B and C, errors e_1 and e_2 jumps from $O(10^{-14})$ to $O(10^{-2})$ or even $O(10^{-1})$.

To further investigate the behaviors of error deterioration between generations (stages of scatterer polymerization computations), another 2-stage scatterer polymerization example is studied. In this example, 4 molecules generated by Procedure A in the previous section are assembled to form a (4×4)-fiber assemblage, as shown in Fig. 6–9. In the computation, the truncation size is set *a priori* at $M = 50$. The T-matrix for the (2×2)-fiber molecule is also re-generated using this truncation size. Table 6–7 lists the T-matrix conformity errors e_1 and e_2, along with Σ, at several frequencies.

In Table 6–7, both e_1 and e_2 remains the same order in each stage, except the

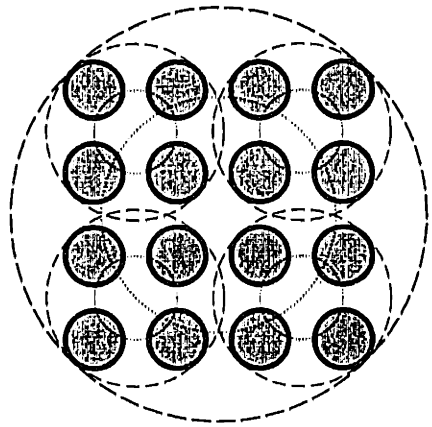

Fig. 6–9 Configuration of (4×4)-fiber molecule comprised of 4 (2×2)-fiber molecules. Dashed circles represent the territories of molecules; dotted circles represent their core regions.

Table 6–7: T-Matrix Property Conformity Errors for 2-Stage Computation of (4×4)-Fiber Molecule

ka	Stage	Σ	e_1	e_2
1	1	4.03127	3.51166×10^{-15}	3.91165×10^{-15}
	2	14.1960	2.58391×10^{-14}	3.56165×10^{-14}
2	1	15.8350	1.36037×10^{-14}	2.86093×10^{-14}
	2	46.4477	1.31330×10^{-13}	3.35293×10^{-13}
3	1	24.8127	4.15652×10^{-14}	1.43479×10^{-13}
	2	71.4637	3.53276×10^{-13}	1.11999×10^{-12}
4	1	37.0132	7.98726×10^{-14}	2.81336×10^{-13}
	2	113.578	5.84423×10^{-13}	2.12677×10^{-12}
5	1	46.0870	1.03914×10^{-13}	4.11462×10^{-13}
	2	158.815	7.87252×10^{-13}	4.58478×10^{-9}

case of $ka = 5$. From the first stage to the second stage, they increase by an order of 10, but the relative errors e_1/Σ and e_1/Σ only increase by a smaller scale, since Σ also increases in the second stage about 3 times. At $ka = 5$, e_2 is significantly larger than e_1, suggesting insufficient truncation terms.

The error levels of e_1 and e_2 in the second stage suggest that the errors simply accumulate across generations in this example. That is, the errors in the previous stage are simply carried on to the next stage of computation without being magnified to a scale that could drastically change the error level in the next stage.

This generational error behavior is very different from that in Table 6–3 and 6–4. The different error behaviors are primarily due to the difference in scatterer configurations, which should not be counted as generational errors. The errors due to scatterer locations are categorized as the *scatterer proximity errors*, which will be examined later.

Table 6–8: T-Matrix Property Conformity Errors for Different First-Stage Truncation Size M_1 (Second-Stage Truncation Size $M_2 = 50$)

	Stage 1		Stage 2	
M_1	e_1	e_2	e_1	e_2
10	2.94867×10^{-14}	0.0537945	2.40010×10^{-13}	0.685969
15	3.89561×10^{-14}	1.05044×10^{-6}	2.75591×10^{-13}	1.06892×10^{-5}
20	4.05413×10^{-14}	4.95397×10^{-13}	2.97937×10^{-13}	5.15507×10^{-12}
25	4.09423×10^{-14}	1.45060×10^{-13}	3.22177×10^{-13}	1.10949×10^{-12}
30	4.15652×10^{-14}	1.43479×10^{-13}	3.21505×10^{-13}	1.10017×10^{-12}
35	4.15652×10^{-14}	1.43479×10^{-13}	3.25946×10^{-13}	1.10750×10^{-12}
40	4.15652×10^{-14}	1.43479×10^{-13}	3.48436×10^{-13}	1.13027×10^{-12}
45	4.15652×10^{-14}	1.43479×10^{-13}	3.52628×10^{-13}	1.13254×10^{-12}
50	4.15652×10^{-14}	1.43479×10^{-13}	3.53276×10^{-13}	1.11999×10^{-12}

6-5.3 Truncation Errors

From the examples so far, it has seen that the larger the number of fibers in the assemblage, as well as the higher the frequency, the larger a truncation size is needed. This trend agrees with that of the multiple-scattering solution as observed in Chapter 5.

Since the scatterer polymerization is intended for producing ever larger assemblages of scatterers, there is naturally a truncation size problem. If in the final stage scatterers span a large area, a large number of truncation terms would be needed. But a large truncation size could cause numerical underflow or overflow in the initial stages of computations in which scatterers span a relatively small area.

From the computational efficiency point of view, it is desirable to have smaller truncation size in the early stages when the radius of the resulting molecule is relatively small, and use larger truncation sizes when the radius becomes larger. During the computations, when the size of a T-matrix for the assemblage is to be enlarged, the newly created T-matrix elements are set to zero.

To observe the error behaviors of using different truncation sizes in different stages, the 16-fiber configuration shown in Fig. 6–9 is recomputed for the case $ka = 3$. In this computation, the truncation size in the second stage is maintained at $M_2 = 50$, which has shown in Table 6–7 to be sufficient for the case. The truncation size in the first stage M_1 is varied from 10 to 50. Table 6–8 lists the T-matrix property conformity errors in both stages of the computation.

From Table 6–8, it is observed that the when truncation size is small in the first stage, such as $M_1 = 10$ and 15, e_2 are much larger than e_1 in both stages. In such cases, from the first stage to the second stage, e_2 grows by an order of 10, which is the usual growth rate of generational error. The difference in the orders of e_1 and e_2 diminishes as the truncation size increases. The first stage errors e_1 and e_2

Table 6–9: T-Matrix Property Conformity Errors for Different Second-Stage Truncation Size M_2 (First-Stage Truncation Size $M_1 = 50$)

M_2	e_1	e_2
20	2.78428×10^{-13}	2.03958
30	3.22026×10^{-13}	2.50841×10^{-6}
35	3.25946×10^{-13}	5.62521×10^{-11}
40	3.48436×10^{-13}	1.13031×10^{-12}
50	3.53276×10^{-13}	1.11999×10^{-12}
60	3.53276×10^{-13}	1.11999×10^{-12}
70	3.53276×10^{-13}	1.11999×10^{-12}

reach the same orders of their respective converged values around $M_1 = 20$, and eventually stabilize around $M_1 = 30$.

The errors in the second stage does not reach a stabilization. This is because the truncation size M_2, although large enough for both e_1 and e_2 to reach the same order, is not large enough to reach the stablization. To verify this, another computation is performed. In this computation, $M_1 = 50$, which gives stabilized errors for the frist stage, is used, but the truncation size in the second stage is varied from 20 to 70. Computational resuts are listed in Table 6–9.

Table 6–9 shows the similar trend as Table 6–8: e_2 is significantly larger than e_1 when the truncation size M_2 is too small; it reaches the same order as e_1 around $M_2 = 35$, and stabilizes around $M_2 = 50$.

In this example, the largest distance among all scatterers D is $3\sqrt{2}a = 4.2426a$ and $6\sqrt{2}a = 8.4853a$ for the first and the second stages, respectively. The truncation sizes at which both e_1 and e_2 reach the same order (20 and 35, respectively) is called *necessary truncation size*, and the truncation size at which both e_1 and e_2 stabilize is called the *stabilization truncation size*. It is found that the necessary truncation sizes in this example, denoted as M_0, roughly fit the following relation

$$M_0 \approx 8 + kD \tag{6–44}$$

Note that exactly the same empirical formula as eqn. (6–44) is concluded from the examples in Chapter 5 as the necessary truncation size for Form II's of multiple-scattering solution. Interestingly, despite the identicalness in formulas, the meanings of D in the two methodologies are different. If the 16-fiber configuration is to be analyzed by directly using the multiple-scattering solution (of Form II), the corresponding D would be $9\sqrt{2}a = 12.7279a$, which would require a larger necessary truncation size.

6-5.4 Scatterer Proximity Errors

Graf's addition theorem requires that any scatterer's territory should not enclose the origin of any other scatterer's local coordinate system. Since all functions

involved in Graf's addition theorem are continuous, before reaching the theoretical limit, the numerical accuracy deteriorates significantly if the locations of scatterers are close to violating the requirement. This type if error is called the *scatterer proximity error*, which explains the large errors incurred during the second stages in the verification examples in the previous section.

Consider another example first, as shown in Fig. 6–10. In this example, a 4-fiber

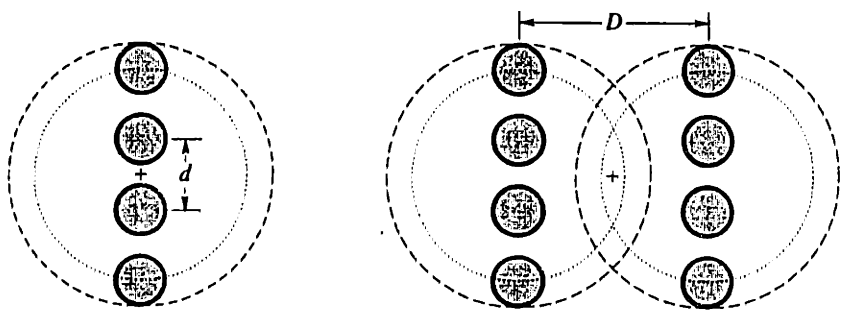

Fig. 6–10 Scatterer polymerization for constructing a 8-fiber assemblage from 2 (2×2)-fiber molecules.

molecule is built first with a fiber spacing $d = 3a$. The core radius of the 4-fiber molecule is $4.5a$ and the radius of its territory is $5.6a$. Then two such molecules are arranged to form an 8-fiber assemblage. The distance between the two molecules is denoted as D, and various values of D are considered.

Since it is expected that errors may be very significant in some cases, in order to provide a reference as the "accurate results", for every value of D considered, the 8-fiber configuration is also analyzed by using a single-stage scatterer polymerization process, which resembles the Procedure A in the previous section, and is also referred to as Procedure A. The 2-stage scatterer polymerization process described above is referred to as Procedure B.

Computations are performed for $ka = 3$. In the computation, when using procedure A, the truncation size is 10 plus the necessary truncation size determine by eqn. (6–44). The extra terms are added to insure a sufficient accuracy of the results. In Procedure B, the truncation size for the first stage (building the 4-fiber molecule) is chosen as $M_1 = 40$, which has been numerically verified to have reached the converged results for e_1 and e_2 for this stage of computation, which are found as $e_1 = 5.21282\times10^{-14}$ and $e_2 = 7.44451\times10^{-14}$. In the second stage of Procedure B, wide ranges of truncation sizes are computed in order to provide a more comprehensive observation.

Table 6–10 lists the computation results. In Table 6–10, M denotes the truncation size for Procedure A and the truncation size in the second stage of Procedure B. Errors e_1 and e_2 of Procedure B are for the second stage of the computation. The amplitude of the scattered wave at the filed point $(r, \theta) = (20a, 0)$ is also calculated to illustrate the overall errors.

Table 6–10: Comparison of Computation Results at Different Truncation Size in the Second Stage of 2-Stage Scatterer Polymerization

D	Procedure	M	Σ	e_1	e_2	$\lvert\phi^5(20a,0)\rvert$
$9a$	A	57	99.1574	1.84205×10^{-13}	1.02080×10^{-12}	1.90252
	B	25	98.9739	2.42294×10^{-13}	0.0206505	1.89275
		30	99.3731	4.73631×10^{-12}	4.56848×10^{-6}	1.90473
		35	99.3253	5.14522×10^{-10}	5.18121×10^{-10}	1.90503
		40	99.2290	1.71060×10^{-9}	1.48076×10^{-9}	1.90329
		45	99.2290	1.71063×10^{-9}	1.48079×10^{-9}	1.90329
		50	99.2290	1.71063×10^{-9}	1.48079×10^{-9}	1.90329
$8a$	A	55	93.1428	1.69865×10^{-13}	1.40359×10^{-12}	1.91590
	B	28	93.1630	1.28425×10^{-7}	2.07864×10^{-5}	1.91693
		30	93.1823	2.66497×10^{-6}	3.53808×10^{-6}	1.91722
		32	93.1911	3.25579×10^{-5}	5.93221×10^{-5}	1.91654
		34	93.2333	0.00130105	0.00179885	1.91432
		36	98.9948	2.01957	0.547526	1.87294
		38	94.1896	1.44630	1.45488	1.91973
$7a$	A	53	88.9730	1.10787×10^{-13}	1.10787×10^{-12}	1.95986
	B	24	88.4921	3.50406×10^{-5}	0.00375492	1.97779
		26	89.8418	0.0109754	0.0134365	1.90812
		28	88.7245	0.398662	0.450806	1.94864
		30	96.6037	9.83633	12.1374	1.99583
$6a$	A	51	85.0747	1.53928×10^{-13}	8.53552×10^{-13}	2.02700
	B	20	82.4380	0.00322202	0.143604	1.97641
		22	82.1802	0.284854	0.284685	1.97700
		24	87.6741	7.27119	7.52665	1.94625
$5a$	A	49	80.9953	1.44632×10^{-13}	6.36177×10^{-12}	2.13086
	B	17	68.5117	0.00176916	0.68684	1.88078
		18	74.2682	0.139311	0.554905	1.96621
		19	74.4003	3.76302	3.89791	1.87010
$4a$	A	46	75.8386	1.47448×10^{-13}	6.98084×10^{-12}	2.2239
	B	15	60.7276	0.0389878	1.68797	1.79168
		16	62.9206	2.20478	2.04475	1.75541

From Table 6–10, it is observed that the case of $D = 9a$ is the only case in which the errors e_1 and e_2 in the second stage of Procedure B reach a stabilization. Even in this case, the errors of $O(10^{-9})$ are significantly larger than those of the first stage of $O(10^{-14})$. This indicates that, since e_1 is the measurement for the overall computaional errors, a new type of error has occured during this stage of computation.

When the distance between the two 4-fiber molecules is reduced, increasing the truncation size in the second stage does not lead to a stabilization. Instead, there is only a small window for the values of M_1 within which results with acceptable

error levels can be achieved. When M_1 is too small, e_2 is much larger than e_1, suggesting insufficient truncation size. When M_1 is too large, both e_1 and e_2 become unacceptably large. Furthermore, the window range decreases as D decreases, and the window completely disappears when $D \leq 5a$.

The theoretical limit set forth by Graf's addition theorem is $D > 5.6a$ for the particular configuration in Fig. 6–10, and it is expected that the numerical accuracy deteriorates when the distance between scatterers approaches this limit. This suggests that the new type of error is caused by the fact that scatterers are too closely situated. This type of error is called the *scatterer proximity error.* It appears that, for the particular configuration, somewhere between $D = 9a$ and $8a$ is the closest the two molecules can be practically arranged, which corresponds to D/a_s between 1.6 and 1.4.

Graf's addition theorem used in the multiple-scattering solution is the same as eqn. (6–12) except the difference in parameter substitutions. The requirement is imposed for the series expression to converge. When the distance is very close to violating the requirement, the convergence rate decreases, and a larger truncation size would be required. On the other hand, a large truncation size means that the difference between the elements of $\{A_i\}$ as computed according to eqn. (6–32) in the scatterer polymerization process could span a large range of magnitudes, and in solving the linear equation system resulted in the multiple-scattering formulation, the numerical accuracy is limited by the number of number significant figures the computer can furnish. The two competing mechanisms set the practical limit as observed above. This also explains why, when proximity errors present, e_1 and e_2 may not reach a stabilization, and even grow as the truncation size increases.

With this understanding of the nature and the behavior of the proximity errors, in the next, the verification example considered in the previous section is re-examined, to observe the effects of the proximity errors in successive stages of a scatterer polymerization process.

In these computations, a 3-stage polymerization is performed. The first two stages are the same as in Procedure B in Fig. 6–8*b* in the previous section, and in the third stage, 4 (2×2)-fiber molecules are assembles as shown Fig. 6–9. Note that in the second stage the two molecules are very closely situated, with the ratio of the inter-molecule distance D to the radius of the molecule a_s being $3/2.6 \approx 1.15$.

In the first two stages, computations are performed for different choices of the truncation sizes, denoted as M_1 and M_2, respectively. Trial first-stage-only computations performed *a priori* show that T-matrix property conformity errors e_1 and e_2 reach the same order around $M_1 = 18$ and stabilize around $M_1 = 30$. Thus, truncation sizes in the first stage are chosen to correspond to an insufficient truncation size (M_1=10), the necessary truncation size (M_1=20), the stabilization truncation size (M_1=30) and an excessively large truncation size (M_1=50). In the second stage, a wide range of truncation sizes are computed in order to locate the window of M_2 in

Table 6–11: T-Matrix Property Conformity Errors During Second Stage in 3-Stage Polymerization for 4×4 Fiber Square Arrangement at $ka = 3$

M_1	M_2	Σ	e_1	e_2	$\lvert\phi^s\rvert(20a, 0)$
12	10	26.3465	1.44729×10^{-12}	0.154814	1.22392
	14	26.2049	6.44736×10^{-11}	4.46694×10^{-5}	1.21670
	18	26.2343	6.55558×10^{-11}	3.79903×10^{-6}	1.21681
	22	26.2343	6.55966×10^{-11}	3.75826×10^{-6}	1.21681
	26	26.2343	6.55967×10^{-11}	3.75827×10^{-6}	1.21681
20	10	26.3465	1.57758×10^{-12}	0.154814	1.22392
	14	25.3255	1.43612×10^{-9}	2.36793×10^{-5}	1.23176
	16	25.0785	9.79468×10^{-9}	2.53018×10^{-7}	1.23176
	18	25.0490	2.13811×10^{-5}	2.07082×10^{-5}	1.24317
	20	24.8907	0.00111257	0.00124126	1.24584
	30	24.8903	0.000340499	0.000397853	1.24584
	40	24.8903	0.000340499	0.000397853	1.24584
30	10	26.3465	1.75667×10^{-12}	0.154814	1.22392
	14	25.3255	2.35347×10^{-9}	2.36801×10^{-5}	1.23176
	18	25.0490	9.35854×10^{-6}	9.48552×10^{-6}	1.24317
	22	24.8846	0.0188650	0.0220535	1.24510
	26	24.8925	0.0778614	0.0724316	1.24692
	30	24.9688	0.150925	0.143635	1.24645
	40	24.9688	0.150925	0.143635	1.24645
50	10	26.3465	1.75667×10^{-12}	0.154814	1.22392
	14	25.3255	1.84734×10^{-9}	2.36792×10^{-5}	1.23176
	18	25.0490	2.18565×10^{-5}	2.20134×10^{-5}	1.24317
	22	24.9174	0.0930882	0.0725059	1.24552
	26	25.0166	0.178316	0.184298	1.24704
	30	24.9811	0.169402	0.164201	1.24642
	40	32.9632	8.18193	8.22188	1.17687

which both e_1 and e_2 are in the acceptable level.

Table 6–11 lists the T-matrix conformity errors for the second stage of the computation. From Table 6–11, it is observed that if the truncation size in either stage is too small, $e_2 \gg e_1$ no mater how large the truncation size is used in the other stage, even when the errors stabilize.

When M_1 is an appropriate size (ranges from the necessary truncation size to stabilization size truncation), errors in the second stage stabilize at sufficiently large M_2, and the stabilized values indicate the presence of the scatterer proximity errors. When excessively large M_1 (50) is used, the windowing appears. Errors increase when M_2 is too large. This indicates that the errors in the first stage of computation are magnified for such an excessively larger truncation size in the presence of the scatterer proximity errors.

For sufficiently large M_1 ($M_1 \geq 20$), the smallest error level is achieved when M_2

Table 6–12: T-Matrix Property Conformity Errors During Third Stage in 3-Stage Polymerization for 4×4 Fiber Square Arrangement at $ka = 3$

M_3	Σ	e_1	e_2	$\lvert\phi^s\rvert(20a, 0)$
20	62.0004	0.00355963	2.06999	0.651491
23	69.8021	0.00428327	0.146171	0.521875
25	71.3057	0.00454446	0.00454446	0.555812
27	71.7275	0.00465042	0.00504224	0.558189
30	71.8246	0.00468508	0.00477444	0.558900
35	71.8314	0.00468913	0.00477852	0.558747
40	71.8315	0.00468916	0.00477855	0.558747
45	71.8315	0.00468916	0.00477855	0.558747
50	71.8315	0.00468916	0.00477855	0.558747

is about 18, which roughly fits the empirical expression for the necessary truncation size given in eqn. (6–44) by noting that $D = 3a$ in this stage.

In the third stage of the computation, the truncation size for the first 2 stages are chosen as $M_1 = M_2 = 20$, which is slightly larger than the necessary truncation size. Again, a wide range of truncation sizes are computed in the third stage. Table 6–12 shows the similar computational results.

From Table 6–12, the same trend is observed: $e_2 \gg e_1$ when M_3 is small, and they reach the same order around $M = 25$, and stabilize around $M = 40$. An important observation can be made from Table 6–12 is that the stabilized errors in this stage are in the same order as in the second stage (5×10^{-3} vs. 1×10^{-3}). Note that, in this stage, the radius of the molecules is $(1.5\sqrt{2} + 1.1)a = 2.6a$ while the smallest distance between molecules is $6a$. That is, the D/a_s ratio is significantly larger than the practical limit of between 1.6 and 1.4. This indicates that, despite the noticeable scatterer proximity errors in the second stage, the errors are not substantially magnified if there are no sever errors occurred in later stages.

6-6 Conclusions

In this chapter, the methodology of scatterer polymerization is proposed, formulated and implemented. Computer program has been verified to give correct results. The error behaviors are systematically examined and can be summarized as follow:

- Generational errors, truncation errors and scatterer proximity errors are the 3 main types of errors involved in a scatterer polymerization computation. The scatterer proximity error is the error due to the fact that scatterers are situate too close to each other and are close to violating the equirement set forth by Graf's addition theorem.

- The T-matrix conformity errors e_1 and e_2 as defined in eqns. (6–40) and (6–41) are excellent measurements of the errors in the resulting T-matrix for the assemblage. When both in the same order and in general $e_2 > e_1$, they represent the error level of the overall computation. When $e_2 \gg e_1$, they indicate that insufficient truncation size has been used. When both are large and in the same order, they indicate the presence of scatterer proximity errors.
- When the scatterers are located sufficiently far away from each other, the necessary truncation size is given in eqn. (6–44), and a larger truncation size will lead to stabilized results.
- In a multiple-stage scatterer polymerization process, if the truncation size is sufficiently large and no noticeable scatterer proximity errors involved, the errors inherited from the previous stage is only magnified by roughly 10. A substantially large magnification ratio suggests the presence of the scatterer proximity errors.
- In the event that scatterer proximity errors are noticeably present, the smallest error is achieved by selecting a truncation size that is near the necessary truncation size as given in eqn. (6–44). Otherwise, either the errors in the T-matrix from the previous stage of computation due to excessively large truncation size will be enlarged or the accuracy in the present stage deteriorates significantly due to insufficient truncation size.

The error behaviors suggest that the practical scatterer proximity limit is the main limitation for the largest number of scatterers can be computed. This practical limit is prompted from the theoretical limit set forth by Graf's addition theorem in the multiple-scattering solution, but it is mainly determined by the numerical accuracy of the computer used in the computation. For the computer used in this study, which has 15 significant figures in its native double-precision floating number representation, and for an assemblage consisting of identical molecules, the practical limit is that ratio of the smallest inter-molecule distance to the molecular radius is about 1.5.

Despite this limitation, the methodology of scatterer polymerization drastically reduces the problem size such that the computer's available amount of memory could no longer be a limiting factor if the scatterer configuration in each stage of a scatterer polymerization process is designed with great care. Furthermore, it is possible to trade, via software approach (see, *e.g.*, [7]), the computer memory for an increase of the number of significant figures such as implementing a data type that represents floating numbers in the quadruple-precision thus to overcome the practical limit of the computer's native double-precision. However, this endeavor is left as a future project.

References

[1] G.N. Watson, *Treaties of Theory of Bessel Functions,* 2nd edn., Cambridge University Press, London, 1945.

[2] M. Abramowiz, I. Stegun, *Handbook of Mathematical Functions,* Dover, New York, 1965.

[3] W. H. Press, B. P. Flannery, S. A. Teukolsky, W. T. Vetterling, *Numerical Recipes: The Art of Scientific Computing, C/FORTRAN/Pascal Versions,* Cambridge University Press, Cambridge, UK, 1986.

[4] Y.-H. Pao, C.-C. Mow, *Diffraction of Elastic Waves and Dynamic Stress Concentrations,* Crane Russak, Co., New York, 1971.

[5] H. Yim, J. H. Williams, Jr, Formulation and its energy balance verification for ultrasonic non-destructive characterization of a single fiber composite interphase, *Ultrasonics,* **33**, 377–387, 1995.

[6] H. Yim, J. H. Williams, Jr, Database generation and parametric study for ultrasonic non-destructive characterization of a single fiber composite interphase, *Ultrasonics,* **33**, 389–401, 1995.

[7] S. L. B. Moshier, *Methods and Programs for Mathematical Functions,* Ellis-Horwood, New York, 1989.

7

Full-Scale Simulations

Abstract: *In this chapter, full-scale simulations of the multiple scattering of elastic waves in fiber reinforced composite materials are performed, using the analytical and computational tools developed in the previous chapters. The computational procedure is outlined. Simulation results are analytically exact and numerically verified. Simulated fields are examined, and relationships between the simulation results and some experimentally measurable parameters are established.*

Contents:

Nomenclature

General Conventions

- Matrices are denoted by bold-faced symbols; symbols for column matrices are enclosed by flower brackets ({}); symbols for rectangular matrices are enclosed by square brackets ([]).
- When referring to a matrix entry, the entry's indicial number is to appear as subscript(s) *outside* the brackets. This distinguishes the indicial subscript(s) from the subscript(s), if any, associated with the entire matrix.

Symbols

A	Amplitude (real) of the out-of-plane displacement u.
a	Radius of the fiber in the fiber-interphase-matrix micromechanics model for fiber reinforced composites.
a_s	Radius of a scatterer: the radius of the smallest circle that circumscribes the entire scatterer or all scatterers that make up the molecule.
b	Outer radius of the interphase in a fiber-interphase-matrix micromechanics model for fiber reinforced composites.
D	Edge length of a square molecule.
d	fiber spacing: the distance between two adjacent fibers in the same row or column in a square fiber arrangement.
E	Energy flux function.
e	Normalized energy flux function.
e_1, e_2	T-matrix conformity errors.
H	The range over which an averaged filed quantity is computed.
I	Cumulative normalized energy flux function.
$\hat{\imath}$	Unit of imaginary numbers, $\hat{\imath} = \sqrt{-1}$.
k	Wave number of SH waves.
M	Truncation term (truncation size) for infinite series and matrices.
N	Total number of *elements* in a multiple-scatterer configuration.
$\mathcal{N}$	Total number of *scatterers* in a multiple-scatterer configuration. A scatterer can be an element or a molecule.
(r, θ)	Global polar coordinates
$[\boldsymbol{T}^{\text{total}}]$	T-matrix of an assemblage of scatterers.
u	Out-of-plane displacement.
(x, y)	Global Cartesian coordinates
ϕ	Complex amplitude of Out-of-plane displacement u for SH waves.
ω	Circular frequency of incident wave.
Σ	The first norm of matrix $[\boldsymbol{T}^{\text{total}}]$, $\Sigma = \|[\boldsymbol{T}^{\text{total}}]\|$.

7-1 Introduction

The emphases in the previous chapters have been on developing the necessary analytical and computational tools that can be used to perform full-scale simulations of elastic wave scattering in fiber reinforced composites. With those tools, it is possible to simulate the multiple-scattering phenomenon in fiber reinforced composites in full scale using a typical desk-top computer.

In this chapter, it is demonstrated that a combined use of these analytical and computational tools is capable of performing full-scale deterministic simulations using a typical desk-top computer. Considerations in this chapter are limited to the case of anti-plane shear (SH) waves.

A model of a plate structure is selected for analysis. Considerations are limited to square arrangements of fibers. Fibers are centrally located within square grids that are confined to a rectangular region, as sketched in Fig. 7–1. The entire assemblage

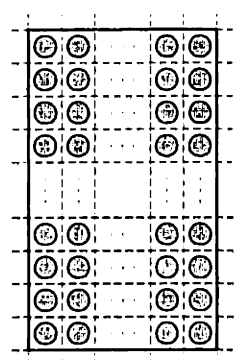

Fig. 7–1 Model for fiber reinforced composite plate; solid line represents boundary of model plate.

of fibers is embedded in an elastic matrix of infinite extent. In Fig. 7–1, the solid line enclosing the fibers is the *boundary* of the plate; fibers located along a grid line parallel to the longer side of the rectangle comprise a *layer* of fibers; and the shorter side of the rectangle is called the *thickness direction*.

The qualifying phrase *full-scale* implies that the region occupied by the deterministic model is of macroscopic dimension. As in previous chapters, assume the radius of a typical fiber is 10μm (after [1]), and the *fiber spacing* between two adjacent fibers, which is the same as the grid size, is three times the fiber radius. With the fiber arrangement sketched in Fig. 7–1, a model consisting of 20 layers of fibers is equivalent to a composite plate of thickness 0.6 mm, which can be considered macroscopic. Therefore, in the thickness direction, the minimum number of fibers considered is 20.

7-2 Review of Computational Tools

Two computational tools, namely, the multiple-scattering solution for elastic waves in two dimensions and the methodology of scatterer polymerization, have been developed, implemented and verified in Chapters 4 through 6. Both tools are analytically exact and can be used to analyze arbitrary numbers of scatterers. In this section, their relative advantages and disadvantages are reviewed and compared in the context of a full-scale simulation.

Various forms of multiple-scattering solutions for elastic waves in two dimensions have been presented in Chapter 4 for both the cases involving anti-plane shear (SH) waves and in-plane (P/SV) waves. Implementations and computational characteristics of all these forms for the case of SH waves have been discussed in detail in Chapter 5.

The multiple-scattering solution is capable of computing all wave fields in the entire problem domain, including waves interior to fibers. This solution is presented in two forms. Form I directly computes the wave fields due to a given incident wave. Form II produces a multiple-scatterer system's characteristic matrix, from which responses to any incident wave can be subsequently computed in a straightforward manner.

In Form I, it is assumed that the wave expansion coefficients of the incident wave are known exactly in each scatterer's local coordinate system. This assumption reduces a level of coordinate transformation, as compared to Form II, making it possible to use a smaller truncation size to achieve the same accuracy for a given configuration.

The limitation of the multiple-scattering solution is that, regardless of the solution form used, the size of the computer memory required to solve the problem grows at a rate of at least $\sim N^2$, where N is the number of fibers. This limitation prevents this solution from being used solely for a full-scale simulation, as the computer used in this study can analyze an assemblage up to about 30 fibers, and increasing the computer's memory does not appear to be a feasible option.

The scatterer polymerization methodology has been presented in Chapter 6. This methodology allows the problem to be folded by using a multiple-stage procedure, thus dramatically reducing the required computer memory. This methodology produces a T-matrix representing the entire assemblage of actual scatterers, which can thus be treated as a single abstract scatterer, called a *molecule*, in subsequent computations. The T-matrix conformity errors defined in Chapter 6 quantitatively describes the error level of the resulting T-matrix for the assemblage.

In any multiple-scattering analysis, a certain minimum distance between scatterers must be maintained. When using the scatterer polymerization methodology,

this requirement becomes the primary limitation, and it has been shown in Chapter 6 that the practical limit for the minimum scatterer separation is significantly larger than the theoretical limit.

Consider the arrangement of a square molecule in which the number of scatterers along each side of a square region is the same and denoted as n, as sketched in Fig. 7–2. This is a useful configuration for multiple-stage scatterer polymerization

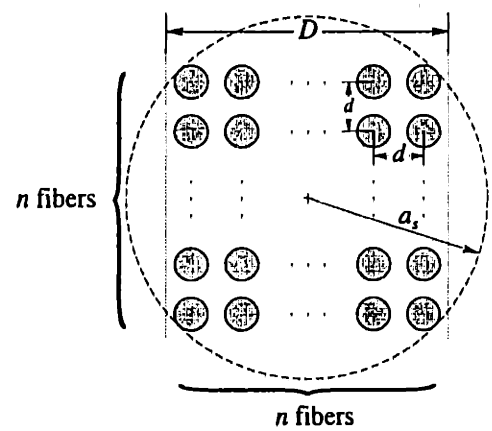

Fig. 7–2 Representative geometry of square molecule.

analyses for fibers in square arrangements. In Fig. 7–2, a_s is the radius of the resulting abstract scatterer, and D is the edge-length of the molecule. For the fibers arranged as in Fig. 7–2, the edge-length to radius ratios is

$$\frac{D}{a_s} = \frac{2nd}{2a + \sqrt{2}(n-1)d} \tag{7–1}$$

where a is the radius of each individual fiber and d is the fiber spacing between two adjacent fibers along a row or a column.

In each subsequent stage of computation when several identical molecules as shown in Fig. 7–2 are assembled, D is the minimum scatterer separation, whose theoretical limit is, according to Chapter 6, $D/a_s > 1$. As observed in Chapter 6, the practical limit for the D/a_s ratio is between 1.6 and 1.4. Figure 7–3 shows the D/a_s versus n curve for the case $d = 3a$. Also, in the limit as $n \to \infty$ is $D/a_s \to \sqrt{2}$. That is, the molecule shown in Fig. 7–2 always satisfies the theoretical limit of minimum scatterer separation no matter how large is n. Unfortunately, the practical limit of D/a_s is reached when n is fairly small, and usually in only a few stages of scatterer polymerization.

7-3 Computational Strategy for Full-Scale Simulation

Assessing the available tools, a tentative plan is formed as follow: the scatterer

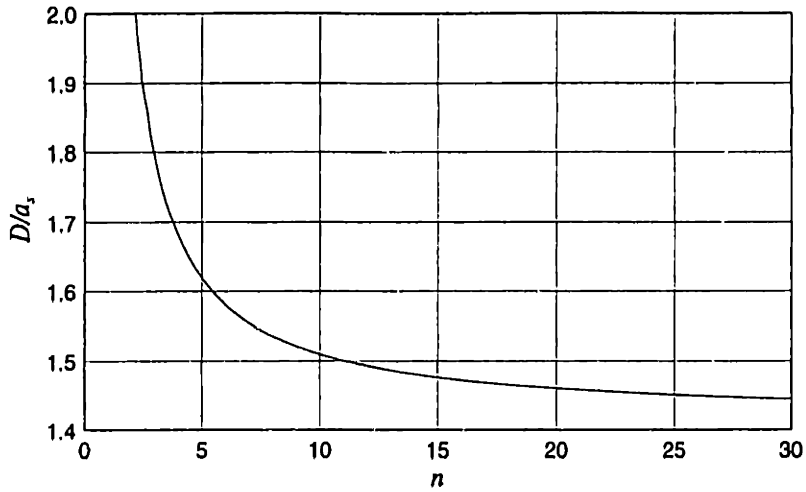

Fig. 7–3 Decrease of D/a_s ratio as number of fibers n increases, as described by eqn. (7–1) when $d = 3a$.

polymerization methodology is first used to build an abstract scatterer that contains as large a number of fibers as the practical limit of minimum scatterer separation permits; then the multiple-scattering solution is used to analyze an assemblage of such abstract scatterers, which are arranged to simulate a model plate.

As in the previous chapters, a fiber-interphase-matrix model is considered for a metal-matrix ceramic fiber composite system. The single scattering problem for this 3-phase model has been studied in Chapter 3 for the SH wave case, by Yim and Williams for the P/SV wave case in [2–1], and numerous multiple-scattering examples have been presented in Chapter 5. For completeness, the material properties, after [1], are listed in Table 7–1. Unless otherwise specified, the outer radius of the interphase is $b = 1.1a$.

Table 7–1: Constituent Material Properties for a Metal-Matrix Ceramic-Fiber Composite System[1].

Property	Matrix (AA520 Aluminium)	Fiber (Alumina, Al_2O_3)	Interphase (Zirconia, ZrO_2)
Density (kg/m^3)	2600	3700	6300
Young's Modulus (GPa)	66	360	97
Poisson's Ratio	0.31	0.25	0.33
Lamé Constant λ (GPa)	41	144	71
Lamé Constant μ (GPa)	25	144	37
P Wave Speed (m/s)	5920	10800	4800
S Wave Speed (m/s)	3100	6240	2420

Table 7–2: Configurations of Various Scatterer Polymerization Procedures.

Procedure	Fiber Configuration	n	$N = n^2$
①	(2×2)⇒(2×2)	4	16
②	(3×3)⇒(2×2)	6	36
③	(2×2)⇒(3×3)	6	36
④	(3×3)⇒(3×3)	9	81
⑤	(2×2)⇒(2×2)⇒(2×2)	8	64
⑥	(3×3)⇒(2×2)⇒(2×2)	12	144
⑦	(2×2)⇒(3×3)⇒(2×2)	12	144
⑧	(2×2)⇒(2×2)⇒(3×3)	12	144
⑨	(3×3)⇒(3×3)⇒(2×2)	18	324
⑩	(2×2)⇒(2×2)⇒(2×2)⇒(2×2)	16	256

7-3.1 Fiber Configurations

In Table 7–2, the configurations to be analyzed are listed. For example, (3×3)⇒(2×2) represents a two-stage polymerization procedure: in the first stage, 9 fibers are assembled as a (3×3) square arrangement; in the second stage, 4 identical scatterers built in the first stage are assembled in a (2×2) square arrangement, which contains 36 fibers with 6 fibers along each edge.

In the computations, the truncation size M is determined *a priori* by the following empirical expression found in Chapter 6:

$$M = 8 + kd_{\max} \tag{7–2}$$

where k is the wave number, and $d_{\max}$ is the largest distance among scatterers. Note that eqn. (7–2) does not necessarily give the optimal truncation size that yields the smallest computational errors, but as it is desirable to perform the simulation in an automated manner with minimal human intervention, this empirical formula is used for its simplicity.

The computation for the T-matrix for the assemblage in each stage of a scatterer polymerization follows the procedure detailed in Chapter 6. Then, the *T-matrix conformity errors* of the resulting T-matrix are calculated.

The T-matrix conformity errors are defined, according to Chapter 6, as

$$e_1 = \sum_{m=0}^{M} \sum_{n=-M}^{M} \left| [T^{\text{total}}]_{mn} - (-1)^{m-n} [T^{\text{total}}]_{(-n)(-m)} \right| \tag{7–3}$$

$$e_2 = \left\| [\tau] \right\|_1 = \sum_{m=-M}^{M} \sum_{n=-M}^{M} |[\tau]_{mn}| \tag{7–4}$$

where $[T^{\text{total}}]$ is the resulting T-matrix for the assemblage, $\|\cdot\|_1$ denotes the *1-norm*

Table 7–3: T-Matrix Conformity Errors at Final Stage of Various Scatterer Polymerization Procedures Listed in Table 2.

	$ka = 1$			$ka = 2$		
	Σ	e_1	e_2	Σ	e_1	e_2
①	14.1962	4.30632×10^{-15}	9.21536×10^{-14}	46.4482	2.00149×10^{-14}	3.98988×10^{-13}
②	28.6239	1.56354×10^{-14}	3.69056×10^{-11}	83.1530	1.13101×10^{-13}	1.56932×10^{-9}
③	28.6381	1.44691×10^{-14}	3.04362×10^{-14}	83.1069	6.78859×10^{-14}	2.51099×10^{-13}
④	55.3384	4.97691×10^{-14}	9.93173×10^{-14}	163.755	2.60739×10^{-13}	9.26272×10^{-13}
⑤	45.4106	3.78836×10^{-13}	1.22926×10^{-9}	137.259	1.07988×10^{-11}	6.89448×10^{-8}
⑥	85.0370	1.87264×10^{-10}	2.90541×10^{-8}	239.611	5.54093×10^{-6}	6.9955×10^{-5}
⑦	83.6609	2.18835×10^{-9}	1.41833×10^{-8}	241.588	0.558468	0.824674
⑧	83.1948	2.60668×10^{-13}	1.82767×10^{-12}	242.377	2.07932×10^{-10}	4.60262×10^{-9}
⑨	145.957	0.00508786	0.00690847	1771.47	1238.47	23601.0
⑩	125.895	7.28824×10^{-8}	1.0801×10^{-6}	373.607	0.0903401	0.0952106

of a matrix (see, *e.g.*, SCHEID, 1968), and

$$[\tau] = \tfrac{1}{2}\left([\boldsymbol{T}^{\text{total}}]^* + [\boldsymbol{T}^{\text{total}}]\right) + [\boldsymbol{T}^{\text{total}}]^*[\boldsymbol{T}^{\text{total}}] \tag{7–5}$$

If $[\boldsymbol{T}^{\text{total}}]$ is exact, e_1 vanishes, and e_2 represents the truncation error. Nonvanishing values of e_1 and e_2 represent errors due to various sources in the process, as detailed in Chapter 6. Relative errors can be observed by comparing e_1 and e_2 with the 1-norm of the T-matrix, denoted as $\Sigma = \|[\boldsymbol{T}^{\text{total}}]\|_1$.

Table 7–3 lists the T-matrix conformity errors of T-matrices for the resulting molecule using the scatterer polymerization procedures listed in Table 7–2 at frequencies $ka = 1$ and $ka = 2$. Note that the nondimensionalized frequency $ka = 2$ corresponds to a frequency of about 100 MHz for this particular material system.

Table 7–3 shows that, among the procedures listed in Table 7–2, either Procedures ⑥ or ⑧ can be used since they contain the largest number of fibers in the final configuration and yet maintain an acceptable error level. Both are 3-stage procedures and produce the same final abstract scatterer. From a computational efficiency perspective, Procedure ⑥ is preferred since it has a larger number of scatterers in the early stage of computation which has smaller truncation sizes. The preparatory computations that produce Table 7–3 show that the overall computer time needed for a 3-stage computation using Procedure ⑧ is a magnitude longer than that of Procedure ⑥. Therefore, Procedure ⑥ is chosen.

7-3.2 Configurations of Model Plates

Several model plates are constructed from a number of identical molecules generated by Procedure ⑥. Molecules are arranged in 2×4, 2×6, 2×8 and 2×10 arrays to represent model plates of the same thickness but different lengths. Model plates are referred to by their molecular configuration. For instance, the model plate consisting of 2×4 molecules is referred to as the 2×4 *model plate*.

These model plates all consist of 24 layers of fibers, corresponding to a thickness of 0.72 mm. They contain different numbers of fibers ranging from 1152 to 2880. Fiber configurations in each stage of the scatterer polymerization, as well as the final configuration of the 2×4 model plate, are shown in Fig. 7–4. In Fig. 7–4, dashed lines depict the arrangements of fibers and molecules.

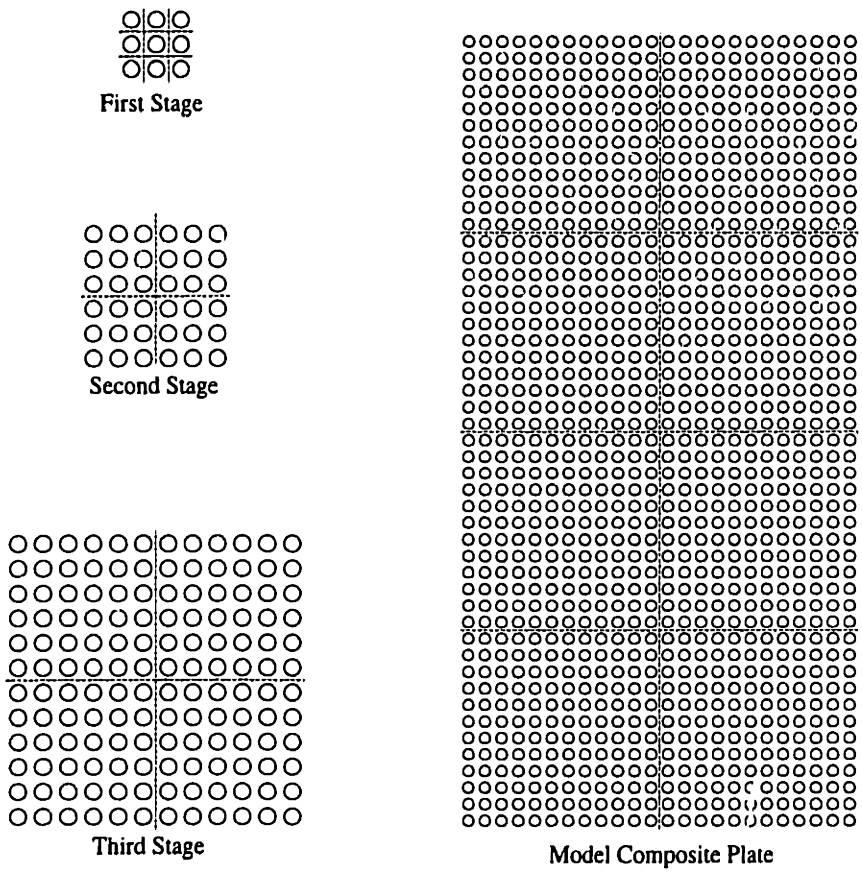

Fig. 7–4 Configurations of various stages of constructing a model fiber reinforced composite plate. (Dashed lines indicate arrangements of fibers and molecules.)

7-3.3 Verifications

For the analysis of the model plates using the multiple-scattering solution, the Cartesian coordinate system OXY is defined as shown in Fig. 7–5, where the 2×4 model plate is shown. A generic field point can be referenced by its Cartesian coordinates (x, y) or its polar coordinates (r, θ), where $x = r\cos\theta$ and $y = r\sin\theta$. The incident wave is a plane wave of unit amplitude propagating along the $+X$ direction, whose expression is (see, *e.g.*, [3])

$$\phi^{\text{inc}} = e^{ikx} = e^{ikr\cos\theta} \tag{7-6}$$

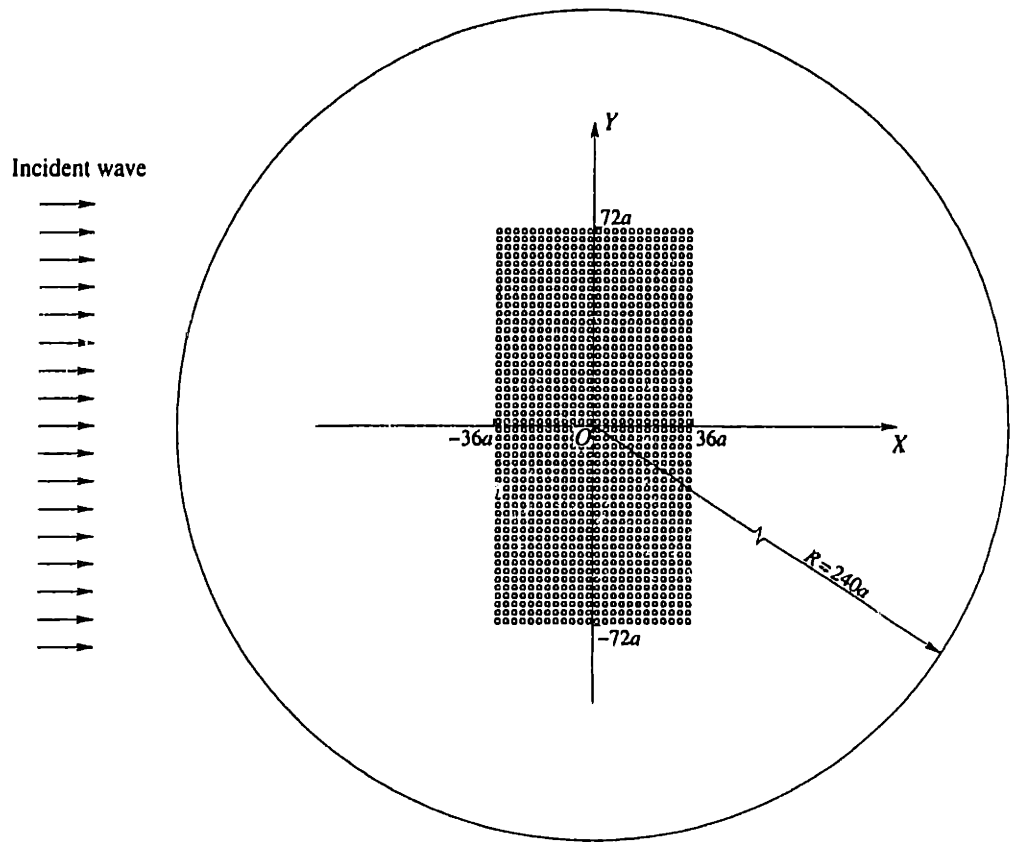

Fig. 7–5 Coordinate system for model composite plate, and boundary of energy balance computations.

By writing the incident wave in nondimensional form in eqn. (7–6), it is implied that all displacement fields are normalized by the amplitude of the incident wave. In the computations, the truncation size of the T-matrix obtained via scatterer polymerization is taken as the same truncation size as for the multiple-scattering analysis.

Figure 7–5 also shows the closed path used for energy balance verification, which is a complete circle of radius $R = 240a$, centered at the origin. The energy balance verification is based on the fundamental physical principle of energy conservation. For such a model subjected to a sourceless incident wave, a form of this principle, known as the *energy balance requirement*, dictates that, for any closed path that encloses neither a source nor a sink, the energy transmitted across the path must be zero.

The expression for the energy balance requirement for two-dimensional steady-state SH wave scattering has been derived in Chapter 3. In particular, for a circular path of radius R centered at the origin of the global polar coordinate system,

$$\int_{\mathcal{A}} \langle \dot{E} \rangle d\mathcal{A} = \pi R \int_0^{2\pi} Im \left\{ \Sigma_{rz} \overline{U}_z \right\}_{r=R} d\theta = 0 \qquad (7\text{–}7)$$

where $\Sigma_{rz}(r,\theta)$ and $U_z(r,\theta)$ are the complex amplitudes of the stress component and the displacement component, respectively, where the overbar denotes the complex conjugate, and $\langle \dot{E}(r,\theta) \rangle = Im\left\{\Sigma_{rz}\overline{U}_z\right\}$ is the *time-averaged energy flux density function*. Furthermore,

$$U_z = \phi \qquad \Sigma_{rz} = \mu\gamma_{rz} \qquad \text{and} \qquad \gamma_{rz} = \frac{\partial\phi}{\partial r} \tag{7-8}$$

where ϕ is the complex amplitude of the z-component displacement given by the multiple-scattering solution, μ is a Lamé constant of the material, and γ_{rz} is the complex amplitude of the engineering shear strain component.

The energy balance verification follows the procedure in Chapter 5. By introducing the *normalized time-averaged energy flux density function*

$$\langle \dot{e}(r,\theta) \rangle = \frac{\langle \dot{E}(r,\theta) \rangle}{\mu|\phi^{\text{inc}}|} = \frac{1}{|\phi^{\text{inc}}|} Im\{\gamma_{rz}\overline{\phi}\} \tag{7-9}$$

and the *cumulative normalized energy flux function*

$$I(R,\theta) = \int_0^\theta \langle \dot{e}(R,\theta') \rangle d\theta' \tag{7-10}$$

the energy balance requirement becomes, by combining eqns. (7–7) through (7–10),

$$I(R,2\pi) = 0 \tag{7-11}$$

where any nonvanishing value of $I(R,2\pi)$ represents the cumulative error of the entire computation. In preforming the intergration of eqn. (7–10) numerically, the entire circle is divided into 2880 subdivisions and $\langle \dot{e}(R,\theta) \rangle$ within each subdivivion is taken as a constant. Table 7–4 lists the computed values of $|I(R,2\pi)|$, as compared to the maximum values of $I(R,\theta)$ during the integration process, $|I(R,\theta)|_{\max}$.

Table 7–4 shows that the overall computational error generally becomes more severe as the frequency increases. For the case of $ka = 1.7$, energy balance verification fails completely as $|I(R,2\pi)|$ is identical $|I(R,\theta)|_{\max}$ for most model plates. For all other frequencies, errors are acceptably small, remaining within a level of 0.1% at $ka = 1.6$.

Figures 7–6 through 7–8 show the angular distributions of the normalized time-averaged energy flux density function $\langle \dot{e}(R,\theta) \rangle$ and the numerical integration progress using eqn. (7–10) for the 2×4 model plate at the frequencies $ka = 0.5$, 1.0 and 1.5. Since the configuration is symmetric about the X-axis, distributions of $\langle \dot{e}(R,\theta) \rangle$ are shown only for the upper-half plane ($0 \leq \theta \leq \pi$).

7-3.4 Summary of Simulation Procedure

The verifications above are in fact examples of full-scale simulations. The complete procedure for a simulation computation can be summarized as follows:

Table 7–4: Results of Energy Balance Computations for Model Plates.

ka	2 × 4 Model Plate		2 × 6 Model Plate	
	$\|I(R,\theta)\|_{max}$	$\|I(R,2\pi)\|$	$\|I(R,\theta)\|_{max}$	$\|I(R,2\pi)\|$
0.1	0.0998013	5.83029×10^{-16}	0.0998225	4.95106×10^{-17}
0.2	0.190027	1.41994×10^{-13}	0.191978	5.53549×10^{-15}
0.3	0.297361	8.36357×10^{-15}	0.296273	4.57884×10^{-14}
0.4	0.388274	1.00813×10^{-14}	0.381587	1.42185×10^{-13}
0.5	0.484011	1.13912×10^{-12}	0.479637	1.59492×10^{-11}
0.6	0.430621	1.87752×10^{-11}	0.342374	6.19969×10^{-11}
0.7	0.676042	6.54799×10^{-11}	0.662474	6.19969×10^{-11}
0.8	0.762003	1.32767×10^{-9}	0.741450	1.46818×10^{-10}
0.9	0.831010	2.03354×10^{-10}	0.789542	3.00779×10^{-10}
1.0	0.722319	3.67241×10^{-7}	0.587337	1.65053×10^{-7}
1.1	0.771428	3.00399×10^{-7}	0.611481	1.41855×10^{-7}
1.2	0.845215	3.01117×10^{-6}	0.669234	1.33219×10^{-6}
1.3	0.911875	1.88263×10^{-5}	0.720437	4.19407×10^{-5}
1.4	0.984537	5.51489×10^{-5}	0.774842	0.000379386
1.5	1.05939	0.00151839	0.835629	0.000770001
1.6	1.14479	0.00339199	0.906330	0.00678579
1.7	2.66588	2.66588	1.97532	1.62603

ka	2 × 8 Model Plate		2 × 10 Model Plate	
	$\|I(R,\theta)\|_{max}$	$\|I(R,2\pi)\|$	$\|I(R,\theta)\|_{max}$	$\|I(R,2\pi)\|$
0.1	0.0987802	2.60924×10^{-16}	0.0999517	5.88622×10^{-16}
0.2	0.184172	2.10456×10^{-12}	0.186904	2.32806×10^{-15}
0.3	0.295023	4.64799×10^{-14}	0.294434	7.60901×10^{-15}
0.4	0.374518	5.46021×10^{-13}	0.369031	1.4854×10^{-12}
0.5	0.473937	2.16084×10^{-12}	0.467537	2.67436×10^{-12}
0.6	0.253416	3.07382×10^{-11}	0.165692	1.84166×10^{-11}
0.7	0.650913	1.23074×10^{-10}	0.638777	4.3206×10^{-10}
0.8	0.720658	1.49923×10^{-10}	0.700319	2.20162×10^{-10}
0.9	0.748229	1.37767×10^{-9}	0.706714	3.53859×10^{-9}
1.0	0.455144	1.08980×10^{-7}	0.323115	1.55120×10^{-7}
1.1	0.448683	9.62562×10^{-8}	0.287590	4.11506×10^{-7}
1.2	0.492328	3.84080×10^{-7}	0.316300	1.76724×10^{-7}
1.3	0.529113	2.72702×10^{-5}	0.337657	8.88051×10^{-6}
1.4	0.564594	0.000131655	0.354404	1.22721×10^{-5}
1.5	0.611071	0.000410107	0.386254	0.000750319
1.6	0.667320	0.000536321	0.429543	0.00019588
1.7	14.4508	14.4508	3.26076	3.26076

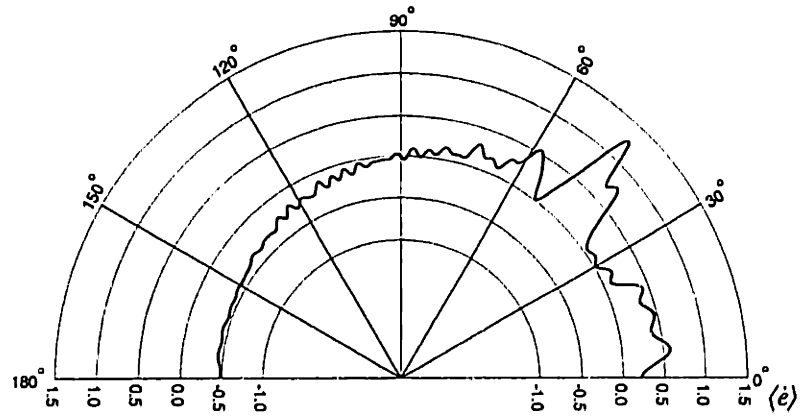

(*a*) Angular distribution of normalized time-averaged energy flux density $\langle \dot{e} \rangle$.

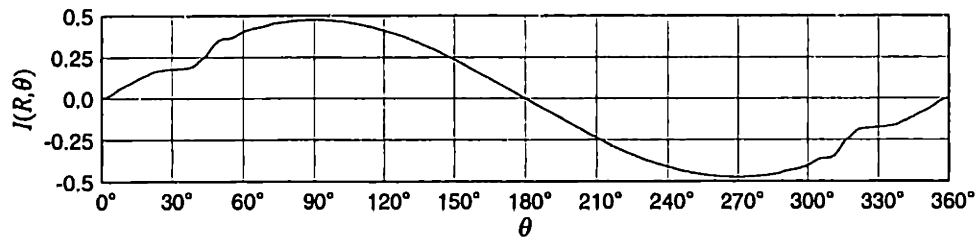

(*b*) Numerical integration of $I(R,\theta) = \int_0^\theta \langle \dot{e}(r,\theta') \rangle|_{r=R}\, d\theta'$.

Fig. 7–6 Energy balance computation for 2×4 model plate when $ka = 0.5$.

- The simulation starts with the solution for the single-fiber model. For the fiber-interphase-matrix model, a closed form analytical solution has been derived in Chapter 2.
- The scatterer polymerization methodology is used for a three-stage procedure denoted as Procedure ⑥ in Table 7–2. The fiber configuration in each stage is shown in Fig. 7–4.
- Several identical molecules, generated by scatterer polymerization, are used to construct a plate model, such as the one shown in Fig. 7–4.
- A plate model is then analyzed using the multiple-scattering solution. The coordinate system is shown in Fig. 7–5. Plate models are subjected to a planar incident wave of unit amplitude propagating in the $+X$ direction. Form I of the multiple-scattering solution (Chapter 4) is used.
- The simulation is limited to incident waves within the frequency range from $ka = 0$ to $ka = 1.5$.
- Finally, filed quantities of interest can be computed in accordance with expressions given in Chapter 4.

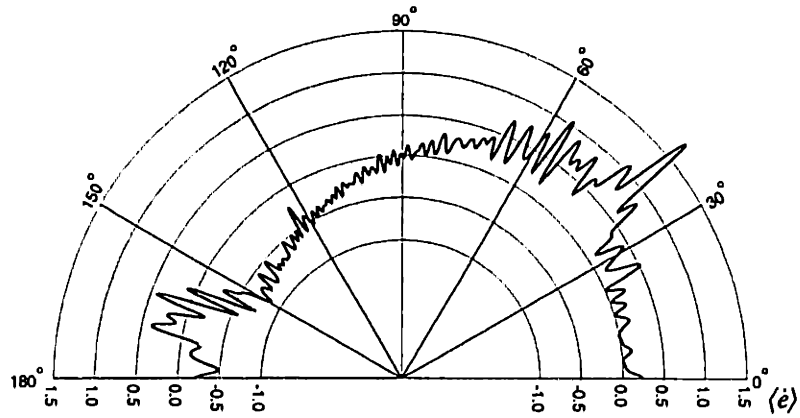

(*a*) Angular distribution of normalized time-averaged energy flux density $\langle \dot{e} \rangle$.

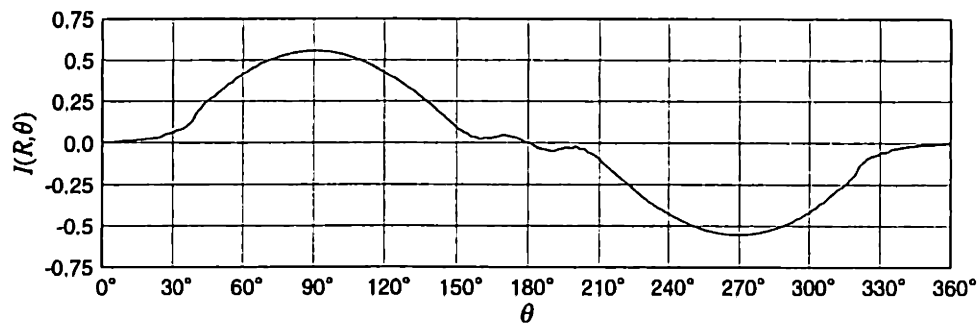

(*b*) Numerical integration of $I(R,\theta) = \int_0^\theta \langle \dot{e}(r,\theta') \rangle|_{r=R}\, d\theta'$.

Fig. 7–7 Energy balance computation for 2 × 4 model plate when $ka = 1.0$.

7-4 Simulation Results

The success of the energy balance verification has confirmed that a combined use of the multiple-scattering solution and the scatterer polymerization methodology is capable of performing full-scale simulations for models containing several thousand fibers.

In this section, computations for models having several lengths are conducted, with an emphasis on observing some of the output wave's field characteristics and on transforming the simulation results into experimentally measurable parameters.

7-4.1 Displacement Fields

The multiple-scattering solution gives the *complex amplitude* of the displacement, denoted as ϕ, in the steady-state for each model subjected to a monotonic incident wave. The physical displacement, denoted as u, is obtained by multiplying the complex amplitude by the temporal term $e^{-i\omega t}$ and then taking the real part of

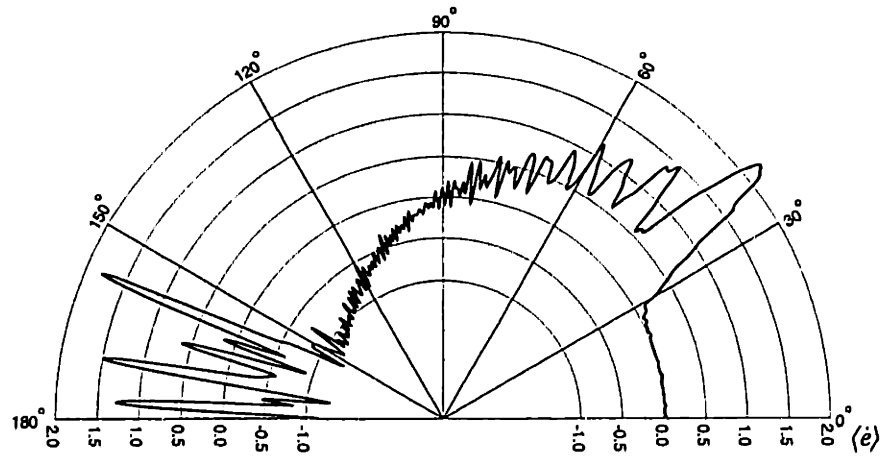

(*a*) Angular distribution of normalized time-averaged energy flux density $\langle \dot{e} \rangle$.

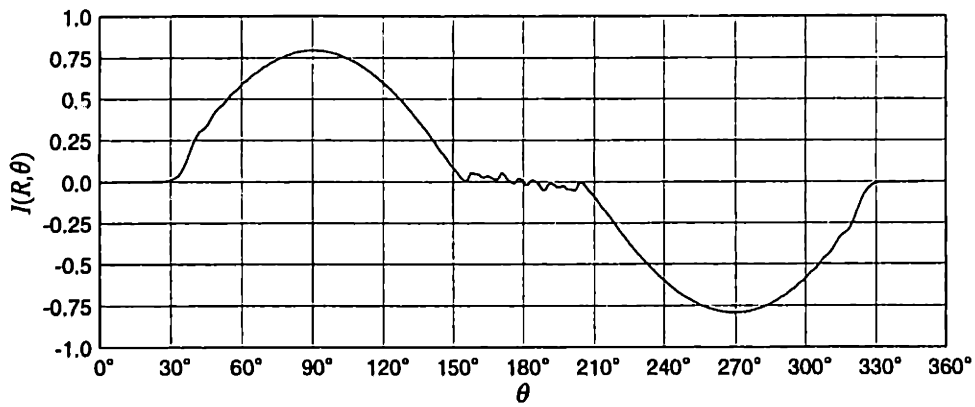

(*b*) Numerical integration of $I(R,\theta) = \int_0^\theta \langle \dot{e}(r,\theta') \rangle|_{r=R}\, d\theta'$.

Fig. 7–8 Energy balance computation for 2×4 model plate when $ka = 1.5$.

the product. That is,

$$u = Re\{\phi e^{-i\omega t}\} = A\cos(\omega t + \alpha) \tag{7–12}$$

where A is the *displacement amplitude* given by $A = |\phi|$; that is, the amplitude of the physical displacement equals the modulus of the complex amplitude.

Figures 7–9 through 7–12 show the distributions of the displacement amplitudes in the vicinity of the fiber clusters for the 2×4, 2×6, 2×8 and 2×10 plate models, respectively, at various frequencies ranging from $ka = 0.1$ to $ka = 0.6$. The regions shown in these figures are bounded by $x = \pm 250a$ and $y = \pm 250a$.

In these figures, the displacements in the regions occupied by the fibers, as well as the regions in close proximity to the fiber clusters, are not computed. When using the methodology of scatterer polymerization, the radius of the resulting molecule is the radius of the smallest circle that circumscribes all the fibers (see Chapter 6), which is $5.5\sqrt{2}d + b$ for the molecule that is used to construct the plate models under consideration. Wave fields within this radius cannot be computed.

The displacement amplitude distribution is very uniform in the region directly

behind the fibers, called the *shadow region*, despite some smaller-scale wiggles. In the *illuminated region*, the region opposite the shadow region, periodic peaks appear as ridges that are primarily parallel to the plate's vertical boundary, provided that either the plate is long enough or the frequency is high enough. The spacing between ridges clearly corresponds to the incident wavelength, which decreases as the linear reciprocal of the frequency. For example, at the frequencies $ka = 0.2$, 0.4 and 0.6, there are approximately 13, 26 and 39 ridges, respectively, in the illuminated region shown ($-250a \leq x \leq 43.5a$). The smaller-scale wiggles (see, for example, Fig. 7–12 when $ka = 0.4$ or 0.5) appear in both the shadow region and the illuminated region as straight lines that are angled with respect to the direction of the incident ave. As the frequency increases, as well the length if the plate increases, these wiggles extend farther from the plate in both the illuminated and the shadow regions.

At most frequencies, as the plate length increases, the distribution pattern within the illuminated and the shadow regions appear to be expanded self-similarly, while the transition regions at eh upper and lower edges remain essentially identical. This suggests that waves in the illuminated and shadow regions consist almost exclusively of the waves reflected from and transmitted through the plates. The exceptions are at lower frequencies and short plate lengths; in which case, the diffracted waves — waves that propagate around the edge into these regions — are substantial.

Finally, Fig. 7–13 shows the distributions of the displacement amplitudes for the 2×4 plate model at higher frequencies ranging from $ka = 0.7$ to $ka = 1.4$. The region shown is bounded by $x = \pm 250a$ and $y = \pm 150a$. The general characteristics observed earlier remain the same here.

7-4.2 Averaged Displacement Fields

In experimental NDE ultrasonics, the response of the interrogated body is usually detected by one or more transducers placed on or near its surface. In most applications, the transducer's size and the region of averaged interrogation are large compared to the diameter of a fiber in a fiber reinforced composite. Therefore, the response measured experimentally is the average of a field quantity over a region of fibers. In the following, the amplitude of the averaged displacement over an extended region of y is analyzed for a plate that is macroscopically symmetric about the X-axis.

Consider a spatially-varying displacement field $u(x, y)$ being averaged over a range $0 \leq y \leq H$. Denote this *averaged displacement* over the range $0 \leq y \leq H$ as $\widehat{u}(x, H)$, so

$$\widehat{u}(x, H) = \widehat{A}(x, H)(\cos \omega t + \widehat{\alpha}) \tag{7–13}$$

where $\widehat{A}(x, H)$ is called the *averaged displacement amplitude* over the range $0 \leq y \leq$

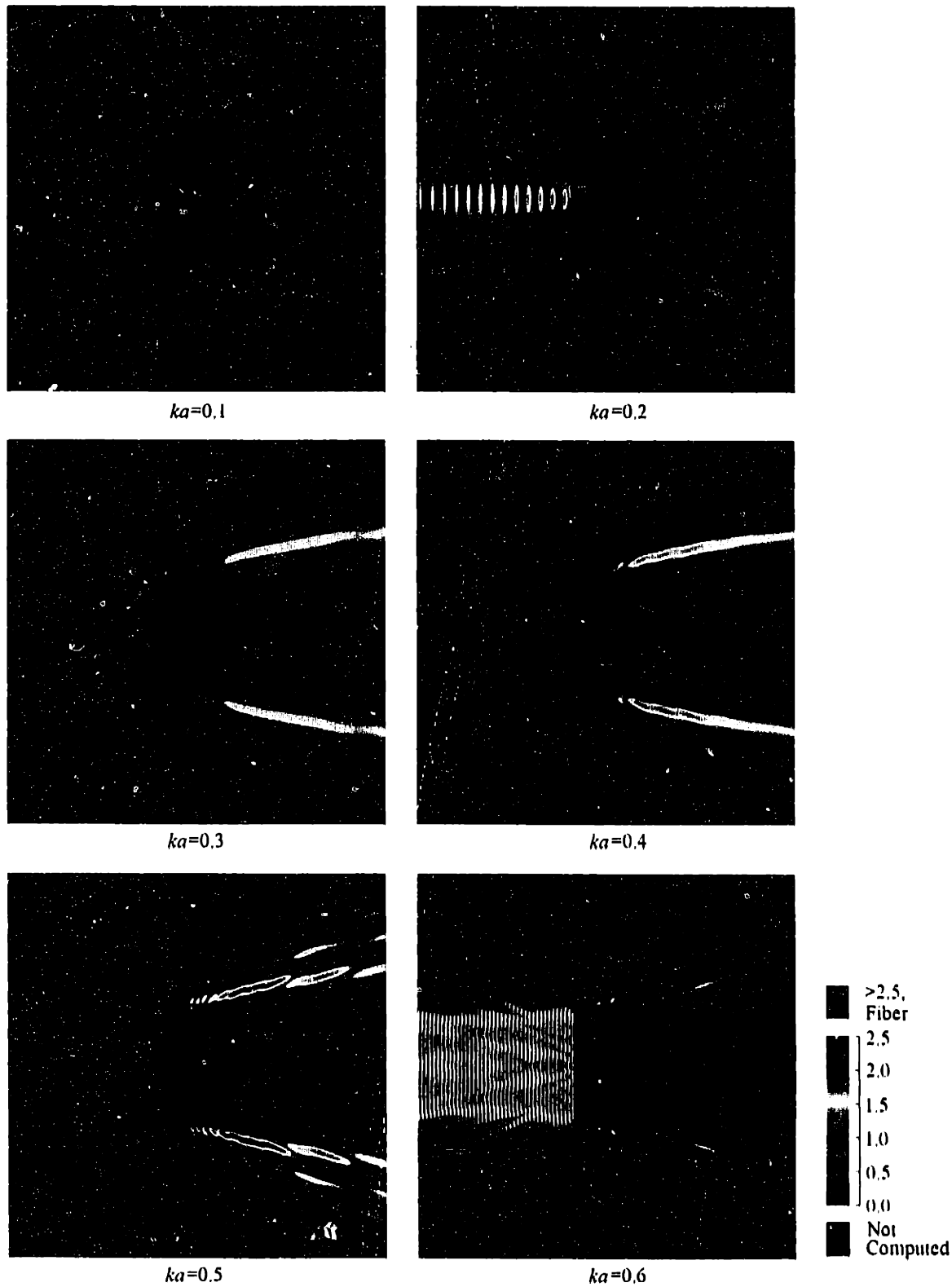

Fig. 7–9 Distribution of displacement amplitude in vicinity of fiber cluster for 2×4 model plate at various frequencies.

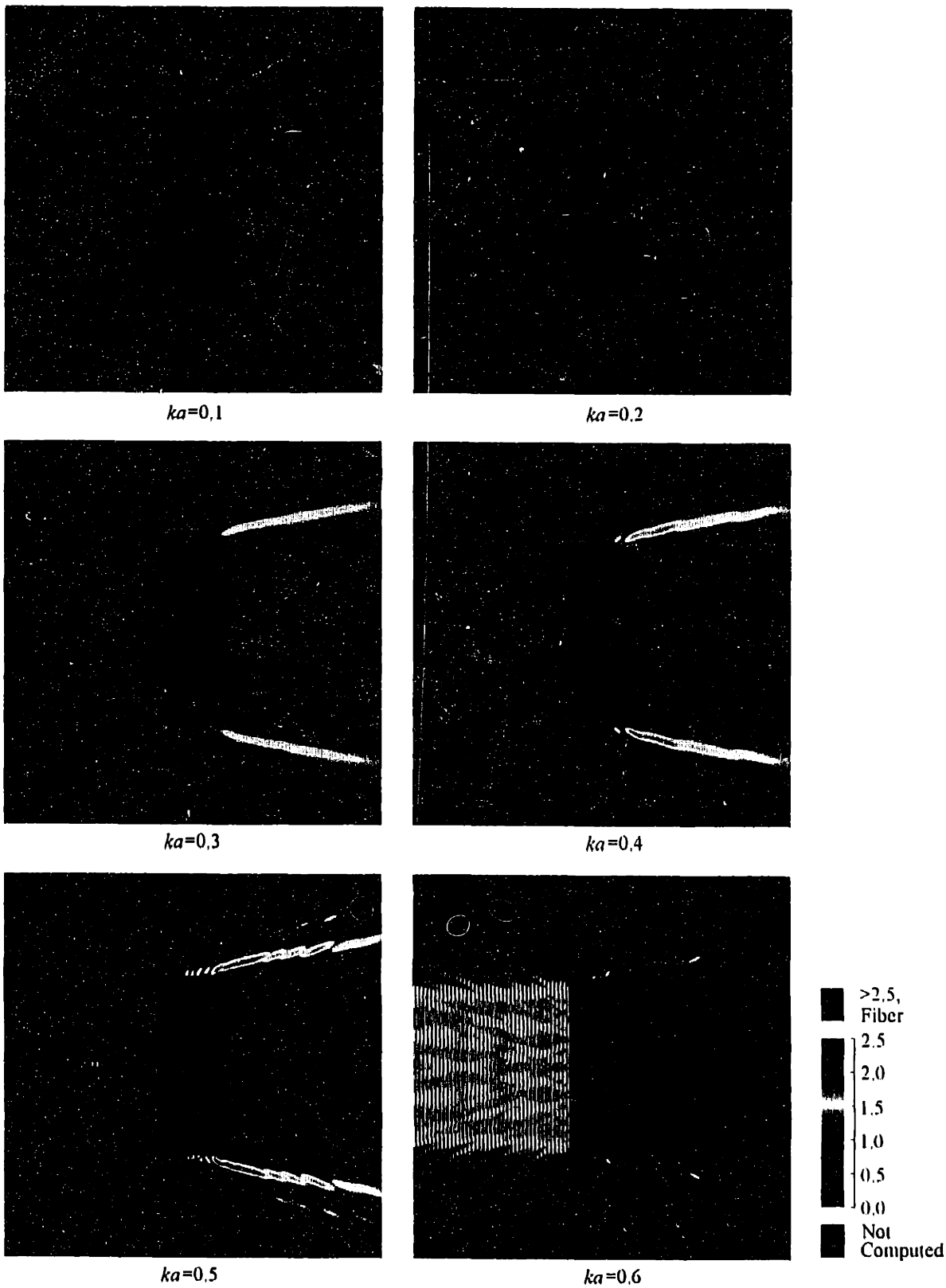

Fig. 7–10 Distribution of displacement amplitude in vicinity of fiber cluster for 2×6 model plate at various frequencies.

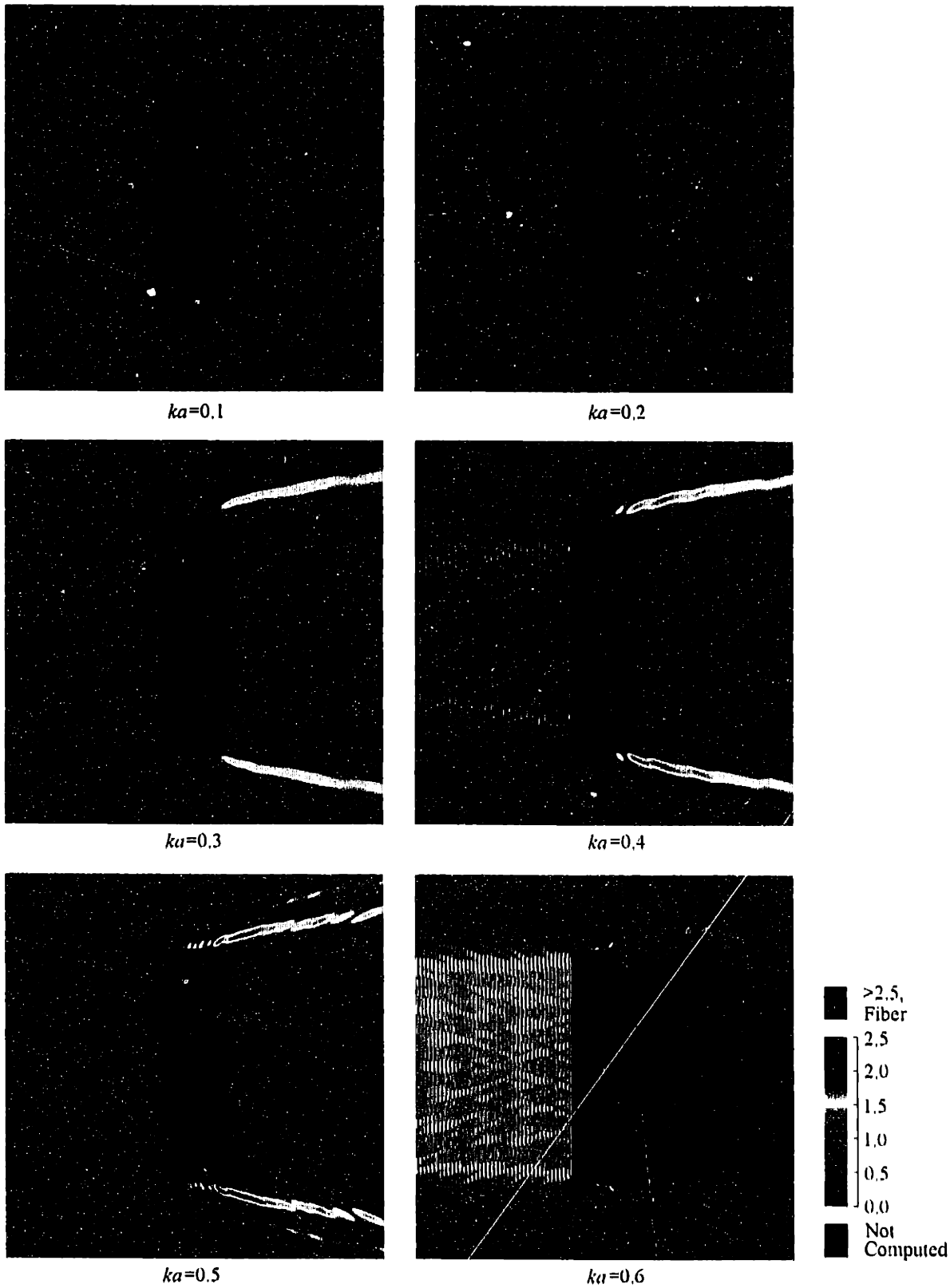

Fig. 7–11 Distribution of displacement amplitude in vicinity of fiber cluster for 2 × 8 model plate at various frequencies.

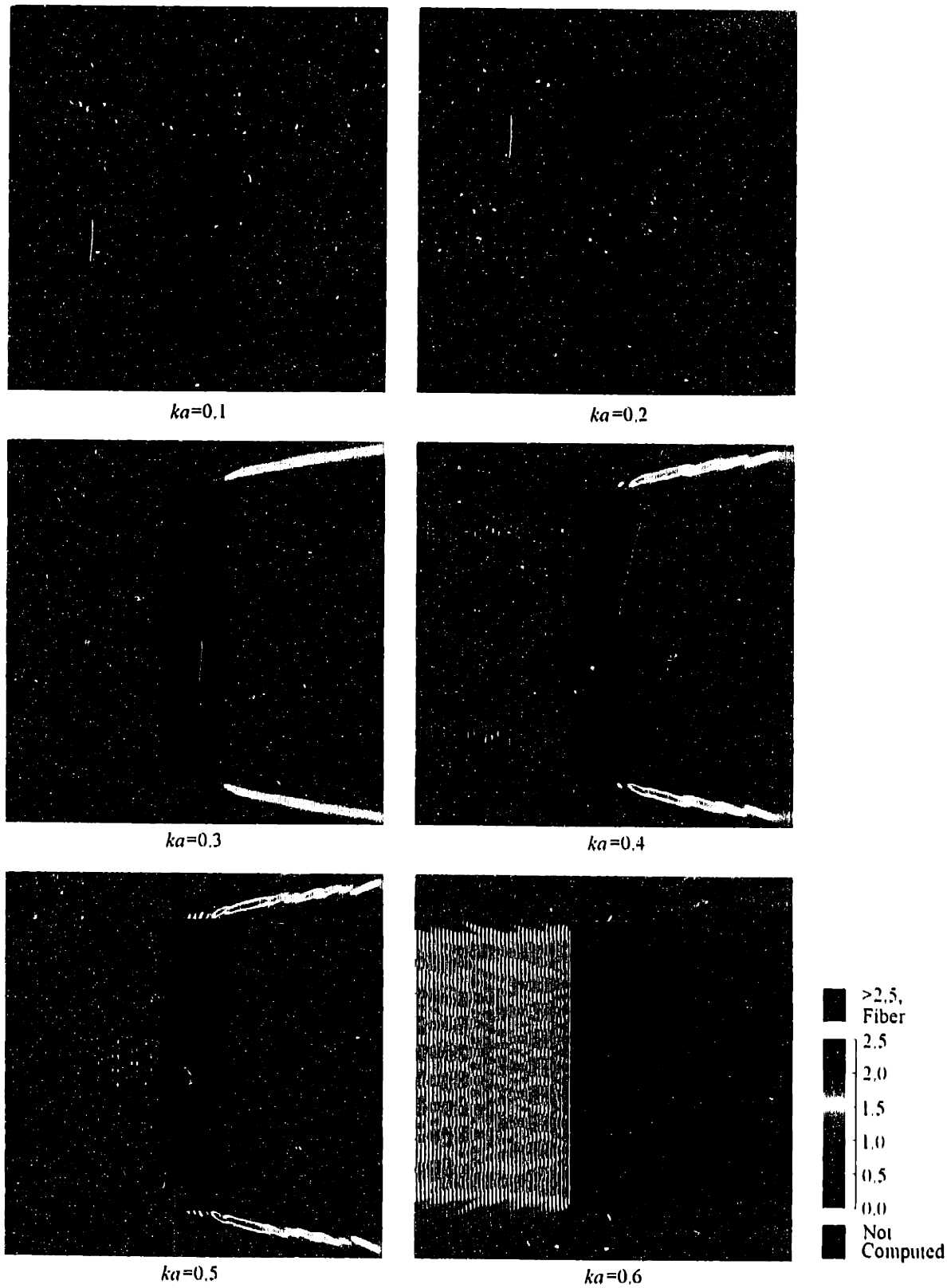

Fig. 7–12 Distribution of displacement amplitude in vicinity of fiber cluster for 2 × 10 model plate at various frequencies.

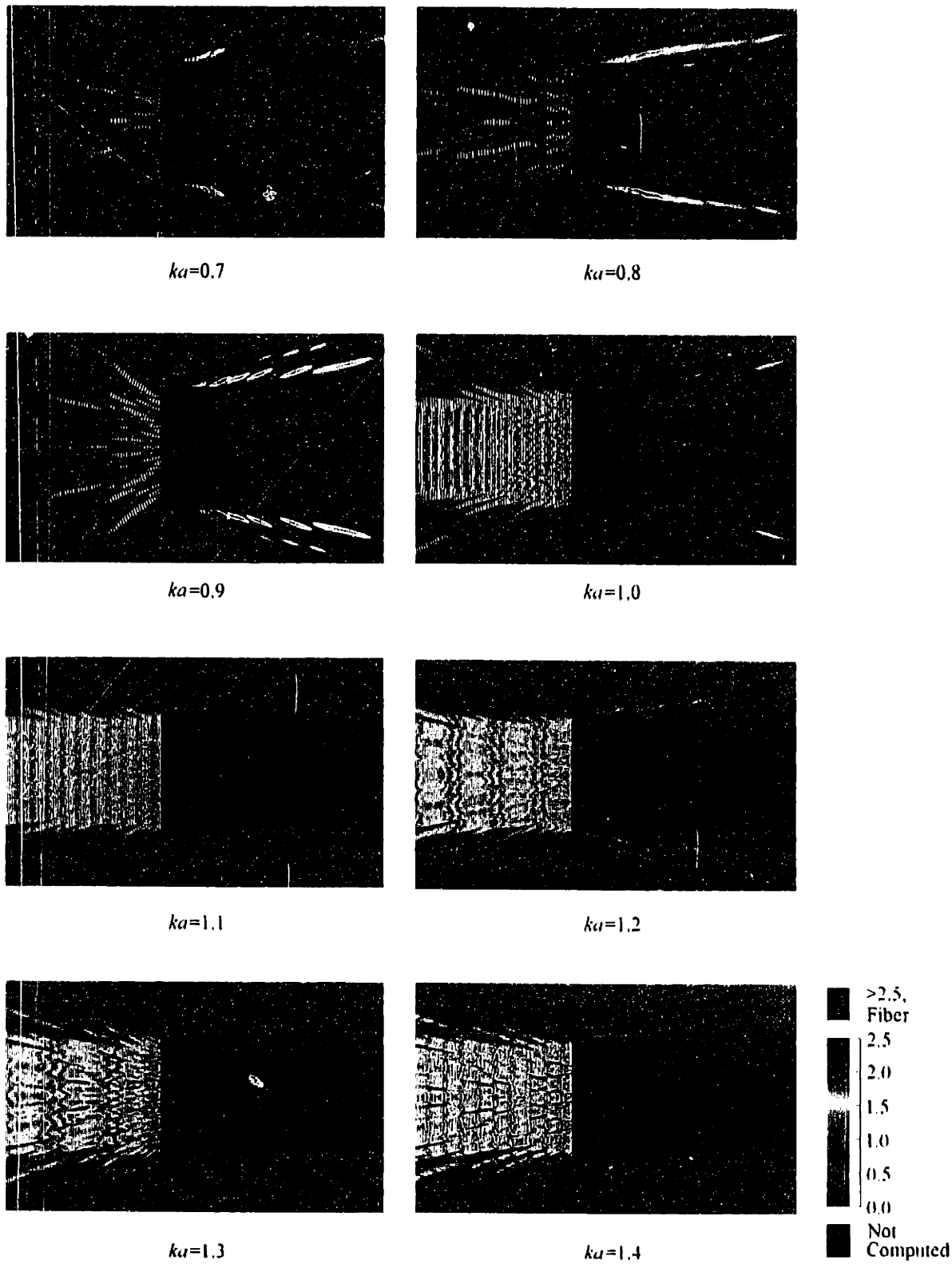

Fig. 7–13 Distribution of displacement amplitude in vicinity of fiber cluster for 2×4 model plate at various higher frequencies.

H. Then, from eqn. (7–12),

$$\hat{u}(x,H) = \frac{1}{H}\int_0^H u\,dy = \frac{1}{H}Re\left\{\int_0^H \phi e^{-i\omega t}dy\right\} = Re\{\hat{\phi}(x,H)e^{-i\omega t}\} \qquad (7\text{–}14)$$

Also,

$$\hat{A}(x,H) = \left|\hat{\phi}(x,H)\right| \qquad (7\text{–}15)$$

that is, the averaged displacement amplitude equals the modulus of the averaged complex amplitude of the displacement.

Figures 7–14 through 7–18 show the change of averaged displacement amplitudes $\hat{A}(x,H)$ with H at several discrete constant-x lines, and the comparison to the distribution of the displacement amplitude A along the same lines, for the 2×4 model plate at frequencies ka = 0.3, 0.6, 0.9, 1.2 and 1.5. For all these cases,

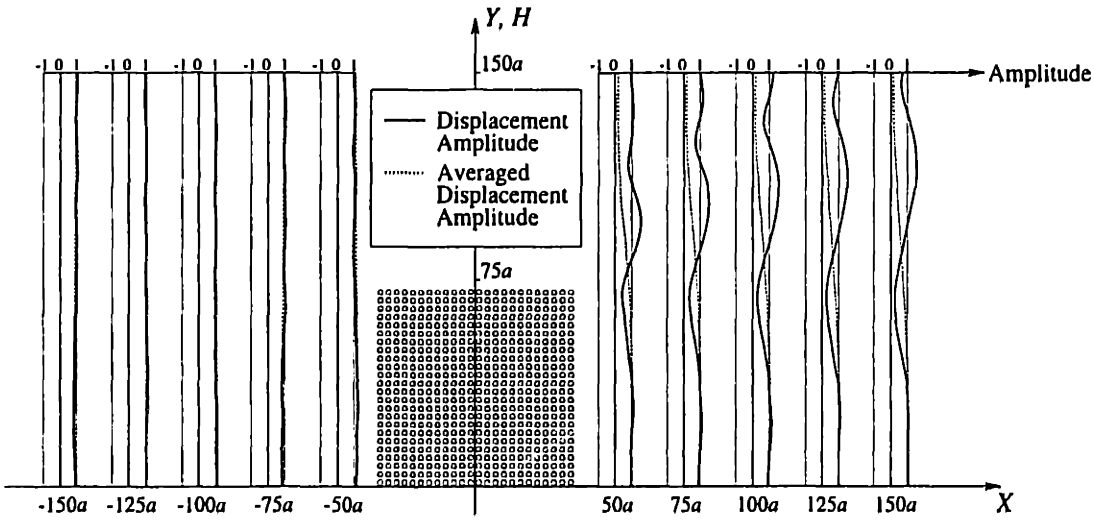

Fig. 7–14 Averaged displacement amplitudes as function of H, as compared to distribution of displacement amplitude, for 2×4 model plate at frequency $ka = 0.3$.

the averaged displacement amplitude starts at its limiting value as $H \to 0$ as the same as the displacement amplitude. As H increases, the averaged displacement amplitudes soon stabilizes; that is, the fluctuation of the displacement amplitude does not change the averaged results noticeably. Then, the edge effect starts to affect the averaged values, which occurs roughly after $H > 50a$.

Figures 7–19 through 7–23 show the distribution of the averaged displacement amplitude of the 2×4 model plate along the X-axis at frequencies ka = 0.3, 0.6, 0.9, 1.2 and 1.5. In these figures, the averaging range is $0 \leq y \leq 48a$ (two-thirds of the plate's half-length) and the region occupied by the molecules, $-43.5a < x < 43.5a$, is not computed.

From Figs. 7–19 through 7–23, it is observed that the distribution of the averaged

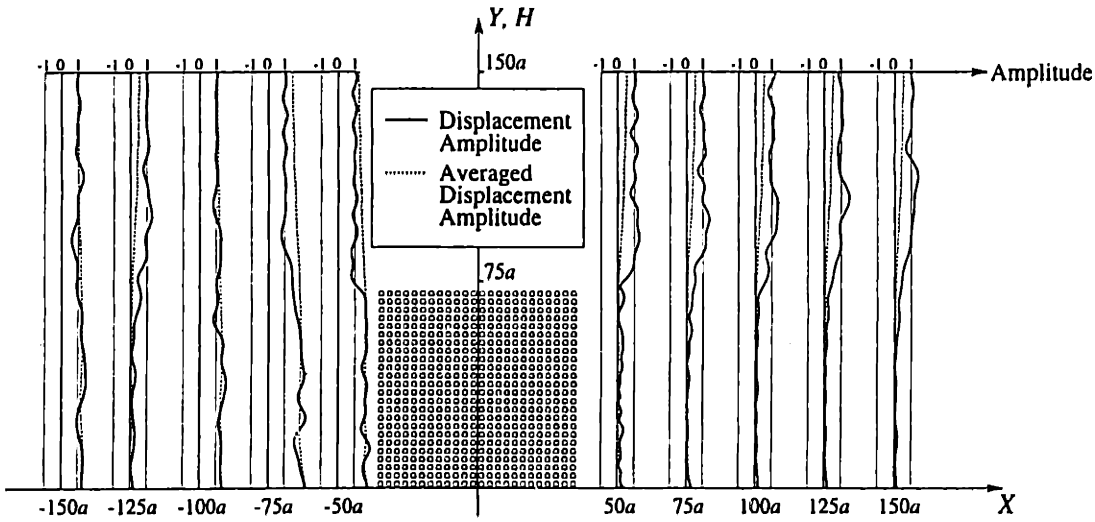

Fig. 7–15 Averaged displacement amplitudes as function of H, as compared to distribution of displacement amplitude, for 2×4 model plate at frequency $ka = 0.6$.

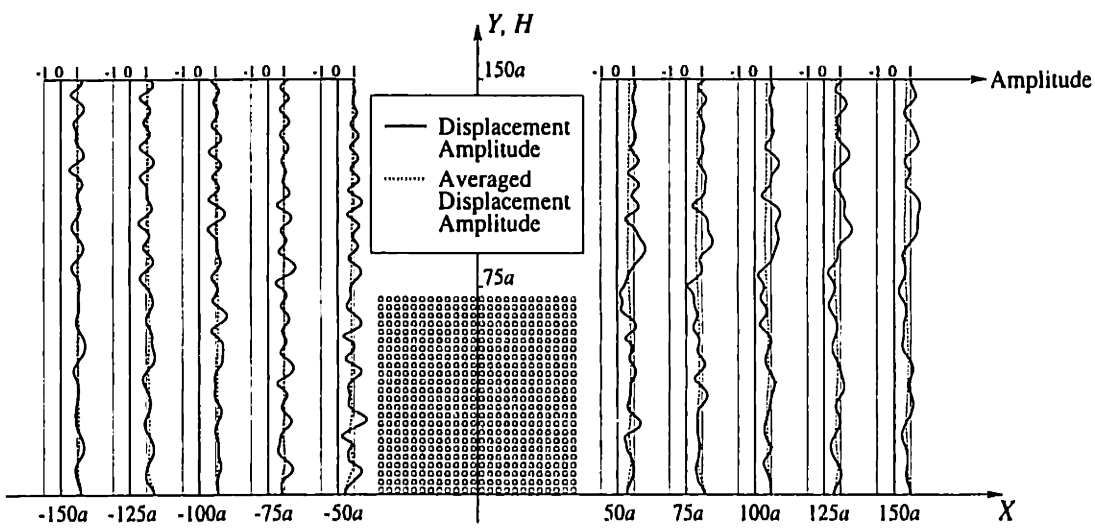

Fig. 7–16 Averaged displacement amplitudes as function of H, as compared to distribution of displacement amplitude, for 2×4 model plate at frequency $ka = 0.9$.

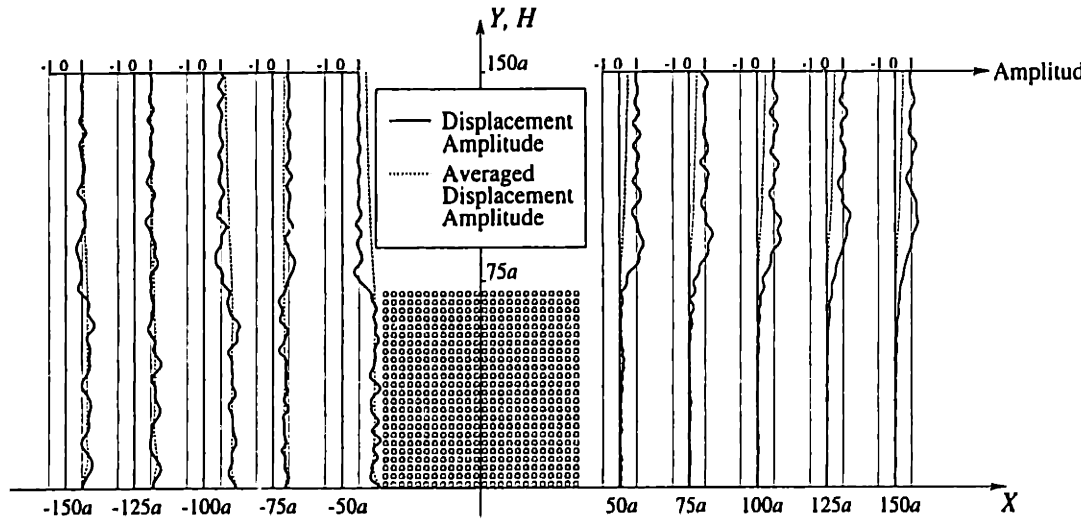

Fig. 7–17 Averaged displacement amplitudes as function of H, as compared to distribution of displacement amplitude, for 2×4 model plate at frequency $ka = 1.2$.

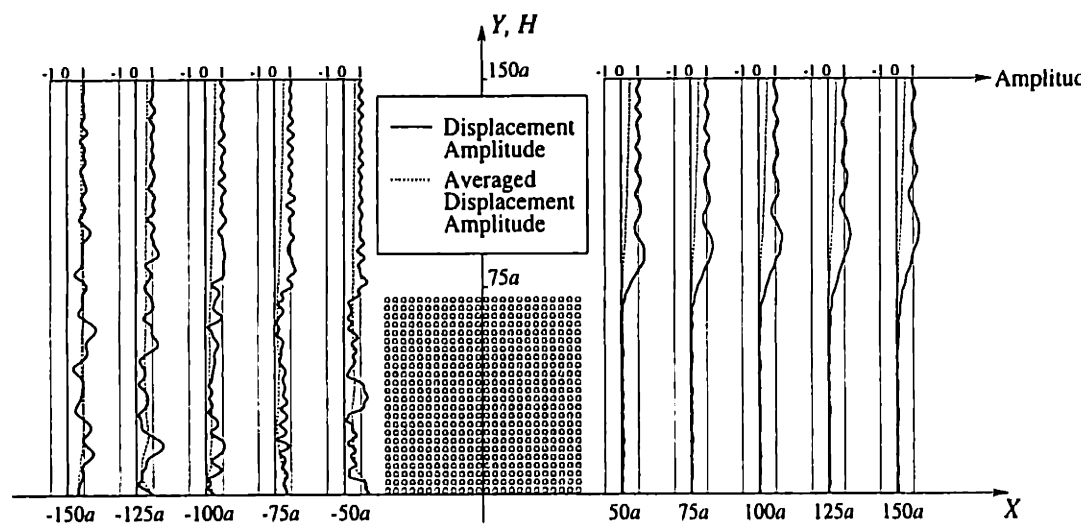

Fig. 7–18 Averaged displacement amplitudes as function of H, as compared to distribution of displacement amplitude, for 2×4 model plate at frequency $ka = 1.5$.

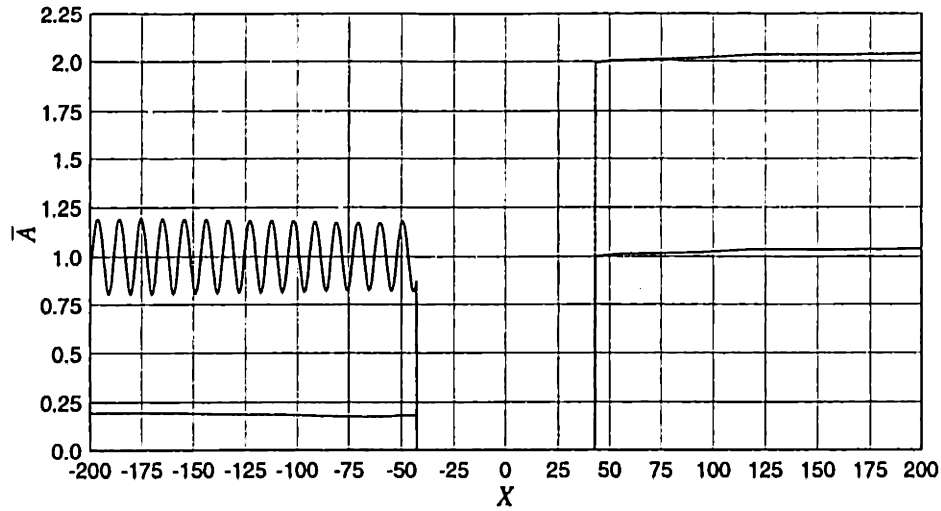

Fig. 7–19 Distribution of averaged displacement amplitude along X-axis for 2×4 model plate at frequency $ka = 0.3$. (——: Total wave; - - - -: scattered wave.)

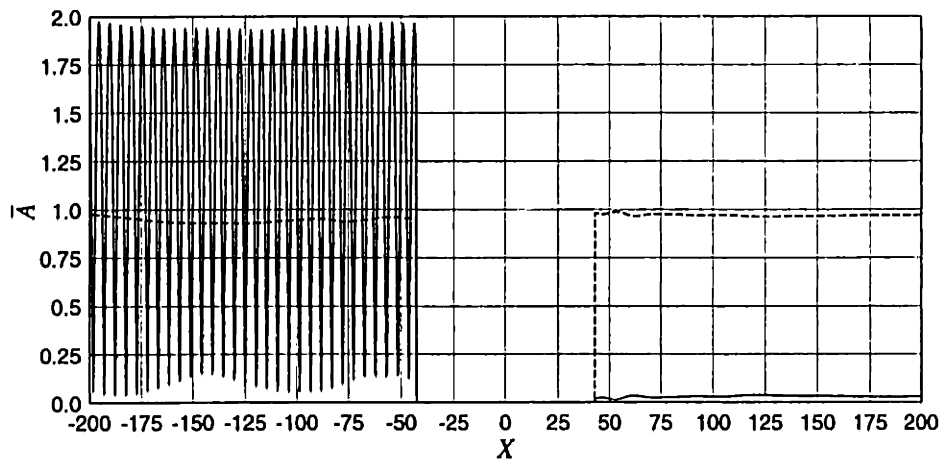

Fig. 7–20 Distribution of averaged displacement amplitude along X-axis for 2×4 model plate at frequency $ka = 0.6$. (——: Total wave; - - - -: scattered wave.)

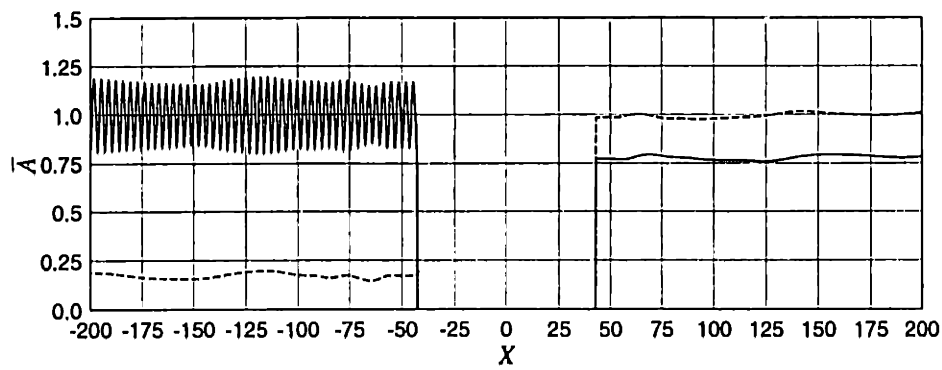

Fig. 7–21 Distribution of averaged displacement amplitude along X-axis for 2×4 model plate at frequency $ka = 0.9$. (——: Total wave; - - - -: scattered wave.)

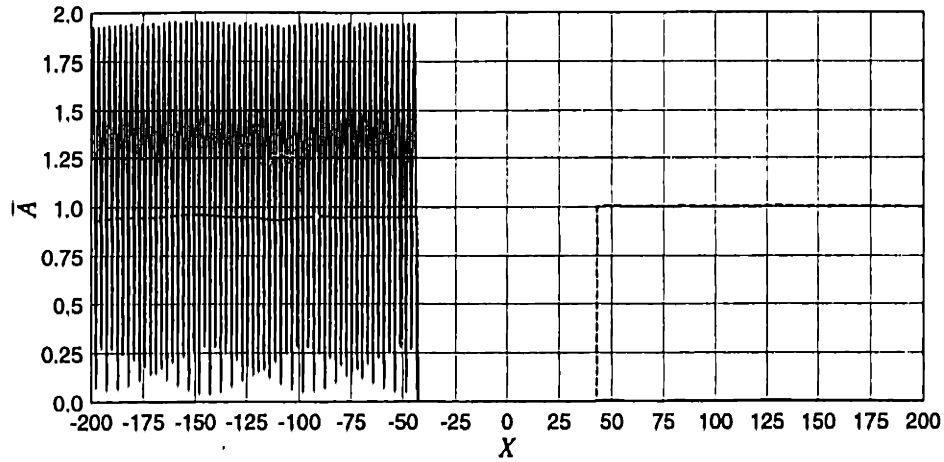

Fig. 7–22 Distribution of averaged displacement amplitude along X-axis for 2×4 model plate at frequency $ka = 1.2$. (——: Total wave; - - - -: scattered wave.)

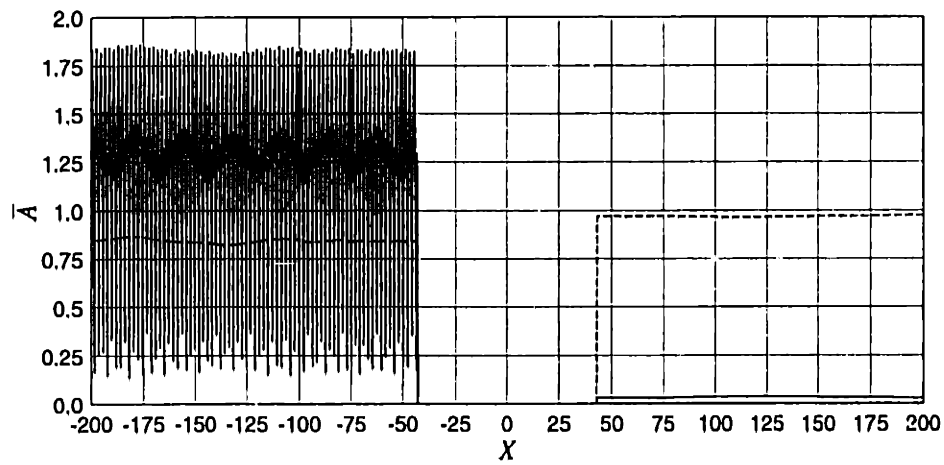

Fig. 7–23 Distribution of averaged displacement amplitude along X-axis for 2×4 model plate at frequency $ka = 1.5$. (——: Total wave; - - - -: scattered wave.)

displacement amplitude (solid curve) in the forward direction does not change significantly throughout the region shown. This implies that the choice of a particular measuring point for such a computational model plate is not critical.

In the backward direction, the averaged displacement amplitude is highly oscillatory along the X-axis. In essence, the averaging process eliminates small-scale fluctuations of the displacement amplitude along a constant-x line. The averaged displacement in the backward direction can be viewed as a planar wave traveling in the $-X$ direction, which can be expressed as

$$\widehat{\phi}\Big|_{x<0} = e^{ikx} + Be^{-ikx} = e^{ikx}(1 + Be^{-2ikx}) \tag{7-16}$$

where B represents the amplitude of the scattered wave. Thus

$$\left|\widehat{\phi}\right|\Big|_{x<0} = |1 + Be^{-2ikx}| \tag{7-17}$$

Equation (7–17) indicates that both the spatial distribution (for a fixed k) and the spectrum (for a fixed x) in the backward direction are highly oscillatory, with envelopes given by $(1 \pm B)$.

Hence, in general, the scattered wave suffices to describe the main characteristics of the backward scattering. In fact, in some ultrasonic NDE techniques, such as the pulse-echo technique, in the backward direction, only the reflected wave (*i.e.*, the scattered wave) is of interest. The dashed curves in Figs. 7–19 through 7–23 correspond to the averaged displacement amplitudes due to the scattered wave only. They all appear uniform similar to those in the forward direction. This implies that the choice of a particular measuring point in the backward direction is not critical.

7-4.3 Plate-Averaged Wave Fields

For the displacement fields, the forward and backward spectra of the averaged displacement amplitude for all four models plate are computed for the frequency range $ka = 0.0025$ to 1.5 with an increment of 0.0025. The measuring points are at $x = \pm 60a$. Displacement amplitudes are averaged over two-thirds of the plate's half-length for all models. The spectra are shown in Figs. 7–24 and 7–25. Note that the backward spectra are shown for the displacements due to scattered waves only.

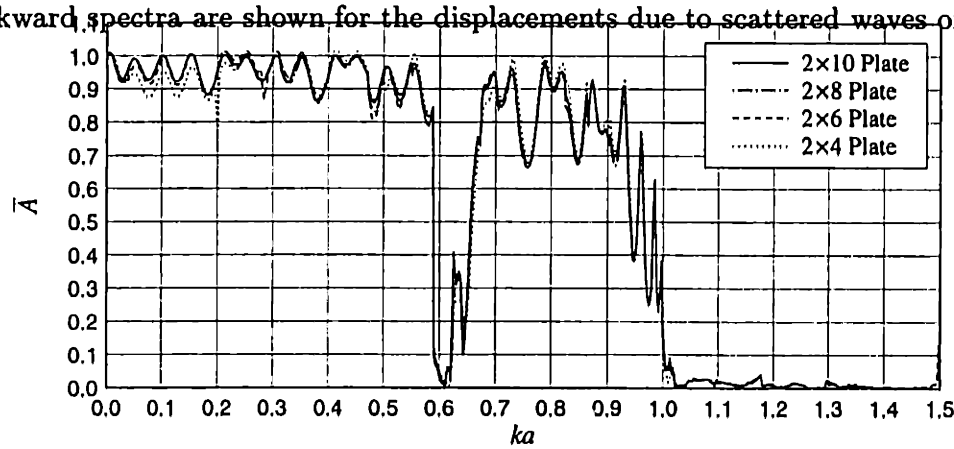

Fig. 7–24 Forward spectra of averaged diaplacement amplitude for various model plates.

Discussions and analyses of the physical characteristics of the spectra are reserved for future more comprehensive studies. The emphasis here is to note an important relationship among the spectra obtained for the four model plates. These spectra are essentially identical: the oscillatory patterns are almost the same and the amplitude deviation of one spectrum from any other is generally, with exceptions at a few discrete frequencies, within 2%.

The similarity among the spectra shown in Figs. 7–24 and 7–25 suggests that, beyond some low frequency regime, the displacement amplitude wave field, averaged over a central portion of a model plate, is independent of the plate length, provided

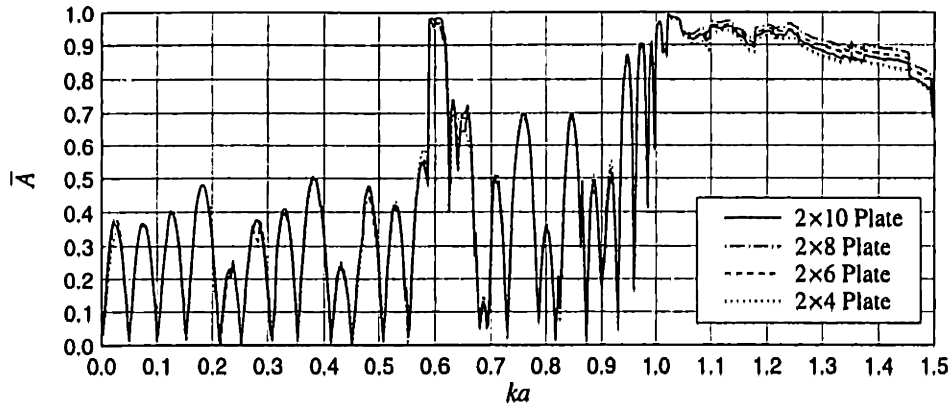

Fig. 7–25 Backward spectra of averaged diaplacement amplitude due to scattered waves for various model plates.

the averaging range is sufficiently large, compared to both the wavelength and the fiber radius, and remains entirely within either the shadow or the illuminated regions. Such an averaged wave field that is independent of the plate length is called a *plate-averaged wave field.*

Furthermore, reviewing the results obtained so far leads to the following proposition: for a model plate involving a macroscopically uniform fiber distribution, if the ridges of amplitude in of the wave field in the illuminated region are predominantly straight lines parallel to the plate's boundary, the plate is adequately long for the frequency and the averaged wave field can be taken as the plate-averaged wave field.

The significance of the concept of plate-averaged wave field is that, in an averaged sense, a model plate of finite length can be used to obtain results for a plate of infinite length, such as one generated by self-similarly repeating the model shown in Fig. 7–5 along the Y-axis from $-\infty$ to ∞. From a numerical computation perspective, using longer plates in general ensures that the averaged wave field is closer to its asymptotic value, especially in the low frequency regime, but at a cost of computation time, which grows at least at the same rate of the required computer memory size: $\sim N^2$ where N is the number of molecules in the model plate.

On the other hand, there are exceptions to the proposition. For example, at $ka = 0.2$, the distribution for the 2×4 model plate is distinctive from other model plates. These exceptions could be due to some other physical phenomena yet to be explored. However, these exceptions appear to occur rarely.

It is also observed that, for each model plate, there are small ranges of frequency along the forward spectrum in which the averaged displacement amplitude exceeds unity, which is the amplitude of the incident wave. Despite that fact that the excess amount is extremely small, this violates the physical principle of energy conservation if the amplitude is taken as the exact plate-averaged amplitude. This implies that, although the computed results are analytically exact and numerically correct, the plate-averaged wave field must be regarded as an approximate numerical result that contains errors, where the errors are introduced in the averaging process when the

results from a finite-length model plate are extrapolated to an infinite-length plate.

7-5 Conclusions

In this chapter, complete simulations are performed to demonstrate that a combined use of the computational tools developed previously, namely the multiple-scattering solutions (Chapters 4 and 5) and the scatterer polymerization methodology (Chapter 6), is capable of performing full-scale simulations.

Through numerical examples, the complete procedure of such a simulation is explored in detail and summarized at the end of Section 3. The examples consists of a series of model fiber reinforced composite plates of thickness 0.72 mm but of different lengths. By exploring various characteristics of the full-scale simulations for this series of examples, the concept of *plate-averaged wave fields* is established. This concept relates the simulation results for a finite-length model plate to experimentally measurable responses of a composite plate of infinite length.

Finally, the simulation results are analytically exact and the simulation implementation has been numerically verified.

References

[1] H. Yim, J. H. Williams, Jr, Database generation and parametric study for ultrasonic non-destructive characterization of a single fiber composite interphase, *Ultrasonics*, **33**, 389–401, 1995.

[2] H. Yim, J. H. Williams, Jr, Formulation and its energy balance verification for ultrasonic non-destructive characterization of a single fiber composite interphase, *Ultrasonics*, **33**, 377–387, 1995.

[3] Y.-H. Pao, C.-C. Mow, *Diffraction of Elastic Waves and Dynamic Stress Concentrations*, Crane Russak & Co., New York, 1971.

8

Application Example

Abstract: *In this chapter, a comprehensive example of full-scale simulations of a fiber reinforced composite system is presented. Based on the numerical procedures developed in the previous chapters, the simulations are conducted to observe the effects on the cut-off and recovery frequencies of a stop band in the response spectra of a composite plate due to changes of its micro-structural parameters.*

Contents:

Nomenclature

Symbols

- $\overline{A}$ Plate-averaged amplitude of the out-of-plane displacement.
- a Radius of the fiber in the fiber-interphase-matrix micromechanics model.
- b Outer radius of the interphase in a fiber-interphase-matrix micromechanics model for fiber reinforced composites.
- d Fiber spacing: the distance between two adjacent fibers in the same row or column in a square fiber arrangement.
- f Frequency of the incident wave.
- $\hat{\imath}$ Unit of imaginary numbers, $\hat{\imath} = \sqrt{-1}$.
- k Wave number in the matrix.
- k_c Wave number corresponding to the cut-off frequency.
- k_r Wave number corresponding to the recovery frequency.
- Λ Wavelength in the matrix.
- μ Lamé constant of the matrix.
- ϕ Complex amplitude of out-of-plane displacement.
- ω Circular frequency of the incident wave.
- ρ Density of the matrix.

Subscripts

- f, i Physical quantities that belong to the fiber and the interphase, respectively. (The same denotation without the subscript signifies that the quantity belongs to the matrix.)

8-1 Introduction

In previous chapters, a computational approach for full-scale simulation of scattering of elastic waves in fiber reinforced composites has been established, implemented and verified. The approach involves two theoretical developments: solutions for multiple-scattering problems of elastic waves in Chapters 4 and 5, and the methodology of *scatterer polymerization* in Chapter 6. In Chapter 7, the combined use of these theoretical tools is demonstrated to be capable of performing full-scale simulations for model composite plates containing thousands of fibers.

In this chapter, a more comprehensive deterministic full-scale simulation is presented, with an attempt to observe the effects on the macroscopic response characteristics of a composite plate due to changes in some parameters of its microstructure. The example is aimed at gaining insights into the nondestructive evaluation (NDE) of composites.

In a fiber reinforced composite, the fiber-matrix interface may possess physical properties that are distinctive from either of the two constituents, due to either chemical interactions between the constituents or coating treatments in the material processing to improve bonding. In some micromechanical models, this distinctive layer at the interface is treated as a third phase of material constituents and is called the *interphase*. The interphase plays a pivotal roll in some of the macroscopic properties of the composites.

The example chosen for study is a composite plate consisting of identical fibers that incorporate the interphase, called the *fiber-interphase-matrix model*. The fiber-interphase-matrix model for fibers in composite has been considered previously. Yim and Williams[1-2] studied the single-scattering problem of such a fiber model subjected to in-plane shear (SV) and pressure (P) waves. The single-scattering problem of anti-plane shear (SH) waves has been studied in Chapter 2, and some multiple-scattering problems of SH waves have been studied throughout this thesis, including an example of full-scale simulation in Chapter 7.

8-2 Numerical Procedure

Deterministic full-scale simulations involve computing the response spectra for various combinations of parameters of the microstructure. The computation for the response spectrum for each set of parameters follows that in Chapter 7. The model plate is constructed in four stages, using a square arrangement of fibers.

In the first three stages, the scatterer polymerization methodology is used to construct molecules of abstract scatterers. Figure 8–1 shows the fiber configuration

in the first stage, which also defines the microstructural parameters in this study: the distance d between two adjacent fibers located along the same row or column, referred to as the *fiber spacing*; and the outer radius of the interphase b. Both parameters d and b are normalized by the fiber radius a, which remains constant. Figure 8–2 shows the configurations of the second and the third stages of scatterer polymerization.

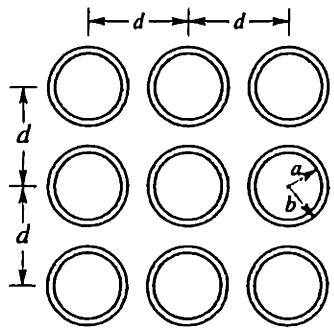

Fig. 8–1 Configuration of first stage for constructing fiber reinforced composite plate model, showing microstructural parameters.

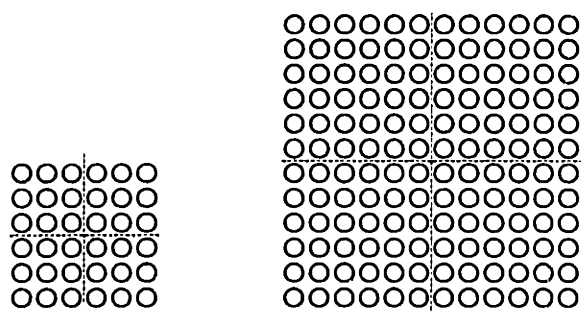

Fig. 8–2 Configurations of second and third stages for constructing fiber reinforced composite plate model. (Dashed lines indicate demarcations of molecules.)

In the fourth stage, the multiple-scattering solution is used to solve a model plate constructed from 8 molecules, built in the third stage. The configuration of the final model plate, containing 1152 fibers, as well as the coordinate system used in the analysis, are shown in Fig. 8–3.

Before computing the response spectra, an energy balance computation is performed. For each set of microstructural parameters, when the frequency is higher than a certain value, numerical errors become too severe and the computational results become erroneous. Energy balance computations compute the total energy transmitted across a closed circular boundary of radius $80d$, as sketched in Fig. 8–3,

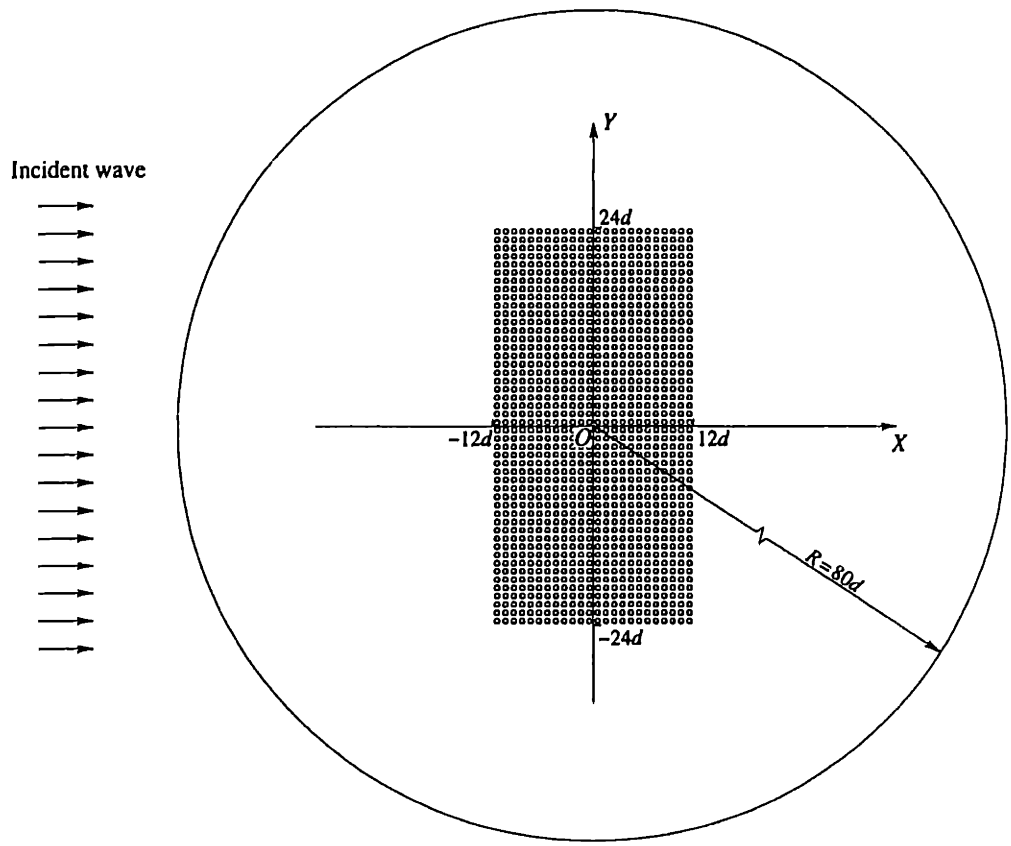

Fig. 8–3 Configuration and coordinate system for composite plate model, and hypothetical boundary for energy balance computations.

when the model plate is subject to a planar incident wave of unit amplitude propagating along the $+X$-axis, whose expression is[3]

$$\phi^{\text{inc}} = \mathrm{e}^{-\mathrm{i}kx} \tag{8–1}$$

where ϕ is the out-of-plane displacement component in complex notation, and k is the wave number in the matrix. When the numerical errors are small, the total energy transmitted across the boundary should balance. This computation determines the computable range of frequencies. The computation uses a coarse frequency step-size ($\Delta ka = 0.05$), and follows the same procedure as described in Chapter 5, where mathematical expressions for the energy balance computation are also given.

Afterwards, a finer step-size ($\Delta ka = 0.0025$) is used to compute both the forward and the backward spectra of the *plate-averaged* displacement amplitude, denoted as $\overline{A}$, due to the incident wave in eqn. (8–1), over the entire computable frequency range. The concept of a *plate-averaged* field quantity has been defined and discussed in Chapter 7. In essence, this is the equivalent averaged response of a plate of infinite length extrapolated from the computed results for a model plate of finite length. In general, a longer model plate would ensure a more accurate extrapolation. But it has been shown in Chapter 7 that a model plate such as the one in Fig. 8–3 is

capable of generating such extrapolations with errors generally no larger than 2%.

In the computation, the plate-averaged displacement amplitudes are computed as the averaged displacement amplitude, whose expression is given in Chapter 7, along the line $x = \pm 20d$ over the range $0 \leq y \leq 16d$, which is $2/3$ of the half-length of the model plate. It has been observed in Chapter 7 that such a computed plate-averaged displacement amplitude does not vary noticeably in an extended range of x in both the forward and backward directions.

Table 8–1 lists the material properties of the constituents that correspond to a metal-matrix ceramic-fiber reinforced composite system, after [2]. A typical radius of the fiber is $a = 10\,\mu\text{m}$[2]. In the computations, the physical properties of all three constituents are fixed.

In the following discussions, the normalized frequency ka is used. The relations between the normalized frequency ka, the frequency f, the wavelength Λ, and material properties are

$$ka = \frac{2\pi a}{\Lambda} = 2\pi a f \sqrt{\frac{\rho}{\mu}} \tag{8–2}$$

where ρ and μ are the density and Lamé constant, respectively, of the matrix. The relations of these parameters among the constituents are

$$\frac{k_i}{k} = \frac{\Lambda}{\Lambda_i} = \sqrt{\frac{\rho_i \mu}{\rho \mu_i}} = 1.2795 \tag{8–3}$$

$$\frac{k_f}{k} = \frac{\Lambda}{\Lambda_f} = \sqrt{\frac{\rho_f \mu}{\rho \mu_f}} = 0.49705 \tag{8–4}$$

where the subscript f signifies that the quantity belongs to the fiber, and the subscript i signifies the interphase. The correspondence between these parameters at several frequencies is listed in Table 8–2.

Table 8–1: Constituent Material Properties for Metal-Matrix Ceramic-Fiber Composite System[2].

Property	Matrix (AA520 Aluminium)	Fiber (Alumina, Al_2O_3)	Interphase (Zirconia, ZrO_2)
Density (kg/m^3)	2600	3700	6300
Young's Modulus (GPa)	66	360	97
Poisson's Ratio	0.31	0.25	0.33
Lamé Constant λ (GPa)	41	144	71
Lamé Constant μ (GPa)	25	144	37
P Wave Speed (m/s)	5920	10800	4800
S Wave Speed (m/s)	3100	6240	2420

Table 8–2: Correspondence Between Frequency, Nondimensional Frequency and Wavelength for Composite System in Table 8–1 ($a = 10\mu$m).

ka	f (MHz)	$k_i a$	$k_f a$	Λ/a	Λ_f/a	Λ_i/a
0.25	12.34	0.3199	0.1243	25.13	50.56	19.64
0.5	24.68	0.6398	0.2485	12.57	25.28	9.821
0.75	37.01	0.9597	0.3729	8.378	16.85	6.547
1	49.35	1.280	0.4971	6.283	12.64	4.911
1.25	61.69	1.599	0.6212	5.027	10.11	3.928
1.5	70.03	1.919	0.7456	4.189	8.427	3.274
1.75	86.37	2.239	0.8698	3.590	7.223	2.806

8-3 Simulation Results

Two sets of computations are performed. In the first, the fiber spacing d is kept constant, and the spectra, for various interphase thicknesses ranging from $b = a$ (no interphase) to $b = 1.3a$, at an interval of $\Delta b = 0.01a$, are computed for 3 fixed fiber spacing values: $d = 3a$, $4a$ and $5a$.

A set of typical plate-averaged response spectra of the displacement amplitude is shown in Fig. 8–4, for the case when $b = 1.1a$ and $d = 3a$. As observed in Chapter 7, the total wave in the backward direction is highly oscillatory and the scattered wave suffices to describe the main characteristics of the scattering. Thus, in all the spectra to be presented, only the scattered wave is shown for the backward direction.

In order to observe the effects of continuously varying parameters, the spectra for a same value of d but different values of b are converted and assembled into a colorized spectrum map, as shown in Fig. 8–5 for the case of $d = 3a$. The conversion is based on a pre-defined one-to-one correspondence between a color and a value of displacement amplitude. This one-to-one correspondence is shown as a *color scale* (also called a *color palette*) accompanying each spectrum map. In a spectrum map, one image line parallel to the ka-axis corresponds to the spectrum for a particular b/a value. Similarly, Figs. 8–6 and 8–7 are spectrum maps for the cases of $d = 4a$ and $d = 5a$, respectively.

In the second set of computations, the interphase thickness is fixed while the fiber spacing d is varied. Two interphase thicknesses are considered. For $b = 1.1a$, the fiber spacing d is varied from $d = 2.25a$ to $d = 5a$ with an interval of $\Delta d = 0.05a$. For $b = 1.2a$, d is varied from $d = 2.4a$ to $d = 5a$ with the same interval. Computed spectra are similarly converted into spectrum maps, as shown Figs. 8–8 and 8–9 for the cases of $b = 1.1a$ and $b = 1.2a$, respectively.

From the spectrum maps in Figs. 8–5 through 8–9, the most striking characteristic is that there is a range of frequency in which the displacement amplitude in the forward direction essentially vanishes. This means that waves whose frequency

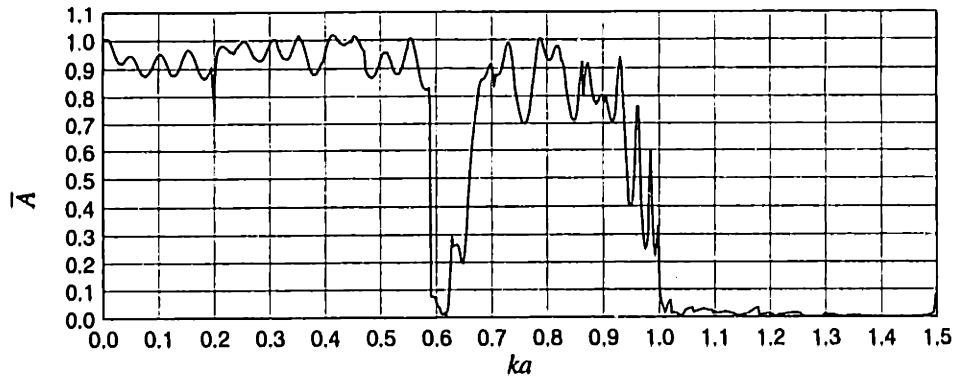

(*a*) Forward spectrum.

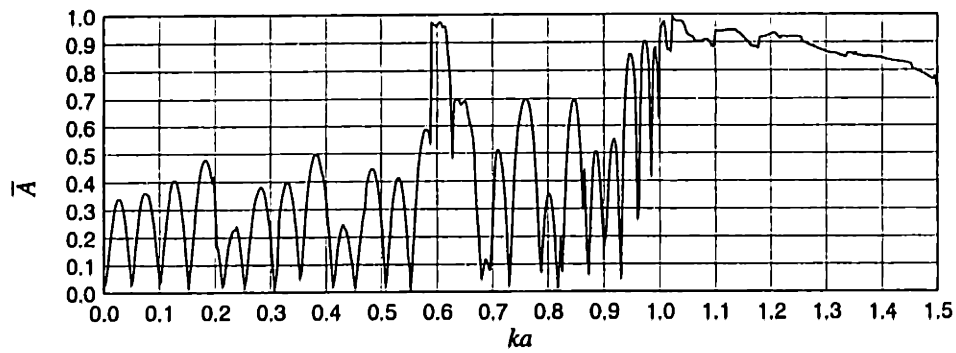

(*b*) Backward scattered wave spectrum.

Fig. 8–4 Spectra of plate-averaged displacement amplitude when $d = 3a$ and $b = 1.1a$.

falls within this range cannot propagate through the model plate, and the plate effectively becomes a *stop-band filter*. This frequency range changes smoothly as one of the parameters changes, and in most cases, the ends of the range are clearly defined.

Other secondary effects can also be observed from these spectrum maps. For a fixed fiber spacing d, in Figs. 8–5 through 8–7, there are numerous streaks along lines at ka equals a constant that appear throughout the frequency range, and are most clearly visible within the stop band. These streaks correspond to small spikes in the spectra, such as the one shown in Figs. 8–4*a* and *b*. Outside the stop band, colors in a spectrum map show less variation as the fiber spacing increases, indicating that the difference between peaks and valleys in a spectrum decreases. In all these spectrum maps, there are patches of features that do not exhibit a pattern of appearance, such as the dip in the forward spectrum in Fig. 8–4*a* around $ka = 0.6$. Another interesting observation is that the number of peaks in these spectra, both the forward and the backward, in the range from $ka = 0$ to the lower edge of the stop band is always 24, the number of fibers in the x-direction, although smaller spikes sometimes interfere with these peaks and valleys to make accounting them from within each spectrum

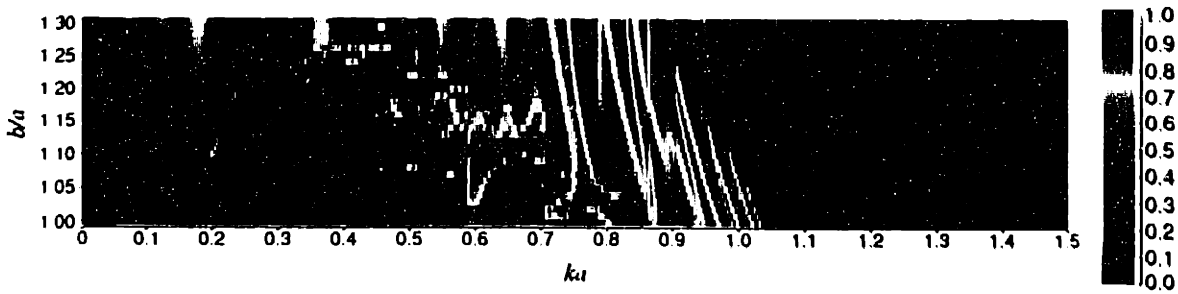

(*a*) Forward spectrum map.

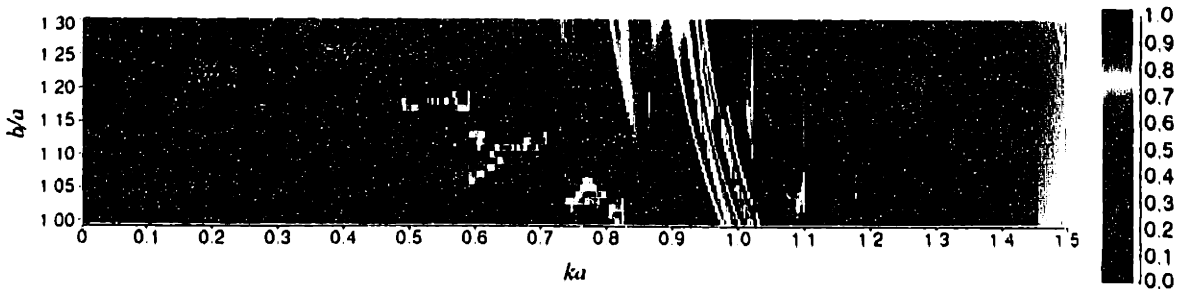

(*b*) Backward scattered wave spectrum map.

Fig. 8–5 Spectrum maps of plate-averaged displacement amplitude when $d = 3a$. (Blocked discrete texture is due to numerical steps.)

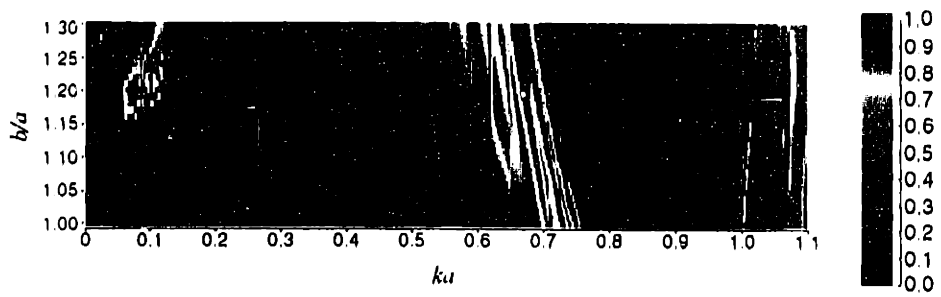

(*a*) Forward spectrum map.

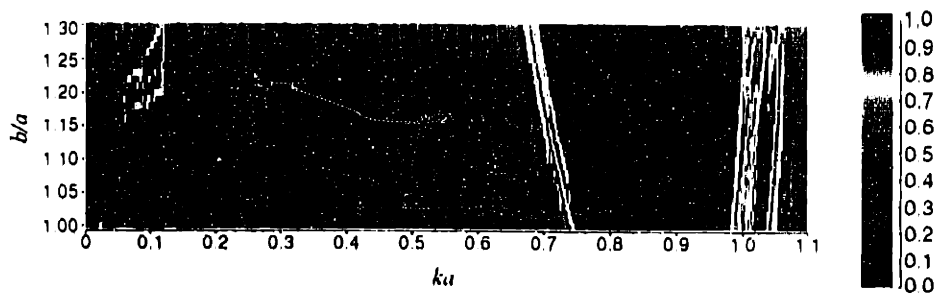

(*b*) Backward scattered wave spectrum map.

Fig. 8–6 Spectrum maps of plate-averaged displacement amplitude when $d = 4a$. (Blocked discrete texture is due to numerical steps.)

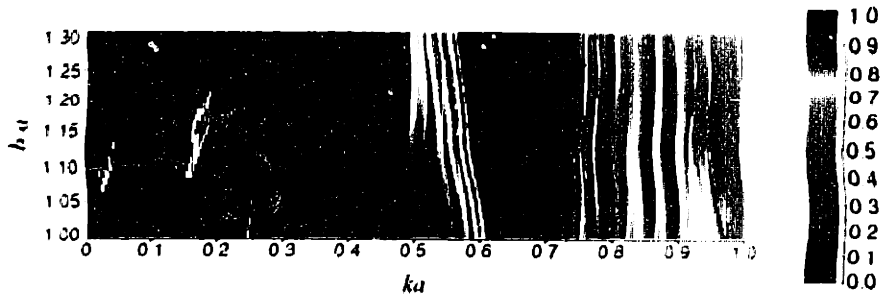

(*a*) Forward spectrum map.

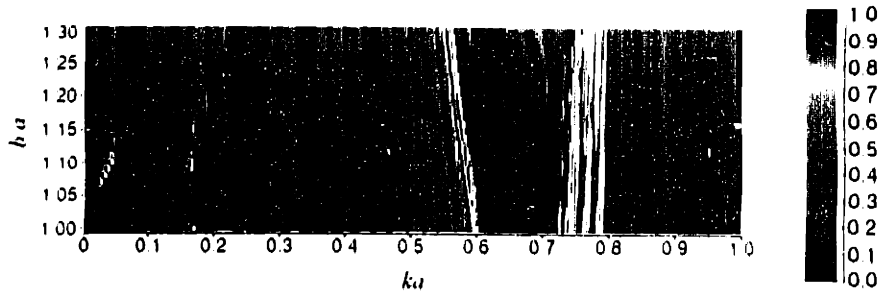

(*b*) Backward scattered wave spectrum map.

Fig. 8–7 Spectrum maps of plate-averaged displacement amplitude when $d = 5a$. (Blocked discrete texture is due to numerical steps.)

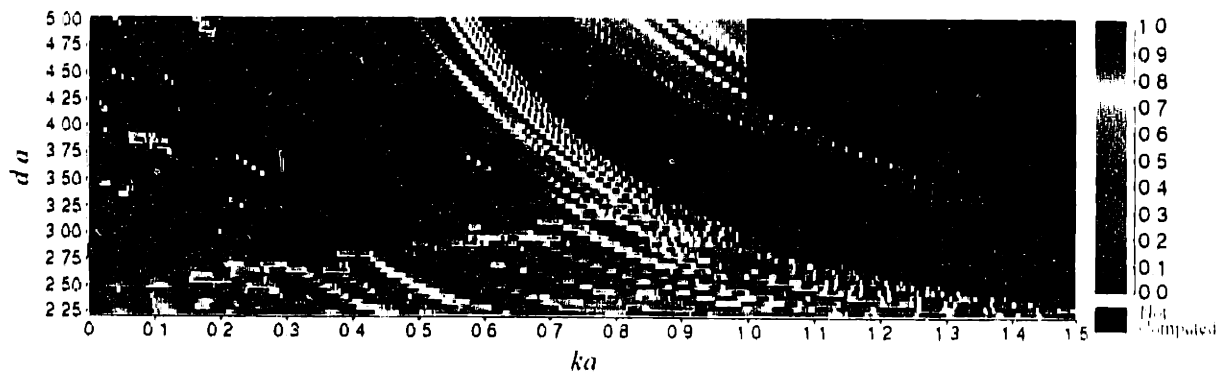

(*a*) Forward spectrum map.

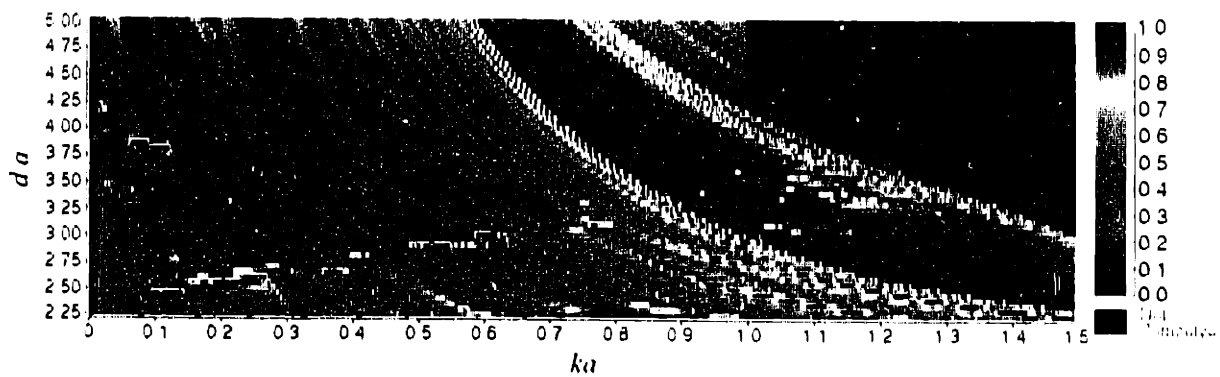

(*b*) Backward scattered wave spectrum map.

Fig. 8–8 Spectrum maps of plate-averaged displacement amplitude when $b = 1.1a$. (Blocked discrete texture is due to numerical steps.)

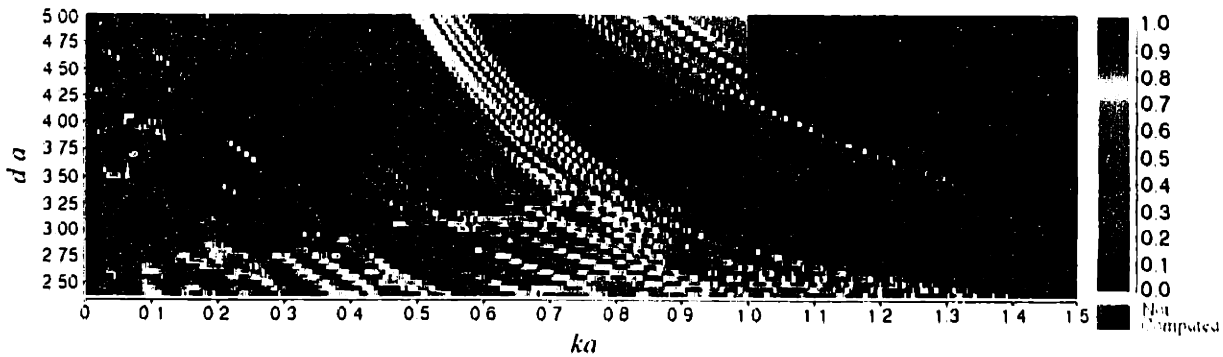

(*a*) Forward spectrum map.

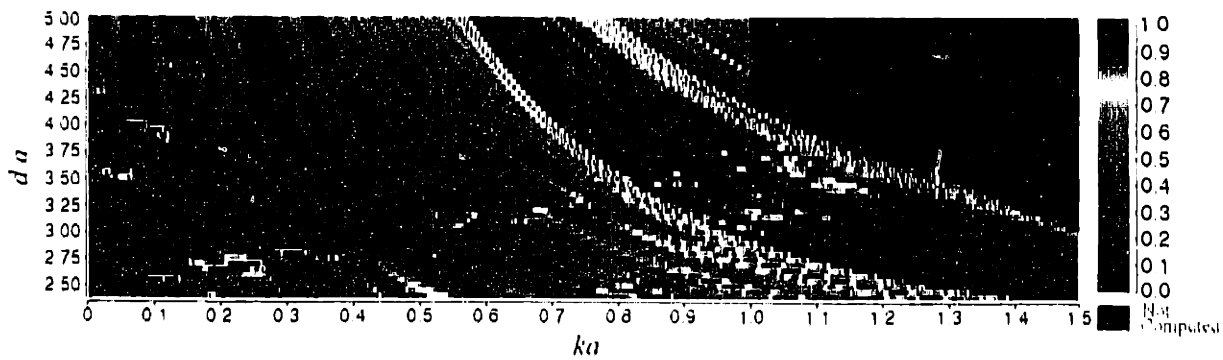

(*b*) Backward scattered wave spectrum map.

Fig. 8–9 Spectrum maps of plate-averaged displacement amplitude when $h = 1.2a$. (Blocked discrete texture is due to numerical steps.)

difficult.

8-4 Data Analyses

Now, relating the characteristics of the stop band with microstructural parameters is attempted. The stop band is the most observable characteristic of the spectra and varies smoothly and monotonically with several parameters. Such characteristics are of significance for material characterization. In these discussions, the lower end frequency of the stop band is referred to as the *cut-off frequency* and the higher end frequency is referred to as the *recovery frequency.* They are collectively called the *critical frequencies.*

8-4.1 A Hypothesis

One of the possible explanations for the appearance of the stop-band is that, at some particular frequency as the wavelength matches one of the structural dimensions, the wave either causes a resonance or is trapped within certain regions of the structure. For the plate model under consideration, Figs. 8–5 through 8–9 indicate that variations in the stop band are more dependent on the parameter d, the fiber spacing, and less so on the parameter b. Therefore, it is likely that the space between the fibers acts as a wave-trapping mechanism, and the regularity of the fiber configuration enhances this wave-trapping effect to form a clearly defined stop band.

Consider a representative element of the model plate as sketched in Fig. 8–10. In accordance with the aforementioned wave-trapping mechanism, it is hypothesized that wave trapping will initiate when the wavelength matches the diagonal dimension along the line AC, the longest dimension of the representative element. Furthermore, waves of shorter wavelength would also be trapped within this space until the wavelength is shorter than the dimension along the line AB, the shortest dimension.

To determine the cut-off frequency, the following relation is proposed:

$$\left(\frac{2a}{\Lambda_f} + \frac{2(b-a)}{\Lambda_i} + \frac{\sqrt{2}d - 2b}{\Lambda}\right)\Bigg|_{\text{cut-off}} = \frac{1}{2} \tag{8–5}$$

where each term on the left-hand side of eqn. (8–5) represents the ratio of the dimenson of one of the constituents to its respective wavelength. In other words, the cut-off occurs when the dimension AC equals one half of the *proportioned wavelength.* Using the relations in eqns. (8–3) and (8–4), and denoting the normalized

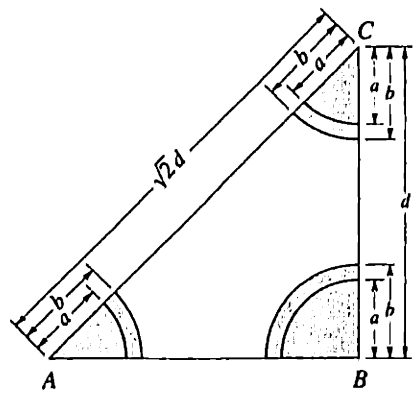

Fig. 8–10 Representative element of microstructure of composite plate model.

cut-off frequency as $k_c a$, then, eqn. (8–5) can be written as

$$k_c a = \frac{\pi}{\frac{\sqrt{2}d}{a} + 2\left(\frac{k_i}{k} - 1\right)\frac{b}{a} + 2\left(\frac{k_f}{k} - \frac{k_i}{k}\right)} = \frac{\pi a}{\sqrt{2}d + 0.5590b - 1.565a} \tag{8–6}$$

where, in writing the last equality, material properties in Table 8–1 have been used.

Similarly, the normalized recovery frequency, denoted as $k_r a$, can be determined by the dimension of line AB as

$$k_r a = \frac{\pi}{\frac{d}{a} + 2\left(\frac{k_i}{k} - 1\right)\frac{b}{a} + 2\left(\frac{k_f}{k} - \frac{k_i}{k}\right)} = \frac{\pi a}{d + 0.5590b - 1.565a} \tag{8–7}$$

8-4.2 Data Fitting

The smooth and monotonic changes of both critical frequencies can be explored using classical data analysis tools. It is noted that the $k_c a$ and $k_r a$ curves in Figs. 8–8 and 8–9 bear a strong resemblance to a curve segment represented by the function $1/d$. And, to take into account the effect of b exhibited in Figs. 8–5 through 8–7, data fitting with the following function is attempted:

$$z = \frac{\pi}{Ax + By + C} \tag{8–8}$$

where $x = d/a$, $y = b/a$, and z can be either $k_c a$ or $k_r a$. In fact, eqn. (8–8) is of the same functional form as eqns. (8–6) and (8–7).

As eqn. (8–8) is a nonlinear equation, an alternative functional form

$$\frac{\pi}{z} = Ax + By + C \tag{8–9}$$

is used in conjunction with the *method of the least squares error* scheme for the data fitting, leading to the following linear equations system:

$$\begin{bmatrix} \sum_{i=1}^{N} x_i^2 & \sum_{i=1}^{N} x_i y_i & \sum_{i=1}^{N} x_i \\ \sum_{i=1}^{N} x_i y_i & \sum_{i=1}^{N} y_i^2 & \sum_{i=1}^{N} y_i \\ \sum_{i=1}^{N} x_i & \sum_{i=1}^{N} y_i & N \end{bmatrix} \begin{Bmatrix} A \\ B \\ C \end{Bmatrix} = \begin{Bmatrix} \sum_{i=1}^{N} \frac{\pi x_i}{z_i} \\ \sum_{i=1}^{N} \frac{\pi y_i}{z_i} \\ \sum_{i=1}^{N} \frac{\pi}{z_i} \end{Bmatrix} \tag{8–10}$$

where (x_i, y_i, z_i) are individual data points, and N is the total number of data points.

In fitting the data, the entire data set, collected from 5 spectrum maps, is placed in a data pool, and only $1/4$ of randomly chosen data is used in a fitting; and the error according to eqn. (8–8) is computed over the entire data set. Such a data fitting process is repeated 50 times, and at the end, the fitted functions, giving the smallest errors, have been found to be

$$k_c a = \frac{\pi a}{1.127563d + 1.217735b - 1.617357} \tag{8–11}$$

and

$$k_r a = \frac{\pi a}{1.131526d - 0.282906b - 1.080639} \tag{8–12}$$

8-4.3 Discussions

Figure 8–11 shows the hypothesized formula for the cut-off frequency in eqn. (8–6) and the data-fiting eqn. (8–11), plotted for several fixed d values, as compared with the cut-off frequencies from the spectrum maps in Figs. 8–5 through 8–7. Figure 8–12 shows eqns. (8–6) and (8–11) plotted for several fixed b values, as compared with the cut-off frequencies from the spectrum maps in Figs. 8–8 and 8–9. Figures 8–13 and 8–14 compare the recovery frequency eqns. (8–7) and (8–12) with similar data.

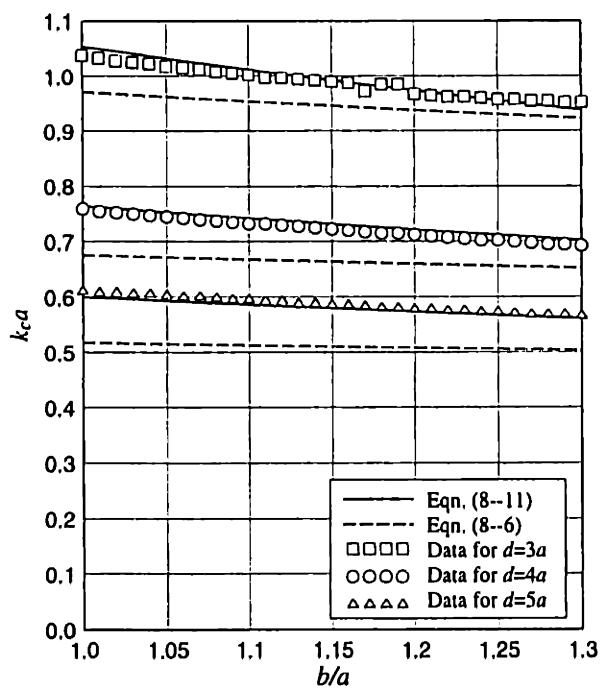

Fig. 8–11 Comparisons of cut-off frequencies according to eqns. (8–6) and (8–11), with simulations from spectrum maps in Figs. 8–5 through 8–7.

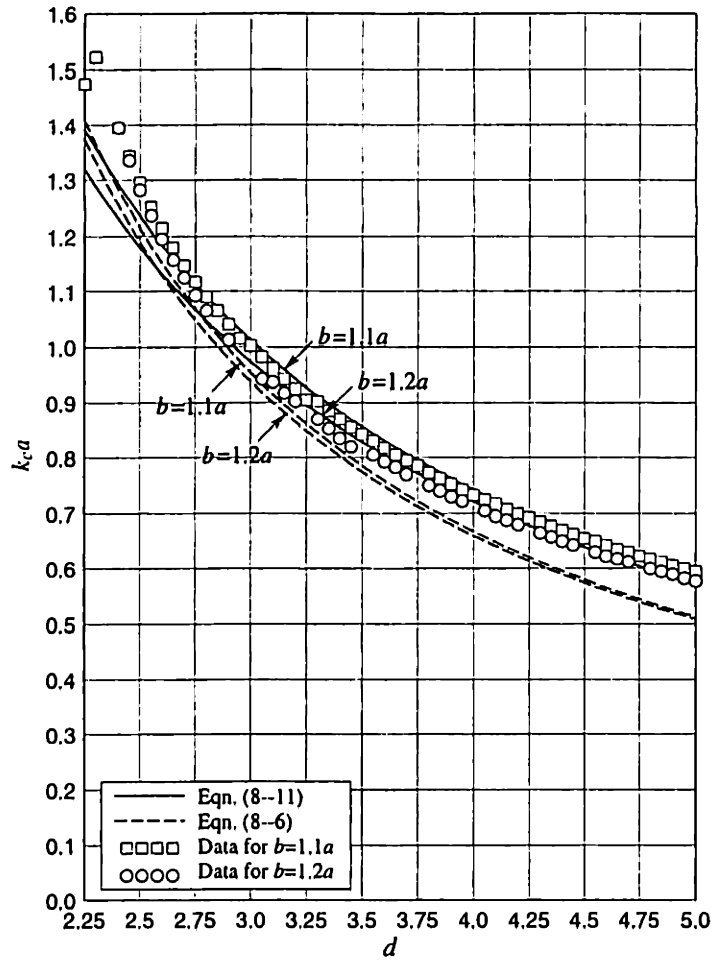

Fig. 8–12 Comparisons of cut-off frequencies according to eqns. (8–6) and (8–11), with simulations from spectrum maps in Figs. 8–8 and 8–9.

From Figs. 8–11 through 8–14, it is observed that the hypothesized formulas predict both the cut-off and the recovery frequencies to a close approximation of the data. Both equations predict the correct functional trends as the parameter d changes. Data in these figures show that parameter b has a lesser effect on both critical frequencies as compared to parameter d. Equation (8–6) predicts the correct trend for the cut-off frequency as the parameter b changes, but eqn. (8–7) predicts an incorrect trend for the recovery frequency.

The data-fitted functions, eqns. (8–11) and (8–12), match the data trends very well. But, in some regions, they do not fit the data as closely as desired. For example, in Fig. 8–11, the curve given by eqn. (8–11) is consistently below or above the data in some cases; in Fig. 8–12, eqn. (8–11) deviates significantly from the data for small d values.

Besides predicting the critical frequencies to a first-order approximation, eqns. (8–6) and (8–7) also incorporate other physical properties of the composite system that are embedded in k_f and k_i. For this reason, such an equation is more

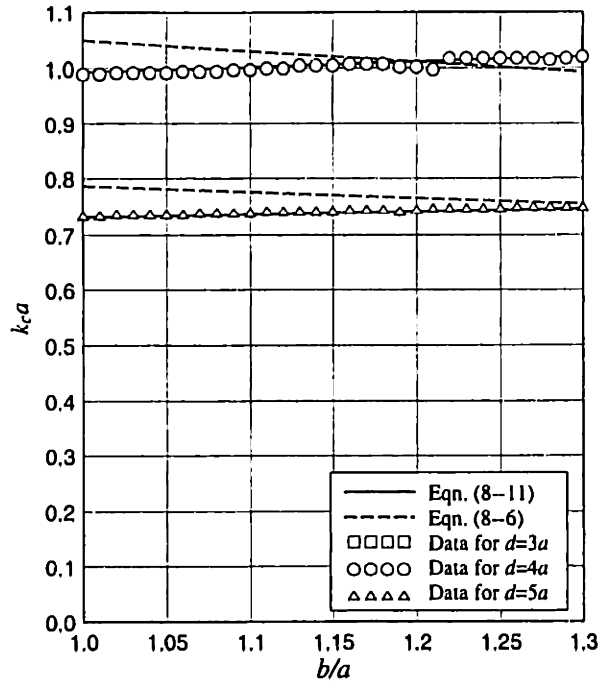

Fig. 8–13 Comparisons of recovery frequencies according to eqns. (8–7) and (8–12), with simulations from spectrum maps in Figs. 8–5 through 8–7.

useful than a data-fitted function since it can be verified by or used for other material systems. In particular, note that the coefficient in front of b/a in these equations is $(k_i/k - 1)$. This causes the formulas to predit different functional trends due to changes of parameter b. As b increases, the predicted critical frequencies decrease for an interphase that is softer than the matrix ($k_i/k > 1$); and decrease for a harder interphase ($k_i/k < 1$).

For the composite system under consideration, the coefficient in front of b/a in eqn. (8–6) is positive and the data show that eqn. (8–6) predicts the correct functional trend of cut-off frequency as b changes, and that eqn. (8–7) predicts an incorrect trend for the recovery frequency. For verification purposes, consider a different composite system — a glass fiber reinforced composite system. The constituents' material properties, after [4], are listed in Table 8–3. For this composite system,

Table 8–3: Constituent Material Properties for a Glass-Fiber Reinforced Epoxy Composite System[4].

Property	Matrix (Epoxy)	Fiber (Glass)	Interphase
Density (kg/m^3)	1250	2560	1905
Young's Modulus (GPa)	4.5	76	40.2
Poisson's Ratio	0.39	0.20	0.33
Lamé Constant μ (GPa)	1.62	31.7	16.6

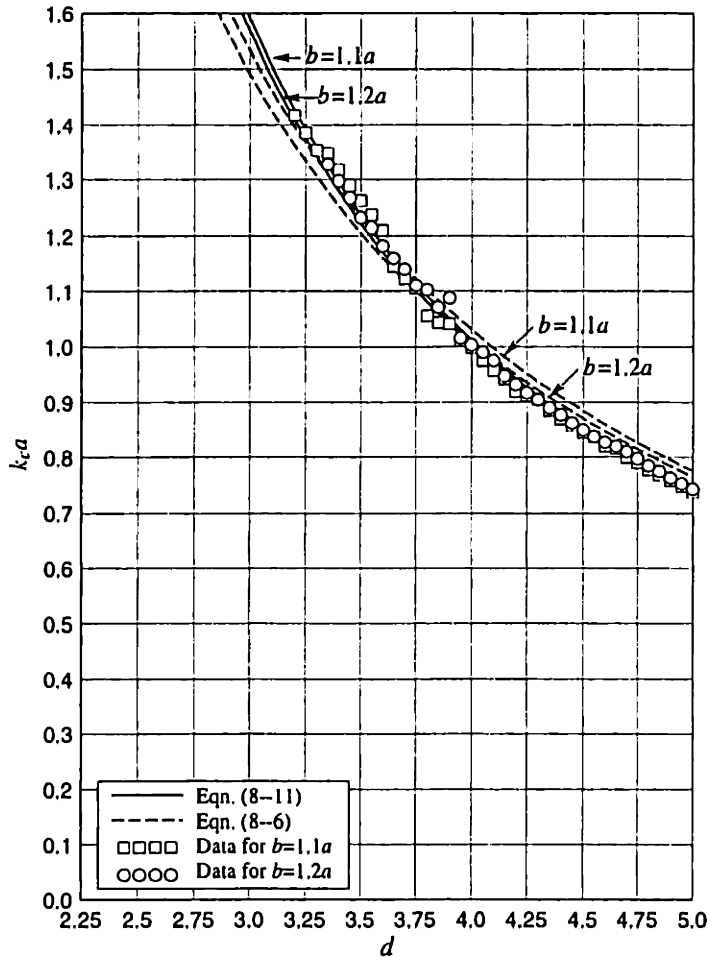

Fig. 8–14 Comparisons of recovery frequencies according to eqns. (8–7) and (8–12), simulation results from spectrum maps in Figs. 8–8 and 8–9.

the properties of the interphase are hypothesized as shown, and $k_i/k = 0.38565 < 1$ and $k_f/k = 0.32351$. The cut-off frequency, according to eqn. (8–5), can be written as

$$k_c a = \frac{\pi a}{\sqrt{2}d - 1.2287b - 0.12428} \tag{8–13}$$

Full-scale simulations for this system are also performed, for the case $d = 3a$ at various b values. The resulting cut-off frequencies as compared to eqn. (8–13) are given in Fig. 8–15. Figure 8–15 shows that the hypothesized formula, eqn. (8–13), again predicts the correct trend due to the change of b, although the data for this case possess a different trend than in the previous case (Figure 8–11). But, the predicted frequencies deviate from the data greater than the previous case.

The inaccuracy of the hypothesized formulas (eqns. (8–6) and (8–7)) and the discrepancy between the data-fitted functions (eqns. (8–11) and (8–12)) and the data suggest a deficiency in this functional form that fails to reflect some secondary effects due to changes of the parameters. These secondary effects may also include

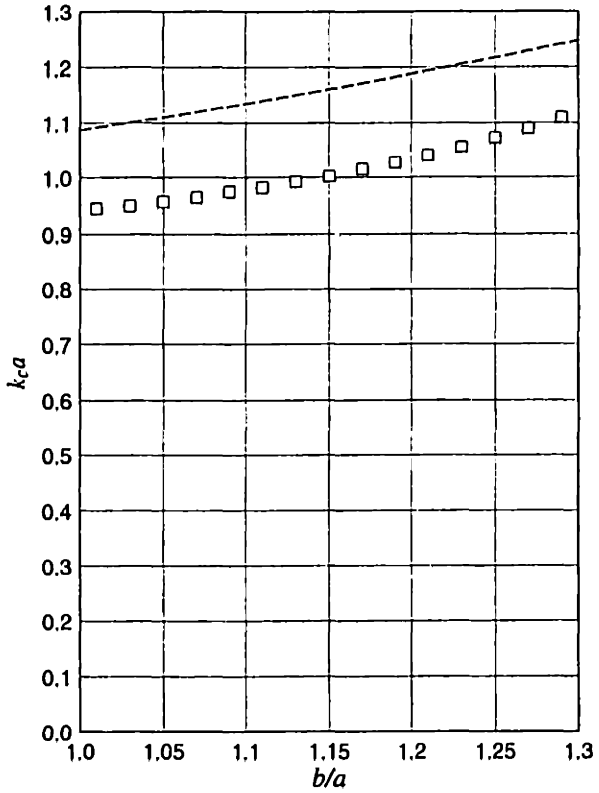

Fig. 8–15 Comparison of cut-off frequencies according to eqn. (8–13) with simulation results for the glass-epoxy composite system.

some other mechanisms that induce the stop-band phenomenon, such as the trapping or the resonance of the waves that reside within the interphase and the fiber.

It is also noted that there are subtle trends in the data that the current functional form, both hypothesized formulas and the data-fitted functions, has failed to capture. For two different b values, as d increases, the difference in their respective cut-off frequencies increases and the difference in their respective recovery frequencies decreases. For the recovery frequency, the curves for different b values cross at a certain d value. These two observations indicate that the functional form, denoted as $f(b,d)$, must have a provision, although very small, such that $\partial f/\partial b \propto d + D$ where D is a constant or be a function of other physical properties.

The simplistic hypothesis proposed in this study is shown to be correct to a first-order approximation, and even correct in the functional trends. Still, a more elaborate model to explain the stop band phenomenon is needed for better accuracy. In exploring a corrected or improved functional form or hypothesis, further trial-and-error data fitting could be helpful.

8-5 Concluding Remarks

In this chapter, more comprehensive deterministic full-scale simulations are performed for the same composite model plate that has been studied in Chapter 6. The simulations are more comprehensive in the sense that two microstructural parameters, the fiber spacing and the outer radius of the interphase, are continuously varied for a wide range in order to examine the effects of their changes.

For the model plate under consideration in which fibers are in a square arrangement, the most striking observation in the simulation response spectra is a feature called the *stop band*. The stop band is a range of frequency within which waves cannot propagate through the model plate. An explanation for the formation of the stop band is hypothesized and a formula is proposed. It is further shown that the proposed formula predicts the critical frequencies of the stop band to a first-order approximation.

Since this chapter is intended only as a comprehensive example of the application of the approach developed in this thesis towards performing full-scale simulations, in-depth study of the stop-band phenomenon and more comprehensive parametric studies of the current model plate are left for future endeavors.

References

[1] H. Yim, J. H. Williams, Jr, Formulation and its energy balance verification for ultrasonic non-destructive characterization of a single fiber composite interphase, *Ultrasonics,* **33**, 377–387, 1995.

[2] H. Yim, J. H. Williams, Jr, Database generation and parametric study for ultrasonic non-destructive characterization of a single fiber composite interphase, *Ultrasonics,* **33**, 389–401, 1995.

[3] Y.-H. Pao, C.-C. Mow, *Diffraction of Elastic Waves and Dynamic Stress Concentrations,* Crane Russak & Co., New York, 1971.

[4] H. Yim, *Acousto-Ultrasonic Nondestructive Characterization of Interphases in Fiber Composites,* Ph. D. Thesis, Massachusetts Institute of Technology, May 1993.

9

Conclusions

Abstract: *In this chapter, the achievements of this thesis and prospective future work are summarized.*

Contents:

9-1 Summary of Achievements

In this thesis, starting from the very basic equations governing the wave fields in elastic media, and classical solutions for a single scatterer problem, a computational system that is capable of obtaining analytically exact solutions for assemblages of thousands of scatterers is built and proved. The achievements of the thesis can be summarized as follows:

- An analytically exact closed-form solution for the single scattering problem involving a layered circular cylindrical scatterer subjected to SH waves is derived. Numerical results are presented for a fiber-interphase-matrix model that is used as a micromechanics model for a ceramic-fiber reinforced metal-matrix composite system.
- The concept of the T-matrix is clarified, and several universal properties of the T-matrix imposed by physical principles and by scatterer geometrical symmetries are derived.
- Analytically exact solutions for multiple scattering of elastic waves in two-dimensions are derived for both the SH and the P/SV wave cases. The solutions are capable of handling an arbitrary number of similar or dissimilar scatterers.
- The multiple-scattering solution is implemented and verified for the SH wave case, and its computational characteristics are observed. Numerical examples for the fiber-interphase-matrix model are presented, and several interesting physical phenomena are noted.
- The methodology of scatterer polymerization is proposed, implemented and verified. Its computational characteristics are discussed.
- Through numerical examples, it is shown that the combined use of the multiple-scattering solution and the scatterer polymerization methodology is capable of performing simulations of fiber-reinforced composites in full scale. Numerical examples are presented to demonstrate the procedure of such a simulation. Relationships between simulation results and experimentally measurable parameters are established, and several interesting physical phenomena are observed.

9-2 Future Work

This thesis explores an approach — theoretical tools and computations procedures — to perform full-scale deterministic simulations of elastic wave scattering in fiber reinforced composites. The emphasis is restricted to formulating, implementing and demonstrating the capability of this approach.

This demonstrated capability opens a new arena for computer simulation of the mechanics of composite materials. Therefore, in the immediate future, comprehensive simulations can be performed to observe the relation between micro-scale parameters and macro-scale properties of composites. Such simulations would enhance the understanding of composite materials, and ultimately assist in relating the parameters in these two scales.

Some interesting physical phenomena have been noted from the limited numerical examples. For example, the appearance of the stop-band characteristics in the spectra of various square fiber arrangements could be explored further. Through more comprehensive numerical examples, further examination of stop-bands and their relations with scatterer properties and configuration should be informative.

There are, however, limitations in this simulation approach. Most noticeably, the methodology of scatterer polymerization is severely restricted by the practical limit of minimum scatterer separation, which is significantly larger than the theoretical limit. It is suspected that this limitation comes from the number of significant figures can be furnished by the native data types of a typical desk-top computer. The possibility of expanding the computation accuracy and decreasing the practical limit of scatterer separation could be explored to extend this approach.

Finally, it is noted that the current implementation was limited to the SH wave cases. Having explored various computational aspects of the SH wave case, it is expected that implementing the P/SV wave case will be straightforward since the two solution forms resemble each other.